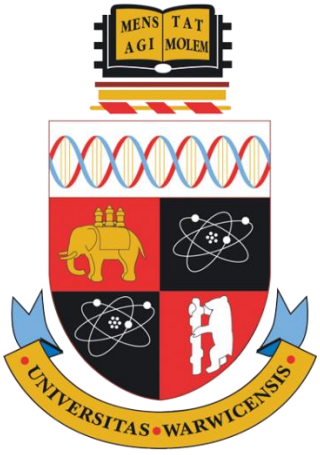

Electrochemical Fundamentals and Application of New Carbon Materials

by

Danqing Liu

Thesis submitted to University of Warwick

For the degree of

Doctor of Philosophy

Department of Chemistry

October 2018

To my baby Yiyi,

And the rest of my loving family,

None of this would have been possible without your support.

Contents

Acknowledgements

I would first like to thank to my supervisor, Prof. Patrick Unwin for giving me the opportunity to initiate my PhD at the Warwick Electrochemistry & Interfaces Group (WEIG) and introducing me into the field of electrochemistry. The present thesis may not be possible without his expert guidance and continuous support. The knowledge, skills and the attitude taught by him in the last four years would definitely guide me in my future career. I also would like to thank Prof. Julie Macpherson for all her help and professional advice.

I deeply appreciate the help of Dr. Chang-hui Chen, Dr. Sharel Pei E., Dr. Guohui Zhang, Dr. David Perry, Binglin Tao, Dr. Minkyung Kang, Dr. Cameron Bentley, Dr. Yangrae Kim, Dr. Aleix Güell, Dr. Robert Lazenby, Dr. Sze-yin Tan, Dr. Ashley Page, Dr. Barak Aaronson, Dr. Lingcong Meng, Lewis Yule and Baoping Chen on the projects during my PhD. Without you all, I may not have reached this far. I thank everyone in the WEIG for being so friendly and helpful.

Furthermore, I want to thank all my friends, Fan Xia, Dr. Sharel Pei. E, Xue Xia, Dr. Geanina Apachitei, Dr. Haiyuan Wang and Zhengdong Luo for sharing happiness and sorrows. I will remember the good time we have spent together!

A special thanks goes to my loving grandpa and parents for all their love and support. I would like to thank my husband, Mingmin Yang. Thanks for always encouraging and supporting me. Thanks for always making my day wonderful. Thanks for your excellent cooking and helping me putting on 20 kg weight during my pregnancy. I am so grateful you are in my life. Finally, I would like to thank my baby. You are my sunshine and I love you more than you can imagine!

Declarations

This thesis is submitted to the University of Warwick in support of my application for the degree of Doctor of Philosophy. The work contained in this thesis is entirely original and my own work, except for the contributions specified below:

Chapter 3: Electron backscatter diffraction image was recorded by Dr. Geoff West. Graphene sample on polycrystalline Cu foil was grew by Xue Xia. Kelvin probe force microscopy was performed by Dr. Neil R. Wilson.

Chapter 4: Electron backscatter diffraction image was recorded by Dr. Geoff West.

Chapter 5: Electrochemical measurements of nickel hydroxide nanoparticles prepared by the direct approach was performed by Dr. Sharel Pei E. High-resolution transmission electron microscopy was done by Dr. Rorbert A. Lazenby. Data analysis of selected diffraction area was done with the help of Dr. Jeremy Sloan. Raman spectroscopy of single-walled carbon nanotubes was done by Dr. Sharel Pei E.

Parts of this thesis have been published or to be submitted, as detailed below:

1. Dan-Qing Liu, Chang-Hui Chen, David Perry, Geoff West, Sam. J. Cobb, Julie V. Macpherson and Patrick R. Unwin. Facet-resolved electrochemistry of polycrystalline boron-doped diamond electrodes: microscopic factors determining the solvent window in aqueous potassium chloride solutions. *Chemelectrochem*, DOI: 10.1002/celc.201800770
2. Sharel P. E, Dan-Qing Liu, Robert A. Lazenby, Jeremy Sloan, Marcio Vidotti, Patrick R. Unwin and Julie V. Macpherson. Electrodeposition of nickel hydroxide nanoparticles on carbon nanotubes electrodes: correlation of particle crystallography with electrocatalytic properties. *J. Phys. Chem. C*, 2016, **120**, 16059-16068
3. Dan-Qing Liu, Bing-Lin Tao, Hong-Cheng Ruan, Cameron Bentley and Patrick R. Unwin. Metal support effects in electrocatalysis at hexagonal boron nitride. *Chem. Commun.*, 2019, **55**, 628-631
4. Dan-Qing Liu, Zachary P. L. Laker, David Perry, Chang-Hui Chen, Xue Xia, Geoff West, Neil R. Wilson and Patrick R. Unwin. Electron transfer kinetics at monolayer, bilayer and multilayer CVD graphene as grown on polycrystalline copper, in preparation

Abstract

The work presented in this thesis focuses on studying the electrochemistry of nanomaterials using an innovative combination of state of the art small-scale electrochemical methods and complementary microscopy techniques. Three classes of material are considered: (i) the functionalization and electrocatalytic applications of sp^2 carbon materials, with a focus on single-walled carbon nanotubes (SWNTs), with nickel hydroxide nanoparticles ($Ni(OH)_2$ NPs) electrodeposited onto them through two different approaches; (ii) a fundamental electrochemical study of boron doped diamond (BDD) (sp^3 carbon), in which the microscopic factors that determine the aqueous solvent window in chloride-containing salt solutions were examined by using scanning electrochemical cell microscopy (SECCM); (iii) a study of the electrochemical behaviour of sp^2 carbon materials at the nanoscale by employing SECCM, focusing on the electron transfer (ET) kinetics of graphene on a Cu foil and the hydrogen evolution reaction (HER) electrocatalytic activities of graphene-like hexagonal boron nitride (h-BN) on different metal substrates (Cu and Au).

Using a macroscale droplet method, functionalized SWNTs with nickel hydroxide, $Ni(OH)_2$, nanoparticles (NPs) of different crystallographic orientations are formed by two approaches. The first involves the electrodeposition of Ni NPs that are converted to $Ni(OH)_2$ through potential cycling in alkaline media to form ordered β-phase $Ni(OH)_2$ NPs (indirect approach). The second uses the electrochemical generation of a relative high concentration of OH^-, in the presence of Ni^{2+}, to lead to the formation of disordered α-phase $Ni(OH)_2$ NPs (direct approach). $Ni(OH)_2$ NPs prepared by the direct approach show a remarkable electrocatalytic activity towards alcohol oxidation, with specific activities (SA) of ~2.8 kA g^{-1} for 0.5 M methanol and ~3.7 kA g^{-1} for 0.5 M ethanol. In contrast, SWNT-$Ni(OH)_2$ produced by the indirect approach shows SA values about an order of magnitude lower. This work reveals the capability of electrochemistry for synthesizing different nanostructures and highlights the correlation of particle crystallography with electrocatalytic properties.

Electrochemical studies can be extended to the microscale and nanoscale by using voltammetric SECCM. The solvent window of BDD, a sp^3 carbon material, in aqueous potassium chloride solutions is investigated both for oxygen- and hydrogen-terminated surfaces. The solvent window is shown to be strongly linked to the local dopant

concentrations, with lower dopant concentrations leading to a wider window. The surface termination is a particularly important factor, with the solvent window of the H-terminated surface being wider than for the O-terminated surface for similar boron dopant levels. Furthermore, the anodic potential window of the O-terminated surface is greatly diminished due to chloride electro-oxidation. This study provides new perspectives on the factors that control the solvent window of BDD at the level of a single facet for a complex heterogeneous electrode.

Finally, the electrochemistry of graphene and graphene-like h-BN is explored, at nanoscale, as examples of very important 2D materials. High-resolution SECCM is employed to assess the ET kinetics for the $Ru(NH_3)_6^{3+/2+}$ couple across as-grown CVD graphene produced by chemical vapour deposition. A correlation between the ET kinetics and the number of graphene layers is found, indicating that monolayer graphene exhibits faster ET kinetics than that observed for the bi- and multilayer graphene. These differences in ET kinetics provide insight into how the electrochemical properties of graphene-based devices can be manipulated with wide-reaching applications including in sensors and energy storage. Furthermore, the electrocatalytic performances of as-grown CVD h-BN on a Cu foil (h-BN/Cu) and h-BN transferred to a Au substrate (h-BN/Au) toward the HER are studied by using single-barrel SECCM. The Tafel slopes are estimated to be 136 mV per decade and 108 mV per decade for h-BN/Cu and h-BN/Au, respectively and the exchange current densities are 4×10^{-8} A cm^{-2} and 1×10^{-6} A cm^{-2}. Importantly, the results suggest that the enhanced HER activity is associated with the interaction between the h-BN and the underlying metal substrate which promotes hydrogen adsorption on the h-BN surface. This work indicates that heterostructures formed by h-BN when supported on different metal substrates could be to modulate the electrocatalytic activity towards the HER.

Abbreviations

AC	Alternating current
AFM	Atomic force microscopy
AM	Amplitude modulation in KPFM
AOR	Alcohol oxidation reactions
ARPES	Angle-resolved photoemission spectroscopy
BDD	Boron-doped diamond
BL	Bilayer graphene
BN	Boron nitride
BNNS	Boron nitride nanosheets
CE	Counter electrode
CNTs	Carbon nanotubes
CPD	Contact potential difference
CV	Cyclic voltammetry
CVD	Chemical vapour deposition
cCVD	Catalyzed chemical vapor deposition
DFT	Density functional theory
DOS	Density of states
EBSD	Electron backscatter diffraction
EDS	Energy-dispersive X-ray spectroscopy (EDS)

EOR	Ethanol oxidation reaction
ET	Electron transfer
FCC	Face centred cubic
FE-SEM	Field emission scanning electron microscopy
FM	Frequency modulation
H-BDD	Hydrogen terminated boron doped diamond
h-BN	Hexagonal boron nitride
HER	Hydrogen evolution reaction
HF	Hot filament
HOPG	Highly ordered pyrolytic graphite
HPHT	High pressure and high temperature
HR-TEM	High resolution transmission electron microscopy
KPFM	Kelvin probe force microscopy
LSV	Linear sweep voltammetry
MC	Microcrystalline
MCEM	Micro-capillary electrochemical method
ME	Mechanically exfoliated
ML	Monolayer graphene
MIL	Multilayer graphene
MIT	Metal-to-insulator transition

MOR	Methanol oxidation reaction
MWs	Microwaves
MWNTs	Multi-walled carbon nanotubes
NC	Nanocrystalline
NDC	Nondiamond carbon
NPs	Nanoparticles
O-BDD	Oxygen terminated boron doped diamond
OER	Oxygen evolution reaction
ORR	Oxygen reduction reaction
PMMA	Polymethylmethacrylate
QRCE	Quasi-reference counter electrode
SAED	Selected area electron diffraction
sccm	Standard cubic centimeters hydrogen
SCE	Saturated calomel reference
SECM	Scanning electrochemical microscopy
SECCM	Scanning electrochemical cell microscopy
SE2	Secondary electrons
SIMS	Secondary ion mass spectrometry
SPEs	Screen printed graphitic electrodes
SWNTs	Single-walled carbon nanotubes

UCN	Ultra-nanocrystalline
UME	Ultramicroelectrode
WE	Working electrode

Glossary of Symbols

A	area
a_O	Activity of species O
a_R	Activity of species R
C	Concentration
C_i	Concentration of species i
C_O	Concentration of oxidized reactant; initial concentration
C_R	Concentration of reduced reactant
D	Diffusion coefficient
D_i	Diffusion coefficient of species i
D_R	Diffusion coefficient of reduced reactant
d	Spacing of diffraction plane; Contact diameter
E	Potential
e	Electron
E_1	Initial potential
E_2	Predetermined potential
$E_{1/2}$	Half-wave potential
$E_{1/4}$	Potential value at i/i_p =1/4
$E_{3/4}$	Potential value at i/i_p =3/4
E^0	Standard redox potential

$E^{0\prime}$	Formal electrode potential
E_{eq}	Equilibrium potential
E_{fs}	Fermi energy level of sample
E_{ft}	Fermi energy level of tip
ΔE_p	Peak-to-peak separation
E_p^a	Anodic peak potential
E_p^c	Cathodic peak potential
E_s	Surface potential in SECCM
E_V	Vacuum energy level
F	Faraday's constant
F_{es}	Electrostatic force
H_{ads}	Hydrogen atom adsorbed on a surface
I_{2D}	2D band intensity of Raman spectrum
I_G	band intensity of Raman spectrum
i_{AC}	AC component of SECCM barrel current
i_{DC}	DC component of SECCM barrel current
i_{lim}	Limiting current
i_p^a	Anodic peak current
i_p^c	Cathodic peak current
i_{surf}	Surface current of SECCM

J_i	Flux of species i
j_0	Exchange current density
k_b	Backward reaction rate constant
k_f	Forward reaction rate constant
k_0	Standard heterogeneous electron transfer rate constant
M	Molar mass
n	Electrons transferred; number of measurements; integer
O	Oxidised form of the redox species
Q_{ox}	Charge associated with oxidation
Q_{red}	Charge associated with reduction
R	Molar gas constant; Reduced form of the redox species
T	Temperature
v	Velocity; scan rate
V_{CPD}	Contact potential difference
z_i	Charge of species i
γ	Activity coefficient
η	Overpotential
α	Charge transfer coefficient
$\emptyset_{tip}$	Work function of tip in KPFM
$\emptyset_{sample}$	Work function of sample in KPFM

λ	Wavelength of electrons
θ	Angel of incidence of the electrons on the diffracting plane

Chapter 1. Introduction

This chapter presents an overview of carbon materials with specific reference to their structure and the different growth methods used for sp^2 and sp^3 carbon materials. The fundamental electrochemical properties of graphene and previous electrochemistry studies of them are summarised. Special consideration is given to the use of boron-doped diamond (BDD) as an electrode material for electrochemical applications. Further introduction is given on the functionalization of single-walled carbon nanotubes (SWNTs) and their electrochemical performance in biosensors. Finally, the electrochemistry of a graphene like material, boron nitride (BN), is reviewed. These topics are developed in the subsequent chapters.

1.1 Dynamic electrochemistry

The investigation of interfaced charge transfer processes at an electrode under the application or measurement of an external potential or current is referred to as dynamic electrochemistry. This field of study encompasses a range of different electrochemical techniques, such as cyclic voltammetry, pulse voltammetry and electrochemical impedance spectroscopy.

1.1.1 Processes involved in an electrode reaction

For a general electrode reaction, $O + ne^- \rightleftharpoons R$, when an external potential is applied, the equilibrium will be disturbed. Processes of an electrode reaction usually involves several steps: 1) mass transfer of the redox species to the electrode surface; 2) electron transfer at the electrode surface; 3) chemical reactions before, or after, the electron transfer; 4) other surface reactions including adsorption, desorption or electrodeposition, as illustrated in Figure 1.1.[1,2]

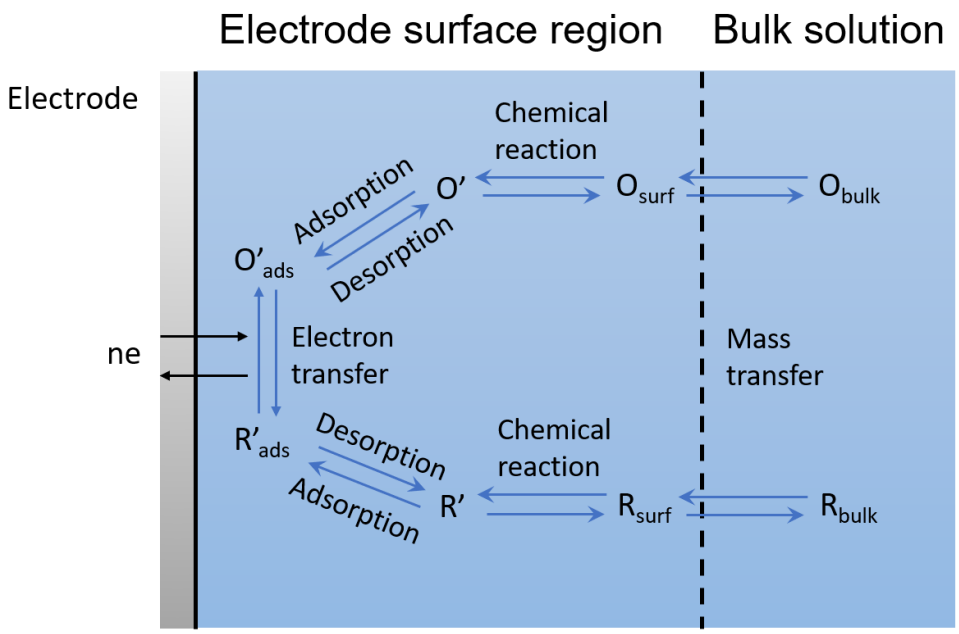

Figure 1.1. Different stages of a general electrochemical reaction at an electrode interface.

The rate constants for some of these electrode reaction processes depend on the external potential that is applied. The simplest electrode reaction only involves the mass transfer of a reactant to the electrode surface, heterogeneous electron transfer, and the mass transfer of the product to the bulk solution. In this case there are two kinds of rate constants involved. One is the mass transfer coefficient which reflects the rate at which the reactant travels from the bulk solution to the electrode surface; the other is the potential-dependent electron transfer rate constant which determines the charge transfer rate across the electrode surface. The overall reaction rate of the electrode reaction is limited by the slowest step which is called the rate determining steps.

1.1.2 Mass transfer

Mass transfer results from one or more of three different modes: migration, diffusion and convection.[3] One dimensional mass transfer to an electrode surface can be presented by the Nernst-Plank equation,[4]

$$J_i(x) = -D_i \frac{\partial C_i(x)}{\partial x} - \frac{z_i F}{RT} D_i C_i \frac{\partial \emptyset(x)}{\partial x} + C_i v(x) \qquad (1.1)$$

where $J_i(x)$ is the flux of species i (mol s^{-1} cm^{-2}) at distance x from the surface, D_i is diffusion coefficient (cm^2/s), $\frac{\partial C_i(x)}{\partial x}$ is the concentration gradient at distance x, $\frac{\partial \emptyset(x)}{\partial x}$ is the potential gradient, z_i and C_i are the charge and concentration (mol cm^{-3}) of species

i, and $v(x)$ is the velocity (cm/s) with which a volume element in solution moves along the axis.

Migration refers to the movement of a charged species under the influence of an electric field. Migration effects of the analyte (if charged) in electrochemical systems can be suppressed by the addition of an inert supporting electrolyte, that is electrolyte which is not involved directly in the electrochemical reaction. The concentration of the supporting electrolyte is typically much larger than the electroactive species (usually by around 100 times), maintaining the ionic strength and increasing the conductivity of the solution, resulting in the minimisation of IR drop in the electrochemical cell.

Diffusion is the most common mechanism of mass transport in electrochemical systems. It is the movement of species through solution due to a gradient in the chemical potential with in a system. Species move from high concentration (e.g. in bulk solution) to low concentration (e.g. the electrode). The lower concentration, at the electrode surface, would result from electrolysis, locally depleting the solution.

The diffusion profiles that are seen in electrochemical systems, vary depending strongly on the geometry, that is the size and shape, of the electrode used. As shown in Figure 1.2, planar diffusion is most commonly observed on macroscale electrodes, whereas a hemispherical diffusion profile is observed at micro/nanoscale electrodes, under steady-state conditions.

Convection is hydrodynamic transport caused as a result of either natural convection (caused by a density gradient) or a forced convection (caused by stirring). Convection can be avoided by preventing stirring and vibrations in electrochemical cell.

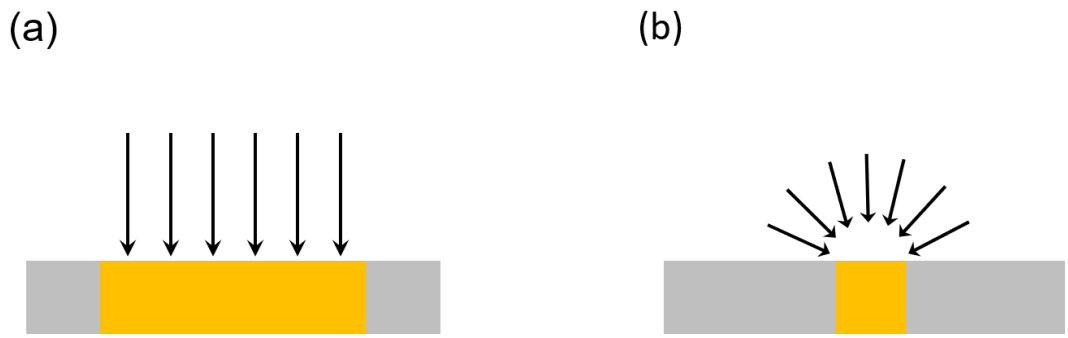

Figure 1.2: Schematic of profiles for (a) planar diffusion and (b) hemispherical diffusion on macroscale electrode and micro/nanoscale electrode, respectively.

1.1.3 Electron transfer (ET) kinetics

In electrochemistry, the Nernst equation links the electrode potential E and the concentrations of the participants in the electrode reaction.

$$E = E^0 + \frac{RT}{nF} ln \frac{a_O}{a_R} \tag{1.2}$$

where E is electrode potential, E^0 is standard redox potential, n is the number of electrons transferred per redox species, R is the gas constant, T is the temperature, F is Faraday's constant and a_O and a_R are the activities of the oxidized and reduced species, respectively. The activity of species, a, can be related to the concentration C via $a = \gamma C$, where γ is the activity coefficient of the species. γ tends to be constant at low concentrations, so can write:

$$E = E^0 + \frac{RT}{nF} ln \frac{\gamma_O}{\gamma_R} + \frac{RT}{nF} ln \frac{C_o}{C_R} \tag{1.3}$$

where C_O and C_R are the concentrations of the oxidized and reduced species, and formal electrode potential ($E^{0\prime}$) can be written as: $E^{0\prime} = E^0 + \frac{RT}{nF} ln \frac{\gamma_O}{\gamma_R}$

For the simple electrode reaction being considered, we can also examine the kinetics:

$$O + ne^- \underset{k_b}{\overset{k_f}{\rightleftharpoons}} R \tag{1.4}$$

k_f and k_b are the heterogeneous rate constants of the forward and backward reactions, respectively.

When a potential is applied to drive the ET occurs, the driving force, the overpotential, is defined as the difference between the applied potential (E) and the formal electrode potential ($E^{0\prime}$):

$$\eta = E - E^{0\prime} \tag{1.5}$$

k_f and k_b have an exponential dependence on the electrode overpotential, η,

$$k_f = k^0 e^{\frac{-\alpha nF\eta}{RT}} \tag{1.6}$$

$$k_b = k^0 e^{\frac{(1-\alpha)nF\eta}{RT}} \tag{1.7}$$

where α is the charge transfer coefficient, k^0 is the standard heterogeneous rate constant. The current that is produced as a result of the overpotential is proportional to the flux of species at the electrode surface, j

$$i = nAFj \tag{1.8}$$

where A is the area of the electrode, and j is defined by:

$$j = k_f C_O - k_b C_R \tag{1.9}$$

Substituting equations 1.6 and 1.7 into 1.9 produces the Butler-Volmer equation.

$$i = nAFk^0\left[C_O e^{\frac{-\alpha nF\eta}{RT}} - C_R e^{\frac{(1-\alpha)nF\eta}{RT}}\right] \quad (1.10)$$

1.1.4 Redox couples

In electrochemical systems, it is important to distinguish outer-sphere and inner-sphere reactions at electrodes. As illustrated in Figure 1.3, in an outer-sphere electrode reaction, the reactant and product species do not strongly interact with the electrode surface, with the species usually localized at a distance of around the dimensions of the solvent layer from the electrode.[5] For example, $Ru(NH_3)_6^{3+/2+}$ is a typical outer-sphere redox couple, in which there is no direct bond between redox partners and no change in coordination sphere. In contrast for an inner-sphere electrode reaction, there is a strong interaction of the reactant and products with the electrode.[5] A typical example of such a reaction is the reduction of oxygen in water. A key feature of inner-sphere electrode reactions is that they tend to be more dependent on the electrode material, and are strongly influenced by surface heterogeneities.[6]

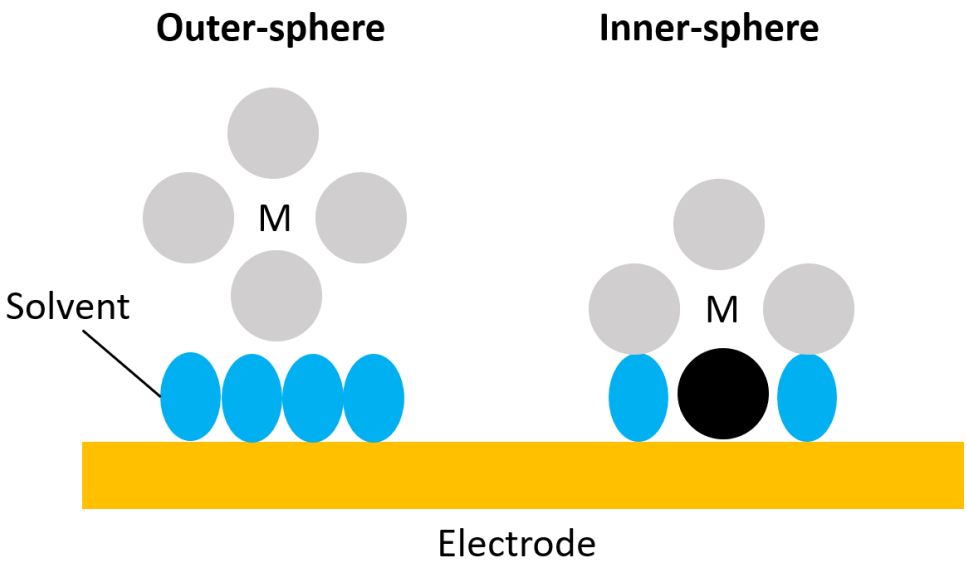

Figure 1.3: Outer-sphere and inner-sphere reactions. In a heterogeneous reaction, a metal ion (M) is surrounded by ligands. In outer-sphere reactions, there is no strong interaction with the electrode. In inner-sphere reactions, a ligand adsorbs on the electrode and bridges to the metal as indicated by the black colour.

1.1.5 Cyclic voltammetry

Cyclic voltammetry (CV) is a type of potentiodynamic electrochemical technique, which has become a popular tool for electrochemical reaction studies.[7,8] In a typical CV experiment, the voltage applied to the working electrode is ramped linearly from an initial potential, E_1, to a predetermined limit, E_2. Different from linear sweep voltammetry (LSV), at this point, the applied potential is swept to its original value E_1 or a different value in a reverse direction (Figure 1.4a). The current is recorded and plotted as a function of applied voltage, with typical current responses for a macroelectrode and an ultramicroelectrode (UME, diameter < 25 μm) shown in Figures 1.4b and c.

In Figure 1.4b, for a macroelectrode, only reduced reactant, R, is present in bulk solution. If the scan is swept to a positive potential, an oxidation reaction takes place. When the scan is at a potential well negative of the $E^{0'}$ for the oxidation process, only a nonfaradaic current flows. When the scan potential reaches the $E^{0'}$, the oxidation begins. As the applied potential becomes more positive, the surface concentration of the reactant drops and there is an enhanced flux to the surface (the current). With more positive potential, the surface concentration drops nearly to zero, and the current increases exponentially until reaching an anodic peak, i_p^a at the potential of E_p^a. Then it declines as depletion effects begin to occur. When the potential is scanned back, a similar feature is obtained, showing a cathodic peak, i_p^c at the potential of E_p^c. The peak to peak separation, ΔE_p,

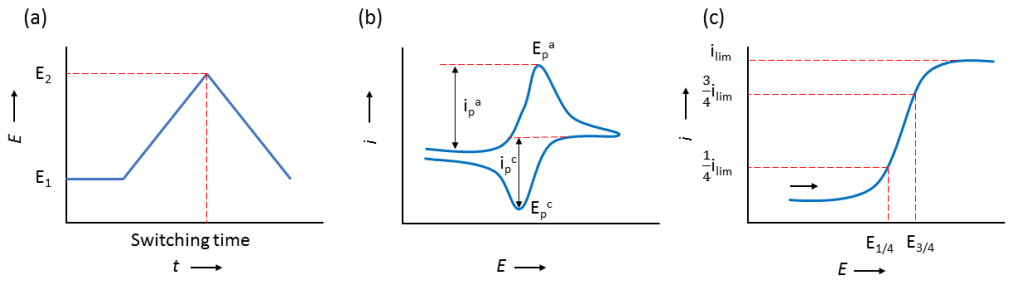

Figure 1.4: (a) Schematic of the potential profile in cyclic potential cycling. (b) A typical CV of a reversible reaction taking place at a macroelectrode. The potential is swept from E_1 to E_2 and then back to reversible direction. E_p^a and E_p^c are the anodic and cathodic peak potentials, respectively. i_p^a and i_p^c are the anodic and cathodic peak currents. (c) A typical CV for an ultramicroelectrode. i_{lim} is the limiting current, where $E_{\frac{3}{4}}$ and $E_{\frac{1}{4}}$ is the potential at current values equals to ¾ and ¼ of i_{lim}.

$$\Delta E_p = E_p^a - E_p^c \tag{1.11}$$

can be used to determine the reversibility of an electrochemical reaction.[9] For a reversible reaction (with high k^0), the processes follow the Nernst equation and an electrochemical equilibrium is established immediately upon any change in applied potential, resulting in a small ΔE_p (59/n mV). By contrast, for quasi-reversible and irreversible processes (with low k^0), ET reactions are sluggish and a larger overpotential is needed, giving rise to an increase in ΔE_p(> 59/n mV). For example, the method developed by Nicholson[9] has been frequently used for extraction of k^0 from quasi-reversible CVs:

$$\psi = \frac{(D_O/D_R)^{\alpha/2} k^0}{(\pi D_O \nu F/RT)^{1/2}} \tag{1.12}$$

Where D_O and D_R are the diffusion coefficient for oxidized and reduced reactant in cm^2/s and υ is the scan rate in V/s. After measuring the ΔE_p experimentally, one can use Table 1.1 to find the corresponding value of ψ.[9] When 0.3< α<0.7, which is most common for simple ET reaction, the ΔE_p is independent of α. Moreover, D_O and D_R are typically similar. Therefore $(D_O/D_R)^{\alpha/2} \cong 1$, and the k^0 can be easily obtained from equation (1.12).

Table 1.1 Variation of ΔE_p with ψ at 25 °C

$\boldsymbol{\psi}$	$\boldsymbol{\Delta E_p}$
20	61
7	63
6	64
5	65
4	66
3	68
2	72
1	84
0.75	92
0.5	105
0.35	121
0.25	141
0.10	212

The peak current, i_p^a or i_p^c, is proportional to the square root of the scan rate ($\nu^{1/2}$) for a reversible process according to the Randles-Sevcik equation:[10]

$$i_p^a = 0.446nFAC_R \left(\frac{nFD_R\nu}{RT}\right)^{\frac{1}{2}} \tag{1.13}$$

At 298 K,

$$i_p^a = (2.69 \times 10^5) n^{\frac{3}{2}} A D_R^{\frac{1}{2}} C_R v^{\frac{1}{2}} \quad (1.14)$$

The shape of the current-voltage response for an UME, can be more complicated. At short timescale (high v), the diffusion layer thickness remains small compared to the diameter of the UME and a CV similar to that shown in Figure 1.4b may be obtained. However, at longer timescale (low v), the diffusion layer thickness is large compared to the diameter of the UME, then hemispherical diffusion dominates. The depletion of the diffusion layer of the redox species does not take place, then a steady-state response in Figure 1.4c occurs. The most common shape of UME is a disk shape electrode, and the limiting current (i_{lim}) obtained is determined by:[11]

$$i_{lim} = 4naFD_R C_R \quad (1.15)$$

where a is the radius of the UME. For a reversible process in a UME system,

$$E_{3/4} - E_{1/4} = \frac{59}{n}\ mV \quad (1.16)$$

where $E_{3/4}$ and $E_{1/4}$ is the potential at current values equals to ¾ and ¼ of i_{lim}, respectively.[12]

For quasi-reversible processes (ET reaction is kinetically limited) studied by steady-state voltammetric techniques, k^0 and α parameters can be found directly from the values of quartile potentials, $E_{1/4} = |E_{1/2} - E_{1/4}|$ and $E_{3/4} = |E_{3/4} - E_{1/2}|$.[13] Two extensive tables are available in reference 13 for uniformly accessible electrodes and for microdisk geometry. For example, the kinetics parameters of a hemispherical microelectrode such as λ, α and $E^{0\prime}$ can be found from Table I for given values of $|E_{1/2} - E_{1/4}|$ and $|E_{3/4} - E_{1/2}|$. k^0 in this case is

$$k^0 = \lambda m_O = \lambda D_O / r_0 \quad (1.17)$$

where m_O is the mass transfer coefficient of oxidized reactant and r_0 is the electrode radius.

1.1.6 Scanning electrochemical cell microscopy (SECCM)

Double-barrel scanning electrochemical cell microscopy (SECCM), developed in 2010 in the Warwick Electrochemistry and Interface Group (WEIG),[14-17] is a micropipette based imaging technique, which allows for simultaneous mapping of heterogeneous ET rates, surface topography and ion conductance. Furthermore, in 2017, single channelled SECCM was employed by our group to address new areas in high-resolution (down to 30 nm) electrochemistry,[18] such as the current-voltage relationship

of nanoscale sites (steps or edges) on the surface of 2D materials, and the electrochemical properties of single entities (nanoparticles). This technique allows for synchronous topographical/electrochemical imaging with high spatial resolution and fast image acquisition rates, helping to provide new views of nanoscale structure dynamics within electrocatalytic materials.

Schematics illustrating the double-barrel and single-barrel SECCM method is shown in Figure 1.5a and 1.5b, respectively. The double-barrel pipette is filled with electrolyte and contains a quasi-reference counter electrode (QRCE) inserted into each barrel (Figure 1.5a). High precision control of the position of meniscus at the end of the pipette across the substrate of interest is achieved through mounting the probe on a piezoelectric positioner, which allows the pipette to move in all three dimensions. Control of the movement is based on a feedback loop using the ion conductance current (i_{DC}), generated by applying a bias, V_2, between the QRCEs. Applying a potential, V_1, to one of the QRCEs means that the effective potential of the substrate, E_s, is - (V_1 + V_2 / 2) relative to the ground.[14] V_2 is fixed and E_s can be adjusted by changing V_1. The current flowing through the working electrode is denoted as i_{surf}.

During SECCM experiments, the pipette may also be oscillated perpendicular to the surface by a lock-in amplifier. This generates an AC component of the current signal (i_{AC}) which can also be used for positional feedback. When the meniscus contacts the surface, an increase in the i_{DC} signal is detected as a result of the change in meniscus size (wetting effect) and hence the local gap resistance. The deformation of the meniscus

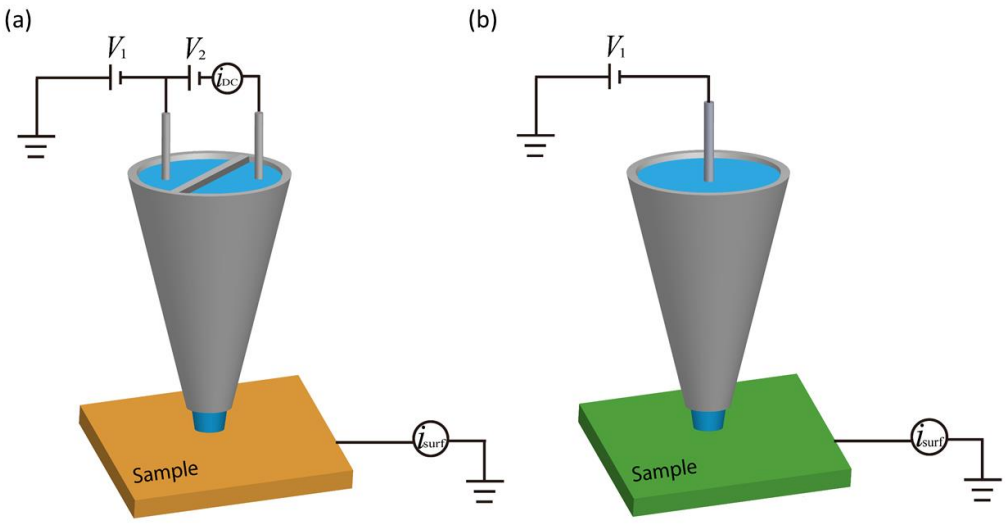

Figure 1.5: Illustration of (a) double-barrel SECCM setup and (b) single-barrel SECCM setup.

also induces an increase in the i_{AC}. A defined threshold of this i_{AC} can be used to control the tip-to-surface separation.

Figure 1.5b demonstrates the single-barrel SECCM setup used in this thesis. A QRCE is inserted into the single-barrel pipette filled with an electrolyte solution. A voltage, V_1, is applied to the QRCE whilst the sample (working electrode) is grounded. The surface current (i_{surf}) can then be used as the positional feedback signal when the meniscus at the end of the pipette has made contact with the sample surface. Importantly, the nature of this feedback means that the pipette itself doesn't make contact with the electrode surface, making SECCM a non-invasive technique.

1.2 Introduction to sp^2 and sp^3 carbon materials

Carbon materials encompass a range of different allotropes including sp^2 (graphite, graphene, carbon nanotubes, fullerenes) and sp^3 structures (diamond), and span a range of microtextures (more or less ordered) owing to the varying possible degrees of graphitization and a variety of dimensionalities (from 0 to 3D). Since Sir Humphrey Davy used graphite electrodes for the electrochemical production of alkali metals, carbon materials have been widely investigated both for fundamental electrochemistry studies and analytical electrochemical applications, due to their extended solvent window, low cost, excellent mechanical properties of some carbon forms and their electrocatalytic activity for a variety of redox reactions.[19,20]

1.2.1 Structure and electronic properties

Carbon materials can be classified into different categories according to the hybridisation of the atomic orbits of carbon, which determines the electronic

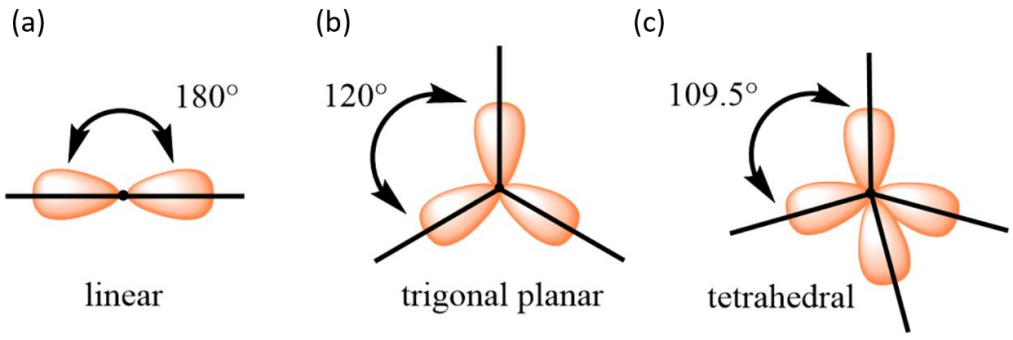

Figure 1.6: Three kinds of hybridisation for carbon atoms: (a) sp, (b) sp^2 and (c) sp^3.

configuration of carbon atoms. There are three kinds of hybridisation, i.e. sp, sp^2 and sp^3 as illustrated in Figure 1.6. This thesis will focus on sp^2 and sp^3 carbon materials.

1.2.1.1 Carbon materials with sp^2

The simplest sp^2 carbon material is graphene, a flat monolayer of carbon atoms, in which they are arranged in a two-dimensional (2D) honeycomb lattice. Based on this basic structure, more complex sp^2 carbon materials can be built with different dimensionalities.[21] It can be wrapped into 0D fullerenes, rolled into 1D nanotubes or stacked into 3D graphite (Figure 1.7). Despite, being constructed from a similar basic structure, these different forms that can be generated, can greatly affect the electrochemical properties of the material. A variety of techniques have been used to characterize the properties of these materials and related electrochemical applications are developed.

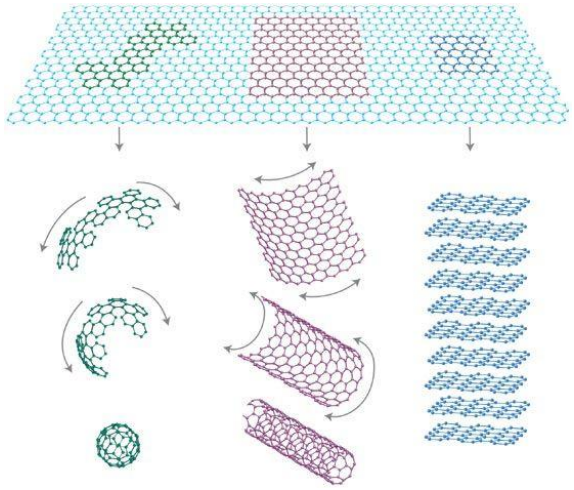

Figure 1.7: Illustration of sp^2 carbon materials of varying dimensionality by using graphene as the basic building element. The possible forms that can be produced are 0D fullerenes, 1D nanotubes and 3D graphite can be formed.[21]

As the common structure element for the other sp^2 carbon materials, the structure of 2D graphene is first introduced. It is useful to define some of the properties possessed by 2D graphene. It is well known that a single layer graphene layer is a zero-gap semiconductor with a linear Dirac-like spectrum around the Fermi energy, while graphite shows a semimetallic behaviour with a band overlap of about 41 meV.[22,23] B. Partoens et al. studied how the electronic structure evolves from a monolayer graphene layer into graphite by computing the band structure of one, two and few layers of

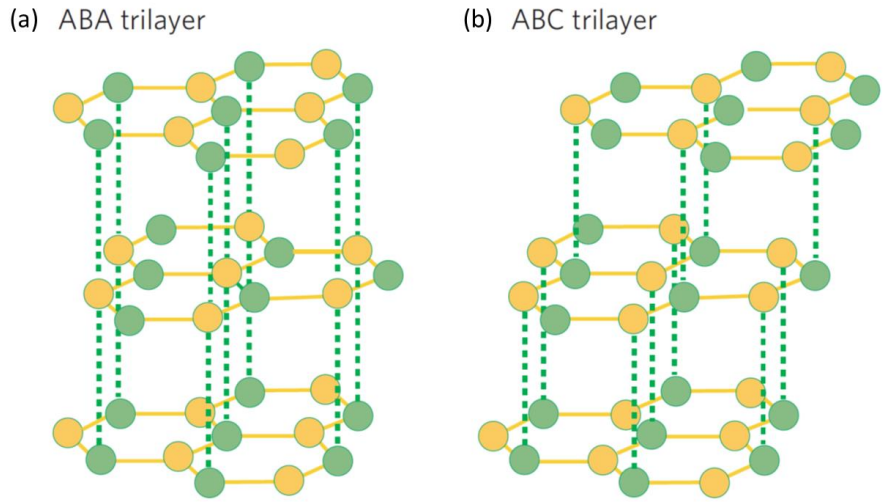

Figure 1.8: Schematic of the crystal structure for trilayer graphene with ABA and ABC stacking order. Crystal structure of ABA (a) and ABC (b) trilayer graphene. The yellow and green dots represent the A and B sublattices of the graphene.[27]

graphene.[23] It shows that the electronic structure approaches the 3D limit of graphite at 10 layers. As a result, we define 2D graphene as no more than 10 layers herein.

The carbon atoms of graphene are densely packed into a regular hexagonal pattern. Each atom has four bonds, one strong planar σ bond to each of its three nearest neighbours[24] and one weak π bond that is oriented out of the graphene plane.[25] The atoms are about 1.42 Å apart.[26] Bilayer graphene can exist in the AB stacking form, where half of the atoms lie directly over the centre of a hexagon in the lower graphene, and half of the atoms lie over an atom.[27] For trilayer graphene, two stacking modes are introduced: 1) ABA (Bernal) stacking and 2) ABC (Rhombohedral) stacking as shown in Figure 1.8. ABA mode exhibits an associated mirror symmetry whereas ABC stacking, like that of the bilayer, has inversion symmetry.

The electronic dispersion in the honeycomb lattice of monolayer graphene is shown in Figure 1.9. The conduction band and the valance band touch each other at the κ-point in the hexagonal first-Brillouin zone and remain equal in energy for symmetry reasons.[28] As a result, graphene is a semimetal or zero-gap semiconductor, combining metallic and semiconducting characteristics. Its density of states (DOS) at the Fermi energy E_F is zero and increases linearly on both sides of E_F.

With the increasing number of graphene layers, the electronic properties vary. In an unperturbed state, both mono- and few-layer graphene lacks a band gap.[29,30] However, few-layer graphene may possess an induced band gap under the application of an electric

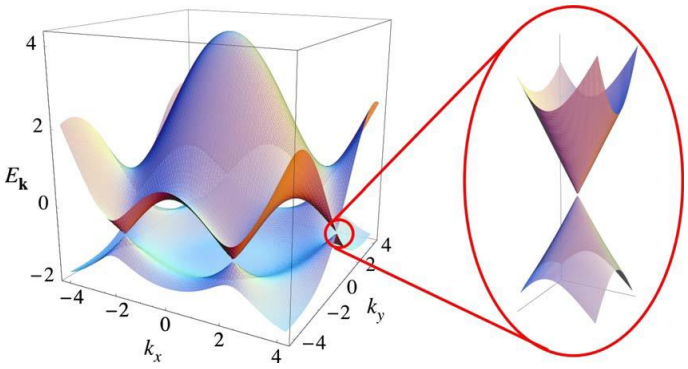

Figure 1.9: Electronic dispersion of graphene. The conduction band and the valence band touch each other at six κ points. The zoom shows that the dispersion relation close to the κ points looks like the energy spectrum of massless Dirac particles.

field,[31-33] making it potentially useful for developing new electronic and optoelectronic devices.[34,35] For example, an experimental and theoretical study of the electronic response of trilayer graphene was reported, both for ABA and ABC stacking graphene, to perpendicular electric fields.[36] A tuneable band gap of ABC stacking graphene was found whereas such a band gap is not observable in ABA stacking trilayer graphene.

Another family of sp^2 carbon materials with the greatest degree of similarity to graphene are carbon nanotubes (CNTs), which have been extensively studied for almost two decades. There are two forms of CNTs: single-walled carbon nanotubes (SWNTs) and multi-walled carbon nanotubes (MWNTs).[37] A SWNT can be considered as the seamless wrapping of monolayer graphene rolled into a hollow cylinder. By adding many rolled-up concentric cylinders, a MWNT is obtained.[38] The diameter and helicity of a defect-free SWNT are described by a chiral vector $\boldsymbol{C}_h$ (Figure 1.10).[39]

$$\boldsymbol{C}_h = n\boldsymbol{a_1} + m\boldsymbol{a_2} \tag{1.18}$$

Where $\boldsymbol{a_1}$ and $\boldsymbol{a_2}$ are the graphene lattice vectors and n and m are integers.

CNTs can show either metallic or semiconducting behaviour predicted by electronic band structure calculations.[40,41] The general rule for electronic properties is illustrated in Figure 1.11:[42] if $(n-m)$ is a multiple of 3, then the CNTs exhibit a metallic behaviour (finite value of carriers in the density of states at the Fermi energy); if $(n-m)$ is not a multiple of 3, then the CNTs exhibit a semiconducting behavior (no charge carriers in the density of states at the Fermi energy). These electronic properties lead to wide potential applications including conductive and high-strength composites; energy storage and energy conversion devices; sensors; field emission displays; hydrogen storage media; and nanometre-sized semiconductor devices and probes.[43]

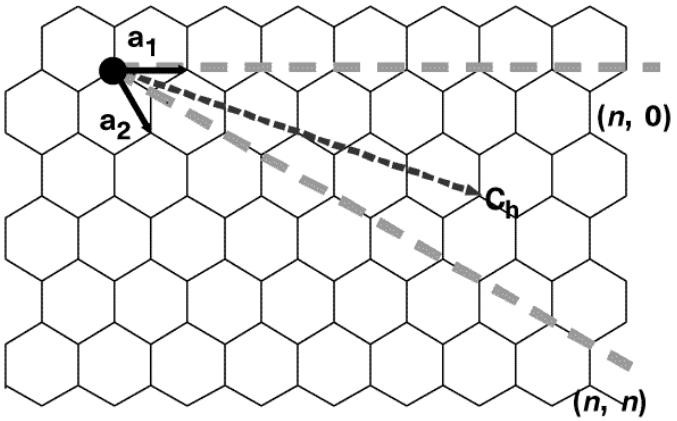

Figure 1.10: Schematic of a 2D graphene sheet illustrating the lattice vectors $\boldsymbol{a_1}$ and $\boldsymbol{a_2}$, and the roll-up vector $\boldsymbol{C_h} = n\boldsymbol{a_1} + m\boldsymbol{a_2}$. The limiting cases of $(n,0)$ zigzag and (n,n) armchair tubes are indicated with dashed lines.[39]

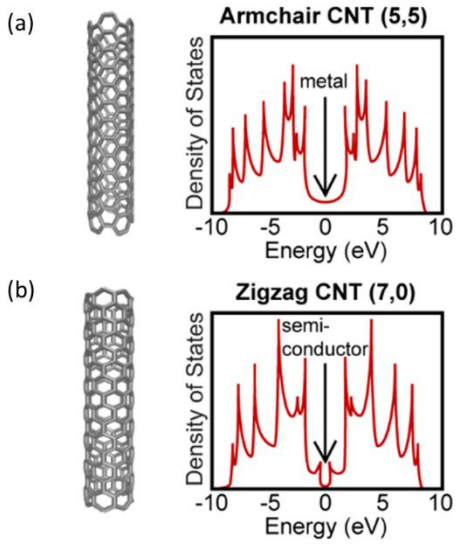

Figure 1.11: Electronic properties of two different CNTs: (a) armchair (5,5) CNT exhibits metallic behaviour (reveals finite charge carrier in the density of states at the Fermi energy) and (b) zigzag (7,0) CNT exhibits semiconductor behaviour (no charge carrier in the density of states at the Fermi energy).[42]

1.2.1.2 Carbon materials with sp^3

Diamond is a well-known carbon material which exhibits a complete carbon sp^3 hybridization and tetrahedral bonding and that displays many unique properties such as a high degree of chemical inertness, extreme hardness and thermal conductivity and high charge carrier mobilities. Diamond is a typical example of a face centred cubic (FCC) lattice and the unit cell of it consists of two FCC unit cells, one of which moves ¼ of the diagonal length towards the diagonal direction of the Bravais lattice (Figure 1.12).[44] The C-C bond length is 0.154 nm with a C-C-C angle of 109.5º.

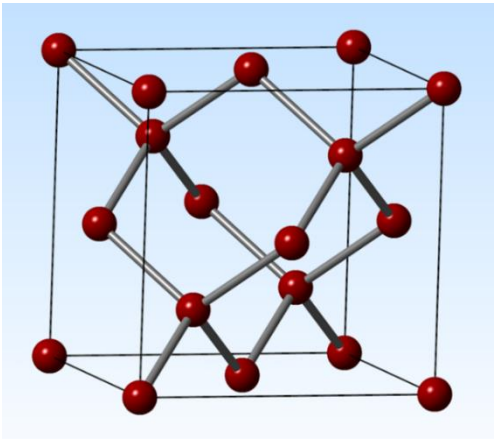

Figure 1.12: Illustration of carbon arrangement of diamond.

Undoped diamond has a wideband gap of 5.47 eV at 300 K, which cannot be used for electrochemistry.[45] However, if doped with an n-type dopant, where the charge carriers are electrons, or p-type dopant, where the charge carriers are holes, the diamond can be conductive. The most common n-type and p-type dopants are nitrogen and boron respectively. Nitrogen n-type doping introduces a donor level, which is 1.7 eV below the conduction band.[46] Boron p-type doping introduces holes, resulting in an impurity level lying about 0.37 eV above the valence band.[47] The impurity band extends up to the top of valence band with the increase of the doping concentration. The research in this thesis is concerned with boron doped diamond.

With increasing boron doping concentration, the material can be considered "metal like". The boron density strongly affects the electrical resistance of this material.[48] The resistivity of semi-metallic BDD is as low as 0.001 Ω·cm and increases with decreasing of boron doping concentration. The resistivity of BDD, plotted as a function of boron concentration, is shown in Figure 1.13.[48]

Figure 1.14, shows the metal-to-insulator transition (MIT) of boron doped diamond.[49] When the boron doping concentration is in the range of 10^{16}-10^{19} atoms cm^{-3}, the

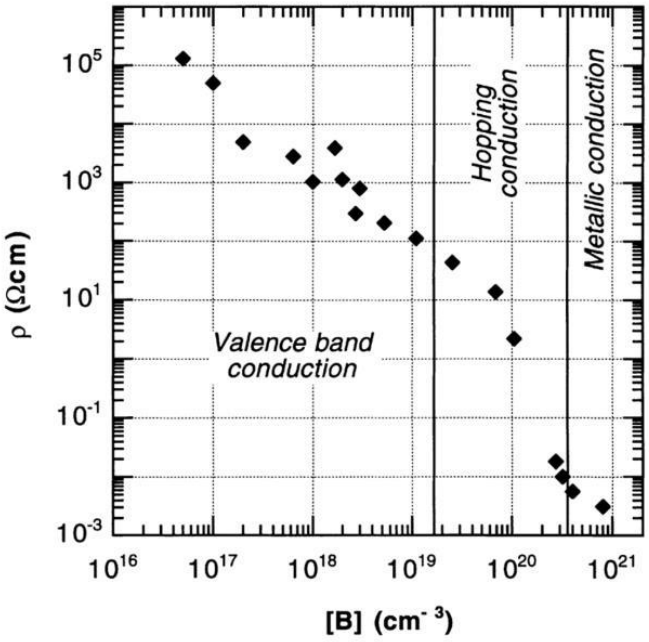

Figure 1.13: Room temperature resistivity of BDD as a function of boron doping concentration.[48]

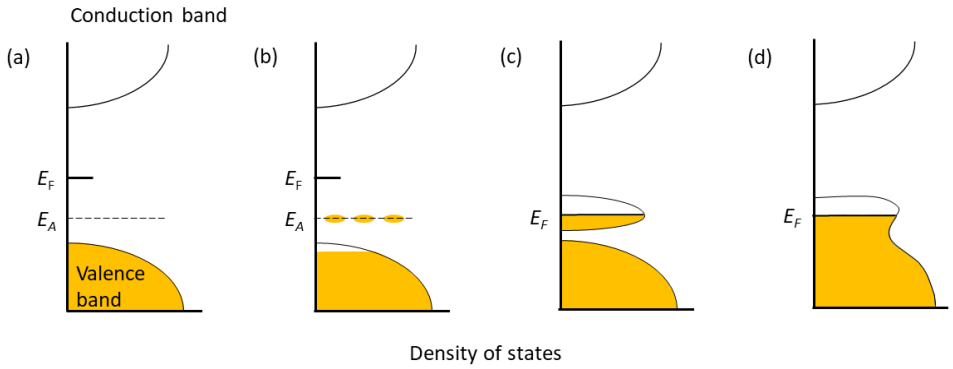

Figure 1.14: P-type low-doped BDD at (a) absolute 0 K, no carriers are thermally excited from the valence band to acceptor states; and (b) nonzero temperature; the number of free carriers in the valence band will depend on the concentration and ionization energy of the boron acceptors (EA) and the temperature, yielding an activated electrical resistivity intermediate between that of an insulator and that of a metal; the Fermi level will move downward toward the top of the valence band. (c) p-type heavily doped BDD (~10^{20} B atoms cm^{-3}), when the impurities are close enough, quantum overlapping of their wave functions results in delocalization leading to metallic behaviour at zero temperature with a Fermi level pinned inside the impurity band; the metal-insulator transition takes place. (d) Very high doping levels >10^{20} B atoms cm^{-3}; screening of the impurities modifies the acceptor activation energy and the intrinsic band gap energy will reduce.[49]

diamond shows a resistivity changes in accordance with p-type semiconductor

behaviour. As the boron doping level reaches above 10^{19} atoms cm^{-3}, the resistivity decreases dramatically as hopping conduction dominates. At a boron doping level of greater than 10^{20} atoms cm^{-3}, when the acceptor density is high enough, this leads to a metallic behaviour with a Fermi level pinned inside the impurity band, and then the MIT happens.

1.2.2 Synthesis of carbon materials

1.2.2.1 sp^2 carbon materials

Novoselov *et al.* have first shown repeatable synthesis of monolayer graphene by exfoliation and cleavage in 2004.[50] Since then, many new processing routes of graphene have been developed including chemical vapour deposition (CVD), chemical methods, thermal decomposition of SiC, unzipping CNTs and so on.[51] Among these methods, exfoliation and CVD are the most commonly used.

The exfoliation method can produce high-quality of graphene with low defect densities but the size of the graphene layer is usually small (no more than hundreds of micrometres) and the size distribution is random. The mechanical exfoliation process of graphene is illustrated in Figure 1.15. First, Scotch tape is applied to the highly ordered pyrolytic graphite (HOPG) surface and thus exerts a normal force. If this normal force is repeated by numerous times, the graphitic layer becomes thinner and thinner and finally a monolayer graphene will be obtained.

Compared to the exfoliation method, CVD offers a compromise between quality, efficiency, consistency, and control over the process. The efficiency is much higher than mechanical exfoliation and can be used for large-scale graphene production.[52] Few-layer

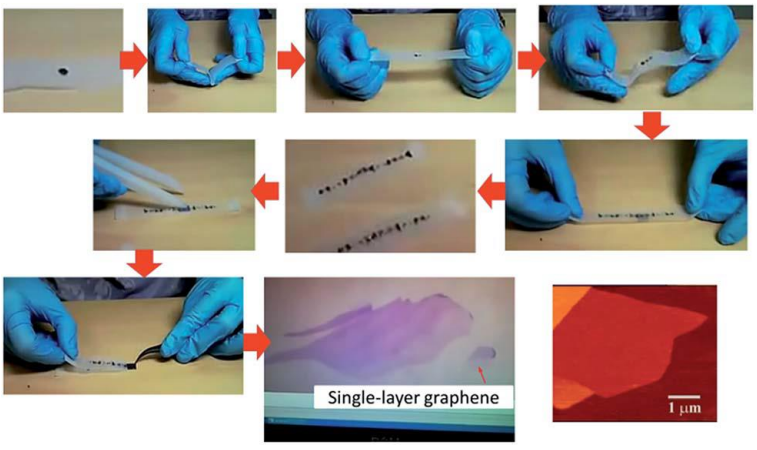

Figure 1.15: Schematic of process of the Scotch-tape based exfoliation of HOPG.

graphene of about 30 layers by CVD using Ni substrate was reported by Somani et al. with camphor as a reactant.[53] Pollard et al. reduced the thickness of graphene to monolayer on a Ni thin film evaporated on SiO_2/Si substrate.[54] Furthermore, Li et al. reported the CVD growth of large-scale single layer graphene on Cu foils. The Cu substrate was mostly covered with single layer graphene, which is more than 95%.[55] On Cu foil, the growth of graphene is restricted to the catalyst substrate due to the low solubility of carbon in Cu.[56] The instrument set-up for CVD grown graphene (Figure 1.16a) and proposed mechanism (Figure 1.16b) are presented here.

Since the first synthesis of CNTs by Iijima,[58] CNTs have been widely studied due to their potential for a range of different applications. Primary synthesis methods for CNTs include arc discharge,[59] laser ablation,[60] gas-phase catalytic growth from carbon monoxide,[61] and CVD from hydrocarbons.[62,63] Arc discharge produces CNTs by applying a stable electrical arc between the cathode and anode high-purity graphite electrodes under a helium atmosphere, in the presence of a metal catalyst (i.e. Co, Ni, and Fe).[64] Laser ablation involves vaporization of a graphite target held in a controlled atmosphere oven at temperatures near 1200 ℃. The graphite target is usually doped with a Co and Ni catalyst.[60] The condensed CNTs are collected on a water-cooled target. Both the arc discharge and laser ablation method are limited in the volume of sample they can

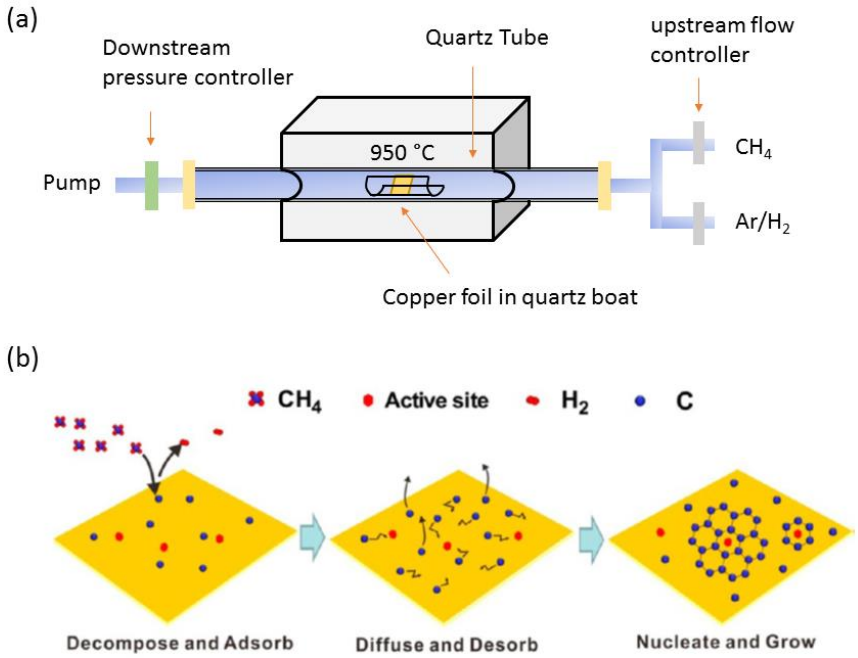

Figure 1.16: (a) Instrument set-up for CVD-grown graphene on Cu foil. (b) Scheme for Cu-based graphene growth mechanism.[57]

produce. In addition, these two methods suffer from contamination from amorphous carbon and metal catalysts.[65,66] These contaminations can interfere with the electrochemistry of CNTs.[67,68] As a result, subsequent purification steps are necessary.[69,70]

These limitations motivate the development of gas-phase methods, such as catalyzed CVD (cCVD). The cCVD process on a supported catalyst contains several steps (Figure 1.17). First, a substrate with metal nanoparticles is prepared. Second, the substrate is put into a furnace and then generally submitted to a reduction upon heating under typical H_2 or NH_3 gases. Third, alkane or CO is passed into the furnace and carbon deposition occurs by decomposition of the hydrocarbon source on the catalytic metal nanoparticles (Co and Fe) by temperatures ranging from 500 to 1200 °C.[71,72] The obtained CNTs are attached to an inert substrate (Si/SiO_2 or quartz).[73] By optimizing the cCVD conditions, CNTs grown have been shown to exhibit a low defect density,[74] negligible amorphous carbon content, and to be relatively free of catalytic NPs.[75]

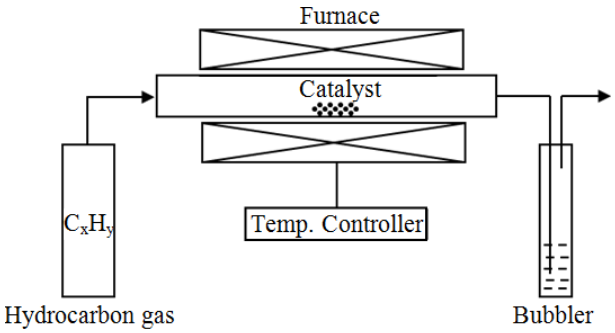

Figure 1.17: Schematic of a CVD set-up for CNT growth.

1.2.2.2 sp^3 carbon materials

Synthetic diamond, as the representative of sp^3 carbon materials, was initially grown in the mid of 1950's using high pressure, high temperature (HPHT) methodologies.[76] In the HPHT process, a synthesis chamber containing graphite, seed crystals and a metal solvent is compressed to 3-5 GPa and heated to over 1800 K.[77] Pure diamond is an electrical insulator and can't be used as an electrode. By doping with boron atoms to a certain level, BDD becomes an ideal electrode for electrochemical studies. HPHT have been used to synthesize diamond for decades, the diamond produced is usually small, in the micrometre to millimetre range. In addition, BDD produced by HPHT techniques exhibits lower conductivity than expected due to compensation with co-doping nitrogen, even though its boron doping concentration can achieve 10^{20} atoms cm^{-3}.

In the 1980's, a CVD method at low temperatures for the synthesis of diamond from a gas phase carbon species was developed.[78] Since then, it has become the most commonly used method, both for laboratory studies and commerce.[45] CVD has several advantages for the preparation of BDD. First, it has high efficiency for the control of dopant incorporation. Second, it's easy to grow large areas and on structured substrates.[79] CVD is the method to produce BDD electrodes that is used in this thesis. A plasma is created in CVD by either a hot filament (HF) or by microwaves (MWs). MWs enable us to generate higher temperatures than using a HF and results in a higher concentration of H atoms. Additionally, using MWs it is possible to achieve higher phase purity and faster growth rates. However, most commercial BDD electrodes are produced through the use of a HF due to the ability to grow large surface areas.

A typical CVD BDD growth protocol requires a mixture of a carbon source, usually methane, and boron (B_2H_6 or $B(OCH_3)_3$ in gaseous form to flow into a reactor at high temperatures of >2000 K (temperature of the plasma).[80] The boron concentration in the gas phase is often expressed in ppm. The measurement of boron concentration of BDD is detected using e.g. secondary ion mass spectrometry (SIMS). Excess hydrogen (95-99 %) is added for generating H atoms under plasma. They are crucial to terminate dangling bonds on the growing diamond surface and suppress the formation of sp^2 carbon.[81]

Polycrystalline BDD is commonly used in electrochemistry as an electrode.[82,83] First, small crystallites of diamond nucleate on the seeds and grow to form a film on the substrate (e.g. Si, Nb, Mb, Ti, Ta, and W) with different grains merging together. A cross section of polycrystalline structure of diamond is generated as shown in Figure 1.18.

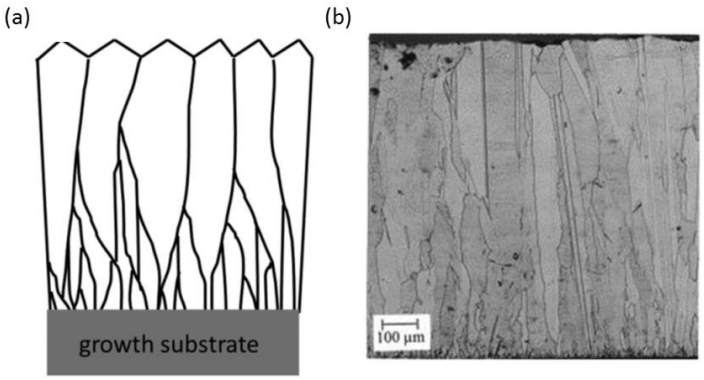

Figure 1.18: (a) Schematic and (b) Scanning electron microscope (SEM) image of cross section of CVD diamond (image copyright Jonathan C. Newland 2014).

The grain size depends on growth conditions including growth time, temperature, gas composition.[84] BDD can be classified according to the grain sizes: ultra-nanocrystalline (UCN), grain sizes <10 nm;[85] nanocrystalline (NC), grain sizes in the range 10 nm-1μm[85] and; microcrystalline (MC), grain sizes >μm.[86]

1.3 Electrochemistry of carbon materials

Carbon materials have been used as electrodes for decades, in application ranging from electroanalysis, to energy storage, such as in capacitors and fuel cells. With the advent of new forms of carbon nanotubes, graphene and boron doped diamond, they have become increasingly studied as electrode materials. Their fundamental electrochemical properties, functionalization, and their applications in electrochemistry have gained interest.

1.3.1 Graphene

In recent years, the electrochemistry of graphene has been intensely researched. However, this research has mainly concerned reduced graphene oxides and liquid extracted graphene on a support electrode at the macroscale. The materials studied have been of variable quality, making fundamental studies complicated.[87] The electrochemical performance of graphene, depending on the reaction, is considered to be affected by defects, functional groups, number of graphene layers and impurities present on the graphene sheets.[88]

For example, a graphene electrode was constructed, as shown in Figure 1.19. Studies on such an electrode have shown that the monolayer and bilayer samples of graphene are electroactive. It has been claimed here monolayer graphene to show higher ET kinetics than multilayer for the reduction of ferricyanide and defects in monolayer graphene made little difference to the voltammetric response of the samples.[89] Graphene may also reveal electrochemical activity differences between step edges and basal planes. It was reported that the edges showed much faster ET rate than the graphene basal plane for electrocatalytic oxygen reduction reaction (ORR).[90] What's more, Jin-Hui Zhong et al. demonstrated that the precise control of density of states (DOS), introduced by Ar^+ irradiation, can tune the heterogeneous ET rate of graphene for the oxidation of ferrocenemethanol (FcMeOH). Scanning electrochemical microscopy (SECM), combined with Raman spectroscopy, showed that graphene has the highest electrochemical activity at a moderate defect level, due to balance in the defect induced

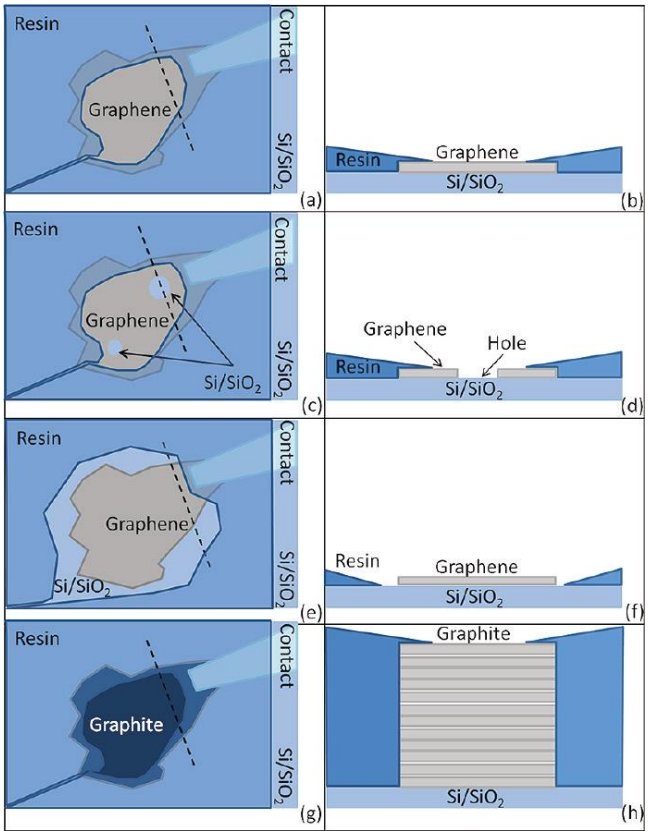

Figure 1.19: Schematic diagram of the graphene samples. On the left, top view of the samples; on the right, cross section along the black dashed line. Defect-free monolayer graphene, with all edges covered by the masking resin (a,b); defective monolayer graphene with holes (c,d); monolayer graphene with exposed edges (e,f), and multilayer graphene (g,h).[89]

increase of DOS, but decrease of conductivity.[91] Electrochemistry is quite sensitive to surface contamination. The contamination on graphene surface such as polymer residue introduced during graphene process can cause electrochemical activity variations, as demonstrated by Ji Won Suk et al. for graphene based field-effect transistors.[92]

In order to characterize variations of structure and surface effects on the electrochemical activity of graphene, some high-resolution techniques have been employed for exfoliated graphene. Using $Ru(NH_3)_6^{3+/2+}$ as a redox mediator, high-resolution scanning cell electrochemical microscopy (SECCM) revealed that there is a strong correlation between the number of graphene layers (on a SiO_2/Si substrate) and the apparent ET kinetics (Figure 1.20). Monolayer graphene had the slowest rate, bilayer graphene has higher rate and ultrathin graphite had the fastest kinetics. However, this was in contrast to observe what for the ferrocenylmethyltrimethylammonium ($FcTMA^{+/2+}$) couple, where both monolayer and multilayer graphene showed fast and

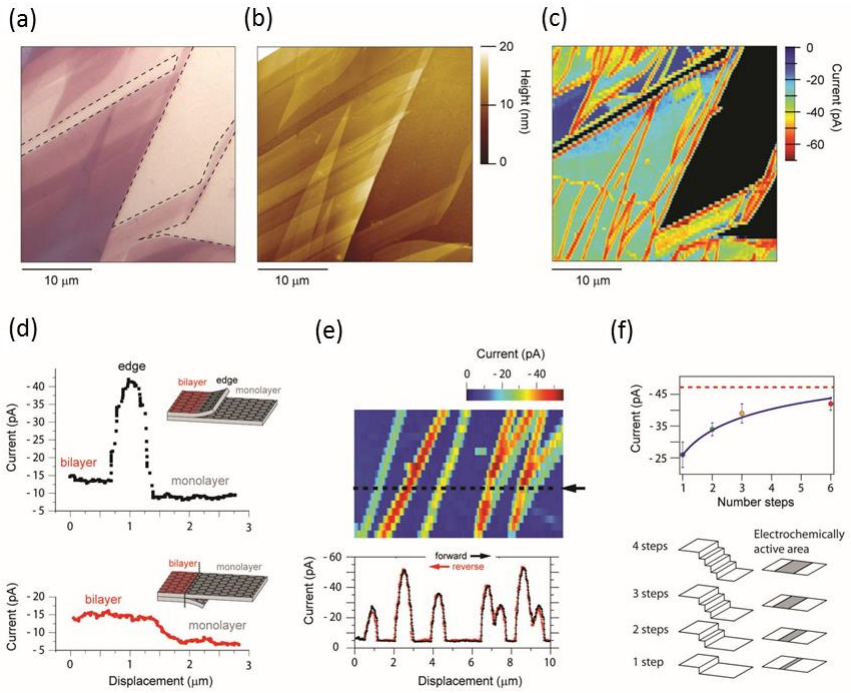

Figure 1.20: Multimicroscopy of exfoliated graphene on a SiO_2/Si substrate. (a) Optical microscopy image. (b) AFM image. (c) SECCM electrochemical map for the reduction of $Ru(NH_3)_6^{3+}$. (d) Two SECCM scan profiles on the transition between monolayer and bilayer graphene, electrochemically active on the top and non-active on the bottom. (e) SECCM electrochemical map of step edges of different overall height. (f) Average surface current for step edges with different height.[93]

reversible ET kinetics. With $Ru(NH_3)_6^{3+/2+}$, there was enhanced activity at some, but not all, step edges, which was attributed to the arrangement of steps.[93]

CVD graphene is often used to fabricate electrochemical devices, thus its fundamental electrochemical properties have been investigated.[91,94] The heterogeneous ET activity of CVD graphene transferred on a SiO_2/Si substrate was investigated using SECCM for oxidation of $FcTMA^+$.[94] The results showed that ET was fast, but that the rate increased systematically with the number of graphene layers up to a reversible (diffusion limited) limit (see Figure 1.21).

Since the Si/SiO_2 substrate may have a doping effect on graphene, it can modulate the intrinsic properties of the graphene, which has been demonstrated with scanning probe microscopy,[95] field effect transistors[96] and Raman microscopy.[97] The study of the electrochemical properties of as-grown CVD graphene directly on a Cu foil is thus of great interest. C Bosch- Navarro et al.[98] used as-grown CVD graphene on Cu foil as an electrode to study its electrochemical activity without any further treatment steps. This electrode fabrication protocol avoids complex graphene transfer steps[92] that may

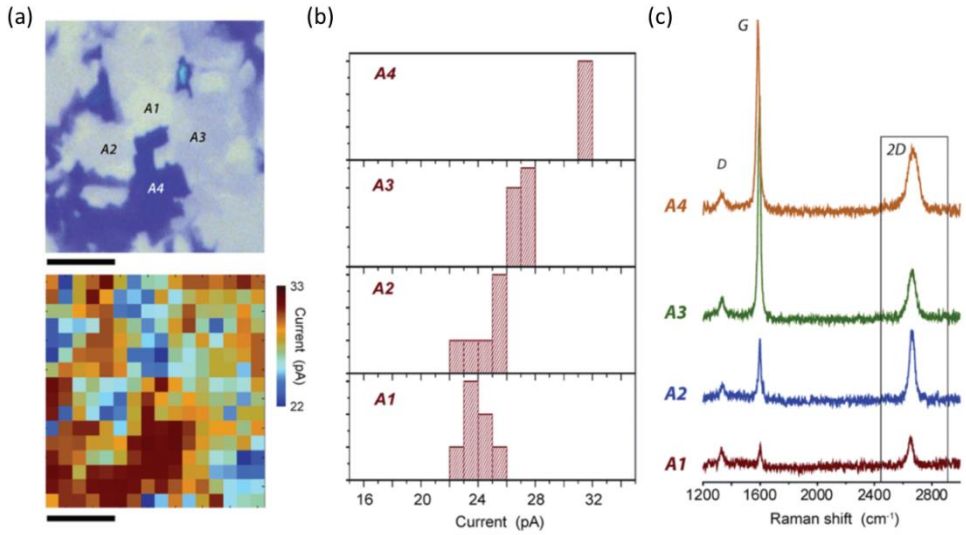

Figure 1.21: (a) Optical image of CVD graphene with four different flakes labelled A_1, A_2, A_3, A_4 presenting monolayer, bilayer, trilayer and multilayer respectively, and corresponding SECCM data. Scale bar is 5 µm. (b) Histograms of the surface current at the potential of E-E_0 = -0.016 V (E_2). (c) Raman spectra acquired with an excitation wavelength of 633 nm.[94]

introduce polymer residues and defects. Fast ET kinetics were observed for both inner and outer sphere redox couples with fully covered graphene on Cu electrodes and the electrochemical response is stable, without any apparent electrode fouling. Joaquín Rodríguez-López *et al.* reported the electrocatalytic activity of graphene on different underlying materials.[99] The underlying material contributed to lower the activation potential for ORR in the order Pt > Au > SiO_x, suggesting the effect of underlayer metals to impact inner-sphere reactions through electronic interactions across ultrathin bulk of graphene.

1.3.2 Boron doped diamond

The first report on conducting nitrogen and argon implanted diamond, as an electrode material, demonstrated a wide solvent window and low capacitance.[100] Swain et al.[101] reported the standard electrochemical behaviour of high-quality, boron-doped polycrystalline diamond thin-film electrodes. The electrochemical response was evaluated using different outer and inner sphere redox couples. The films were additionally characterized by SEM and Raman imaging microscopy. Strategies have been used to modify doped diamond with metallic nanoparticles and/or electropolymerized films to improve the performance of diamond electrodes. Also,

biofunctionalization of diamond films has developed to foster several useful bioanalytical applications.[102]

'High-quality' boron doped diamond has a very high overpotential for both oxygen and hydrogen evolution reactions, as reported by Pleskov et al.[103] The solvent window of BDD is defined by the potential range in both the anodic and cathodic directions in which it is possible to carry out electrochemical reactions without the oxygen and hydrogen evolution reactions taking place significantly. The voltammetric responses of BDD in different aqueous electrolytes exhibit a wide solvent window.[104-107] This wide solvent window of BDD has some advantages. First, the extended solvent window can facilitate a wide range of redox reactions which happen at extreme potentials. Second, the water oxidation by the conventional OER route is strongly retarded and can occur in parallel with the outer sphere oxidation of water. As a result, BDD can produce the highly reactive hydroxyl radical ($OH^{\cdot}$), which is useful for electrochemical water treatment. Third, the chemically inert nature of BDD results in the ability to resist fouling, which gives BDD potential applications in the detection of biological species, such as dopamine, which is known to seriously foul electrode surfaces constructed from other materials.

'High-quality' BDD also possesses a relatively low background current ($\leq 10\ \mu F\ cm^{-2}$),[80] provided that there is negligible nondiamond carbon (NDC). Because of the low capacitance of BDD, it can be used to improve the detection sensitivity of metal ions

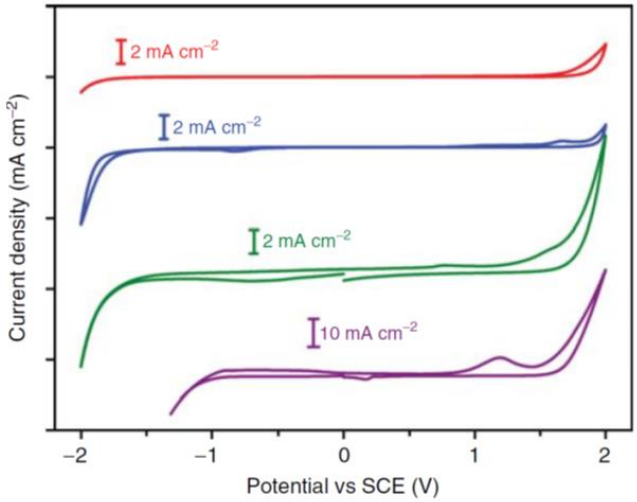

Figure 1.22: CVs recorded in 0.1 M KNO_3 at a scan rate of 0.1 V s^{-1} for highly doped NDC-free free-standing, microcrystalline BDD (top), NDC-containing free-standing, microcrystalline BDD (second down), glassy carbon (third down), and platinum (bottom).[82]

(Hg^{2+}) compared to conventional electrodes.[108] As the concentration of NDC increases, it narrows the solvent window of BDD. NDC content provides catalytic sites for ORR, as shown in Figure 1.22 (blue line), and an oxidation peak for sp^2-bonded carbon impurities is seen.[109] However, 'High-quality' BDD does not show any of these features (red line in Figure 1.22). NDC components in diamond can be detected by surface coverage measurements of electroactive quinone groups,[110] and also can be measured by Raman spectroscopy.[111,112]

There are two kinds of surface terminations for BDD: oxygen termination and hydrogen termination. The termination affects not only the electrochemical performance, especially ET kinetics of inner-sphere reactions,[113] but also the wetting properties of the surface. As-grown BDD by the CVD method is hydrogen terminated boron doped diamond (H-BDD). The surface is hydrophobic with water contact angles as high as 90 degrees (Figure 1.23a).[114] The hydrogen terminated surface is usually stable in air for several months before it is oxidized with time.[115] The oxygen terminated boron doped diamond (O-BDD) surface is more hydrophilic with a much lower water contact angle (Figure 1.23b). Oxygen termination can be generated by anodically polarizing,[116] oxygen plasma treatment,[117] and hot acid treatment.[118] O-BDD surfaces have an opposite bond polarity to H-BDD which typically results in a lowering of the energy levels and a positive electron affinity.

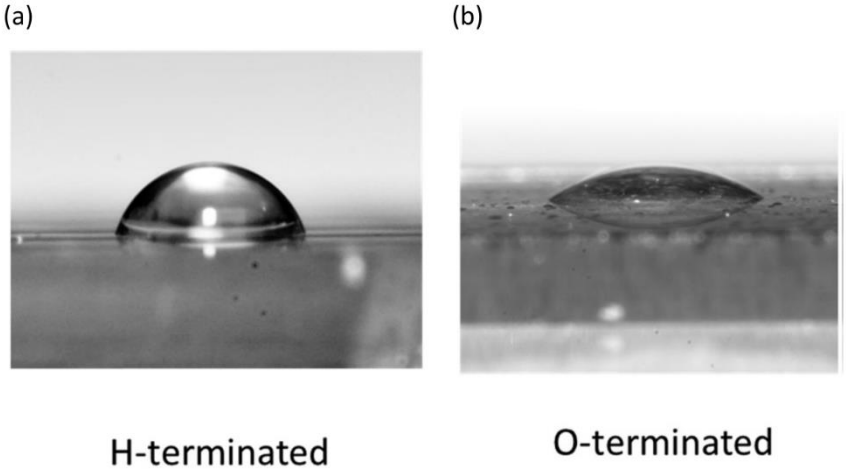

Figure 1.23: Contact angle measurements of a water droplet on (a) a hydrogen terminated BDD and (b) an oxygen terminated BDD surface.[80]

1.3.3 Carbon nanotubes

Advantages of CNTs for electrochemistry have become increasingly apparent for energy storage and sensors applications. There are four main advantages including increased voltammetric currents,[119-121] increased heterogeneous ET rates,[122] insignificant surface fouling of CNTs based electrodes[123,124] and electrocatalytic effects towards a variety of substances.[125,126] These advantages have attracted great research interest towards the functionalization of CNTs and their electrochemical applications. Recent progress of CNTs based electrochemical sensors can be divided into organic modifications (oxygen functional groups, DNA, polymers, etc.), inorganic modifications (metal nanoparticles, metal oxide) and organic-inorganic hybrids.[127]

CNTs functionalized with metal nanoparticles (NPs) and metal oxides for electrochemical sensor have received particular attention. Two approaches are taken for the modification of CNTs. One is that NPs or their oxide are synthesized prior to being connected to the CNTs with linkers. The other is that NPs or their oxide can be deposited directly onto the CNTs.[127] These inorganic NPs are dispersed onto the CNT's surface homogeneously and increase the active surface area dramatically.

Current metal NPs modifiers focus on noble metals such as Au, Pt, Ag.[128] For example, Au NPs can be deposited onto the sidewalls of CNTs under potential control (in Figure 1.24). The size of particle can be changed with varied potential, deposition time and metal salt concentration.[129] CNTs modified with Au NPs have been applied for detecting hydroxylamine and paraoxon, etc.[130,131] Moreover, Au NP-functionalized CNTs can be employed to measure heavy metal ions. Au NP-CNT composites were applied for the

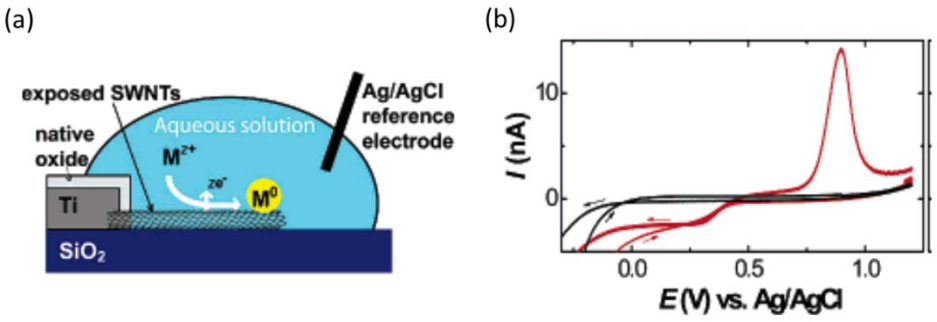

Figure 1.24: (a) Schematic of the Au NP modified CNT electrode. (b) CV response of the Au NP modified CNT electrode (red line) in the presence of 0.2 mM $HAuCl_4$ and 100 mM KCl. The response from an identical Ti/native oxide electrode without the CNTs is also shown (black line).[129]

detection of trace mercury (II) by anodic stripping voltammetry, which exhibited high sensitivity with a limit of detection of 3×10^{-10} mol/L. At the same time, a wide linear range (5×10^{-10} - 1.25×10^{-6} mol/L) and good repeatability can be achieved.[132]

Ag NPs have been mainly used in the fields of high-sensitivity biomolecule detection, catalysis and micro-electronics.[133,134] Similar to Au NPs, Ag NP-functionalized CNTs have also been applied in electrochemical sensors. For instance, CNT-Ag NP composites were employed for the electrochemical determination of H_2O_2.[135,136] The hybrids were also employed to detect hydrazine.[137,138] In addition, Ag-CNT composites showed electrochemical catalytic activity towards dopamine and ascorbic acid.[139]

A variety of electrochemical sensors based on Pt-CNT hybrids have been constructed. The most widely researched area is in glucose detection. The Pt-CNTs were first synthesized by a two step-pyrolysis and showed excellent electrocatalytic activity towards glucose oxidation.[140] Another example has shown that the soluble CNT-hemoglobin (CNT-HGB) composites can be prepared by using a phase-transfer method and these materials were used as templates to bind $PtCl_6^{2-}$ in the presence of $NaBH_4$ (reducing agent). As a result, Pt NP modified CNTs with high dispersion were synthesized. This sensor displayed a linear concentration range of 28.0 mM - 46.6 mM for the detection of glucose.[141]

The high cost and scarcity of noble metals limits their large scale practical applications. Thus, metal oxide nanostructures have been studied as electrochemical sensors, but they are affected by poor electrical conductivity. This disadvantage can be overcome by functionalizing the metal oxides onto electronically conducting substrate. Several different types of metal oxide have been deposited onto CNTs and the electrochemical performance of these composites has been investigated including CuO/Cu_2O,[142,143] ZnO,[144,145] FeO[146] etc. Nickel and nickel hydroxide have been applied widely as electrocalalysts for fuel cells[147] and glucose sensors.[148,149] The electrocatalytic performance of nickel hydroxide comes from unpaired d electrons or empty d-orbitals resulting from the oxidized form of Ni(OOH)[150,151] that is available to bond with adsorbed species. The outstanding electrocatalytic characteristics of nickel hydroxide makes them become good candidates for modifying CNTs, as demonstrated in chapter 5 of this thesis.

Recent efforts have been focused on the synthesis of functionalized carbon materials as electrocatalysts for various applications, particularly as electrochemical biosensors and for alcohol oxidation reactions (AOR), including the methanol oxidation reaction

(MOR) and the ethanol oxidation reaction (EOR). AOR is crucial for fuel cell research, which is of tremendous interest, from both an energy and environmental standpoint.[152] Direct alcohol fuel cells (DAFCs), based on liquid fuels, have drawn great attention as power sources owing to the much higher energy density of liquid fuels than gaseous fuels.[153] Unfortunately, the commercial success of DAFCs is still prohibitive due to the high cost of Pt and Pt based electrocatalysts.[154] CNTs are a good candidate for a supporting material for loading metal and metal oxides electrocatalysts, and provide a high electric conductivity for fast electrocatalysis of the AOR.[155,156] To find cheaper materials to substitute noble material such as Pt is necessary. As discussed above, nickel hydroxide ($Ni(OH)_2$) is such a material that exhibits high electrocatalytic performance and at a much cheaper cost. Thus, it is a suitable electrocatalyst material which has been widely studied.[157-159] $Ni(OH)_2$ clusters improve the kinetics for the electrochemical reduction of water to form hydrogen in alkaline electrolytes.[160] Besides, it is well known that the $Ni(OH)_2$ has electrocatalytic activity due to the oxidized form, Ni(OOH):[150]

$$Ni(OH)_2 + OH^- \rightleftharpoons NiOOH + H_2O + e^- \quad (1.19)$$

The superior catalytic activity for the AOR results from the interconversion of $Ni(OH)_2$/NiOOH acts as an electronic mediator:[161]

$$NiOOH + \text{organic compound} \rightarrow Ni(OH)_2 + \text{byproduct} \quad (1.20)$$

1.4 Hexagonal boron nitride (h-BN)

Boron nitride (BN), a graphene like material, has attracted continuous attention for demonstrating fundamental physics in materials and potential applications for electronics.[162] There are various structures of BN, of which h-BN, in particular, has been an appealing substrate dielectric for use in improved graphene-based devices.[163]

In recent years, the electrochemistry of boron nitride has been explored as an electrocatalyst towards the oxygen reduction reaction (ORR) and hydrogen evolution reaction (HER).[164-166]

1.4.1 Structure and synthesis of h-BN

h-BN is an sp^2-bonded, layered compound, similar to the graphene lattice constant, which is sometimes referred to as 'white graphene'.[167,168] Monolayer h-BN is a lattice, with alternatively arranged by boron and nitrogen atoms in a two-dimensional plane, resulting in a honeycomb structure, akin to graphene (Figure 1.25).[169] Boron and nitrogen atoms within each layer are bound by strong covalent σ bonds,[170,171] whereas

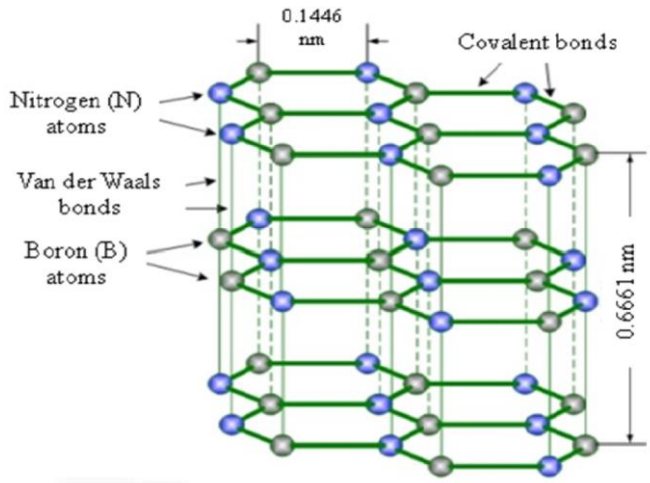

Figure 1.25: Schematic of h-BN structure taken from reference 169.

the layers are held together by weak van der Waals forces.[172-174] The B-N bond length in the plane is 1.45 Å and the interlayer spacing of h-BN is 0.333 nm. h-BN has a wide-gap of 5.97 eV[170] in contrast to the semimetallic nature of graphite.

The synthesis of large area, few-layer h-BN on metal substrates has been explored by CVD growth.[175,176] Yumeng Shi et al.[175] reported a h-BN thin film synthesis method by using ambient pressure CVD on polycrystalline Ni films. The continuous h-BN film was formed on a Ni surface and the size of the h-BN film was only limited by the size of the Ni single crystal grains. Two-dimensional atomic layers of h-BN films on Cu foil were synthesized by Li Song et al.,[176] using the CVD method and were transferred successfully to many different types of substrates. Few layer h-BN films were usually produced by using these atmospheric pressure CVD methods. In order to achieve a good control of the number of h-BN layers and obtain monolayer h-BN films, low pressure CVD was employed as illustrated in Figure 1.26.[177]

Ammonia borane was used as a BN precursor in this study and a two-heating zone system was installed (Figure 1.25). T_1 was between 60-90 °C to generate borazine vapor from its solid and T_2 was fixed at 1000 °C to thermally decompose borazine for h-BN growth.

1.4.2 Electrochemistry of h-BN

Recently, two-dimensional (2D) layered structure materials such as MoS_2 and WS_2 have shown great importance in the study of the hydrogen evolution reaction (HER).[178-181] Particularly, a simple single-barrel SECCM technique has been used to resolve HER on MoS_2 at nanoscale, where it is shown that the basal plane possesses uniform activity,

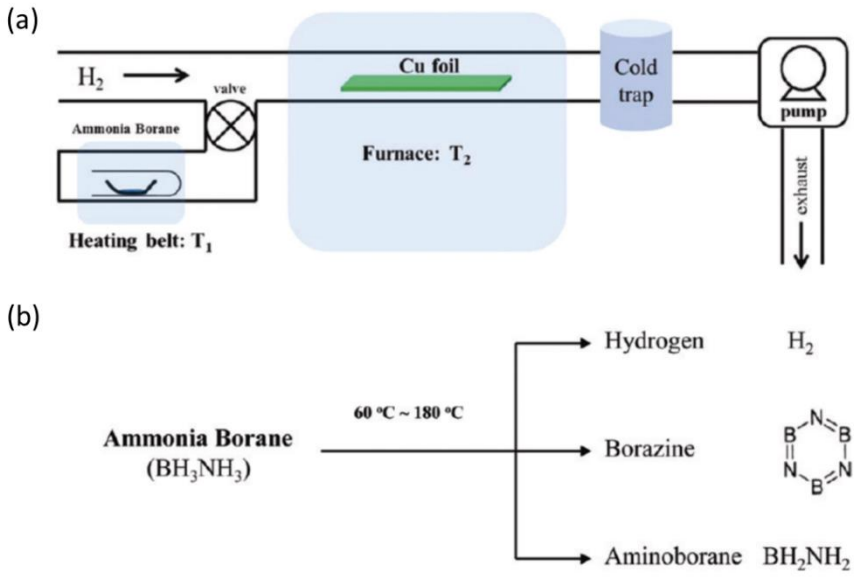

Figure 1.26: (a) Schematic of h-BN low pressure CVD synthesis setup. (b) Thermal decomposition of ammonia borane precursor.[177]

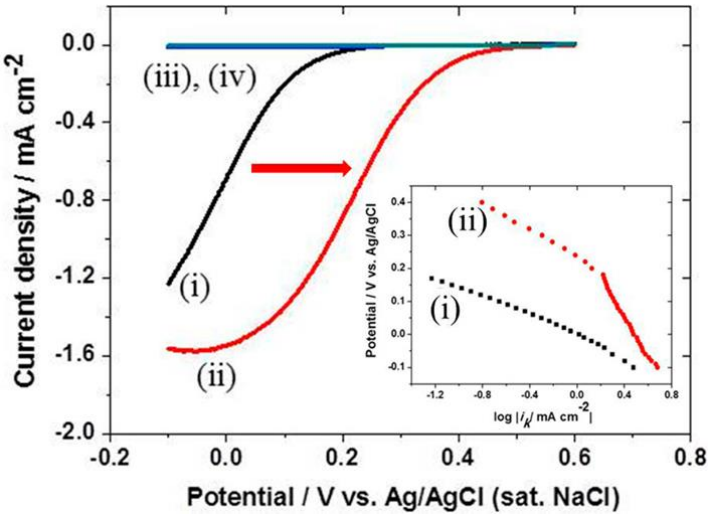

Figure 1.27: (a) LSV of (i) bare Au, (ii) BN nanosheet/Au, (iii) bare glass carbon, and (iv) BN nanosheet/glass carbon in O_2 saturated 0.5 M H_2SO_4. Rotation rate: 1500 rpm. Scan rate: 10 mV/s. Inset: Tafel plot of kinetic currents at (i) bare Au and (ii) BN nanosheet/Au.[164]

while steps and edges have a height-dependent enhancement in electrocatalytic activity.[18]

h-BN has also been reported to act as an electrocatalyst for the ORR.[164,165] For example, h-BN is introduced onto metal substrates to produce an electrocatalyst for the ORR since the bandgap of the h-BN can be considerably reduced on a metal substrate.[182,183] Experiments conducted on a BN nanosheet modified Au electrode by

Uosaki et al.[164] showed that the potential for the ORR to occur on a gold electrode with 2D-hBN was 0.27 V lower than that of a bare gold electrode (Figure 1.27). The density-functional theory calculations presented in this work revealed a slight protrusion of the unoccupied BN states toward the Fermi level when the h-BN is supported on Au (111) caused by interaction between BN and Au.

The hydrogen evolution reaction (HER) is of great importance for various energy storage and renewable energy conversion systems. The electrocatalytic performance towards HER of insulating BN nanosheets (BNNS) on inert gold substrate has been studied.[166] The size controlled BNNS (<1 um) on a gold electrode showed the higher efficiency for the electrochemical HER. The smallest BNNS (0.1-0.22 um) had the highest efficiency for the modification where overpotentials were 30 mV and 40 mV larger than those at Pt electrode at 5 mA cm^{-2} and at 15 mA cm^{-2} (Figure 1.28) respectively. The theoretical calculation presented suggests the highly active HER may be due to the edge atoms of BNNS providing energetically favoured sites for adsorbed hydrogen. The HER electrocatalytic performance of CVD grown hBN on metal substrates (Cu and Au) will be investigated in chapter 6.

1.5 Aims and objectives

The main aim of this thesis is to study fundamental electrochemical properties of carbon materials including sp^2 and sp^3 structured carbon and graphene-like boron nitride,

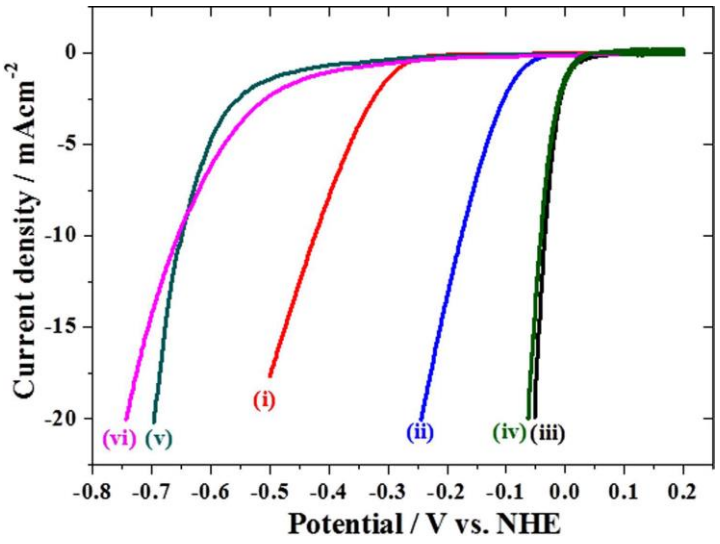

Figure 1.28: LSVs at (i) bare Au, (ii) BNNS/Au, (iii) bare Pt, (iv) BNNS/Pt, (v) Bare glass carbon, and (vi) BNNS/glass carbon in Ar saturated 0.5 M H_2SO_4 solution. Scan rate=1 mV s^{-1}.

by microscopic and macroscopic methods. Additionally, a further goal is to highlight the wide applications of the experimental approach towards a range of nanomaterials in electrochemistry. The methodology used involves a combination of multiple microscopies for surface characterisation to investigate structure-activity effects. Chapter 2 outlines the experimental details and the characterisation techniques that are used throughout the subsequent chapters.

In chapter 3, the ET kinetics of monolayer, bilayer and multilayer as-grown CVD graphene on Cu foil are studied by using voltammetric SECCM. Correlative microscopy study coupled with Raman microscopy and field emission-scanning electron microscopy, is a tool to highlight and distinguish differences in the ET kinetics among monolayer, bilayer and multilayer graphene for hexaammineruthenium (III) chloride ($Ru(NH_3)_6^{3+/2+}$). These studies are important for expanding knowledge of substrate effects in the electrochemistry of substrate-supported graphene.

In chapter 4, the microscopic factors that determine the solvent window in aqueous potassium chloride solution of polycrystalline BDD are investigated using SECCM, in conjunction with electron backscatter diffraction (EBSD) and Raman microscopy. This study is important because chloride-salt media are an important class for electroanalysis, but the influence of chloride ion on the oxidation processes is not well studied. This study focuses on boron dopant concentration and BDD surface termination as factors affecting the solvent window of BDD electrodes in chloride solution.

In chapter 5, the use of direct and indirect electrodeposition approaches to form $Ni(OH)_2$ NPs, two different crystallographic orientations of $Ni(OH)_2$ NPs on a SWNT network are demonstrated for preparing electrodes. The $Ni(OH)_2$ NPs-SWNT composite by the direct approach exhibits more excellent electrocatalytic activity towards effective AOR than $Ni(OH)_2$ NPs-SWNT composite by the indirect approach.

In chapter 6, SECCM technique has been employed to study the intrinsic activities of HER on a ‘graphene-like’ material, CVD grown h-BN directly on Cu foils, and transferred CVD grown h-BN on Au evaporated SiO_2/Si substrate. Local (spatially-resolved) voltammetry and Tafel analysis reveals that electronic interaction with the underlying metal substrate plays a significant role in modulating the electrocatalytic activity of h-BN, with Au-supported h-BN exhibiting significantly enhanced HER charge-transfer kinetics (exchange current is *ca.* two orders of magnitude larger) compared to Cu-supported h-BN. Conclusions and future works are summarised in chapter 7.

1.6 Reference

1 Bard, A. J., Faulkner, L. R., Leddy, J. and Zoski, C. G. *Electrochemical methods: fundamentals and applications*. Vol. 2 (wiley New York, 1980).

2 Anderson, J. L., Coury, L. A. and Leddy, J. Dynamic electrochemistry: methodology and application. *Analytical chemistry* **72**, 4497-4520 (2000).

3 Fisher, A. C. *Electrode Dynamics*. (Oxford University Press, 1996).

4 Oldham, K. and Myland, J. *Fundamentals of electrochemical science*. (Elsevier, 2012).

5 Taube, H. *Electron transfer reactions of complex ions in solution*. (Elsevier, 2012).

6 Thirsk, H. R. and Harrison, J. A. *A guide to the study of electrode kinetics*. (Academic Press, 1972).

7 Miao, W. Handbook of Electrochemistry. *Elsevier, Amsterdam*, 556 (2007).

8 Mabbott, G. A. An introduction to cyclic voltammetry. *Journal of Chemical Education*, **60**, 697 (1983).

9 Nicholson, R. S. Theory and application of cyclic voltammetry for measurement of electrode reaction kinetics. *Analytical chemistry* **37**, 1351-1355 (1965).

10 Randles, J. E. B. A cathode ray polarograph. Part II.—The current-voltage curves. *Transactions of the Faraday Society* **44**, 327-338 (1948).

11 Wightman, R., Wipf, D. and Bard, A. Electroanalytical chemistry, vol. 15. *Marcel Dekker, New York* (1989).

12 Forster, R. J. Microelectrodes: new dimensions in electrochemistry. *Chemical Society Reviews* **23**, 289-297 (1994).

13 Mirkin, M. V. and Bard, A. J. Simple analysis of quasi-reversible steady-state voltammograms. *Analytical chemistry* **64**, 2293-2302 (1992).

14 Snowden, M. E., Güell A. G., Lai, S. C., Mckelvey, K., Ebejer, N., O'Connell, M. A., Colburn, A. W., and Unwin, P. R. Scanning electrochemical cell microscopy: Theory and experiment for quantitative high resolution spatially-resolved voltammetry and simultaneous ion-conductance measurements. *Analytical chemistry* **84**, 2483-2491 (2012).

15 Ebejer, N., Schnippering, M., Colburn, A. W., Edwards, M. A. and Unwin, P. R. Localized high resolution electrochemistry and multifunctional imaging: Scanning electrochemical cell microscopy. *Analytical chemistry* **82**, 9141-9145 (2010).

16 Güell, A. G., Ebejer, N., O'Connell, M. A., Mckelvey, K., Macpherson, J. V. and Unwin, P. R. Quantitative nanoscale visualization of heterogeneous electron transfer rates in 2D carbon nanotube networks. *Proceedings of the National Academy of Sciences* **109**, 11487-11492 (2012).

17 Ebejer, N., Güell, A. G., Lai, S. C., Mckelvey, K., Snowden, M. E. and Unwin, P. R. Scanning electrochemical cell microscopy: a versatile technique for nanoscale electrochemistry and functional imaging. *Annual Review of Analytical Chemistry* **6**, 329-351 (2013).

18 Bentley, C. L., Kang, M. and Unwin, P. R. Nanoscale Structure Dynamics within Electrocatalytic Materials. *Journal of the American Chemical Society* **139**, 16813-16821 (2017).

19 McCreery, R. L. Advanced carbon electrode materials for molecular electrochemistry. *Chemal reviews* **108**, 2646-2687 (2008).

20 McCreery, R. L. Electroanalytical chemistry. *Marcel Dekker, Inc., New York* **17**, 221-374 (1991).

21 Novoselov, K. S. and Geim, A. The rise of graphene. *Nature materials* **6**, 183-191 (2007).

22 Schultz, B. J., Dennis, R. V., Lee, V. and Banerjee, S. J. N. An electronic structure perspective of graphene interfaces. *Nanoscale* **6**, 3444-3466 (2014).

23 Partoens, B. and Peeters, F. From graphene to graphite: Electronic structure around the K point. *Physical review B* **74**, 075404 (2006).

24 Bernal, J. The structure of graphite. *Proceedings of the Royal Society of London. Series A, Containing Papers of a Mathematical and Physical Character* **106**, 749-773 (1924).

25 Spanu, L., Sorella, S. and Galli, G. Nature and strength of interlayer binding in graphite. *Physical review letters* **103**, 196401 (2009).

26 Cooper, D. R., D'Anjou, B., Ghattamaneni, N., Harack, B., Hilke, M., Horth, A., Majlis, N., Massicotte M., Vandsburger, L., Whiteway, E. and Yu V. Experimental review of graphene. *ISRN Condensed Matter Physics* **2012**, 501686 (2012).

27 Liu, Z., Suenaga, K., Harris, P. J. and Iijima, S. Open and closed edges of graphene layers. *Physical review letters* **102**, 015501 (2009).

28 Neto, A. C., Guinea, F., Peres, N. M., Novoselov, K. S. and Geim, A. K. The electronic properties of graphene. *Reviews of modern physics* **81**, 109 (2009).

29 Latil, S. and Henrard, L. Charge carriers in few-layer graphene films. *Physical Review Letters* **97**, 036803 (2006).

30 Min, H. and MacDonald, A. H. Electronic structure of multilayer graphene. *Progress of Theoretical Physics Supplement* **176**, 227-252 (2008).

31 Zhang, F., Sahu, B., Min, H. and MacDonald, A. H. Band structure of A B C-stacked graphene trilayers. *Physical Review B* **82**, 035409 (2010).

32 Avetisyan, A., Partoens, B. and Peeters, F. Electric-field control of the band gap and Fermi energy in graphene multilayers by top and back gates. *Physical Review B* **80**, 195401 (2009).

33 Tang, K., Qin, R., Zhou, J., Qu, H., Zheng, J., Fei, R., Li, H., Zheng, Q., Gao, Z. and Lu, J. Electric-field-induced energy gap in few-layer graphene. *The Journal of Physical Chemistry C* **115**, 9458-9464 (2011).

34 Liu, Y., Lew, W., Goolaup, S., Liew, H., Wong, S. and Zhou, T. Observation of oscillatory resistance behavior in coupled bernal and rhombohedral stacking graphene. *Acs Nano* **5**, 5490-5498 (2011).

35 Zou, K., Zhang, F., Clapp, C., MacDonald, A. and Zhu, J. Transport studies of dual-gated ABC and ABA trilayer graphene: band gap opening and band structure tuning in very large perpendicular electric fields. *Nano letters* **13**, 369-373 (2013).

36 Lui, C. H., Li, Z., Mak, K. F., Cappelluti, E. and Heinz, T. F. Observation of an electrically tunable band gap in trilayer graphene. *Nature Physics* **7**, 944-947 (2011).

37 Dresselhaus, M. S., Jorio, A., Hofmann, M., Dresselhaus, G. and Saito, R. Perspectives on carbon nanotubes and graphene Raman spectroscopy. *Nano letters* **10**, 751-758 (2010).

38 Dumitrescu, I., Unwin, P. R. and Macpherson, J. V. Electrochemistry at carbon nanotubes: perspective and issues. *Chemical Communications*, 6886-6901 (2009).

39 Odom, T. W., Huang, J.-L., Kim, P. and Lieber, C. M. Atomic structure and electronic properties of single-walled carbon nanotubes. *Nature* **391**, 62-64 (1998).

40 Hamada, N., Sawada, S.-I. and Oshiyama, A. New one-dimensional conductors: Graphitic microtubules. *Physical review letters* **68**, 1579 (1992).

41 Saito, R., Fujita, M., Dresselhaus, G. and Dresselhaus, u. M. Electronic structure of chiral graphene tubules. *Applied physics letters* **60**, 2204-2206 (1992).

42 Charlier, J.-C. Defects in carbon nanotubes. *Accounts of chemical research* **35**, 1063-1069 (2002).

43 Baughman, R. H., Zakhidov, A. A. and De Heer, W. A. Carbon nanotubes--the route toward applications. *science* **297**, 787-792 (2002).

44 Spear, K. E. and Dismukes, J. P. *Synthetic diamond: emerging CVD science and technology*. Vol. 25 (John Wiley & Sons, 1994).

45 Balmer, R., Brandon, J., Clewes, L., Dhillon, H., Dodson, J., Friel, I., Inglis, P., Madgwick, T., Markham, M. and Mollart, T. Chemical vapour deposition synthetic diamond: materials, technology and applications. *Journal of Physics: Condensed Matter* **21**, 364221 (2009).

46 Dyer, H. and Preez, L. d. Irradiation damage in type I diamond. *The Journal of Chemical Physics* **42**, 1898-1906 (1965).

47 Prins, J. F. Activation of boron-dopant atoms in ion-implanted diamonds. *Physical Review B* **38**, 5576 (1988).

48 Lagrange, J.-P., Deneuville, A. and Gheeraert, E. Activation energy in low compensated homoepitaxial boron-doped diamond films. *Diamond and Related Materials* **7**, 1390-1393 (1998).

49 Blase, X., Bustarret, E., Chapelier, C., Klein, T. and Marcenat, C. Superconducting group-IV semiconductors. *Nature materials* **8**, 375-382 (2009).

50 Novoselov, K. S., Geim, A. K., Morozov, S. V., Jiang, D., Zhang, Y., Dubonos, S. V., Grigorieva, I. V. and Firsov, A. A. Electric field effect in atomically thin carbon films. *science* **306**, 666-669 (2004).

51 Yi, M. and Shen, Z. A review on mechanical exfoliation for the scalable production of graphene. *Journal of Materials Chemistry A* **3**, 11700-11715 (2015).

52 Yu, J., Li, J., Zhang, W. and Chang, H. Synthesis of high quality two-dimensional materials via chemical vapor deposition. *Chemical Science* **6**, 6705-6716 (2015).

53 Somani, P. R., Somani, S. P. and Umeno, M. Planer nano-graphenes from camphor by CVD. *Chemical Physics Letters* **430**, 56-59 (2006).

54 Pollard, A., Nair, R. R., Sabki, S. N., Staddon, C. R., Perdigao, L. M. A., Hsu, C. H., Garfitt, J. M., Gangopadhyay, S., Gleeson, H. F., Geim, A. K. and Beton P. H. Formation of monolayer graphene by annealing sacrificial nickel thin films. *The Journal of Physical Chemistry C* **113**, 16565-16567 (2009).

55 Li, X., Cai W., An, J., Kim, S., Nah, J., Yang, D., Piner, R., Velamakanni, A., Jung, I., Tutuc, E., Banerjee, S., Colombo, L. and Ruoff, R. S. Large-area synthesis of high-quality and uniform graphene films on copper foils. *Science* **324**, 1312-1314 (2009).

56 Bhaviripudi, S., Jia, X., Dresselhaus, M. S. and Kong, J. Role of kinetic factors in chemical vapor deposition synthesis of uniform large area graphene using copper catalyst. *Nano letters* **10**, 4128-4133 (2010).

57 Yan, Z., Lin, J., Peng, Z., Sun, Z., Zhu, Y., Li, L., Xiang, C., Samuel, E., Kittrell, C. and Tour, J. Toward the synthesis of wafer-scale single-crystal graphene on copper foils. *ACS nano* **6**, 9110-9117 (2012).

58 Iijima, S. Helical microtubules of graphitic carbon. *nature* **354**, 56 (1991).

59 Journet, C., Maser, W. K., Bernier, P., Loiseau, A., Chapelle, M., Lefrant, S., Deniard, P., Lee, R. and Fischer, J. E. Large-scale production of single-walled carbon nanotubes by the electric-arc technique. *Nature* **388**, 756-758 (1997).

60 Rinzler, A., Liu, J., Dai, H., Nikolaev, P., Huffman, C. B., Rodríguez-Macías, F. J., Boul, P. J., Lu, A. H., Heymann, D., Colbert, D. T., Lee, R. S., Fischer, J. E., Rao, A. M., Eklund, P. C. and Smalley, R. E. Large-scale purification of single-wall carbon nanotubes: process, product, and characterization. *Applied Physics A: Materials Science & Processing* **67**, 29-37 (1998).

61 Nikolaev, P., Bronikowski, M., Bradley, R. K., Rohmund, F., Colbert, D. T., Smith, K. A. and Smalley, R. E. Gas-phase catalytic growth of single-walled carbon nanotubes from carbon monoxide. *Chemical physics letters* **313**, 91-97 (1999).

62 Ren, Z., Huang, Z. P., Xu, J. W., Wang, J. H., Bush, P., Siegal, M. P., and Provencio, P. N. Synthesis of large arrays of well-aligned carbon nanotubes on glass. *Science* **282**, 1105-1107 (1998).

63 Huang, Z., Xu, J. W., Ren, Z. F. and Wang, J. H. Growth of highly oriented carbon nanotubes by plasma-enhanced hot filament chemical vapor deposition. *Applied physics letters* **73**, 3845-3847 (1998).

64 Bethune, D., Kiang, C. H., Vries, M. S., Gorman, G., Savoy, R., Vazquez, J. and Beyers, R. Cobalt-catalysed growth of carbon nanotubes with single-atomic-layer walls. *Nature* **363**, 605-607 (1993).

65 Hiura, H., Ebbesen, T. W. and Tanigaki, K. Opening and purification of carbon nanotubes in high yields. *Advanced Materials* **7**, 275-276 (1995).

66 Montoro, L. A. and Rosolen, J. M. A multi-step treatment to effective purification of single-walled carbon nanotubes. *Carbon* **44**, 3293-3301 (2006).

67 Banks, C. E., Crossley, A., Salter, C., Wilkins, S. J. and Compton, R. G. Carbon nanotubes contain metal impurities which are responsible for the "electrocatalysis" seen at some nanotube-modified electrodes. *Angewandte Chemie International Edition* **45**, 2533-2537 (2006).

68 Pumera, M. and Iwai, H. Multicomponent metallic impurities and their influence upon the electrochemistry of carbon nanotubes. *The Journal of Physical Chemistry C* **113**, 4401-4405 (2009).

69 Balasubramanian, K. and Burghard, M. Chemically functionalized carbon nanotubes. *Small* **1**, 180-192 (2005).

70 Jurkschat, K., Ji, X., Crossley, A., Compton, R. G. and Banks, C. E. Super-washing does not leave single walled carbon nanotubes iron-free. *Analyst* **132**, 21-23 (2006).

71 Dupuis, A.-C. The catalyst in the CCVD of carbon nanotubes—a review. *Progress in Materials Science* **50**, 929-961 (2005).

72 Prasek, J., Drbohlavova, J., Chomoucka, J., Hubalek, J., Jasek, O., Adam, V. and Kizek, R. Methods for carbon nanotubes synthesis. *Journal of Materials Chemistry* **21**, 15872-15884 (2011).

73 Ivanov, V., Nagy, J. B., Lambin, Ph., Lucas, A., Zhang, X. B., Zhang, X. F., Bemaerts, D., Tendeloo, G., Amelinckx, S. and Landuyt, J. The study of carbon nanotubules produced by catalytic method. *Chemical Physics Letters* **223**, 329-335 (1994).

74 Fan, Y., Goldsmith, B. R. and Collins, P. G. Identifying and counting point defects in carbon nanotubes. *Nature materials* **4**, 906-911 (2005).

75 Dumitrescu, I., Wilson, N. R. and Macpherson, J. V. Functionalizing single-walled carbon nanotube networks: effect on electrical and electrochemical properties. *The Journal of Physical Chemistry C* **111**, 12944-12953 (2007).

76 Bundy, F., Hall, H. T., Strong, H. and Wentorf, R. Man-made diamonds. *nature* **176**, 51-55 (1955).

77 Bundy, F. Direct conversion of graphite to diamond in static pressure apparatus. *The Journal of Chemical Physics* **38**, 631-643 (1963).

78 Sato, Y. and Kamo, M. Synthesis of diamond from the vapour phase. *The Properties of Natural and Synthetic Diamond, Academic Press, New York*, 427 (1992).

79 Zanin, H., May, P. W., Fermin, D. J., Plana, D., Vieira, M. C., Milne, W. I. and Corat, E. J. Porous boron-doped diamond/carbon nanotube electrodes. *ACS applied materials & interfaces* **6**, 990-995 (2014).

80 Macpherson, J. V. A practical guide to using boron doped diamond in electrochemical research. *Physical Chemistry Chemical Physics* **17**, 2935-2949 (2015).

81 Butler, J., Mankelevich, Y. A., Cheesman, A., Ma, J. and Ashfold, M. Understanding the chemical vapor deposition of diamond: recent progress. *Journal of Physics: Condensed Matter* **21**, 364201 (2009).

82 Hutton, L. A., Lacobini, J. G., Bitziou, E., Channon, R. B., Newton, M. E. and Macpherson, J. V. Examination of the factors affecting the electrochemical performance of oxygen-terminated polycrystalline boron-doped diamond electrodes. *Analytical chemistry* **85**, 7230-7240 (2013).

83 Macpherson, J. V. The Use of Conducting Diamond in Electrochemistry. *Electrochemistry of Carbon Electrodes* **16** (2015).

84 May, P. W. and Mankelevich, Y. A. From ultrananocrystalline diamond to single crystal diamond growth in hot filament and microwave plasma-enhanced CVD reactors: a unified model for growth rates and grain sizes. *The Journal of Physical Chemistry C* **112**, 12432-12441 (2008).

85 Williams, O. Nanocrystalline diamond. *Diamond and Related Materials* **20**, 621-640 (2011).

86 Wilson, N. R., Clewes, S. L., Newton, M. E., Unwin, P. R. and Macpherson, J. V. Impact of grain-dependent boron uptake on the electrochemical and electrical properties of polycrystalline boron doped diamond electrodes. *The Journal of Physical Chemistry B* **110**, 5639-5646 (2006).

87 Patten, H. V., Velický, M. and Dryfe, R. A. *Electrochemistry of Graphene*. (Wiley-VCH Verlag GmbH and Co. KGaA: Weinheim, Germany, 2015).

88 Pumera, M. Graphene-based nanomaterials and their electrochemistry. *Chemical Society Reviews* **39**, 4146-4157 (2010).

89 Valota, A. T., Kinloch, I. A., Novoselov, K. S., Casiraghi, C., Eckmann, A., Hill, E. and Dryfe, R. A. Electrochemical behavior of monolayer and bilayer graphene. *ACS nano* **5**, 8809-8815 (2011).

90 Yuan, W., Zhou, Y., Li, Y., Li, C., Peng, H., Zhang, J., Liu, Z., Dai, L. and Shi, G. The edge-and basal-plane-specific electrochemistry of a single-layer graphene sheet. *Scientific reports* **3** (2013).

91 Zhong, J.-H., Zhang, J., Jin, X., Liu, J., Li, Q., Li, M. and Cai, W., Wu, D., Zhan, D. and Ren, B. Quantitative correlation between defect density and heterogeneous electron transfer rate of single layer graphene. *Journal of the American Chemical Society* **136**, 16609-16617 (2014).

92 Suk, J. W., Lee, W., Lee, J., Chou, H., Piner, R. D., Hao, Y., Akinwande, D. and Ruoff, R. S. Enhancement of the electrical properties of graphene grown by chemical vapor deposition via controlling the effects of polymer residue. *Nano letters* **13**, 1462-1467 (2013).

93 Güell, A. G., Cuharuc, A. S., Kim, Y., Zhang, G., Tan, S., Ebejer, N. and Unwin, P. R. Redox-dependent spatially resolved electrochemistry at graphene and graphite step edges. *ACS nano* **9**, 3558-3571 (2015).

94 Güell, A. G., Ebejer, N., Snowden, M. E., Macpherson, J. V. and Unwin, P. R. Structural correlations in heterogeneous electron transfer at monolayer and multilayer graphene electrodes. *Journal of the American Chemical Society* **134**, 7258-7261 (2012).

95 Ishigami, M., Chen, J., Cullen, W., Fuhrer, M. and Williams, E. Atomic structure of graphene on SiO_2. *Nano letters* **7**, 1643-1648 (2007).

96 Romero, H. E., Shen, N., Joshi, P., Gutierrez, H. R., Tadigadapa, S. A., Sofo, J. O. and Eklund, P. C. n-type behavior of graphene supported on Si/SiO_2 substrates. *Acs nano* **2**, 2037-2044 (2008).

97 Berciaud, S., Ryu, S., Brus, L. E. and Heinz, T. F. Probing the intrinsic properties of exfoliated graphene: Raman spectroscopy of free-standing monolayers. *Nano letters* **9**, 346-352 (2008).

98 Bosch-Navarro, C., Laker, Z. P., Rourke, J. P. and Wilson, N. R. Reproducible, stable and fast electrochemical activity from easy to make graphene on copper electrodes. *Physical Chemistry Chemical Physics* **17**, 29628-29636 (2015).

99 Hui, J., Pakhira, S., Bhargava, R., Barton, Z. J., Zhou, X., Chinderle, A. J., Mendoza-Cortes, J. L. and Rodríguez-López, J. Modulating Electrocatalysis on Graphene Heterostructures: Physically Impermeable Yet Electronically Transparent Electrodes. *ACS nano* **12**, 2980-2990 (2018).

100 Iwaki, M., Sato, S., Takahashi, K. and Sakairi, H. Electrical conductivity of nitrogen and argon implanted diamond. *Nuclear Instruments and Methods In Physics Research* **209**, 1129-1133 (1983).

101 Granger, M. C., Witek, M., Xu, J., Wang, J., Hupert, M., Hanks, A., Koppang, M. D., Butler, J. E., Lucazeau, G., Mermoux, M., Strojek, J. W. and Swain, G. M. Standard electrochemical behavior of high-quality, boron-doped polycrystalline diamond thin-film electrodes. *Analytical Chemistry* **72**, 3793-3804 (2000).

102 Luong, J. H., Male, K. B. and Glennon, J. D. Boron-doped diamond electrode: synthesis, characterization, functionalization and analytical applications. *Analyst* **134**, 1965-1979 (2009).

103 Pelskov, Y. V., Sakharova, A. Y., Krotova, M., Bouilov, L. and Spitsyn, B. Photoelectrochemical properties of semiconductor diamond. *Journal of electroanalytical chemistry and interfacial electrochemistry* **228**, 19-27 (1987).

104 Beck, F., Krohn, H., Kaiser, W., Fryda, M., Klages, C. P., Schäfer, L. Boron doped diamond/titanium composite electrodes for electrochemical gas generation from aqueous electrolytes. *Electrochimica acta* **44**, 525-532 (1998).

105 Martin, H. B., Argoitia, A., Landau, U., Anderson, A. B. and Angus, J. C. Hydrogen and oxygen evolution on boron-doped diamond electrodes. *Journal of The Electrochemical Society* **143**, L133-L136 (1996).

106 Katsuki, N., Takahashi, E., Toyoda, M., Kurosu, T., Iida, M., Wakita, S., Nishiki, Y. and Shimamune, T. Water electrolysis using diamond thin-film electrodes. *Journal of The Electrochemical Society* **145**, 2358-2362 (1998).

107 Beck, F., Kaiser, W. and Krohn, H. Boron doped diamond (BDD)-layers on titanium substrates as electrodes in applied electrochemistry. *Electrochimica Acta* **45**, 4691-4695 (2000).

108 Manivannan, A., Seehra, M., Tryk, D. and Fujishima, A. Electrochemical detection of ionic mercury at boron-doped diamond electrodes. *Analytical letters* **35**, 355-368 (2002).

109 Bennett, J. A., Wang, J., Show, Y. and Swain, G. M. Effect of sp2-bonded nondiamond carbon impurity on the response of boron-doped polycrystalline diamond thin-film electrodes. *Journal of The Electrochemical Society* **151**, E306-E313 (2004).

110 Ayres, Z. J., Cobb, S. J., Newton, M. E. and Macpherson, J. V. Quinone electrochemistry for the comparative assessment of sp 2 surface content of boron doped diamond electrodes. *Electrochemistry Communications* **72**, 59-63 (2016).

111 Knight, D. S. and White, W. B. Characterization of diamond films by Raman spectroscopy. *Journal of Materials Research* **4**, 385-393 (1989).

112 Ferrari, A. C. and Robertson, J. Raman spectroscopy of amorphous, nanostructured, diamond–like carbon, and nanodiamond. *Philosophical Transactions of the Royal Society of London A: Mathematical, Physical and Engineering Sciences* **362**, 2477-2512 (2004).

113 Bard, A. J. Inner-sphere heterogeneous electrode reactions. Electrocatalysis and photocatalysis: the challenge. *Journal of the American Chemical Society* **132**, 7559-7567 (2010).

114 Boukherroub, R., Wallart, X., Szunerits, B., Bouvier, P. and Mermoux, M. Photochemical oxidation of hydrogenated boron-doped diamond surfaces. *Electrochemistry Communications* **7**, 937-940 (2005).

115 Salazar-Banda, G. R., Andrade, L. S., Nascente, P. P. and Pizani, P. S., Rocha-Filho, R. C. and Avaca, L. A. On the changing electrochemical behaviour of boron-doped diamond surfaces with time after cathodic pre-treatments. *Electrochimica Acta* **51**, 4612-4619 (2006).

116 Duo, I., Levy-Clement, C., Fujishima, A. and Comninellis, C. Electron transfer kinetics on boron-doped diamond Part I: Influence of anodic treatment. *Journal of Applied Electrochemistry* **34**, 935-943 (2004).

117 Živcová, Z. V., Petrák, V., Frank, O. and Kavan, L. Electrochemical impedance spectroscopy of polycrystalline boron doped diamond layers with hydrogen and oxygen terminated surface. *Diamond and Related Materials* **55**, 70-76 (2015).

118 Liu, F., Wang, J., Liu, B., Li, X. and Chen, D. Effect of electronic structures on electrochemical behaviors of surface-terminated boron-doped diamond film electrodes. *Diamond and related materials* **16**, 454-460 (2007).

119 Crevillén, A. G., Ávila, M., Pumera, M., González, M. C. and Escarpa, A. Food analysis on microfluidic devices using ultrasensitive carbon nanotubes detectors. *Analytical chemistry* **79**, 7408-7415 (2007).

120 Wei, B., Wang, J., Chen, Z. and Chen, G. Carbon-Nanotube–Alginate Composite Modified Electrode Fabricated by In Situ Gelation for Capillary Electrophoresis. *Chemistry-A European Journal* **14**, 9779-9785 (2008).

121 Pumera, M., Llopis, X., Merkoçi, A. and Alegret, S. Microchip capillary electrophoresis with a single-wall carbon nanotube/gold electrochemical detector for determination of aminophenols and neurotransmitters. *Microchimica Acta* **152**, 261-265 (2006).

122 Nugent, J., Santhanam, K., Rubio, A. and Ajayan, P. Fast electron transfer kinetics on multiwalled carbon nanotube microbundle electrodes. *Nano letters* **1**, 87-91 (2001).

123 Musameh, M., Wang, J., Merkoci, A. and Lin, Y. Low-potential stable NADH detection at carbon-nanotube-modified glassy carbon electrodes. *Electrochemistry Communications* **4**, 743-746 (2002).

124 Pumera, M., Merkoçi, A. and Alegret, S. Carbon nanotube-epoxy composites for electrochemical sensing. *Sensors and Actuators B: Chemical* **113**, 617-622 (2006).

125 Wang, J., Musameh, M. and Lin, Y. Solubilization of carbon nanotubes by Nafion toward the preparation of amperometric biosensors. *Journal of the American Chemical Society* **125**, 2408-2409 (2003).
126 Zhao, Y.-D., Zhang, W.-D., Chen, H. and Luo, Q.-M. Anodic oxidation of hydrazine at carbon nanotube powder microelectrode and its detection. *Talanta* **58**, 529-534 (2002).
127 Gao, C., Guo, Z., Liu, J.-H. and Huang, X.-J. The new age of carbon nanotubes: An updated review of functionalized carbon nanotubes in electrochemical sensors. *Nanoscale* **4**, 1948-1963 (2012).
128 Georgakilas, V., Gournis, D., Tzitzios, V., Pasquato, L., Guldi, D. M. and Prato, M. Decorating carbon nanotubes with metal or semiconductor nanoparticles. *Journal of Materials Chemistry* **17**, 2679-2694 (2007).
129 Quinn, B. M., Dekker, C. and Lemay, S. G. Electrodeposition of noble metal nanoparticles on carbon nanotubes. *Journal of the American Chemical Society* **127**, 6146-6147 (2005).
130 Bui, M.-P. N., Pham, X.-H., Han, K. N., Li, C. A., Lee, E. K., Chang, H. J. and Seong, G. H. Electrochemical sensing of hydroxylamine by gold nanoparticles on single-walled carbon nanotube films. *Electrochemistry Communications* **12**, 250-253 (2010).
131 Jha, N. and Ramaprabhu, S. Development of Au nanoparticles dispersed carbon nanotube-based biosensor for the detection of paraoxon. *Nanoscale* **2**, 806-810 (2010).
132 Xu, H., Zeng, L., Xing, S., Shi, G., Xian, Y. and Jin, L. Microwave-radiated synthesis of gold nanoparticles/carbon nanotubes composites and its application to voltammetric detection of trace mercury (II). *Electrochemistry Communications* **10**, 1839-1843 (2008).
133 Schultz, S., Smith, D. R., Mock, J. J. and Schultz, D. A. Single-target molecule detection with nonbleaching multicolor optical immunolabels. *Proceedings of the National Academy of Sciences* **97**, 996-1001 (2000).
134 Gittins, D. I., Bethell, D., Schiffrin, D. J. and Nichols, R. J. A nanometre-scale electronic switch consisting of a metal cluster and redox-addressable groups. *Nature* **408**, 67-69 (2000).
135 Zhao, W., Wang, H., Qin, X., Wang, X., Zhao, Z., Miao, Z., Chen, L., Shan, M., Fang, Y. and Chen, Q. A novel nonenzymatic hydrogen peroxide sensor based on multi-wall carbon nanotube/silver nanoparticle nanohybrids modified gold electrode. *Talanta* **80**, 1029-1033 (2009).
136 Bui, M.-P. N., Pham, X.-H., Han, K. N., Li, C. A., Kim, Y. S. and Seong, G. H. Electrocatalytic reduction of hydrogen peroxide by silver particles patterned on single-walled carbon nanotubes. *Sensors and Actuators B: Chemical* **150**, 436-441 (2010).
137 Yang, G.-W., Gao, G.-Y., Wang, C., Xu, C.-L. and Li, H.-L. Controllable deposition of Ag nanoparticles on carbon nanotubes as a catalyst for hydrazine oxidation. *Carbon* **46**, 747-752 (2008).
138 Gao, G., Guo, D., Wang, C. and Li, H. Electrocrystallized Ag nanoparticle on functional multi-walled carbon nanotube surfaces for hydrazine oxidation. *Electrochemistry communications* **9**, 1582-1586 (2007).
139 Tashkhourian, J., Nezhad, M. H., Khodavesi, J. and Javadi, S. Silver nanoparticles modified carbon nanotube paste electrode for simultaneous determination of dopamine and ascorbic acid. *Journal of Electroanalytical Chemistry* **633**, 85-91 (2009).

140 Rong, L.-Q., Yang, C., Qian, Q.-Y. and Xia, X.-H. Study of the nonenzymatic glucose sensor based on highly dispersed Pt nanoparticles supported on carbon nanotubes. *Talanta* **72**, 819-824 (2007).

141 Wei, G., Xu, F., Li, Z. and Jandt, K. D. Protein-promoted synthesis of Pt nanoparticles on carbon nanotubes for electrocatalytic nanohybrids with enhanced glucose sensing. *The Journal of Physical Chemistry C* **115**, 11453-11460 (2011).

142 Yang, J., Jiang, L.-C., Zhang, W.-D. and Gunasekaran, S. A highly sensitive non-enzymatic glucose sensor based on a simple two-step electrodeposition of cupric oxide (CuO) nanoparticles onto multi-walled carbon nanotube arrays. *Talanta* **82**, 25-33 (2010).

143 Zhang, X., Wang, G., Zhang, W., Wei, Y. and Fang, B. Fixure-reduce method for the synthesis of Cu 2 O/MWCNTs nanocomposites and its application as enzyme-free glucose sensor. *Biosensors and Bioelectronics* **24**, 3395-3398 (2009).

144 Zhang, C., Wang, G., Liu, M., Feng, Y., Zhang, Z. and Fang, B. A hydroxylamine electrochemical sensor based on electrodeposition of porous ZnO nanofilms onto carbon nanotubes films modified electrode. *Electrochimica Acta* **55**, 2835-2840 (2010).

145 Mo, G.-Q., Ye, J.-S. and Zhang, W.-D. Unusual electrochemical response of ZnO nanowires-decorated multiwalled carbon nanotubes. *Electrochimica Acta* **55**, 511-515 (2009).

146 Siegert, L., Kampouris, D. K., Kruusma, J., Sammelselg, V. and Banks, C. E. The Heterogeneity of Multiwalled and Single-Walled Carbon Nanotubes: Iron Oxide Impurities Can Catalyze the Electrochemical Oxidation of Glucose. *Electroanalysis* **21**, 48-51 (2009).

147 Sarantaridis, D. and Atkinson, A. Redox Cycling of Ni-Based Solid Oxide Fuel Cell Anodes: A Review. *Fuel Cells* **7**, 246-258 (2007).

148 Lin, K.-C., Lin, Y.-C. and Chen, S.-M. A highly sensitive nonenzymatic glucose sensor based on multi-walled carbon nanotubes decorated with nickel and copper nanoparticles. *Electrochimica Acta* **96**, 164-172 (2013).

149 Shamsipur, M., Najafi, M. and Hosseini, M.-R. M. Highly improved electrooxidation of glucose at a nickel (II) oxide/multi-walled carbon nanotube modified glassy carbon electrode. *Bioelectrochemistry* **77**, 120-124 (2010).

150 Hutton, L. A., Vidotti, M., Patel, A. N., Newton, M. E., Unwin, P. R. and Macpherson, J. V. Electrodeposition of nickel hydroxide nanoparticles on boron-doped diamond electrodes for oxidative electrocatalysis. *The Journal of Physical Chemistry C* **115**, 1649-1658 (2010).

151 Reim, R. E. and Van Effen, R. M. Determination of carbohydrates by liquid chromatography with oxidation at a nickel (III) oxide electrode. *Analytical Chemistry* **58**, 3203-3207 (1986).

152 Steele, B. C. and Heinzel, A. in *Materials For Sustainable Energy: A Collection of Peer-Reviewed Research and Review Articles from Nature Publishing Group* 224-231 (World Scientific, 2011).

153 Varcoe, J. R. and Slade, R. C. Prospects for alkaline anion-exchange membranes in low temperature fuel cells. *Fuel cells* **5**, 187-200 (2005).

154 Zhao, X., Yin, M., Ma, L., Liang, L., Liu, C., Liao, J., Lu, T. and Xing, W. Recent advances in catalysts for direct methanol fuel cells. *Energy & Environmental Science* **4**, 2736-2753 (2011).

155 Maiyalagan, T., Viswanathan, B. and Varadaraju, U. Nitrogen containing carbon nanotubes as supports for Pt–Alternate anodes for fuel cell applications. *Electrochemistry Communications* **7**, 905-912 (2005).

156 Liu, H., Song, C., Zhang, L., Zhang, J., Wang, H. and Wilkinson, D. P. A review of anode catalysis in the direct methanol fuel cell. *Journal of Power Sources* **155**, 95-110 (2006).

157 Li, H., Yu, M. H., Wang, F. X., Liu, P., Liang, Y., Xiao, J., Wang, C. X., Tong, Y. X. and Yang, G. W. Amorphous nickel hydroxide nanospheres with ultrahigh capacitance and energy density as electrochemical pseudocapacitor materials. *Nature communications* **4**, 1894 (2013).

158 Gong, M., Zhou, W., Tsai, M.-C., Zhou, J., Guan, M., Lin, M.-C. and Zhang, B., Hu, Y., Wang, D.-Y., Yang, J., Pennycook, S. J., Hwang, B.-J. and Dai, H. Nanoscale nickel oxide/nickel heterostructures for active hydrogen evolution electrocatalysis. *Nature communications* **5**, 4695 (2014).

159 Liu, J., Chen, M., Zhang, L., Jiang, J., Yan, J., Huang, Y. and Lin, J. A flexible alkaline rechargeable Ni/Fe battery based on graphene foam/carbon nanotubes hybrid film. *Nano letters* **14**, 7180-7187 (2014).

160 Subbaraman, R., Tripkovic, D., Strmcnik, D., Chang, K.-C., Uchimura, M., Paulikas, A. P., Stamenkovic, V. and Markovic, N. M. Enhancing hydrogen evolution activity in water splitting by tailoring Li^+-Ni $(OH)_2$-Pt interfaces. *Science* **334**, 1256-1260 (2011).

161 El-Shafei, A. Electrocatalytic oxidation of methanol at a nickel hydroxide/glassy carbon modified electrode in alkaline medium. *Journal of Electroanalytical Chemistry* **471**, 89-95 (1999).

162 Lee, K. H., Shin, H.-J., Lee, J., Lee, I.-V., Kim, G.-H., Choi, J.-Y. and Kim, S.-W. Large-scale synthesis of high-quality hexagonal boron nitride nanosheets for large-area graphene electronics. *Nano letters* **12**, 714-718 (2012).

163 Britnell, L., Gorbachev, R. V., Jalil, R., Belle, B. D., Schedin, F., Mishchenko, A., Georgiou, T., Katsnelson, M. I., L. Eaves, Morozov, M. I., Eaves, L., Morozov, S. V., Peres, N. M. R., Leist, J., Geim, A. K., Novoselov, K. S., Ponomarenko, L. A. Field-effect tunneling transistor based on vertical graphene heterostructures. *Science* **335**, 947-950 (2012).

164 Uosaki, K., Elumalai, G., Noguchi, H., Masuda, T., Lyalin, A., Nakayama, A. and Taketsugu, T. Boron nitride nanosheet on gold as an electrocatalyst for oxygen reduction reaction: Theoretical suggestion and experimental proof. *Journal of the American Chemical Society* **136**, 6542-6545 (2014).

165 Elumalai, G., Noguchi, H. and Uosaki, K. Electrocatalytic activity of various types of h-BN for the oxygen reduction reaction. *Physical Chemistry Chemical Physics* **16**, 13755-13761 (2014).

166 Uosaki, K., Elumalai, G., Dinh, H. C., Lyalin, A., Taketsugu, T. and Noguchi, H. Highly efficient electrochemical hydrogen evolution reaction at insulating boron nitride nanosheet on inert gold substrate. *Scientific reports* **6**, 32217 (2016).

167 Wheelock, P., Cook, B., Harringa, J. and Russell, A. Phase changes induced in hexagonal boron nitride by high energy mechanical milling. *Journal of materials science* **39**, 343-347 (2004).

168 Lei, G., Jian, Y. and Tai, Q. Study progress of preparation methods of hexagonal boron nitride [J]. *Electronic Components and Materials* **6**, 007 (2008).

169 Manijeh, R., Tournie, E. and Brown, G. J. *Quantum Sensing and Nanophotonic Devices IX*. 82682R (International Society for Optics and Photonics).

170 Watanabe, K., Taniguchi, T. and Kanda, H. Direct-bandgap properties and evidence for ultraviolet lasing of hexagonal boron nitride single crystal. *Nature materials* **3**, 404 (2004).

171 Kubota, Y., Watanabe, K., Tsuda, O. and Taniguchi, T. Deep ultraviolet light-emitting hexagonal boron nitride synthesized at atmospheric pressure. *Science* **317**, 932-934 (2007).

172 Mortazavi, B. and Cuniberti, G. Mechanical properties of polycrystalline boron-nitride nanosheets. *RSC Advances* **4**, 19137-19143 (2014).

173 Laskowski, R., Blaha, P., Gallauner, T. and Schwarz, K. Single-layer model of the hexagonal boron nitride nanomesh on the Rh (111) surface. *Physical review letters* **98**, 106802 (2007).

174 Tonkikh, A., Voloshina, E. N., Werner, P., Blumtritt, H., Senkovskiy, B., Güntherodt, G., Parkin, S. S. P. and Dedkov, Y. S. Structural and electronic properties of epitaxial multilayer h-BN on Ni (111) for spintronics applications. *Scientific reports* **6**, 23547 (2016).

175 Shi, Y., Hamsen, C., Jia, X., Kim, K. K., Reina, A., Hofmann, M., Hsu, A. L., Zhang, K., Li, H., Juang, Z.-Y., Dresselhaus, M. S., Li, L.-J. and Kong, J. Synthesis of few-layer hexagonal boron nitride thin film by chemical vapor deposition. *Nano letters* **10**, 4134-4139 (2010).

176 Song, L., Ci, L., Lu, H., Sorokin, P. B., Jin, C., Ni, J., Kvashnin, A. G., Kvashnin, D. G., Lou, J., Yakobson, B. I. and Ajayan, P. M. Large scale growth and characterization of atomic hexagonal boron nitride layers. *Nano letters* **10**, 3209-3215 (2010).

177 Kim, K. K., Hsu, A., Jia, X., Kim, S. M, Shi, Y., Hofmann, M., Nezich, D., Rodriguez-Nieva, J. F., Dresselhaus, M., Palacios, T. and Kong, J. Synthesis of monolayer hexagonal boron nitride on Cu foil using chemical vapor deposition. *Nano letters* **12**, 161-166 (2011).

178 Chia, X., Eng, A. Y. S., Ambrosi, A., Tan, S. M. and Pumera, M. Electrochemistry of nanostructured layered transition-metal dichalcogenides. *Chemical reviews* **115**, 11941-11966 (2015).

179 Cai, Z., Liu, B., Zou, X. and Cheng, H.-M. Chemical Vapor Deposition Growth and Applications of Two-Dimensional Materials and Their Heterostructures. *Chemical reviews* **118**, 6091-6133 (2018).

180 Merki, D., Fierro, S., Vrubel, H. and Hu, X. Amorphous molybdenum sulfide films as catalysts for electrochemical hydrogen production in water. *Chemical Science* **2**, 1262-1267 (2011).

181 Jaramillo, T. F., Jørgensen, K. P., Bonde, J., Nielsen, J. H., Horch, S. and Chorkendorff, I. Identification of active edge sites for electrochemical H_2 evolution from MoS_2 nanocatalysts. *science* **317**, 100-102 (2007).

182 Lyalin, A., Nakayama, A., Uosaki, K. and Taketsugu, T. Functionalization of monolayer h-BN by a metal support for the oxygen reduction reaction. *The Journal of Physical Chemistry C* **117**, 21359-21370 (2013).

183 Koitz, R., Nørskov, J. K. and Studt, F. A systematic study of metal-supported boron nitride materials for the oxygen reduction reaction. *Physical Chemistry Chemical Physics* **17**, 12722-12727 (2015).

Chapter 2. Experimental Section

This chapter introduces the materials, chemicals, experimental procedures and characterization techniques used throughout the work described in this thesis.

2.1 Materials and chemicals

2.1.1 CVD graphene

The graphene samples used in this work was grown on polycrystalline Cu foil by the CVD method as reported in the literature.[1] The Cu foil was electrochemically polished[2] before loading into a 1-inch diameter tube furnace pumped to 4.4 mTorr by a turbomolecular pump. The CVD procedure began with the foil being heated to 950 °C, followed by equilibration for 10 min. The growth of graphene was initiated by exposing the substrate to a mixture gas containing 10 standard cubic centimeters (sccm) of hydrogen and 3 sccm of methane (purity 99.95 %) for 25 min. This system was left to cool to room temperature for 1 hour.

To study the effect of the Cu crystal orientation on the ET kinetics of the supported graphene, a polycrystalline Cu foil with smaller grain size (10 - 300 μm) from Goodfellow Cambridge Limited (purity 99.95 %, 0.025 mm thick) was used for graphene growth. The CVD procedures are the same except the growth time for this graphene sample was 30 min.

2.1.2 CVD diamond

The BDD sample used in this thesis was provided by Element Six Ltd., Ascot, UK, and synthesised using microwave plasma-assisted CVD. The average boron doping concentration is around 5×10^{20} atoms cm^{-3}, and the thickness of BDD is 350 μm.

2.1.3 cCVD SWNT network

SWNT networks were grown on 2 cm × 2 cm Si/SiO_2 substrates (IDB Technologies Ltd., n-type, 525 μm thick with 300 nm of thermally grown SiO_2 on both sides) by cCVD.[3] A low density (LD) SWNT network was grown using Fe NPs[4] as catalysts. High density (HD) and super high density (SHD) SWNT networks were prepared using Co NPs[5] as the catalysts. Fe NPs were deposited by soaking the Si/SiO_2 in 1 % ferritin (50-150 mg mL^{-1}, Aldrich) aqueous solution for 1 hour followed by a 2 min exposure to 100

W oxygen plasma (Emitech K1050X plasma asher). Co NPs were deposited through sputtering (SC7640 sputter coater, Quorum Technologies Ltd., U.K.) at 1 kV for 20 s and 30 s for the growth of the HD and SHD SWNT networks respectively.

The cCVD procedure is shown in Figure 2.1. First, the substrate was heated from room temperature (RT) to 850 ^{o}C in 14 min under H_2 (BOC Gases, 99.95 %) atmosphere at a flow rate of 150 sccm. Then the temperature was stabilized at 850 ^{o}C for 1 min. The growth of SWNT networks began with bubbling Ar (BOC Gases, 99.9995 %) (850 sccm) through EtOH (Fisher, 99.99 %) held at 0 ^{o}C. Growth was then carried out for 10, 20 and 30 mins for the LD, HD and SHD SWNT networks respectively. The system was left to cool under just H_2 gas.

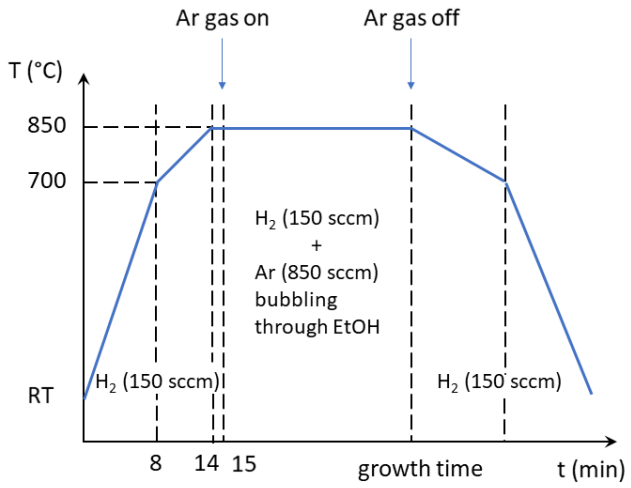

Figure 2.1: Graphical representation of the growth procedure of cCVD for SWNT network.

2.1.4 CVD Boron nitride

h-BN samples, used in this thesis, were grown on polycrystalline Cu foils by the atmospheric pressure CVD method. The h-BN samples were kindly provided by Professor Tianyou Zhai. The Cu foil was polished using an aqueous solution of 0.4 M $FeCl_3$ in 0.8 M HCl. The foil was loaded onto the center of a 25 mm diameter tube furnace pumped to a pressure of 15 mTorr and then heated to 1015 °C under a mixture gas of 16 sccm of hydrogen (purity 99.99 %) and 260 sccm of Ar (purity 99.99%). The foil was annealed for 30 min at 1015 °C. Ammonia borane (purity 97 %, Sigma Aldrich 682098) was used as the precursor for h-BN growth. 1 mg ammonia borane was placed in a specially designed boat and loaded upstream of the CVD growth tube. The precursor temperature was controlled by a heating belt around the tube, separated from the heating

zone of the furnace. After h-BN growth, the system was quickly cooled down to <200 °C under the same gas flow as during the growth. The h-BN sample was removed from the furnace and stored under vacuum.

2.1.5 Chemicals

All solutions were prepared using Milli-Q water (resistivity 18.2 MΩ cm at 25 °C) and all reagents were used as received. Table 2.1 provides a list of the chemicals, along with their formula, purity and supplier, used in this thesis.

Table 2.1: List of chemicals and materials used for the work described in this thesis

Chemicals/ Materials	Suppliers & Details
Chemicals	-------
Hexaammineruthenium (III) chloride ($Ru(NH_3)_6Cl_3$)	Strem Chemical Co., 99 %
Potassium chloride (KCl)	Sigma-Aldrich, ≥99 %
Concentrated sulfuric acid (H_2SO_4)	Sigma Aldrich, >95 %
Dichlorodimethylsilane ($Si(CH_3)_2Cl_2$)	Acros Organics, >99 %
Ferritin (horse-spleen)	50 – 150 mg mL^{-1} in 150 mM aqueous NaCl, Sigma-Aldrich Co., U.K.
Nickel nitrate ($Ni(NO_3)_2$	Sigma-Aldrich, 99.999 %
Nickel sulphate ($NiSO_4$)	Sigma-Aldrich, 99 %
Potassium hydroxide (KOH)	Sigma-Aldrich, 90 %
EtOH	Fisher Scientific, 99.99 %
MeOH	VWR International Ltd., 99 %
Propan-2-ol	Fisher Scientific, 99.99 %
Acetone	Fisher Scientific, 99 %

Water	≥18 MΩ resistivity, Purite Select HP system
Argon (Ar)	BOC Gases, U.K., 99.9995 %
Hydrogen (H_2)	BOC Gases U.K., 99.95 %
Oxygen (O_2)	BOC Gases, U.K., 99.5 %
Ammonia borane	Sigma Aldrich, 97 %
Materials	-------
Silver (Ag) wire	Good fellow Cambridge Ltd., 99.99 %
SiO_2/Si substrates	IDB Technologies Ltd. (n-type, 525 µm thickness with 300 nm of thermally grown SiO_2 layer, single side polished)
Copper (Cu) foil	Alfa-Aesar, 99.8 % (#46365, 25 µm)
Copper (Cu) foil	Good fellow Cambridge Ltd., 99.95 % (25 µm)
Chromium (Cr) coated tungsten bar	Good fellow Cambridge Ltd., 99.9 %
Gold (Au) wire for thermal evaporation	MaTeck, 99.995 %
Cobalt (Co) target	Testbourne Ltd., U.K., 99.95 %
AM-grade HOPG	Originating from Dr. A. Moore, Union Carbide (now GE Advanced Ceramics), and kindly provided by Prof. Richard L. McCreery (University of Alberta, Canada).
SPI-3 grade HOPG	SPI Supplies (West Chester, PA).
Si/SiO_2 substrates	IDB Technologies Ltd. (n-type, 525 µm thickness with 300 nm of thermally grown SiO_2 on both sides)

Borosilicate glass capillary	Harvard Apparatus Ltd. (outer diameter (OD) = 1.2 mm, internal diameter (ID) = 0.69 mm)
Double barreled borosilicate theta capillary	Harvard Apparatus Ltd. (#30-0114)
Single barreled quartz filamented capillary	Friedrich & Dimmock, Inc., U.S.A (QTF120-90-100)
Lacey carbon TEM grid	Agar Scientific

2.2 BDD sample preparation

The BDD sample was cleaned by heating it in a concentrated H_2SO_4 (> 95 %) solution containing saturated KNO_3 solution at 300 °C for 30 minutes prior to use. The resulting surface from this procedure would be oxygen terminated.[6] Hydrogen termination was achieved by hydrogen plasma heating at 1 kW under 60 Torr of hydrogen for 10 min. The sample was left to cool by passing over hydrogen at a flow rate of 500 cm^3 min^{-1} for 10 min.

Ohmic contact was made by sputtering (Moorfields) Ti/Au (10/300 nm) on the back of the BDD. Then the sample was annealed in a tube furnace (Carbolite, U.K.) at 400 ℃ for 5 hours, during which time titanium carbide is formed.

2.3 PMMA transfer of BN sample

The polymethyl-methacrylate (PMMA) method was used to transfer the as-grown h-BN sample onto an Au evaporated SiO_2/Si (Au/SiO_2/Si) substrate.[7,8] First, the as-grown h-BN on Cu foil was spin-coated with PMMA (AR-P. 679.04, ALLRESIST, GmbH) at 4000 rpm for 50 s. Then the Cu foil was etched away by floating it on the surface of an aqueous solution of ferric chloride (0.4 M) for 5 h. The PMMA film was washed with fresh deionized water three times and placed on the target substrates. Then the PMMA film on Au/SiO_2/Si substrate was heated to 150 °C to get rid of any water adsorbed on the PMMA and substrate, as well as to promote good adhesion of the PMMA to the target substrate. The PMMA was then dissolved in acetone. The h-BN on Au/SiO_2/Si

sample was annealed in a tube furnace under nitrogen gas at 350 °C for 5 min to remove the PMMA residue.

2.4 Gold evaporation

Electrical contact to the SWNT networks was made by evaporating Cr (3 nm), followed by Au (60 nm) with a shadow mask covering on the side of the SiO_2/Si substrate using a Moorfield MiniLab deposition system (Moorfield Associates).

2.5 Droplet experiments and MCEM

The functionalization of the SWNT network with nickel hydroxide NPs was carried out in a 3-electrode setup using a droplet method, as shown in Figure 2.2. The SWNT network acted as the working electrode (WE). A side electrical contact to the Au band was achieved via a pin for the WE. A droplet of $Ni(NO_3)_2$ or Ni_2SO_4 in alkaline solution (~15 µL, ~ 4 mm diameter) was placed on the electrode surface, in proximity to the Au band, but without contacting it. A Pt wire was used as the counter electrode (CE) and AgCl-coated Ag wire (Ag/AgCl) acted as a quasi-reference electrode (QRCE). The QRCE used was found to be sufficiently stable under the experimental conditions and timescale.[9] Both the CE and QRCE were positioned within the droplet of the solution to complete the circuit. Electrochemical measurements were performed with a CHI 730 EC workstation (CH Instruments, TX, USA).

For the micro-capillary electrochemical method (MCEM) experiment (Figure 2.2),[9,10] contact to the Au band was made via a Au pin. The SWNT network sample was mounted inside a humidity cell (de-aerated with N_2) and this acted as a WE. The MCEM cell was fabricated using a borosilicate glass capillary (1.2 mm outer diameter, 0.69 mm internal diameter, Harvard Apparatus Ltd.). The capillary was pulled to a small opening using a laser pipette puller (P-2000, Sutter Instrument Co.) and the end was polished flat to produce a cell with an inner diameter of 60 - 62 µm for MOR and EOR studies. The capillary was rendered hydrophobic through immersion in dichlorodimethylsilane (Acros Organics, ≥99 %) for 90 s, with Ar gas flowing through to prevent any internal silanization.

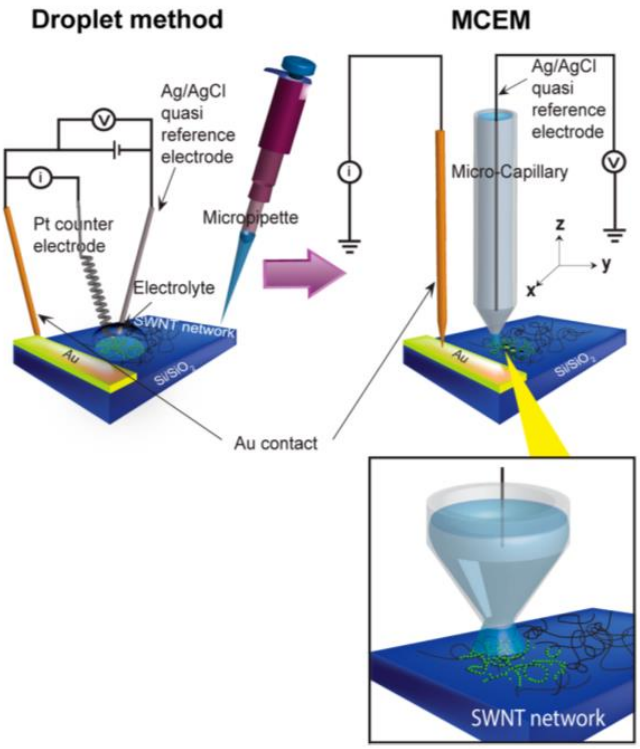

Figure 2.2: Schematic of a 3-electrode droplet experimental setup and 2-electrode MCEM setup for investigations of the electrochemistry of SWNT networks.[10]

2.6 Voltammetric SECCM

In this thesis, voltammetric SECCM[11] was used for all electrochemical scanning imagings. The working mechanism and hardware setup of double-barrel and single-barrel SECCM have been discussed in chapter 1. In this part, the pipettes fabrication procedure and the approach-hold-withdraw (hopping) mode of voltammetric SECCM will be discussed in more detail.

Double-barrel and single-barrel SECCM pipettes are pulled from double-barrel borosilicate theta capillaries and single-barrel quartz filamented capillaries respectively, using a Sutter P-2000 laser puller to produce nanopipettes with different diameters. The sizes and geometries of the pipettes can be tuned by changing the pulling parameters including the pull strength, the delay time and heating power. Two closely similar pipettes are obtained in each pulling action. One was used for SECCM imaging and the other can be characterised to determine the diameter of the pipette precisely by field emission scanning electron microscopy (FE-SEM).

All SECCM experiments in this thesis were carried out in aqueous solutions. When the size of the pipettes was greater than 400 nm, a silanization procedure for confining

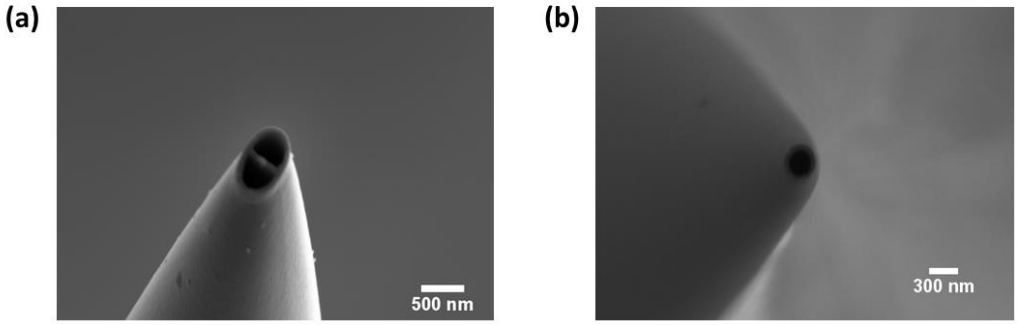

Figure 2.3: FE-SEM image of the end of (a) double-barrel SECCM pipette and (b) single-barrel SECCM pipette.

the meniscus at the end of the pipette was required. In this procedure, the pipettes were immersed in dichlorodimethylsilane solution while argon gas was flowed through to avoid silanization of the internal walls. FE-SEM images of a typical double-barrel and single-barrel pipette used in this thesis are shown in Figure 2.3.

The prepared nanopipette probe (detailed above) is mounted on a *z*-piezoelectric positioner (P-753.3CD, Physik Instrumente), and the substrate is mounted on an *xy*-piezoelectric positioner (P-622.2CD, Physik Instrumente). A cyclic voltammogram (CV) or linear sweep voltammogram (LSV) was recorded at every pixel in the area of interest of a substrate. An approach-hold-withdraw (hopping) mode was employed (Figure 2.4). First, the pipette was approached towards the surface. Once meniscus contact was achieved, a hold time was employed while the meniscus stabilized. Following this, either a CV or LSV measurement was performed. Afterwards, the pipette was retracted to break the meniscus contact by moving a certain distance normal to and away from the surface. Finally, the pipette was moved (spatial resolution) in the *xy* plane laterally to

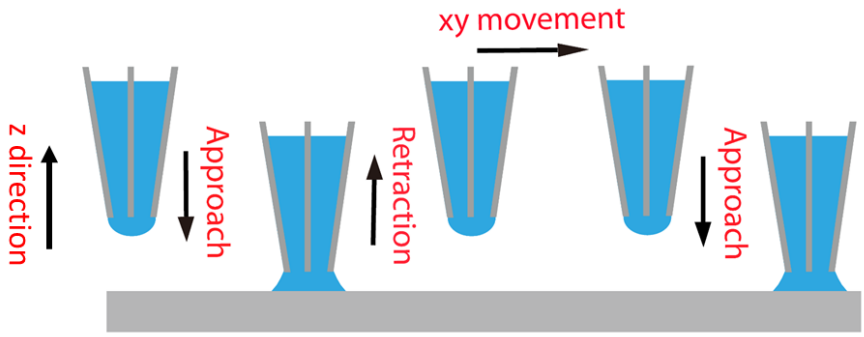

Figure 2.4: Schematic of an approach-hold-withdraw (hopping) mode for SECCM.

the next pixel, where the same measurement procedure was implemented. This protocol was repeated until all the pixels in the area of interest were covered.

2.7 Characterization techniques

2.7.1 Optical microscopy

Optical microscopy was performed using an Olympus BH2 light microscope fitted with lenses in the magnification range ×20 to ×100.

2.7.2 Atomic force microscopy

Atomic force microscopy (AFM) is a useful scanning probe microscopy with resolution on the order of the nanometre scale possible.[12] The basic AFM contains the following features as shown in Figure 2.5. A sharp tip (1) is fixed at the free end of a cantilever (2). The tip scans across the sample (3), which is mounted on the sample stage (4). The interaction between the tip (1) and the sample (3) is reflected by a change in the cantilever motion, which is monitored by recording the deflection from shining a laser on the tip on a coordinate system (5).

There are two main imaging modes for AFM: contact mode and tapping mode. For contact mode, a constant force is maintained between the tip and the surface. The topographical information is obtained by the deflection of the cantilever. Low stiffness cantilevers (cantilevers with a low spring constant) are usually used to achieve a large

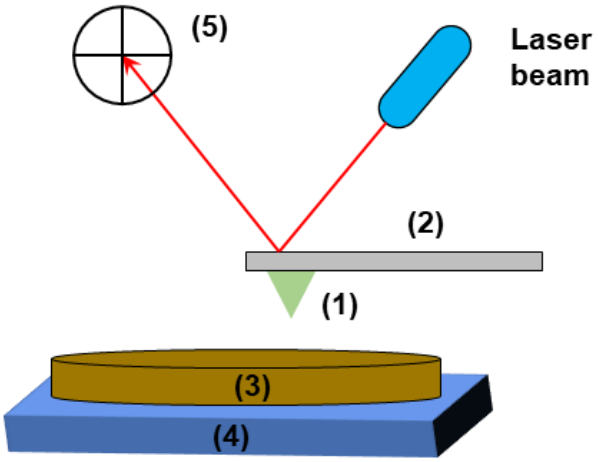

Figure 2.5: Schematic of AFM configuration. (1): Sample, (2): Cantilever, (3): Sample, (4): Sample stage, (5): Coordinate system.

enough deflection while keeping the interaction force low. The measurements are close to the surface of the sample at a depth where the overall force is repulsive, in firm "contact" with the surface. In tapping mode, the cantilever of oscillates at its resonant frequency. This oscillation is commonly achieved with a small piezo element in the cantilever holder. When the tip is close to the surface of the sample, the interaction of forces acting on the cantilever, such as Van der Waals forces and electrostatic forces, causes a change in the amplitude of the cantilever's oscillation. The feedback system employed in AFM will then adjust the height to maintain a set cantilever oscillation amplitude as the cantilever is scanned over the sample.[13]

AFM measurements were recorded in air by using tapping mode (Innova, Veeco and Nano Enviroscope, Bruker) and Bruker MPP-21100-10 AFM tips were used. AFM images allowed the determination of the diameters of SWNT and the size/height of particles.

2.7.3 Kelvin probe force microscopy

With Kelvin probe force microscopy (KPFM) presented first in reference 14, it enables the mapping of the surface potential or work function at atomic or molecular scales, and is a noncontact variant of AFM.[15,16] The work function is the minimum energy which is required to move an electron from a solid (Fermi level) to a point in the vacuum immediately outside the solid surface (vacuum level). The work function measurements of KPFM relate to the analysis of electrical property of nanostructures including reconstruction of surfaces, doping and band-bending of semiconductors and corrosion.

The KPFM is based on an AFM set-up and the determination of the work function is dependent on the measurement of the contact potential difference (CPD) between the sample surface and the conducting AFM tip. The CPD (VCPD) between the tip and the sample is defined as:

$$V_{CPD} = \frac{\phi_{tip} - \phi_{sample}}{e} \tag{2.1}$$

where ϕ_{tip} and ϕ_{sample} are the work functions of the tip and sample, and e is the elementary electron charge.

An AC voltage (V_{AC}) and a DC voltage (V_{DC}) are applied to the AFM tip for KPFM measurement of work function. The V_{AC} generates oscillating electrical force between the AFM tip and sample surface, and V_{DC} nullifies the electrical force. The electrostatic force (F_{es}) is given by:

$$F_{es}(z,t) = -\frac{1}{2}\frac{\partial C(z)}{\partial z}[(V_{DC} \pm V_{CPD}) + V_{AC}\, sin(\omega t)]^2 \quad (2.2)$$

Where z is the direction normal to the sample surface, $\frac{\partial C(z)}{\partial z}$ is the capacitance gradience between the tip and the sample.

This equation can be split up into three parts:

$$F_{DC} = -\frac{\partial C(z)}{\partial z}[\frac{1}{2}(V_{DC} \pm V_{CPD})^2] \quad (2.3)$$

$$F_{\omega} = -\frac{\partial C(z)}{\partial z}(V_{DC} \pm V_{CPD})V_{AC}\, sin(\omega t) \quad (2.4)$$

$$F_{2\omega} = \frac{\partial C(z)}{\partial z}\frac{1}{4}{V_{AC}}^2[cos(2\omega t) - 1] \quad (2.5)$$

Equation 2.4 can be used to measure the V_{CPD}.[17] During KPFM scanning, F_{es} is applied by V_{AC} with V_{DC}, the F_{ω} term depends on $V_{DC} \pm V_{CPD}$. The V_{DC} term can be adjusted to make F_{es} zero and thus the response at the frequency ω becomes zero. The value of the V_{DC} at each point can be used to map the work function of the whole surface, if the tip is calibrated against a reference sample of known work function.

Two modes can be used to detect atomic forces during KPFM: amplitude modulation (AM) and frequency modulation (FM), respectively. In AM mode, F_{ω} is measured by the change in the oscillation amplitude. Then V_{CPD} value is obtained by applying V_{DC} to the AFM tip to nullify the measured amplitude. While in FM mode, F_{ω} is detected by the frequency shift at ω by applying V_{DC} to the AFM tip to nullify the frequency shift, thereby measuring the V_{CPD}.

2.7.4 Field emission scanning electron microscopy

FE-SEM is a technique to probe topographical and elemental information by scanning the sample with a focused electron beam.[18,19]

A typical accelerating voltage (0.2 - 40 keV) is used to generate the high energy beam. When this beam interacts with the sample, the electrons lose energy by scattering and absorption within an interaction volume, ranging from less than 100 nm to 5 µm into the surface. Several types of signals can be recorded. The most commonly used are the backscattered electrons and secondary electrons. The former is obtained due to the elastic scattering interactions with the atoms in the specimen. The backscattered electrons consist of high-energy electrons originating from the electron beam, which are reflected or back-scattered out of the specimen interaction volume. The latter is low energy secondary electrons (SE2) that are ejected from the k-shell of the specimen,

which can be collected either by an in-lens detector or an SE2 detector. The in-lens detector is inside the electron column of the microscope and it can collect SE2 with high efficiency, in particular, at low voltages and small working distances. SE2 is more sensitive to surface structure and topographical information.

For all works in this thesis, an in-lens detector was employed. Metal NPs on SWNTs and BDD scanning areas were characterized using FE-SEM (Zeiss Supra 55-VP) with a 5 keV acceleration voltage. SWNT network density was determined using FE-SEM images (n = 3) with a magnification of ×10000. Graphene scanning areas were characterized using FE-SEM (Zeiss Supra 55-VP) with a 10 keV acceleration voltage. BN scanning areas were characterized using FE-SEM (Zeiss Gemini 500) with a 2 keV accelerating voltage.

2.7.5 Electron backscatter diffraction[20]

Electron backscatter diffraction (EBSD) is used to provide information on the crystalline, polycrystalline materials, such as the crystal orientation, structure and phase of materials.[20] The basic principle of EBSD is a beam of electrons is directed onto the sample. Some of them are incident on the atomic planes at angles which satisfy the Bragg equation:

$$n\lambda = 2dsin\theta \tag{2.6}$$

where n is an integer, λ is the wavelength of the electrons, d is the spacing of the diffraction plane, and θ is the angle of incidence of the electrons on the diffracting plane.

These electrons give rise to diffraction patterns which consist of well-defined Kikuchi lines and can be visualized on a fluorescent phosphor screen. The scanned areas can range from several millimetres to tens of nanometres. The patterns collected can be converted to orientation maps in an inverse pole figure.

The crystallographic orientation of BDD scanning areas, graphene scanning areas and BN scanning areas were recorded on an EBSD equipped Zeiss Sigma FE-SEM system. These measurements were carried out with a pixel spacing of 0.4 μm both for the BDD and the underlying Cu foil of h-BN. The pixel spacing of the underlying Cu foil of graphene is 0.3 μm. All EBSD measurements were carried out at a 20 keV accelerating voltage with the sample tilted at 70°. Data analysis was performed using AZtec 3.1 software (Oxford Instruments, UK). The crystallographic orientation is identified from the colour map with a ‘colour key’ triangle, where the three corners with red, green and

blue represent the three basic planes. High-index facets are represented by a mixture of these three colours.

2.7.6 Contact angle measurements

The contact angle arises from the equilibrium between three phases: the solid phase (S), the liquid phase (L) and the gas phase (G), usually where a liquid-vapour interface meets a solid surface.[21]

Contact angle measurements are used to distinguish surface hydrophilicity.[22] A drop shape analyser (Krüss drop shape analyser system DSA100, Germany) was employed for contact angle measurements of the BDD surface, which enabled the determination of whether the BDD is oxygen terminated or hydrogen terminated.

2.7.7 High resolution transmission electron microscopy (HR-TEM)

Crystalline formation of $Ni(OH)_2$ NPs in chapter 5 was investigated by HR-TEM. Before measurement, $Ni(OH)_2$ NPs samples were mechanically scratched from the growth substrate using a blade and dispersed in absolute EtOH (Fisher Scientific) solution. The suspension was sonicated for 4 minutes and centrifuged for 15 minutes at 10,000 rpm (Eppendorf) to cause particle sedimentation. A drop of 3 µL solution that contains the sedimented particles, was then placed onto a lacey carbon TEM grid (Agar Scientific) and left until the EtOH had evaporated. HR-TEM was conducted (n = 3) using a JEM 2100 TEM (JEOL, LaB_6 filament, operated at 200 kV) equipped with energy-dispersive X-ray spectroscopy (EDS) and selected area electron diffraction (SAED).

2.7.8 Raman microscopy

Raman spectroscopy is a technique to study vibrational, rotational, and other low frequency modes characteristics of molecules.[23] Monochromatic light, usually from a laser in the visible, near infrared, or near ultraviolet range, is used to illuminate a sample. Inelastic or Raman scattering occurs when the laser interacts with molecular vibrations or phonons, resulting in the energy of the laser phonons being shifted up or down. The shifts give the information of the vibrational mode of the sample.

Micro-Raman spectra and Raman mapping were recorded on a Renishaw inVia Raman microscope with a diode-pumped solid-state laser (excitation wavelength of 532 nm). A laser power of 10 mW was employed through a 50× magnification lens. Step sizes of 0.6 µm and 1 µm were chosen for Raman mapping of BDD and graphene respectively.

2.8 References

1 Wilson, N. R., Marsden, A. J., Saghir, M., Bromley, C. J., Schaub, R., Costantini, G., White, T. W., Partridge, C., Barinov, A., Dudin, P., Sanchez, A. M., Mudd, J. J., Walker, M. and Bell, G. R. Weak mismatch epitaxy and structural feedback in graphene growth on copper foil. *Nano Research* **6**, 99 (2013).

2 Chen, S., Ji, H., Chou, H., Li, Q., Li, H., Suk, W., Piner, R., Liao, L., Cai, W., Ruoff, R. S. Millimeter-size single-crystal graphene by suppressing evaporative loss of Cu during low pressure chemical vapor deposition. *Advanced Materials* **25**, 2062-2065 (2013).

3 Edgeworth, J. P., Wilson, N. R. and Macpherson, J. V. Controlled Growth and Characterization of Two-Dimensional Single-Walled Carbon-Nanotube Networks for Electrical Applications. *Small* **3**, 860-870 (2007).

4 Dudin, P. V., Unwin, P. R. and Macpherson, J. V. Electrochemical nucleation and growth of gold nanoparticles on single-walled carbon nanotubes: New mechanistic insights. *The Journal of Physical Chemistry C* **114**, 13241-13248 (2010).

5 Dudin, P. V., Unwin, P. R. and Macpherson, J. V. Electro-oxidation of hydrazine at gold nanoparticle functionalised single walled carbon nanotube network ultramicroelectrodes. *Physical Chemistry Chemical Physics* **13**, 17146-17152 (2011).

6 Wilson, N. R., Clewes, S. L., Newton, M. E., Unwin, P. R. and Macpherson, J. V. Impact of grain-dependent boron uptake on the electrochemical and electrical properties of polycrystalline boron doped diamond electrodes. *The Journal of Physical Chemistry B* **110**, 5639-5646 (2006).

7 Reina, A., Jia, X., Ho, J., Nezich, D., Son, H., Bulovic, V., Dresselhaus, M. S. and Kong, J. Large area, few-layer graphene films on arbitrary substrates by chemical vapor deposition. *Nano letters* **9**, 30-35 (2008).

8 Li, X., Zhu, Y., Cai, W., Borysiak, M., Han, B., Chen, D., Piner, R. D., Colombo, L. and Ruoff, R. S. Transfer of large-area graphene films for high-performance transparent conductive electrodes. *Nano letters* **9**, 4359-4363 (2009).

9 Day, T. M., Unwin, P. R. and Macpherson, J. V. Factors controlling the electrodeposition of metal nanoparticles on pristine single walled carbon nanotubes. *Nano Letters* **7**, 51-57 (2007).

10 Sharel, P., Liu, D., Lazenby, R. A., Sloan, J., Vidotti, M., Unwin, P. R. and Macpherson, J. V. Electrodeposition of nickel hydroxide nanoparticles on carbon nanotube electrodes: Correlation of particle crystallography with electrocatalytic properties. *J. Phys. Chem. C* **120**, 16059-16068 (2016).

11 Chen, C.-H., Jacobse, L., Mckelvey, K., Lai, S. C., Koper, T. M. and Unwin, P. R. Voltammetric scanning electrochemical cell microscopy: dynamic imaging of hydrazine electro-oxidation on platinum electrodes. *Analytical chemistry* **87**, 5782-5789 (2015).

12 Ohnesorge, F. and Binnig, G. J. S. True atomic resolution by atomic force microscopy through repulsive and attractive forces. *Science* **260**, 1451-1456 (1993).

13 Geisse, N. A. AFM and combined optical techniques. *Materials today* **12**, 40-45 (2009).

14 Nonnenmacher, M., o'Boyle, M. and Wickramasinghe, H. K. J. A. p. l. Kelvin probe force microscopy. *Applied physics letters* **58**, 2921-2923 (1991).

15 Melitz, W., Shen, J., Kummel, A. C. and Lee, S. Kelvin probe force microscopy and its application. *Surface science reports* **66**, 1-27 (2011).
16 Nonnenmacher, M., o'Boyle, M. and Wickramasinghe, H. K. Kelvin probe force microscopy. *Applied physics letters* **58**, 2921-2923 (1991).
17 Kalinin, S. V. and Gruverman, A. *Scanning probe microscopy: electrical and electromechanical phenomena at the nanoscale*. Vol. 1 (Springer Science & Business Media, 2007).
18 Goldstein, J. I., Newbury, D. E., Joy, D. C., Lyman, C. E., Echlin, P., Lifshin, E., Sawyer, L. and Michael, J. R. *Scanning electron microscopy and X-ray microanalysis*. (Springer, 2017).
19 Zhou, W. and Wang, Z. L. *Scanning microscopy for nanotechnology: techniques and applications*. (Springer science & business media, 2007).
20 Schwartz, A. J., Kumar, M., Adams, B. L. and Field, D. P. *Electron backscatter diffraction in materials science*. Vol. 2 (Springer, 2009).
21 Yuan, Y. and Lee, T. R. *Surface science techniques*. (Springer, 2013).
22 Marmur, A. Soft contact: measurement and interpretation of contact angles. *Soft Matter* **2**, 12-17 (2016).
23 Graves, P. and Gardiner, D. *Practical Raman spectroscopy*. (Springer, 1989).

Chapter 3. Electron transfer kinetics at monolayer, bilayer and multilayer CVD graphene as grown on polycrystalline copper

The effect of the support substrate on the electrochemical properties of graphene and other 2D materials is of considerable interest. In this study, high-resolution scanning electrochemical cell microscopy (SECCM) is employed to assess and gain insights into the heterogeneous electron transfer (ET) kinetics at graphene, grown on a Cu substrate using the chemical vapor deposition (CVD) method. The small-scale electrochemical cell (ca. 700 nm – 1 μm diameter) constructed when an SECCM droplet is positioned directly on as-grown CVD graphene enables measurements to be made in more than a 1000 different areas of a graphene/copper working electrode. By employing co-located correlative microscopy, in the form of Raman microscopy and field emission-scanning electron microscopy (FE-SEM), the nature of the sites of the electrochemical measurements is identified. Clear differences in ET kinetics between monolayer, bilayer and multilayer graphene for the hexaammineruthenium (III) chloride ($Ru(NH_3)_6^{3+/2+}$) redox couple, whose standard potential is close to the intrinsic Fermi level of uncharged graphitic materials, are revealed. In contrast to previous studies of graphene on SiO_2/Si surfaces, monolayer graphene on copper exhibits faster ET kinetics than for bilayer and multilayer, as judged from the half-wave overpotential and quartile potentials in SECCM voltammetric measurements. However, all three types of graphene display slower apparent kinetics than for highly oriented pyrolytic graphite (HOPG), both freshly cleaved and aged in air. These differences in ET kinetics are attributed to the modification of the electronic properties of graphene, in line with electronic structure calculations and Kelvin probe force microscopy (KPFM) measurements. The results are fundamentally important for understanding the electrochemical properties of graphene-based devices, and illustrating the significance of the underlying support and the consequent possibility of tuning the electrochemical characteristics. This study further illustrates that activity movies from SECCM in tandem with structure and properties from co-located microscopy is a powerful strategy for revealing the electrochemical properties of complex surfaces.

3.1 Introduction

Graphene has generated considerable interest in electrochemistry owing to a range of outstanding physicochemical properties, including electrical conductivity,[1] high specific surface area,[2] scope for tuning heterogeneous electron transfer (ET) rates,[3] and mechanical strength.[4] Promising electrochemical applications of graphene span energy storage,[5-7] chemical sensing,[8,9] and biochemical analysis.[10] Despite this large body of work, the electrochemical performance of graphene in these applications is not straightforward to analyze at a fundamental level due to the complex interplay of effects arising from the graphene itself, such as the source of the graphene (mechanical exfoliation, ME or chemical vapor deposition, CVD),[11,12] number of graphene layers,[13-16] edges and defects,[17-21] the support on which the graphene is placed,[22,23] and contamination of the surface from polymer residues (in the case of transferred CVD graphene) or atmospheric contamination.[3,24,25]

SiO_2/Si substrates are widely used in constructing both ME and CVD graphene working electrodes for electrochemical studies.[3,11-15,17,20-23,25-27] However, doping effects from this type of substrate can modulate the electronic properties of graphene, as studied with scanning probe microscopy,[28] in field effect transistors[29] and by Raman microscopy.[30] Expanding the range of graphene substrate supports, as in this paper, would thus be very valuable.

Compared to ME graphene,[31] CVD graphene is more suitable for producing large areas of monolayer graphene whilst low defect densities can be achieved,[32] making it compatible for mass production and for the fabrication of graphene based-devices. Furthermore, a few studies have shown that it is possible to study the electrochemical behavior of CVD-graphene directly on the metal growth support, eliminating the complications arising from graphene transfer, as-exemplifed by studies of CVD-graphene on Cu foil.[23,25] Such studies raise the interesting prospect of elucidating substrate effects in modulating ET kinetics at graphene.[22,23]

It is well known that CVD-graphene grown on Cu foil and other metals often contains some islands of bilayer or multilayer graphene, alongside the predominant monolayer form.[33,34] These different forms are present as distinct grains, separated by grain boundaries. Additionally, over extended areas, pinholes within the graphene layer to the underlying Cu support are expected.[35] As such, macroscopic voltammetry of such materials will represent the average of all such sites and will "wash out" the

characteristics of the electrochemistry of different grains, which might be expected to be different, based on local measurements of graphene electrochemistry made hitherto.[14,15,17,36] In this chapter, we make use of scanning electrochemical cell microscopy (SECCM),[37,38] a meniscus-based electrochemical probe technique in which a series of tiny temporary electrochemical cells are made across a working electrode surface, by bringing a pipette probe containing electrolyte and quasi-reference counter electrodes (QRCEs) into meniscus contact. SECCM studies have previously shown that the standard heterogeneous ET rate constant for the one-electrode oxidation of (ferrocenylmethyl) trimethylammonium at CVD graphene on SiO_2/Si prepared by the polymer transfer method, increases with the increasing number of graphene layers, becoming diffusion-limited (reversible) for few-layer graphene.[14] Furthermore, the electrochemical kinetics of the $Ru(NH_3)_6^{3+/2+}$ couple at ME graphene on SiO_2/Si[17] also demonstrated a correlation with the number of graphene layers, with monolayer graphene having the slowest ET rate, increasing for bilayer, and ultrathin graphite promoting the fastest kinetics.

In this work, we report on the ET kinetics of mono-, bi- and multilayer CVD graphene, as-grown on Cu foil using $Ru(NH_3)_6^{3+}$ as a redox mediator. $Ru(NH)_3^{3+/2+}$ is a particularly interesting redox probe, as its standard potential is close to the intrinsic Fermi level of uncharged graphitic materials.[17] With voltammetric SECCM a cyclic voltammogram (CV) is obtained at each pixel, enabling the investigation of spatial heterogeneities in ET kinetics. One voltammetric SECCM scan comprises CVs recorded in thousands of different areas of the surface, and this is equivalent to performing CVs at thousands of graphene micro-electrodes of different known structure. Together with co-located Raman microscopy characterization and field emission-scanning electron microscopy (FE-SEM) experiments, the combinatorial methodology presented herein reveals unequivocally the electrochemical behavior of monolayer, bilayer and multilayer graphene on copper, advancing fundamental understanding of substrate supports on the electrochemistry of 2D materials and aiding the design of novel graphene based electromaterials and electrochemical devices.

3.2 Materials and methodology

3.2.1 Chemicals and materials

All aqueous solutions were prepared from ultrapure water (SELECT-HP, Purity, 18.2 MΩ cm resistivity at 25 °C). Potassium chloride (KCl, ACS grade) and hexaaminеruthenium (III) chloride ($Ru(NH_3)_6Cl_3$, purity 99.9 %) were purchased from Sigma Aldrich. Fresh solutions comprising of 1 mM $Ru(NH_3)_6Cl_3$ in 50 mM KCl electrolyte were prepared prior to each experiment. Silver-chloride coated silver (Ag/AgCl) wires were used as quasi-reference counter electrodes (QRCEs) for SECCM.[39] All reported potentials are against the Ag/AgCl (50 mM KCl) QRCEs (56 mV vs. saturated calomel reference (SCE)), herein referred to as Ag/AgCl. High quality n-type silicon/silicon dioxide substrates (SiO_2/Si, 525 μm thickness with 300 nm of thermally grown SiO_2) were obtained from IDB Technologies Ltd. Copper foil was purchased from Alfa-Aesar (purity 99.8 %, 0.025 mm thick, product number 46365). Copper foil with smaller grain size was obtained from Goodfellow Cambridge Limited (purity 99.95 %, 0.025 mm thick).

3.2.2 Preparation of CVD graphene

Graphene substrates used in this work were grown on polycrystalline copper foils as reported in literature.[40] The copper foil was pre-treated by electrochemical polishing clean.[41] It was then placed in a 1 inch diameter tube furnace pumped to 4.4 mTorr by a turbomolecular pump. The foil was heated to 950 °C and annealed for 10 min, followed by exposure to a gas mixture of 10 standard cubic centimeters hydrogen (sccm) and 3 sccm methane (purity 99.95 %) for 25 min. After cooling linearly to room temperature (around 1 h), the fully covered graphene sample was removed from the furnace and stored. The rear surface of the sample was fixed to a Au (300 nm) evaporated SiO_2/Si wafer by using silver paint (Agar Scientific, Ltd, U.K.). The whole sample was then connected to a copper wire for electrochemical measurements.

For studies of any copper surface crystallographic orientation effect on the ET kinetics at supported graphene, a polycrystalline copper foil with smaller grain size (10 - 300 μm) was used for graphene growth. The CVD graphene procedures and growth parameters were as outlined above, except the growth time for this graphene was 30 min.

3.2.3 Pipette fabrication

The pipettes used for SECCM were pulled from borosilicate theta capillaries (TG C150-10, Harvard Part No.30-0114) by using a Sutter P-2000 laser puller (Sutter Instruments, USA). The inner diameters of pipettes were in the range 700 nm – 1 μm, determined accurately by using a Zeiss SUPRA 55 FE-SEM. The outer walls of the pipettes were rendered hydrophobic by silanization with dichlorodimethylsilane (99+ % purity, Acros), by flowing argon through the pipette to protect the inside from silanization.

3.2.4 Voltammetric SECCM setup

The SECCM setup was reported in previous papers from our group.[42,43] Referring to Figure 3.1, a bias voltage V_2 (200 mV) was applied between two Ag/AgCl QRCEs inserted into the tapered pipette filled with 1 mM $Ru(NH_3)_6^{3+/2+}$ as the chloride salt, in 50 mM KCl electrolyte, to generate an ion conductance current (i_{DC}). The *z*-position of the pipette (normal to the substrate surface) was modulated sinusoidally (268 Hz, 40 nm peak amplitude) by a lock-in amplifier (Stanford Research, SR830), generating an alternating current component in the ion conductance current at the same frequency (i_{AC}).

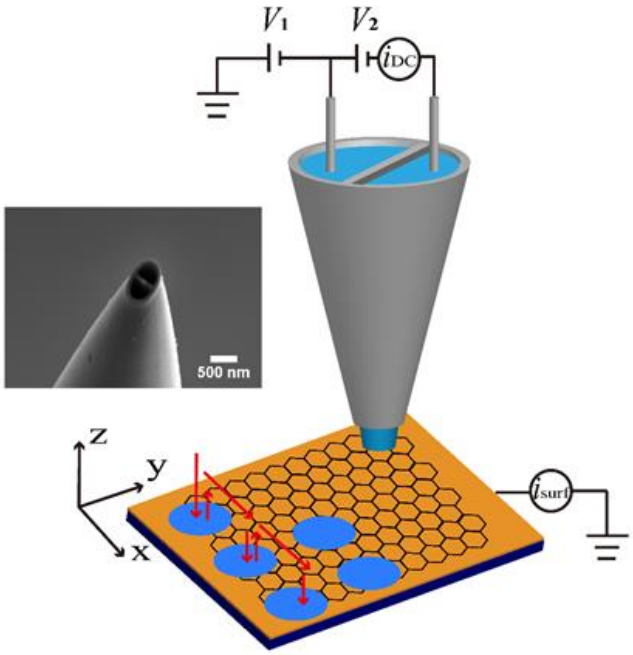

Figure 3.1: Schematic (not to scale) of voltammetric SECCM setup. A hopping mode was used in which the pipette probe was moved to and from the substrate working electrode surface (meniscus contact), with a CV recorded at 0.5 V/s at each pixel.

i_{AC} is negligible when the pipette is in air, but has a measurable value when the pipette is in meniscus contact with the surface. A threshold (setpoint) value of i_{AC} magnitude (6 pA) was set to position the meniscus on the sample. By monitoring i_{AC} during the pipette approach towards the sample at each position, vertical movement of the pipette ceased when this value was attained, indicating that the meniscus (but not the pipette itself) was in contact with the substrate. The effective potential of the sample with respect to Ag/AgCl QRCEs (E_s) was approximately $-(V_1+V_2/2)$, which could be changed via the value of V_1 while maintaining the QRCE bias voltage, V_2.[44] The electrochemical current flowing through the sample is denoted as i_{surf}.

Voltammetric SECCM scanning was operated in a hopping mode.[45] The pipette was approached towards the surface at a speed of 0.3 μm s^{-1}, and once the meniscus had contacted the surface, the pipette was held in that position for 0.1 s before a potential sweep (0.5 V s^{-1}) was applied, from the starting potential of 0 V to the reverse potential of -0.6 V and back to the starting potential to generate CVs for $Ru(NH_3)_6^{3+}$ reduction. The pipette was then retracted a distance of 1.5 μm at a speed of 2 μm s^{-1} to break the meniscus contact with the working electrode surface and the pipette was moved to the next pixel with a hopping distance of 600 nm in *x*-*y* plane at a rate of 1 μm s^{-1}. This protocol was repeated at each pixel in the area of interest.

Current-potential data (recorded every 3 mV in each CV) at each *xy* position could be plotted as a series of spatially-resolved current map that constituted a potentiodynamic movie, containing 121 frames herein. This and other data analyses were performed with Matlab (R2014b, Mathworks). Half-wave potential ($E_{1/2}$) maps were generated by extracting the potentials of each pixel at which the substrate working electrode current was equal to half of the steady-state diffusion-limited current (i_{lim}) value. Similarly, the potentials of each pixel at which surface current was 3/4 and 1/4 of i_{lim} were obtained to generate maps of quartile potential difference magnitude $|E_{3/4} - E_{1/4}|$.

3.2.5 Structural characterization

FE-SEM. The morphology of the scanned area (particularly to identify graphene grains) was imaged on a Zeiss Supra 55-VP FE-SEM by using the in-lens secondary electron detector, operated at 10 kV.

Raman microscopy. Raman spectra of graphene were obtained with a Renishaw Invia micro-Raman spectrometer, using a diode-pumped solid-state laser (Renishaw RL523C50) with an excitation wavelength of 532 nm. Spectra were obtained at 100 %

power with an integration time of 10 s. The same parameters were used for Raman mapping. A 50× lens was used to record each spectrum with a step size of 1 μm. For imaging purposes, the peak intensities of the 2D peak and G peak were extracted for each pixel to provide the 2D/G ratio that was plotted as maps (*vide infra*).

Electron backscatter diffraction (EBSD). The crystal orientation of the Cu foil underlying the graphene areas imaged by SECCM was determined by FE-SEM EBSD (Zeiss Sigma) imaging with a Nordlys F (Oxford Instruments) camera. Measurements were performed at an accelerating voltage of 20 kV, with a collection step of 0.4 μm, with the sample tilted at 70°. Data analysis was performed using Aztec 3.1 (Oxford Instruments).

Kelvin probe force microscopy (KPFM). The surface potentials of graphene grown on polycrystalline Cu foil were obtained under ambient conditions by KPFM measurements on an atomic force microscope (Asylum Research MFP3D-SA) with NSC14/PT AFM tip. An AC voltage of U_{AC} ~ 1 V and f_{AC} ~ 66.5 kHz. The built in lock-in amplifier of the MFP3D controller was used to apply a DC voltage in order to minimize the resulting electrostatic force caused by the contact potential difference between the tip and surface.

3.3 Results and Discussions

3.3.1 Voltammetric SECCM of graphene on Cu

Voltammetric SECCM[45,46] was used to obtain electrochemical maps of the graphene grown on Cu foil. A typical area (referred to as area 1 herein) scanned by a pipette with a diameter of about 700 nm is considered here. An FE-SEM image of the scanned area is given in Figure 3.2 a, and a magnified region is given in Figure 3.2b, which shows that the surface is covered by an array of salt residues from the SECCM measurements. The overall quality of the graphene area imaged was assessed by Raman spectroscopy, as detailed in Figure 3.2c. The spectrum shows a negligible D peak (expected at 1350 cm^{-1}), indicating very low defect density in the graphene. As discussed later, the number of graphene layers can be estimated by the peak intensity ratio of 2D to G (I_{2D}/I_G), as well as the shape and position of these peaks.[47,48] at each pixel in a Raman image. The graphene film that covered the Cu foil was mainly found to be single layer graphene, with some bilayer islands, and our ability to map the same regions with SECCM and

Raman microscopy, allowed correlation of the electrochemical response to the number of graphene layers (*vide infra*).

The CVs at each pixel started at a potential of 0 V, with the potential swept cathodically to -0.6 V, and then reversed back to 0 V. Current maps are presented as current density to allow comparison between tips of different sizes. To estimate the current density we approximated the meniscus size as the tip size (700 nm), which is a good approximation for SECCM measurements graphene, graphite, and metal and metal oxide surfaces.[14,17,44,49,50] Maps of the DC ion conductance current obtained during SECCM measurements are revealing of the meniscus size.[17,44,51] DC ion conductance current histograms obtained from SECCM scanning of area 1 at -0.1 V (foot of the CV) and -0.6 V (diffusion-limit region) are detailed in Figure 3.3. The distributions are similar. When reporting current density, we normalized the current by the tip dimensions, which is a good approximation for graphitic materials.[17,44,50]

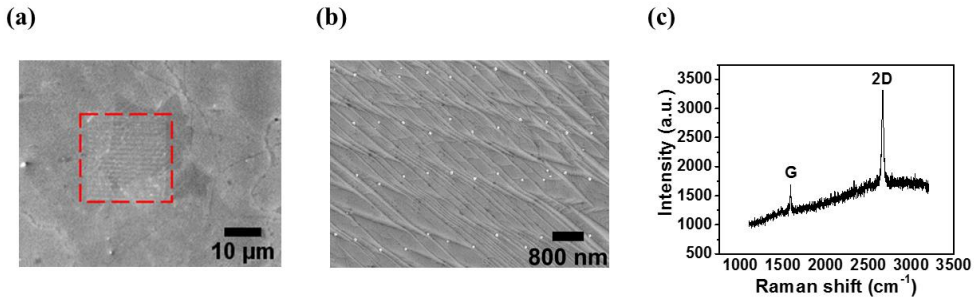

Figure 3.2: Wide area FE-SEM image of graphene on Cu foil, showing area 1 where SECCM measurements were performed, indicated by the red box. (b) FE-SEM image of residues on area 1 with higher magnification. (c) Typical Raman spectrum of graphene on Cu foil. Laser wavelength: 532 nm.

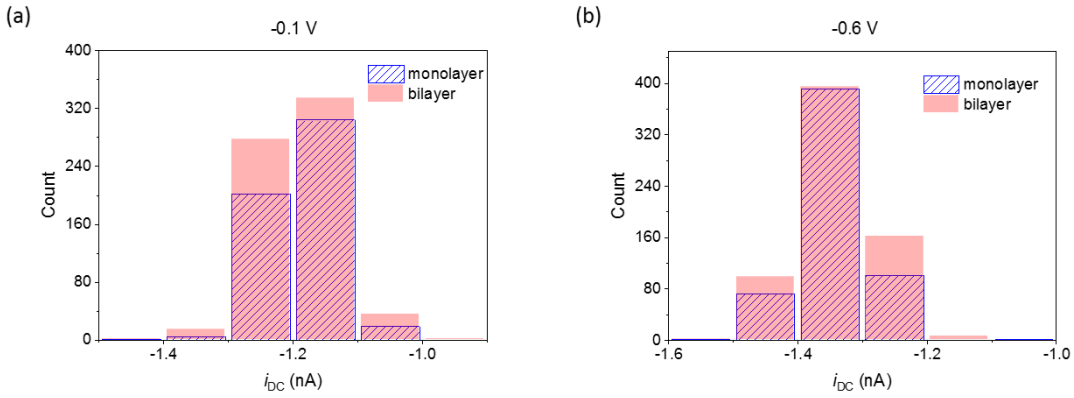

Figure 3.3: DC ion conductance current (i_{DC}) histogram distributions of area 1 at – 0.1 V (a) and -0.6 V (b) vs. Ag/AgCl in 1 mM $Ru(NH_3)_6^{3+}$ (chloride salt) in 50 mM KCl.

A current density map, extracted at a potential of E_{sub} = 0 V vs. Ag/AgCl (beginning of CV) is shown in Figure 3.4a. This map shows that for most of the surface area there is very little electrochemical activity (essentially zero current on the pA scale), but there are a few pixels that show a significant positive current. This implies that there are some pinholes in the graphene, which exposes the Cu foil beneath to the electrolyte solution, with Cu undergoing anodic dissolution in the chloride medium at this potential. As a CV is run at each pixel in the image, CVs could be extracted and examined for the pinholes, as exemplified by the two typical pinholes, marked on the SECCM image. The CV of pinhole 1, shown in Figure 3.4b, displays a positive current in the applied range 0 V to -0.05 V, and can be explained by the anodic dissolution, oxidizing Cu to be Cu^+ ($CuCl_2^-$).[52,53] This is superimposed on a well-defined sigmoidal voltammogram for $Ru(NH_3)_6^{3+}$ one-electron reduction to $Ru(NH_3)_6^{2+}$ at more cathodic potentials that is expected for the SECCM configuration.[14,17,44] The CV of pinhole 2 (see Figure 3.4c) reveals a pair of more significant reduction (peak i) and oxidation (peak ii) peaks superimposed on the $Ru(NH_3)_6^{3+}$ reduction wave. Note that the reduction peak is only just discernable in Figure 3.4b. Cuprous chloride may react with water to generate cuprous oxide (Cu_2O) and is further oxidized to cupric hydroxide ($Cu(OH)_2$), atacamite ($(Cu_2(OH)_3Cl$) or malachite ($CuCO_3 \cdot Cu(OH)_2$).[54,55] The second peak (ii) is attributed to Cu oxidation to Cu(I).[52]

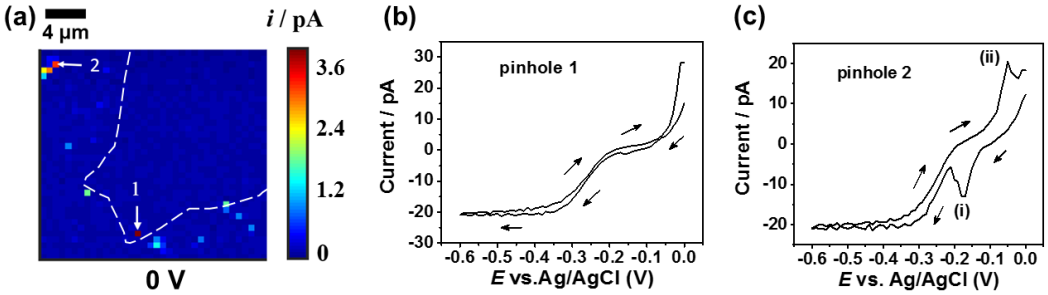

Figure 3.4: (a) SECCM image of area 1 at 0 V vs. Ag/AgCl in 1 mM $Ru(NH_3)_6^{3+/2+}$ in 50 mM KCl. The scan rate was 0.5 V/s. (b) and (c) CVs extracted at pinhole 1 and pinhole 2 marked in Figure 3.4a.

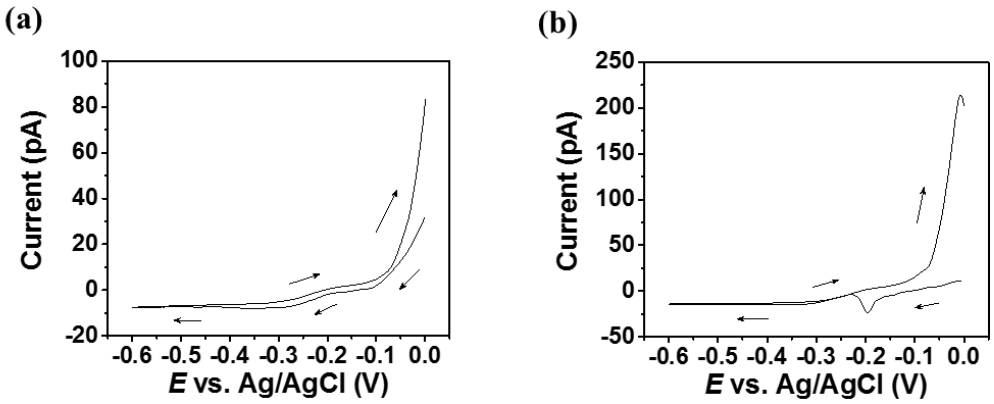

Figure 3.5: Two spot CVs for the reduction of 1 mM $Ru(NH_3)_6^{3+/2+}$ in 50 mM KCl at 0.5 V/s run by SECCM on electropolished Cu foil in different areas.

To further validate that the current signatures were from exposed Cu, CVs were run on a pure Cu foil after electropolishing (the same procedure as used for graphene growth) using the same SECCM scanning parameters (see Figure 3.5). The voltammograms obtained exhibit similar characteristics demonstrating that voltammetric SECCM is able to resolve pinholes on the CVD grown graphene on a Cu foil. This is an important aspect of SECCM. Not only can pinholes be identified, but these areas can be ignored, by inspecting SECCM images and ensuring that only the electrochemistry of pure graphene is examined.

The FE-SEM image of area 1 shown in Figure 3.2a reveals some contrast in the image intensity across the surface, which suggests there are regions with different numbers of graphene layers. To confirm this and to identify the number of graphene layers, this area was characterized by Raman microscopy with results shown in Figure 3.6. Figure 3.6b shows three characteristic graphene peaks for the D, G, and 2D bands.[56] For the spectrum of A, using the ratio of peak intensities I_D/I_G, the level of disordered graphene can be estimated. The low ratio, around 0.073, displays low defect of graphene.[57] The decrease of I_{2D}/I_G from 2.1 (A) to 1.2 (B) reveals an increased number of graphene layer from 1 to 2. The position of 2D peak for A seats at 2672 cm^{-1}, this value for B red shifts to 2706 cm^{-1}, which further proves that A and B correspond to monolayer (ML) and bilayer (BL) graphene, respectively.[56] Instead of single Raman spectrum, Raman mapping of area 1 was performed with a spatial resolution of 1 μm. The number of graphene layers was determined from the 2D/G ratio (Figure 3.6c). The 2D to G ratio of Raman spectra indicate that area 1 comprises of regions of monolayer graphene (labelled A) and bilayer graphene (labelled as B).

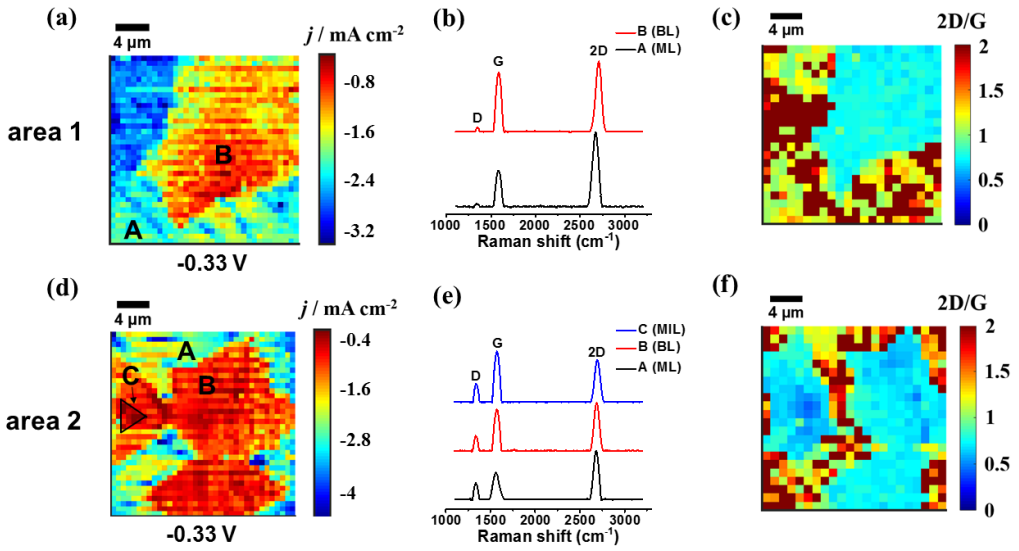

Figure 3.6: (a) SECCM image of area 1 at -0.33 V vs. Ag/AgCl. (b) Raman spectra from A and B of area 1. (c) 2D/G ratio Raman mapping of area 1. (d) SECCM image of area 2 at -0.33 V vs. Ag/AgCl. (e) Raman spectra from A, B and C of area 2. (f) 2D/G ratio Raman mapping of area 2.

The electrochemical data can be represented and played as a potentiometric movie (SI, Movie S1), which shows the electrochemical activity (substrate current) as a function of applied potential during the CV measurement. There is a clear correlation between the potential-dependent electrochemical activity spatial distribution in the SECCM movie, and in the example extracted image at a potential of E_{sub} = -0.33 V (Figure 3.7a), and the corresponding FE-SEM image (see Figure 3.7b). When the applied potential is in the kinetic region (e.g. Figure 3.7a), the current recorded over bilayer graphene is lower than over monolayer graphene. At more cathodic potentials, beyond -0.5 V when the current

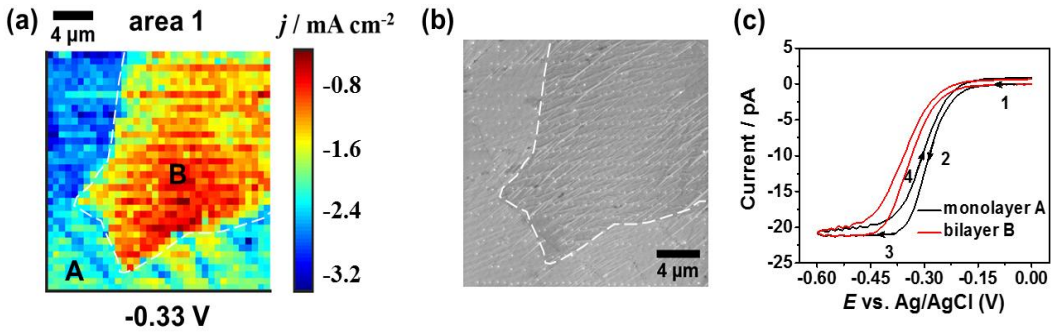

Figure 3.7: (a) SECCM image of area 1 for $Ru(NH_3)_6^{3+}$ reduction at -0.33 V vs. Ag/AgCl. The scan rate was 0.5 V/s. (b) Corresponding FE-SEM image of area 1. (c) Averaged CV response for monolayer graphene (region A) and bilayer graphene (region B).

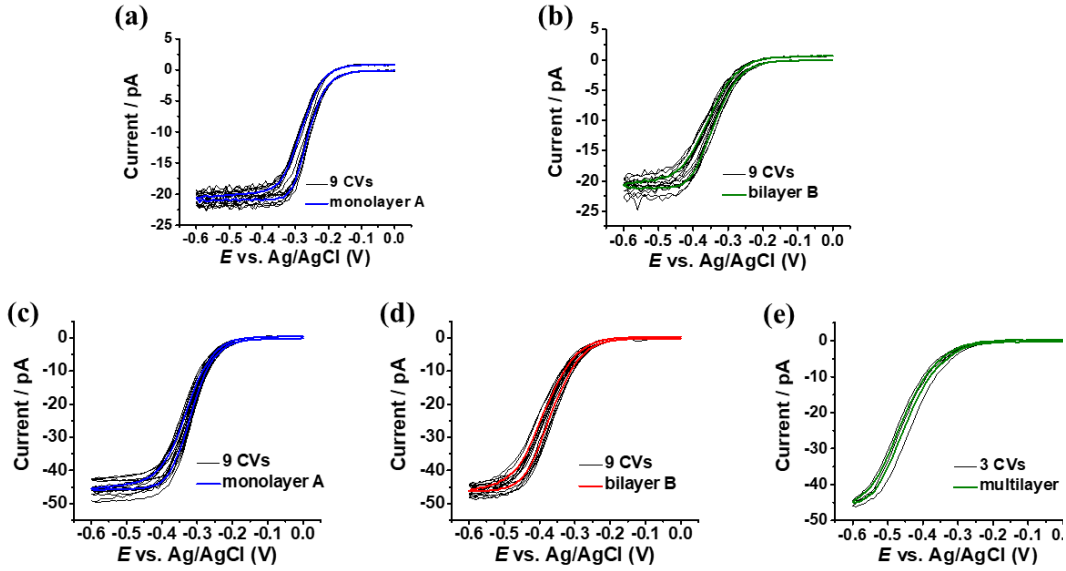

Figure 3.8: Individual CVs extracted from (a) monolayer A and (b) bilayer B as marked on SECCM image of area 1. Individual CVs extracted from (c) monolayer A, (d) bilayer B and (e) multilayer C as marked on SECCM image of area 2.

becomes diffusion-limited and reaches a steady-state (see, for example, Figure 3.4b and Figure 3.4c), the current is similar over the entire surface, ca. 21 pA in the 2 regions.

The average CV responses taken from the different regions, A and B, produced from 9 individual CVs in each case, are shown in Figure 3.7c. The individual CVs used to obtain the averaged CV response are provided in Figure 3.8. These data highlight the high reproducibility of the measurements. There is a small hysteresis between the forward and reverse waves, as the scan rate of 0.5 V/s means that the measurement is not at true steady-state (the mass transport coefficient in SECCM is about 10% of that for the equivalent disk-shaped UME for a neutral species, but is also enhanced by the applied potential between the QRCEs[44,58,59]). The current reaches a steady-state limiting value at cathodic driving potentials. However, as with the movie and current activity map (Figure 3.7a), for less driving potentials, the monolayer graphene region for area 1 displays apparently faster kinetics for the $Ru(NH_3)_6^{3+/2+}$ process than bilayer graphene.

3.3.2 ET kinetics: Comparison of Monolayer, Bilayer and Multilayer Graphene

We now consider data from a second area, area 2 (Figure 3.9). Raman characterization of area 2 (Figure 3.6) confirmed there were 3 types of graphene comprising monolayer (A), bilayer (B) and multilayer (C), where $3 \leq$ layer number < 10 is due to the self-limiting graphene growth on Cu,[60] and so this sample provided an interesting material

to reveal any differences between different numbers of layers on graphene on the Cu support. An FE-SEM image of the end of pipette used for imaging area 2 (diameter ~1 μm) is displayed in Figure 3.10a. In terms of image contrast, the FE-SEM image of scanned area 2 (Figure 3.10b) is similar to that discussed for area 1, except that there is an even darker small region, alongside the other 2 regions, which is attributed to multilayer graphene. The potential-resolved substrate current activity movie (SI, Movie S2) and an example snapshot from the movie at a potential of -0.33 V, shows again that there is significant variations in electrochemical activity that match to the local graphene character.

The averaged CVs comparing monolayer, bilayer and multilayer graphene areas (marked as A, B and C in Figure 3.9a) are shown in Figure 3.9b. The transport-limited current is independent of the number of layers (~ 46 pA), as found for area 1. The monolayer graphene region shows faster kinetics than for the bilayer region, with the multilayer region, exhibiting even slower apparent kinetics. The individual CVs used to obtain the averaged CVs for area 2 are provided in Figure 3.8. The change in onset of reduction for different number of graphene layers is observed herein. This may be concerned with the doping effect of the underlying metal substrate, which was studied by Kelvin probe force microscopy (KPFM) measurements in the later section.

To obtain more insight into the apparent kinetics, half-wave potential ($E_{1/2}$) maps and maps of the absolute difference in the quartile potential, $|E_{3/4} - E_{1/4}|$, from area 2 were extracted and are plotted in Figures 3.9c and 3.9d, respectively. As our interest is to look for trends in activity, for simplicity, we used the forward wave for these and all similar analyses herein. There is a clear correlation between the $E_{1/2}$ map and the different number of graphene layers. The $E_{1/2}$ value for the reduction of $Ru(NH_3)_6^{3+}$ at monolayer graphene (region A) is seen to be more positive than for bilayer graphene (region B), which in turn is more positive than for multilayer graphene (region C). A histogram of $E_{1/2}$ values (Figure 3.9e) shows two major peaks which are attributed to monolayer and bilayer graphene, with peak values at -0.318 V and -0.375 V, respectively. Region C was so small that it is difficult to see this (at ca. -0.423 V based on the voltammogram in Figure 3.9b) above the background.

The $|E_{3/4} - E_{1/4}|$ map is indicative of the degree of reversibility of the electrochemical process, being 56 mV at 298K for a one-electron electrochemically reversible process (Toměs criterion), and taking increasingly larger value with increasing kinetic

limitations.[61,62] This map also shows a strong correlation with the number of graphene layers. As shown in the histogram in Figure 3.9f, the one-electron reduction of

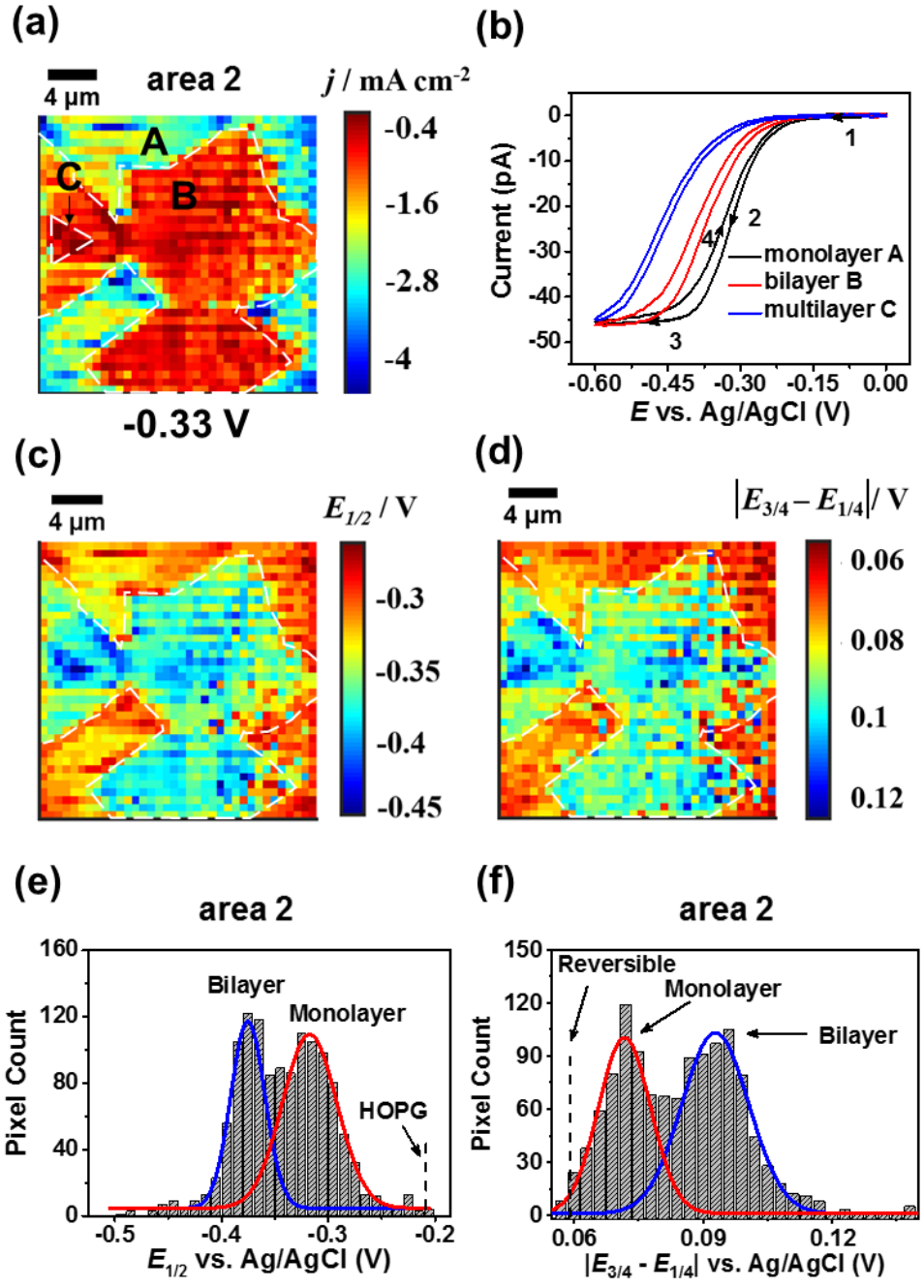

Figure 3.9: (a) SECCM image of area 2 for $Ru(NH_3)_6^{3+}$ reduction at -0.33 V vs. Ag/AgCl. The scan rate was 0.5 V/s. (b) Averaged CV comparison for monolayer graphene from region A, bilayer graphene from region B and multilayer graphene from region C. (c) $E_{1/2}$ map of area 2. (d) $|E_{3/4} - E_{1/4}|$ map of area 2. (e) Histogram distribution of $E_{1/2}$ from Figure 3.9c. (f) Histogram distribution of $|E_{3/4} - E_{1/4}|$ from Figure 3.9d.

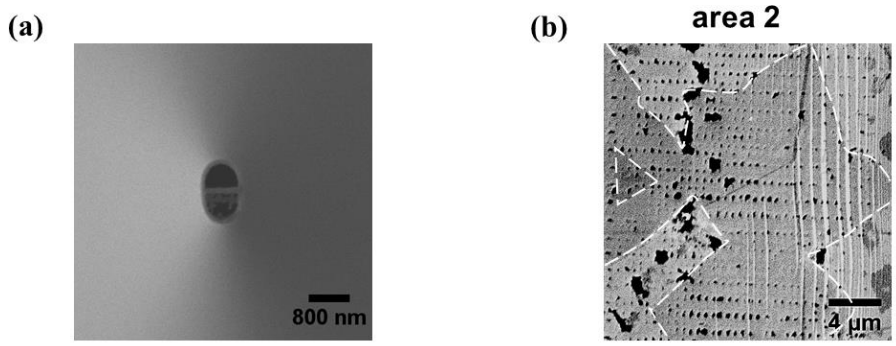

Figure 3.10: (a) Typical FE-SEM image of the end of pipette used for scanning area 2. (b) Corresponding FE-SEM image of the scanned area 2.

$Ru(NH_3)_6^{3+}$ the $|E_{3/4} - E_{1/4}|$ of 72 ± 6 mV is relatively fast, but slows for bilayer graphene, $|E_{3/4} - E_{1/4}|$ of 93 ± 8 mV.

Interestingly, the $E_{1/2}$ value of the multilayer graphene region shifts to a more negative value than that for mono- and bilayer graphene, and the multilayer graphene gave an $|E_{3/4} - E_{1/4}|$ value of 110 ± 15 mV, suggesting more sluggish ET kinetics, in line with the increasing overpotential for multilayer graphene observed in the $E_{1/2}$ data.

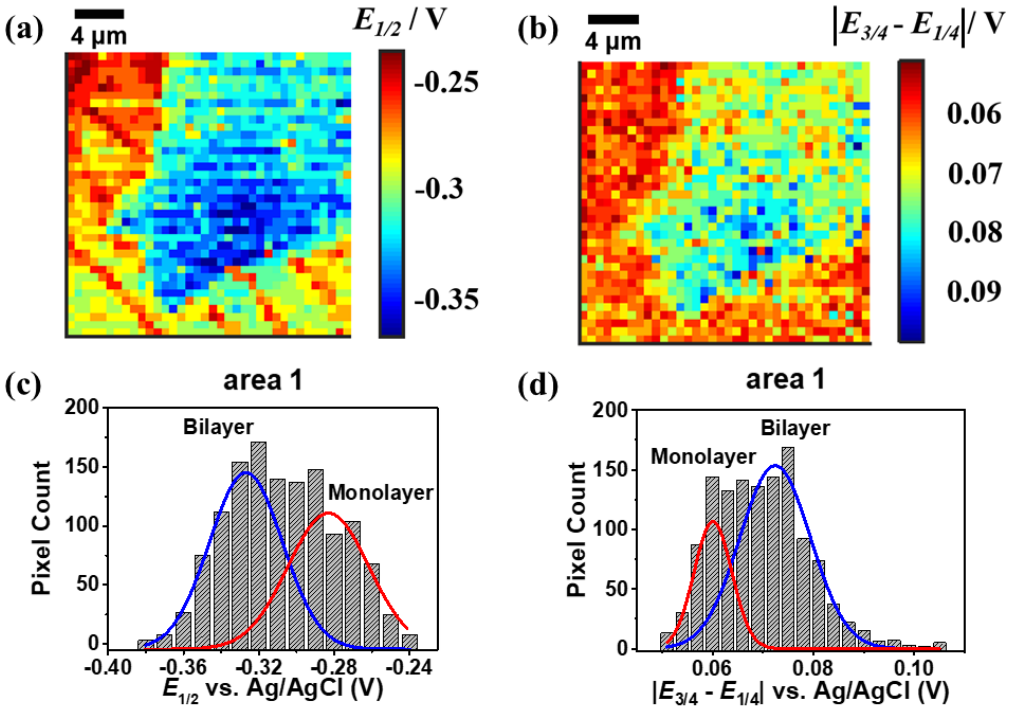

Figure 3.11: (a) $E_{1/2}$ map of area 1. (b) $|E_{3/4} - E_{1/4}|$ map of area 1. (c) Histogram distribution of Figure 3.11a. (d) Histogram distribution of Figure 3.11b.

The $E_{1/2}$ map, $|E_{3/4} - E_{1/4}|$ map and their corresponding histograms from area 1 are presented in Figure 3.11, are consistent with the results presented above for area 2.

For comparison with the graphene samples, we ran some SECCM CVs on HOPG samples, with the same parameters as above, noting that we have reported extensively on such measurements elsewhere.[17,63,64] Two grades of HOPG with very different step edge coverage were assessed: (i) a special low density sample originating from Arthur Moore, then of Union Carbide, via Prof. Rick McCreery, which we have termed AM grade with 0.09% set edge coverage on the basal surface and SPI-3 with 31% step edge coverage on the basal surface.[63] As detailed in Figure 3.12, CVs were run on freshly cleaved HOPG (within 15 mins of cleavage) and on HOPG that had been aged in air for 20 h, to mimic any possible atmospheric contamination that might occur on the CVD graphene samples. As we have previously reported detailed SECCM imaging studies on HOPG compared to ME graphene,[17] we made a few point measurements. CVs displayed close to reversible behavior, independent of aging time in air. The $E_{1/2}$ on both grades of HOPG (not corrected for slight non-steady state), is close to the potential from measurement of $Ru(NH_3)_6^{3+}$ reduction on HOPG or Pt under very similar conditions.[17] Notably, the $E_{1/2}$ for $Ru(NH_3)_6^{3+/2+}$ at both grades of HOPG are more positive than that for monolayer graphene that was seen in Figures 3.7c and 3.9b. The density of states (DOS) of HOPG is sufficiently high[65,66] to facilitate fast ET,[64] whereas graphene is a zero-band semi-metal, whose electronic structure is modulated by the support as considered below.

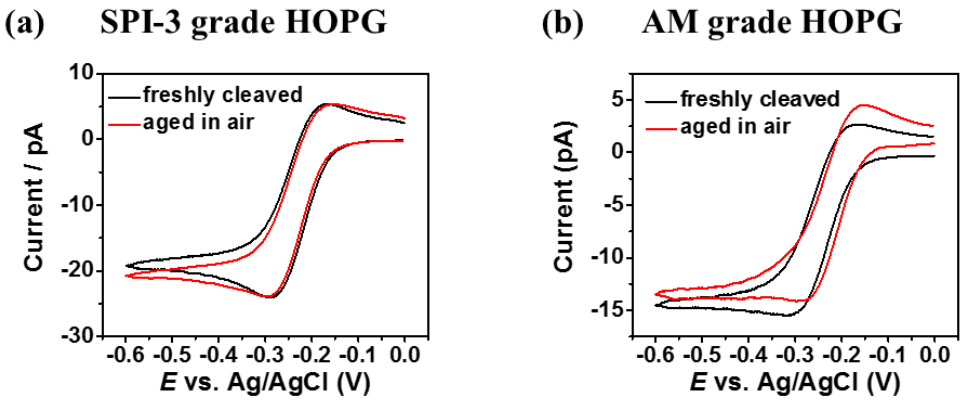

Figure 3.12: (a) CV on SPI-3 grade HOPG run by SECCM. (b) CV on AM grade HOPG run by SECCM. Scan rate 0.5 V/s.

3.3.3 Effect of crystal orientation of support on ET kinetics of graphene

To determine whether there was any effect of crystal orientation of the underlying polycrystalline Cu foil on electrochemical kinetic trends observed at graphene, EBSD measurements were performed on area 1 and area 2 (Figure 3.13). Figure 3.13a indicates that area 1 is mainly comprised of Cu (111), whereas area 2 (Figure 3.13b) is mainly close to Cu (100). Thus, the trends in ET kinetics with the number of graphene layers, is not caused by the crystal orientation of Cu foil, and can be attributed unequivocally to an effect of graphene on the support.

To further examine the impact of crystal structure on the electrochemistry of graphene, graphene was grown on polycrystalline Cu foil which possessed smaller grains sizes (10 -300 μm, see Figure 3.14). The quality of the graphene film was assessed by Raman spectroscopy, with spectra shown in Figure 3.14c.[67] Voltammetric SECCM

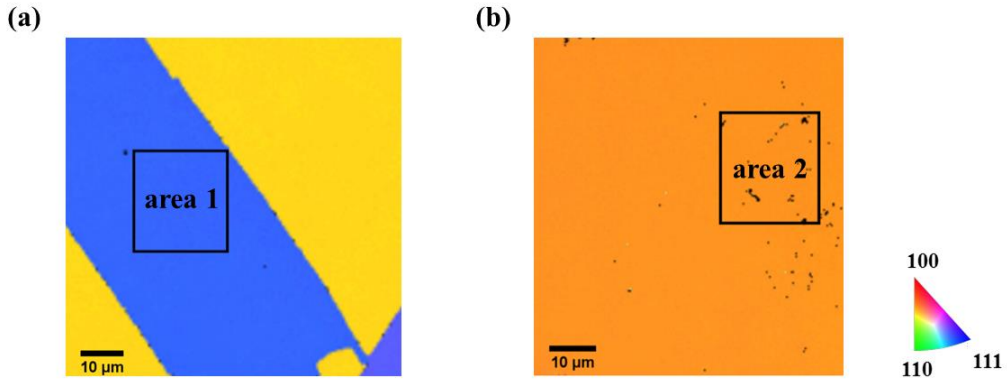

Figure 3.13: EBSD images of (a) area 1 and (b) area 2. The orientation maps are color coded according to the growth direction.

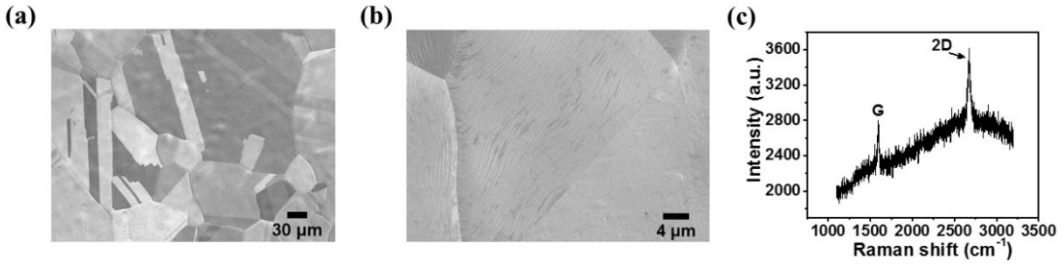

Figure 3.14: (a) FE-SEM image of graphene on polycrystalline Cu substrate. (b) Higher magnification FE-SEM image of the sample. (c) Raman spectrum of graphene on polycrystalline Cu substrate

measurements were performed on a typical area (62 × 42 μm) with a hopping distance of 2 μm. A 700 nm diameter pipette containing 1 mM $Ru(NH_3)_6^{3+}$ (chloride salt) in 50 mM KCl was used for this scan. The $E_{1/2}$ map of the scanned area was extracted and is presented in Figure 3.15a with a histogram of values from this shown in Figure 3.15b. Only one peak was observed, centered at -0.246 V, suggesting that the different regions of the graphene, do not exhibit significantly different kinetic behavior. Individual CVs from points of different crystal orientation, as marked in EBSD map, (see Figure 3.15e) were plotted in Figure 3.15c. These CV curves are quite similar with no clear $E_{1/2}$ variation. The corresponding FE-SEM image of the scanned area is shown in Figure 3.15d. By analyzing this area's EBSD map as well as the $E_{1/2}$ and $|E_{3/4} - E_{1/4}|$ maps (see Figure 3.16), it is confirmed that there is little variation across the different crystal orientation grains, at least on the resolution of these measurments. Consequently, we can again be confident that the differences in ET behavior among monolayer, bilayer and multilayer graphene is attributed to the different number of graphene layers, largely independent of crystal orientation of the underlying Cu substrate.

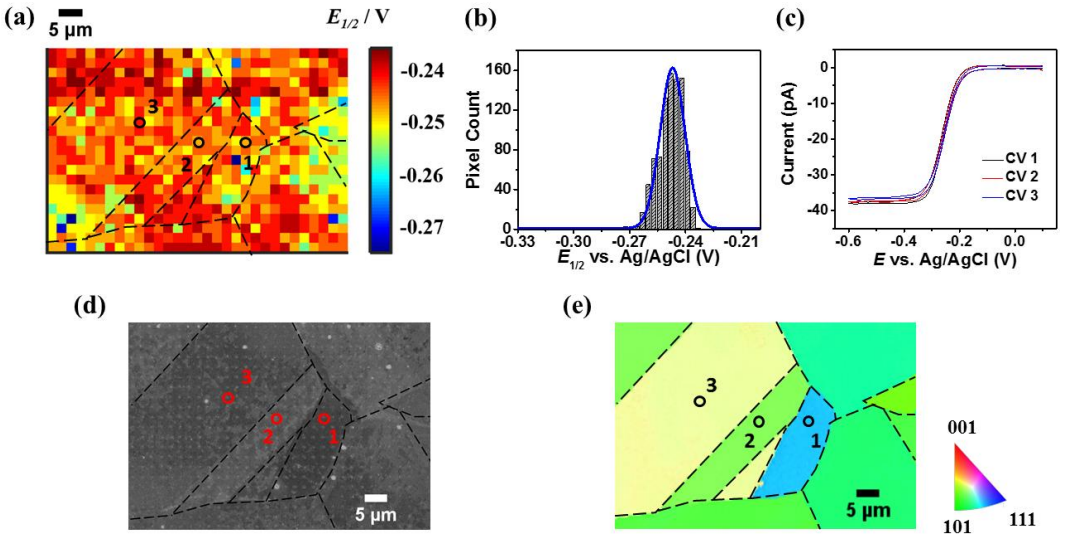

Figure 3.15: (a) $E_{1/2}$ map of graphene on polycrystalline Cu substrate. (b) Histogram distribution of Figure 3.15a. (c) Individual CVs comparison from region 1, 2, and 3 marked in EBSD map. (d) Corresponding FE-SEM image of SECCM scanned area. (e) Corresponding EBSD map of SECCM scanned area. The orientation maps are color coded according to the growth direction.

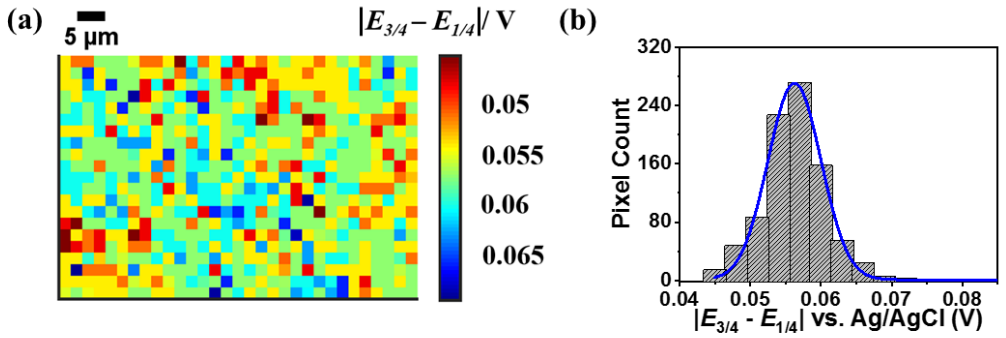

Figure 3.16: (a) $|E_{3/4} - E_{1/4}|$ map of graphene on polycrystalline Cu substrate. (b) Histogram distribution of Figure 3.16a.

3.3.4 Factors affecting the ET kinetics at graphene layers

A surface potential map of the graphene grown on Cu foil, used for SECCM experiments of area 1 and area 2, was obtained by KPFM, as shown in Figure 3.17a. The higher surface potential region corresponds to bilayer graphene. As a result, the work

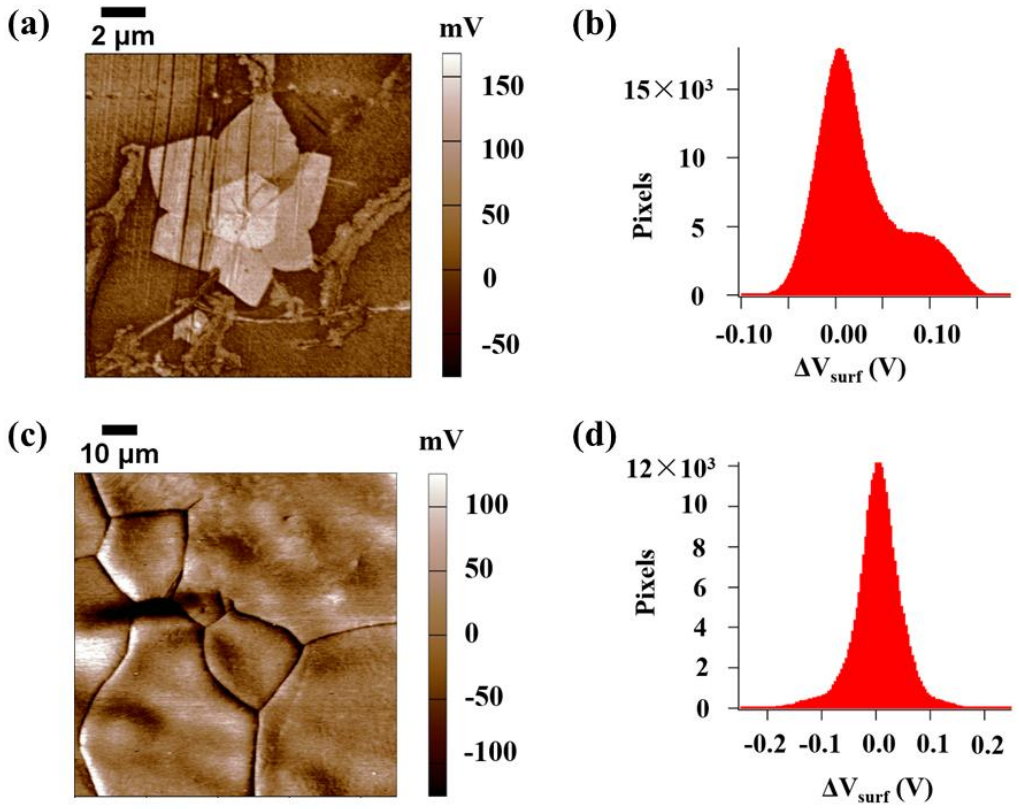

Figure 3.17: (a) Surface potential map of graphene used for SECCM experiments of area 1 and area 2. (b) Histogram distribution of Figure 3.17a. (c) Surface potential map of graphene used for crystal orientation effect study. (d) Histogram distribution of Figure 3.17c.

function of bilayer is lower than that for monolayer, indicating a p-type doping graphene in ambient environment without any applied voltage.[68-70] KPFM data for the graphene sample grown on Cu foil with smaller crystal grains (Figure 3.17b) shows that there is only one peak centred at around 0 mV, suggesting no obvious work function variation across different Cu crystal orientation grains. Thus, there appears to be some correlation between differences in the work function of monolayer and bilayer graphene on copper and the corresponding ET kinetics. To understand further the origin of this correlation requires electronic structure calculations, which are being undertaken by a collaborator.

3.4 Conclusions

Herein, it has been demonstrated how SECCM is a powerful tool for elucidating electrochemical-structure relations for CVD graphene grown directly on a Cu foil. Voltammetric SECCM has detected pinholes in the graphene layer on Cu foil by revealing positive currents that result from the anodic dissolution of exposed Cu. Voltammetric SECCM, coupled with other complementary techniques, particularly co-located Raman microscopy and FE-SEM, has been proved to be a powerful tool to reveal the ET kinetics of the $Ru(NH_3)_6^{3+/2+}$ couple at graphene which correlate with the number of graphene layers. The trend in kinetics is monolayer (fastest), bilayer and multilayer (slowest) graphene.

The multimicroscopy methodology has also been applied to consider any crystal orientation effects on the same sample, considering the crystal grains of the underlying Cu foil. These measurements establish that there is no significant ET kinetics variation across different crystal orientation grains, further proving that spatial differences in ET kinetics are due to from different number of graphene layers.

One scan area of voltammetric SECCM essentially comprises thousands of micro-scale electrodes, which would be practically difficult (impossible) to manufacture and test, highlighting the power of the strategy outlined. The results presented here provide fundamental information about the ET kinetics of graphene, a material that remains of considerable increase in interest, with applications in energy storage, as an electrode material in electrochemical sensors and in biochemical analysis.

3.5 References

1 Wang, X.; Zhi, L.; Müllen, K. Transparent, conductive graphene electrodes for dye-sensitized solar cells. *Nano letters* **8**, 323-327 (2008).

2 Meyer, J. C.; Geim, A. K.; Katsnelson, M. I.; Novoselov, K. S.; Booth, T. J.; Roth, S. The structure of suspended graphene sheets. *Nature* **446**, 60-63 (2007).

3 Chen, R.; Nioradze, N.; Santhosh, P.; Li, Z.; Surwade, S. P.; Shenoy, G. J.; Parobek, D. G.; Kim, M. A.; Liu, H., Amemiya, S. Ultrafast electron transfer kinetics of graphene grown by chemical vapor deposition. *Angewandte Chemie International Edition* **54**, 15134-15137 (2015).

4 Lee, C.; Wei, X.; Kysar, J. W.; Hone, J. Measurement of the elastic properties and intrinsic strength of monolayer graphene. *Science* **321**, 385-388 (2008).

5 Raccichini, R.; Varzi, A.; Passerini, S.; Scrosati, B. The role of graphene for electrochemical energy storage. *Nature Materials* **14**, 271-279 (2015).

6 Yang, X.; Cheng, C.; Wang, Y.; Qiu, L.; Li, D. Liquid-mediated dense integration of graphene materials for compact capacitive energy storage. *Science* **341**, 534-537 (2013).

7 Xu, C.; Xu, B.; Gu, Y.; Xiong, Z.; Sun, J.; Zhao, X. S. Graphene-based electrodes for electrochemical energy storage. *Energy & Environmental Science* **6**, 1388-1414 (2013).

8 Lawal, A. T. Synthesis and utilisation of graphene for fabrication of electrochemical sensors. *Talanta* **131**, 424-443 (2015).

9 Bahadır, E. B.; Sezgintürk, M. K. Applications of graphene in electrochemical sensing and biosensing. *Trends in Analytical Chemistry* **76**, 1-14 (2016).

10 Song, Y.; Luo, Y.; Zhu, C.; Li, He.; Du, D.; Lin, Y. Recent advances in electrochemical biosensors based on graphene two-dimensional nanomaterials. *Biosensors & Bioelectronics* **76**, 195-212 (2016).

11 Li, W.; Tan, C.; Lowe, M. A.; Abruna, H. D.; Ralph, D. C. Electrochemistry of individual monolayer graphene sheets. *ACS nano* **5**, 2264-2270 (2011).

12 Toth, P. S.; Valota, A. T.; Velick, M.; Kinloch, I. A.; Novoselov, K. S.; Hilld, E. W.; Dryfe, R. W. Electrochemistry in a drop: a study of the electrochemical behaviour of mechanically exfoliated graphene on photoresist coated silicon substrate. *Chemical Science* **5**, 582-589 (2014).

13 Valota, A. T.; Kinloch, I. A.; Novoselov, K. S.; Casiraghi, C.; Eckmann, A.; Hill, E. W.; Dryfe, R. W. Electrochemical behavior of monolayer and bilayer graphene. *ACS nano* **5**, 8809-8815 (2011).

14 Güell, A. G.; Ebejer, N.; Snowden, M. E.; Macpherson, J. V.; Unwin, P. R. Structural correlations in heterogeneous electron transfer at monolayer and multilayer graphene electrodes. *Journal of the American Chemistry Society* **134**, 7258-7261 (2012).

15 Velicky, M.; Bradley, D. F.; Cooper, A. J.; Hill, E. W.; Kinloch, I. A.; Mishchenko, A.; Novoselov, K. S.; Patten, H. V.; Toth, P. S.; Valota, A. T.; Worrall, S. D.; Dryfe, R. W. Electron transfer kinetics on mono-and multilayer graphene. *ACS nano* **8**, 10089-10100 (2014).

16 Valota, A. T.; Totha, P. S.; Kim, Y.-J.; Hong, B. H.; Kinloch, I. A.; Novoselov, K. S.; Hill, E. W.; Dryfe, R. A. Electrochemical investigation of chemical vapour deposition monolayer and bilayer graphene on the microscale. *Electrochimica Acta* **110**, 9-15 (2013).

17 Güell, A. G.; Cuharuc, A. S.; Kim, Y.-R.; Zhang, G.; Tan, S.-Z.; Ebejer, N.; Unwin, P. R. Redox-dependent spatially resolved electrochemistry at graphene

and graphite step edges. *ACS Nano* **9**, 3558-3571 (2015).
18 Zhong, J.-H. *et al.* Quantitative correlation between defect density and heterogeneous electron transfer rate of single layer graphene. *Journal of the American Chemistry Society* **136**, 16609-16617 (2014).
19 Zhang, B.; Fan, L.; Zhong, H.; Liu, Y.; Chen, S. Graphene nanoelectrodes: fabrication and size-dependent electrochemistry. *Journal of the American Chemistry Society* **135**, 10073-10080 (2013).
20 Tan, C.; Rodríguez-López, J.; Parks, J. J.; Ritzert, N. L.; Ralph, D. C.; Abruna, H. D. Reactivity of monolayer chemical vapor deposited graphene imperfections studied using scanning electrochemical microscopy. *ACS nano* **6**, 3070-3079 (2012).
21 Yuan, W.; Zhou, Y.; Li, Y.; Li, C.; Peng, H.; Zhang, J.; Liu, Z.; Dai, L.; Shi, G. The edge-and basal-plane-specific electrochemistry of a single-layer graphene sheet. *Scientific Reports* **3**, 2248 (2013).
22 Hui, J.; Pakhira, S.; Bhargava, R.; Barton, Z. J.; Zhou, X.; Chinderle, A. J.; Mendoza-Cortes, J. L.; Rodríguez-López, J. Modulating Electrocatalysis on Graphene Heterostructures: Physically Impermeable Yet Electronically Transparent Electrodes. *ACS nano* **12**, 2980-2990 (2018).
23 Hui, J.; Zhou, X.; Bhargava, R.; Chinderle, A.; Zhang, J.; Rodríguez-López, J. Kinetic modulation of outer-sphere electron transfer reactions on graphene electrode with a sub-surface metal substrate. *Electrochimica Acta* **211**, 1016-1023 (2016).
24 Zhang, G.; Güell, A. G.; Kirkman, P. M.; Lazenby, R. A.; Miller, T. S.; Unwin, P. R. Versatile polymer-free graphene transfer method and applications. *ACS Applied Materials and Interfaces* **8**, 8008-8016 (2016).
25 Bosch-Navarro, C.; Laker, Z. P.; Rourke, J. P.; Wilson, N. R. Reproducible, stable and fast electrochemical activity from easy to make graphene on copper electrodes. *Physical Chemistry Chemical Physics* **17**, 29628-29636 (2015).
26 Zhong, J.-H.; Liu, J.-Y.; Li, Q.; Li, M.-G.; Zeng, Z.-C.; Hua, S.; Wu, D.-Y.; Cai, W.; Ren, B. Interfacial capacitance of graphene: Correlated differential capacitance and in situ electrochemical Raman spectroscopy study. *Electrochimica Acta* **110**, 754-761 (2013).
27 Ritzert, N. L.; Rodríguez-López, J.; Tan, C.; Abruña, H. D. Kinetics of interfacial electron transfer at single-layer graphene electrodes in aqueous and nonaqueous solutions. *Langmuir* **29**, 1683-1694 (2013).
28 Ishigami, M.; Chen, J.; Cullen, W.; Fuhrer, M.; Williams, E. Atomic structure of graphene on SiO_2. *Nano letters* **7**, 1643-1648 (2007).
29 Romero, H. E.; Shen, N.; Joshi, P.; Gutierrez, H. R.; Tadigadapa, S. A.; Sofo, J. O.; Eklund, P. C. n-type behavior of graphene supported on Si/SiO_2 substrates. *Acs nano* **2**, 2037-2044 (2008).
30 Berciaud, S.; Ryu, S.; Brus, L. E.; Heinz, T. F. Probing the intrinsic properties of exfoliated graphene: Raman spectroscopy of free-standing monolayers. *Nano letters* **9**, 346-352 (2008).
31 Novoselov, K. S.; Geim, A. K.; Morozov, S. V.; Jiang, D.; Zhang, Y.; Dubonos, S. V.; Grigorieva, I. V.; Firsov, A. A. Electric field effect in atomically thin carbon films. *Science* **306**, 666-669 (2004).
32 Zhang, Y.; Zhang, L.; Zhou, C. Review of chemical vapor deposition of graphene and related applications. *Accounts of Chemical Research* **46**, 2329-2339 (2013).
33 Li, X.; Cai, W.; Colombo, L.; Ruoff, R. S. Evolution of graphene growth on Ni and Cu by carbon isotope labeling. *Nano letters* **9**, 4268-4272 (2009).
34 Wassei, J. K.; Mecklenburg, M.; Torres, J. A.; Fowler, J. D.; Regan, B. C.; Kaner,

R. B.; Weiller, B. H. Chemical vapor deposition of graphene on copper from methane, ethane and propane: Evidence for bilayer selectivity. *Small* **8**, 1415-1422 (2012).

35 Son, J.-H.; Baeck, S.-J.; Park, M.-H.; Lee, J.-B.; Yang, C.-W.; Song, J.-K.; Zin, W.-C.; Ahn, J.-H. Detection of graphene domains and defects using liquid crystals. *Nature Communications* **5**, 3484 (2014).

36 Unwin, P. R.; Güell, A. G.; Zhang, G. Nanoscale electrochemistry of sp^2 carbon materials: from graphite and graphene to carbon nanotubes. *Accounts of Chemical Research* **49**, 2041-2048 (2016).

37 Ebejer, N.; Schnippering, M.; Colburn, A. W.; Edwards, M. A.; Unwin, P. R. Localized high resolution electrochemistry and multifunctional imaging: Scanning electrochemical cell microscopy. *Analytical Chemistry* **82**, 9141-9145 (2010).

38 Ebejer, N.; .; Güell, A. G.; Lai, S. C.; Mckelvey, K.; Snowden, M. E.; Unwin, P. R. Scanning electrochemical cell microscopy: a versatile technique for nanoscale electrochemistry and functional imaging. *Annual Review of Analytical Chemistry* **6**, 329-351 (2013).

39 Bentley, C. L.; Perry, D.; Unwin, P. R. Stability and Placement of Ag/AgCl Quasi-Reference Counter Electrodes in Confined Electrochemical Cells. *Analytical Chemistry* **90**, 7700-7708 (2018).

40 Wilson, N. R.; Marsden, A. J.; Saghir, M.; Bromley, C. J.; Schaub, R.; Costantini, G., White, T. W.; Partridge, C.; Barinov, A.; Dudin, P.; Sanchez, A. M.; Mudd, J. J.; Walker, M.; Bell, G. R. Weak mismatch epitaxy and structural feedback in graphene growth on copper foil. *Nano Research* **6**, 99-112 (2013).

41 Miseikis, V., Convertino, D.; Mishra, N.; Gemmi, M.; Mashoff, T.; Heun, S.; Haghighian, N.; Bisio, F.; Canepa, M.; Piazza, V.; Coletti, C. Rapid CVD growth of millimetre-sized single crystal graphene using a cold-wall reactor. *2D Materials* **2**, 014006 (2015).

42 Patel, A. N.; McKelvey, K.; Unwin, P. R. Nanoscale electrochemical patterning reveals the active sites for catechol oxidation at graphite surfaces. *Journal of the Ameriacn Chemistry Society* **134**, 20246-20249 (2012).

43 Lai, S. C.; Patel, A. N.; McKelvey, K.; Unwin, P. R. Definitive Evidence for Fast Electron Transfer at Pristine Basal Plane Graphite from High-Resolution Electrochemical Imaging. *Angewandte Chemie* **51**, 5405-5408 (2012).

44 Snowden, M. E.; Güell, A. G.; Lai, S. C.; Mckelvey, K.; Ebejer, N.; O'Connell, M. A.; Colburn, A. W.; Unwin, P. R. Scanning electrochemical cell microscopy: Theory and experiment for quantitative high resolution spatially-resolved voltammetry and simultaneous ion-conductance measurements. *Analytical Chemistry* **84**, 2483-2491 (2012).

45 Chen, C.-H.; Jacobse, L.; Mckelvey, K.; Lai, S. C.; Koper, T. M.; Unwin, P. R. Voltammetric scanning electrochemical cell microscopy: dynamic imaging of hydrazine electro-oxidation on platinum electrodes. *Analytical Chemistry* **87**, 5782-5789 (2015).

46 Maddar, F. M.; Lazenby, R. A.; Patel, A. N.; Unwin, P. R. Electrochemical oxidation of dihydronicotinamide adenine dinucleotide (NADH): comparison of highly oriented pyrolytic graphite (HOPG) and polycrystalline boron-doped diamond (pBDD) electrodes. *Physical Chemistry Chemical Physics* **18**, 26404-26411 (2016).

47 Lin, Z.; Ye, X.; Han, J.; Chen, Q.; Fan, P.; Zhang, H.; Xie, D.; Zhu, H.; Zhong, M. Precise control of the number of layers of graphene by picosecond laser thinning. *Scientific Reports* **5**, 11662 (2015).

48 Wu, J.-B.; Lin, M.-L; Cong, X.; Liu, H.-N.; Tan, P.-H. Raman spectroscopy of graphene based materials and its applications in related devices. *Chemical Society Reviews* **47***,* 1822-1873 (2018).

49 Chen, C.-H.; Meadows, K. E.; Cuharuc, A.; Lai, S. C.; Unwin, P. R. High resolution mapping of oxygen reduction reaction kinetics at polycrystalline platinum electrodes. *Physical Chemistry Chemical Physics* **16**, 18545-18552 (2014).

50 Güell, A. G.; Meadown, K. E.; Dudin, P. V.; Ebejer, N.; Macpherson, J. V.; Unwin, P. R. Mapping nanoscale electrochemistry of individual single-walled carbon nanotubes. *Nano letters* **14**, 220-224 (2013).

51 Güell, A. G.; Ebejera, N.; Snowden, M. E.; Mckelvey, K.; Macpherson, J. V.; Unwin, P. R. Quantitative nanoscale visualization of heterogeneous electron transfer rates in 2D carbon nanotube networks. *Proceedings of the National Academy Sciences* **109**, 11487-11492 (2012).

52 Kear, G.; Walsh, F.; Barker, D.; Stokes, K. The electrochemical corrosion characteristics of copper in filtered and artificial seawater as a function of mass transfer conditions. *European Corrosion* **September**, 10-14 (2000).

53 Lee, H.; Nobe, K. Kinetics and mechanisms of Cu electrodissolution in chloride media. *Journal of the Electrochemical Society* **133**, 2035-2043 (1986).

54 Kear, G.; Barker, B.; Walsh, F. Electrochemical corrosion of unalloyed copper in chloride media—a critical review. *Corrosion Science* **46**, 109-135 (2004).

55 Deslouis, C.; Tribollet, B.; Mengoli, G.; Musiani, M. M. Electrochemical behaviour of copper in neutral aerated chloride solution. I. Steady-state investigation. *Journal of the Applied Electrochemistry* **18**, 374-383 (1988).

56 Ferrari, A. C. *et al.* Raman spectrum of graphene and graphene layers. *Physical review letters* **97**, 187401 (2006).

57 Lucchese, M. M. *et al.* Quantifying ion-induced defects and Raman relaxation length in graphene. *Carbon* **48**, 1592-1597 (2010).

58 Momotenko, D.; Byers, J. C.; McKelvey, K.; Kang, M.; Unwin, P. R. High-speed electrochemical imaging. *ACS nano* **9**, 8942-8952 (2015).

59 Kirkman, P. M.; Güell, A. G.; Cuharuc, A. S.; Unwin, P. R. Spatial and temporal control of the diazonium modification of sp^2 carbon surfaces. *Journal of the Americam Chemistry Society* **136**, 36-39 (2013).

60 Li, X.; Cai, W.; An, J.; Kim, S.; Nah, J.; Yang, D.; Piner, R.; Velamakanni, A.; Jung, I.; Tutuc, E.; Banerjee, S. K.; Colombo, L.; Ruoff, R. S. Large-area synthesis of high-quality and uniform graphene films on copper foils. *Science* **324**, 1312-1314 (2009).

61 Bard, A. J.; Faulkner, L. R. Fundamentals and applications. *Electrochemical Methods*, **2**, 482 (2001).

62 Mirkin, M. V.; Bard, A. J. Simple analysis of quasi-reversible steady-state voltammograms. *Analytical Chemistry* **64**, 2293-2302 (1992).

63 Patel, A. N. *et al.* A new view of electrochemistry at highly oriented pyrolytic graphite. *Journal of the American Chemistry Society* **134**, 20117-20130 (2012).

64 Zhang, G.; Cuharuc, A. S.; Güell, A. G.; Unwin, P. R. Electrochemistry at highly oriented pyrolytic graphite (HOPG): lower limit for the kinetics of outer-sphere redox processes and general implications for electron transfer models. *Physical Chemistry Chemical Physics* **17**, 11827-11838 (2015).

65 Li, G.; Luican, A; Andrei, E. Y. Scanning tunneling spectroscopy of graphene on graphite. *Physical Review Letters* **102**, 176804 (2009).

66 Andrei, E. Y.; Li, G.; Du, X. Electronic properties of graphene: a perspective from scanning tunneling microscopy and magnetotransport. *Reports on Progress*

in Physics **75**, 056501 (2012).

67 Ferrari, A. C. Raman spectroscopy of graphene and graphite: disorder, electron–phonon coupling, doping and nonadiabatic effects. *Solid State Communications* **143**, 47-57 (2007).

68 Ochedowski, O.; Bussmann, B. K.; Schleberger, M. Graphene on mica-intercalated water trapped for life. *Scientific Reports* **4**, 6003 (2014).

69 Ziegler, D.; Gava, P.; Güttinger, F.; Wirtz, L.; Lazzeri, M.; Saitta, A. M.; Stemmer, A.; Mauri, F.; Stamper, C. Variation in the work function of doped single- and few-layer graphene assessed by Kelvin probe force microscopy and density functional theory. *Physical Review B* **83**, 235434 (2011).

70 Datta, S. S.; Strachan, D. R.; Mele, E. J.; Johnson, A. C. Surface potentials and layer charge distributions in few-layer graphene films. *Nano letters* **9**, 7-11 (2009).

Chapter 4. Facet-Resolved Electrochemistry of Poly-crystalline Boron-doped Diamond Electrodes: Microscopic Factors Determining the Aqueous Solvent Window in Aqueous Potassium Chloride Solutions

A systematic examination of the microscopic factors affecting the aqueous solvent (electrolyte) window of polycrystalline (p) boron-doped diamond (BDD) electrodes in chloride-containing salt solutions is undertaken by using scanning electrochemical cell microscopy (SECCM) in conjunction with electron backscatter diffraction (EBSD) and Raman microscopy. A major focus is to determine the effect of the local boron doping level, within the same orientation grains, on the solvent window response. EBSD is used to select the predominant (110) orientated areas of the surface with different boron-doped facets, thereby eliminating crystallographic effects from the electrochemical response. Voltammetric SECCM is employed, whereby a cyclic voltammogram is recorded at each pixel mapped by the meniscus-contact SECCM cell. The data obtained can be played as an *electrochemical movie* of potential-resolved current maps of the surface to reveal spatial variations of electroactivity, over a wide potential range, including the solvent (electrolyte) window. Local heterogeneities are observed, indicating that the solvent window is mainly linked to local dopant levels, with lower dopant levels leading to a wider window, that is, slower electrode kinetics for solvent/electrolyte electrolysis. Furthermore, the effects of O- and H-surface termination of the BDD surface are investigated for the same electrode (in the same area). The surface termination is a particularly important factor: the solvent window of an H-terminated surface is wider than for O-termination for similar boron dopant levels. Furthermore, the anodic potential window of the O-terminated surface is greatly diminished due to chloride electro-oxidation. These studies provide new perspectives on the local electrochemical properties of BDD and highlight the importance of probing the electrochemistry of BDD at the level of a single crystalline grain (facet) to unravel the factors that control the solvent (aqueous) window of these complex heterogeneous electrodes.

4.1 Introduction

Conductive boron doped diamond (BDD) is gaining remarkable interest as an electrode material for electrochemical studies and applications, particularly in aqueous solutions, due to properties such as its wide solvent (electrolyte) window, low background current, reduced susceptibility to fouling, chemical inertness and mechanical durability.[1-3] The solvent (electrolyte) window defines the potential range over which an electrode can be used for voltammetric/amperometric detection of solute molecules (analyte), without significant impact from electrolysis of either the solvent or supporting electrolyte. For water, this often constitutes the oxygen evolution reaction (OER) at anodic potentials and the hydrogen evolution reaction (HER) at cathodic potentials, although the electrolyte itself can also have an influence, as examined herein.

Compared to other carbon-based and metallic electrodes, BDD presents a wider solvent window in aqueous solution, allowing the detection of various analytes at extreme potentials,[4] and opening up novel applications in electroanalysis and electrode functionalization.[5-7] On BDD, water oxidation by the conventional OER route is strongly retarded and oxidation can occur via an alternative pathway, which results in the production of the hydroxyl radical ($OH^{\cdot}$).[8,9] As a consequence, BDD electrodes are used widely for electrochemical water treatment (formation of $OH^{\cdot}$ desirable), while BDD itself is resistant to $OH^{\cdot}$ attack.[10-12] In the presence of chloride, oxidation to chlorine may also define the anodic window.[13]

Although the wide solvent window is a well-known electrochemical characteristic of polycrystalline (p) BDD, the effect of intrinsic microscopic factors on this property, including crystallographic orientation, boron dopant concentration, and surface termination within this complex heterogeneous material are much less well understood. The surface of freshly grown BDD is hydrogen (H)-terminated and hydrophobic, but slowly in air it oxidizes to the oxygen (O)-terminated form.[14] As outlined below, most studies have relied on macroscopic measurements to probe these factors, which can be restrictive in terms of obtaining microscopic insight. During the growth of pBDD, different crystal facets (grains) take up boron to different extents,[15,16] and thus the BDD electrode presents a heterogeneously doped surface, making microscopic characterization measurements essential.

For macroscopic measurements of pBDD, it has been reported that the solvent window decreases slightly as the boron doping level increases,[17] and that this effect is

more marked on the cathodic side.[18] However, others report no effect of boron doping and instead show the importance of sp^2 content, with the window narrowing with increasing sp^2 content of the electrode surface.[19] sp^2 carbon has also been shown to catalyze water electrolysis[17,20] resulting in both a measurable oxygen reduction reaction (ORR) signal[17] and features in the anodic window just before the onset of water oxidation.[21] There is also a report that the surface orientation of BDD influences the solvent window, attributed to different electrode kinetics on the different crystal faces of BDD.[22] However, as the boron concentration also changes within different crystal planes exposed on the BDD surface, it is not possible to distinguish between doping and surface orientation effects from these reported measurements.[23,24] The effect of surface termination has also been investigated, with the solvent window response of H- and O-terminated (prepared e.g. by oxygen plasma,[25,26] acid boiling[27]) surfaces compared.[25,26] In sulfate media, the solvent window was found to be larger on O-BDD than H-BDD.[26]

High-resolution correlative electrochemical imaging methods have provided considerable information for different outer sphere redox couples (on different surface terminations), and both inner sphere and more complex proton-coupled electron transfer processes, on individual grains and defects of pBDD.[28-31] Such approaches therefore have considerable prospect to elucidate some of the key microscopic factors determining the solvent window of BDD directly. In this paper, we use voltammetric scanning cell microscopy (SECCM),[32-34] combined with electron backscatter diffraction (EBSD) and Raman microscopy, applied to the same areas of a BDD electrode, to investigate how the local properties of BDD surfaces influence the aqueous solvent window in chloride media and identify the factors that are most important. We use a chloride supporting electrolyte for these studies, as it is used commonly in electroanalytical measurements and in real world applications, e.g. electroanalytical/disinfection measurements in seawater,[35,36] and it presents a competing pathway to OER for control of the anodic potential window.

4.2 Materials and methodology

4.2.1Chemicals and materials

Potassium chloride (KCl, ACS reagent grade, Sigma Aldrich) was used as a background electrolyte, and concentrated sulfuric acid (H_2SO_4, > 95 %, Fisher Chemicals) and potassium nitrate (KNO_3, ACS reagent grade, Sigma Aldrich) were

employed for BDD cleaning. 50 mM KCl electrolyte solutions were prepared immediately prior to use. All aqueous solutions were prepared from ultrapure water (SELECT-HP, Purity, 18.2 MΩ cm resistivity at 25 °C). Silver-chloride coated silver wires (Ag/AgCl) were used as QRCEs for SECCM. All potentials reported for SECCM herein are against the Ag/AgCl QRCEs, which had a stable potential of 59.60 mV (at a temperature of 298 K) vs. saturated calomel reference (SCE) in 50 mM KCl. As reported elsewhere,[37] this QRCE functions as a very stable electrode over long time periods in SECCM.

4.2.2 Preparation of BDD samples

The BDD electrode (350 μm thick) was grown using a commercial MW-CVD process (Element Six, Harwell, UK) to be metal-like doped[2,17] and the surface was mechanically polished to sub nm surface roughness.[17] Prior to use, the freestanding BDD was cleaned by heating in a concentrated H_2SO_4 (> 95 %) solution containing saturated KNO_3 solution at 300 °C for 30 minutes. This also resulted in O-termination of the surface.[38] For H-BDD studies, the surface was H-terminated using a hydrogen plasma CVD reactor, heated at 1 kW under 60 Torr of H_2 for 10 min. After that, the CVD reactor was powered down, and H_2 was continually passed over the surface at a flow rate of 500 cm^3 min^{-1} for another 10 min.

The back side of the BDD was sputtered (Moorfield) with Ti/Au (10 nm/300 nm) and then annealed in a tube furnace (Carbolite, U.K.) at 400 °C for 5 hours to form an ohmic titanium carbide contact.[2] A conducting connection to the BDD was made by attaching the sample to a Ti/Au (10/300 nm) sputtered SiO_2/Si wafer, using silver paint (Agar Scientific, Ltd, U.K.), electrically connected using a copper wire. Prior to electrochemical studies, the electrode was marked, using laser-cut crossed lines of ca. 14 μm width (E-355H-ATHI-O system, Oxford Lasers Ltd.), for ease of finding the same scanned area in SECCM and with other microscopic measurements (correlative microscopy).

4.2.3 Pipette fabrication

Pipettes used were pulled from borosilicate theta capillaries (Harvard Part No.30-0114), using a Sutter P-2000 laser puller (Sutter Instruments, USA). After pulling, the inner diameters of the end of the pipettes were in the range 700 - 900 nm, with the dimension determined accurately by field-emission scanning electron microscopy (FE-

SEM, Zeiss SUPRA 55). To confine an aqueous meniscus to the very end of the pipette, the outer walls were silanized by placing the probe in dichlorodimethylsilane (99+ % purity, Acros), with argon flowing through to protect the inside from silanization.

4.2.4 Voltammetric SECCM setup

Figure 4.1 illustrates the voltammetric SECCM setup (Figure 4.1a) used in this work.[34,39] Briefly, a theta pipette (Figure 4.1b), filled with 50 mM KCl and containing a quasi-reference counter electrodes (QRCEs) in each channel, functions as a microelectrode. The pipette was approached toward the BDD surface until the meniscus made contact (the pipette itself not making contact). The method allows (multiple) CVs to be recorded at individual pixels in an area of interest on the BDD substrate.

A bias voltage, V_2 (200 mV), was applied between the QRCEs to generate an ion conductance current (i_{DC}). Modulation of the *z* position of the pipette (266 Hz, 50 nm peak amplitude) by a lock-in amplifier (Stanford Research, SR830) generated an alternating current (AC) component of the ion conductance current, i_{AC}, at the modulation frequency. This was used for positional feedback[40,41] to detect when meniscus contact with the BDD surface was made via the probe. The potential of the BDD electrode was controlled by varying the potential applied to one of the QRCEs (V_1), and was $-(V_1+V_2/2)$ vs. Ag/AgCl QRCE; see Figure 4.1a.[42] Current that flowed through the substrate, which served as the working electrode, is denoted as i_{surf}.

An approach-hold-withdraw (hopping) mode[34] was employed for measurements at each pixel, as shown in Figure 4.1a. First, the pipette approached the BDD surface at a speed of 0.2 μm s^{-1}. Once meniscus contact was established, the pipette was held fixed in position for 0.1 s, before CV measurements at a sweep rate of 10 V s^{-1}, resulting in < 1 s measurement time for each pixel even over the wide potential range of these measurements (*vide infra*). The pipette probe was then retracted away from the surface at a speed of 2 μm s^{-1} by a distance of 2.5 μm, and then by 2 μm in the *xy* plane laterally to a neighboring pixel, where the same measurement procedure was implemented. This protocol was repeated until all the pixels in the area of interest were covered. The short residence time at each pixel minimized the chance of substrate wetting (meniscus spreading), especially for O-BDD, a very hydrophilic surface.

The current, i_{surf}, plotted against the corresponding *xy* position, as a function of potential, generated a sequence of SECCM image frames that constituted a potentiodynamic movie. The movies obtained, contained 820 frames, with a potential

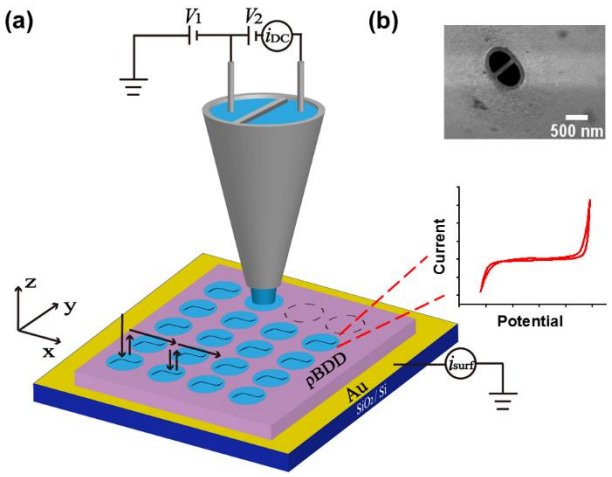

Figure 4.1: (a) Schematic of voltammetric SECCM. The blue circles on the pBDD surface represent the probed areas and constitute an individual pixel, as described in the text. A 10 V s^{-1} scan rate was used for the CVs at each pixel (inset response). (b) Field emission scanning electron microscopy image of the end of a typical pipette used for SECCM.

resolution of 10 mV (see, for example, Supporting Information, Movie S1 and S2, which are referred to herein). All data analysis was performed with Matlab (R2014b, Mathworks).

4.2.5 Structural characterization

EBSD. The crystal orientation of the polished pBDD for the SECCM scanned areas was determined by FE-SEM: Zeiss SUPRA, with a Nordlys F (Oxford Instruments) camera. EBSD measurements were performed with a pixel spacing of 0.3 µm at 20 kV, with the BDD electrode tilted at 70°. Data were analyzed using Aztec 3.1 (Oxford Instruments).

FE-SEM. The scanned areas including any droplet residues, were imaged using a Zeiss SUPRA 55 FE-SEM, at 5 keV with the inlens mode.

Contact angle measurements. Static contact angle measurements[43] were performed on a Krüss DSA 100 by depositing a volume of ~5 µL deionized water on the BDD surface.

Raman mapping. Raman microscopy mapping was performed using a Renishaw InVia micro-Raman spectrometer, with a diode-pumped solid-state laser (excitation wavelength of 532 nm). Spectral acquisition was performed at 100 % power with an integration time of 10 s. A step size of 0.6 µm was chosen for Raman mapping.

4.3 Results and Discussions

4.3.1 EBSD characterization of BDD electrodes

In this study, BDD was grown using microwave plasma-chemical vapor deposition (MW-CVD) under conditions which produce the highest quality electrodes for electrochemistry, minimizing sp^2 carbon content (grown using procedures similar to that

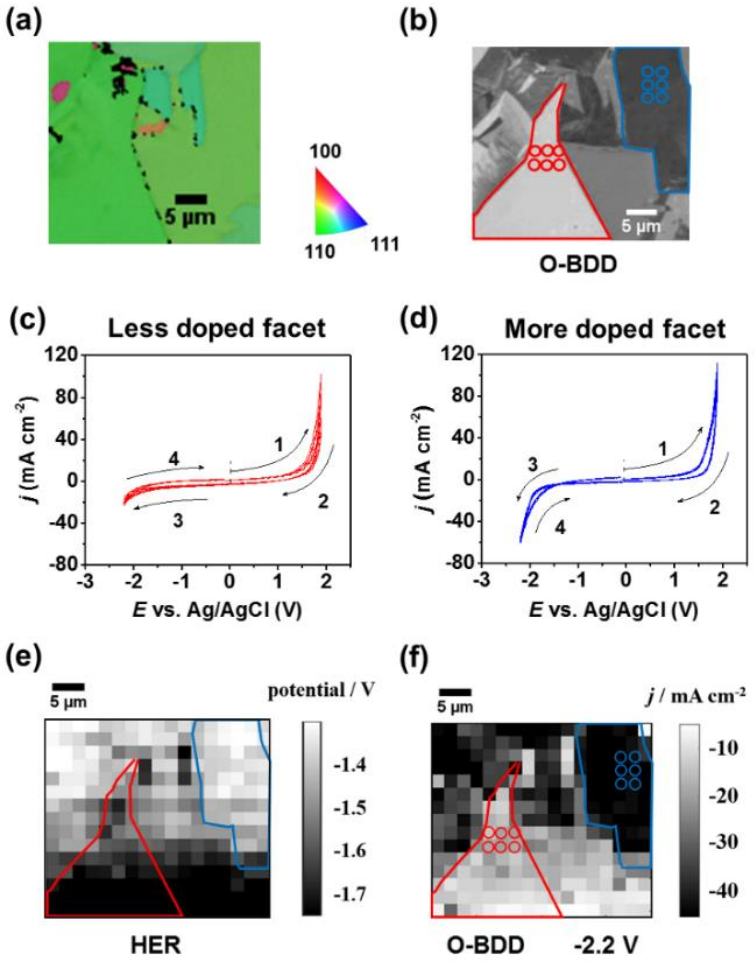

Figure 4.2: (a) EBSD and (b) corresponding FE-SEM image of area I on the pBDD electrode. The orientation maps in (a) are colour-coded according to the growth direction. The facet with the red boundary in (b) denotes a less doped grain, whilst that in blue represents a more doped grain. Six individual CVs (overlaid) recorded at different locations on an O-terminated surface in each of (c) the less doped facet (red circles) and (d) the more doped facet (blue circles). The numbers and arrows highlight the scan starting potential and scan directions. (e) SECCM onset cathodic potential image of area I for a current density of -3.5 mA cm^{-2}. (f) SECCM current density image of area I at -2.20 V.

used to produce electrode E in reference 17). Crystallographic orientation information of the areas studied by electrochemical imaging (*vide infra*) was obtained by EBSD. Typical data are shown in Figure 4.2a. EBSD demonstrates that the majority of the surface, post-polishing, has an orientation of (110), with a minor contribution from (100).[44]

4.3.2 Raman characterisation of BDD electrodes

First, Raman mapping was used to assess the boron concentration and the material sp^2 content. Figure 4.3a shows the Raman nondiamond carbon (NDC) mapping of an area including area I and area I′, which is generated from the integrated NDC peak intensity (between 1470 and 1600 cm^{-1})[45] after background correction. Example spectra for three regions, containing relatively different amounts of NDC are shown in Figure 4.3b-d. In the Raman spectrum, signals at 1332 cm^{-1} represent sp^3 carbon while signals centred between 1470 and 1600 cm^{-1} denote NDC. The intensity ratio of sp^2 carbon (G-band, the broad peak around 1550 cm^{-1}) to sp^3 carbon (1322-1333 cm^{-1}) was used to quantify the relative NDC.[46] Region 1 has higher NDC with a sp^2/sp^3 ratio of 0.12 and the calculated ratio of region 2 is 0.058. These regions are both in high boron regions. Region 3 (low-doped facet) has negligible NDC, as the ratio is as low as 0.016. The corresponding averaged CVs (region 1 from 4 CVs, region 2 from 6 CVs, and region 3 from 16 CVs) of these regions on O-BDD are shown in Figures 4.3e-g. The individual CVs (overlaid) used to obtain the averaged CVs are shown in Figure 4.4.

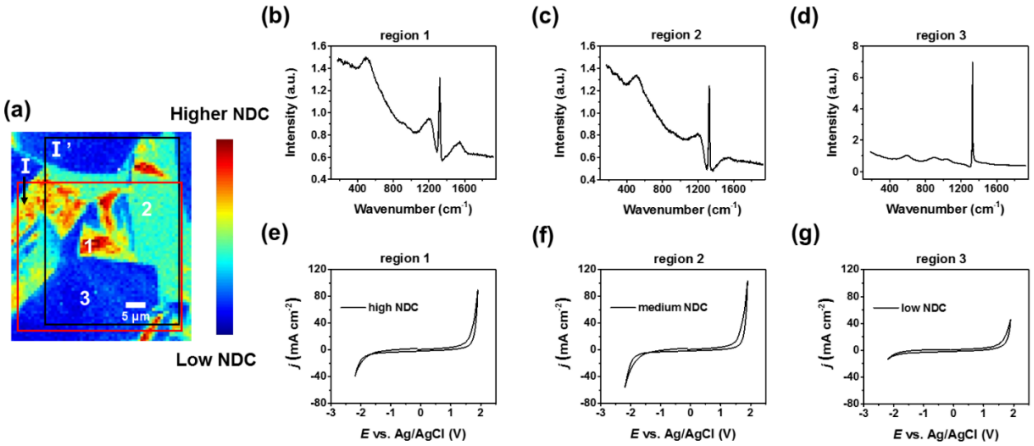

Figure 4.3: (a) Raman mapping of NDC on an area including area I and area I′. (b-c) Spectrum of regions containing high and medium NDC in more doped facet. (d) Spectrum of region 3 showing low NDC in less doped facet. (e-g) Averaged CVs obtained from region 1 to 3 on O-BDD.

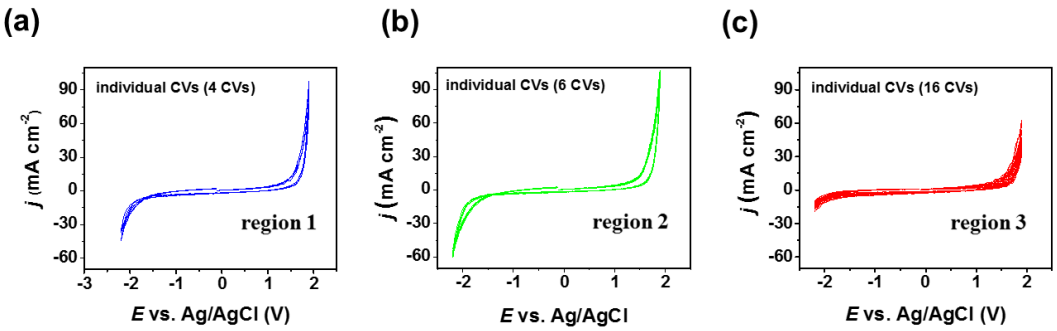

Figure 4.4: (a-b) Individual CVs of region 1 and 2 containing high and medium NDC in more doped facet on area I of O-BDD. (c) Individual CVs of region 3 containing low NDC in less doped facet on area I of O-BDD.

The ratio of sp^2/sp^3 features i.e. the intensity of the G-band to that of the diamond peak was found to be spatially heterogeneous, ranging from 0.016-0.12.[46,47] This suggests the sp^2 content is low in all grains. Grains with low dopant density have the lowest apparent sp^2 levels, and those with high dopant density, have a wider spread of slightly higher sp^2 levels. It should be noted, however, that the diamond peak varies in intensity, and position, with boron doping level,[48] decreasing in intensity and shifting to lower wavenumbers as boron doping increases. The increased size of the diamond peak in low doped samples can explain the apparent lower sp^2 content in lower doped grains and therefore quantification should be treated carefully. However, it is valid to comment that the sp^2 content is low in all regions. Finally, it is important to note that although Raman microscopy reveals a heterogeneous distribution of sp^2 carbon across the BDD electrode, the Raman signal represents information from the surface down to several microns into BDD,[49] and therefore is not necessarily a true reflection of surface sp^2 carbon, unlike electrochemical signals.[50]

4.3.3 Voltammetric SECCM at O-BDD

The solvent window for the O-BDD electrode was recorded at high resolution using voltammetric SECCM. The O-BDD surface is hydrophilic, with an aqueous contact angle value of 26° in Figure 4.5a. As a consequence, the SECCM approach adopted, where meniscus contact at each position was brief (< 1 s; *vide supra*) served to prevent extensive local wetting of the surface (from leakage of solution from the tip).

Figure 4.2b is a field emission scanning electron microscopy (FE-SEM) image of area I (34 × 30 μm). Darker regions in the FE-SEM image correspond to the more boron

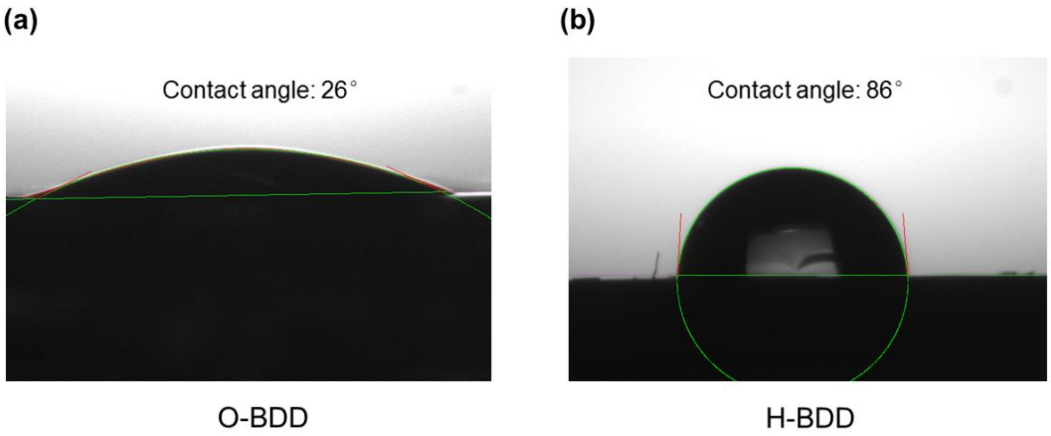

Figure 4.5: Static contact angle measurements of a water droplet on (a) O- and (b) H-BDD surfaces.

doped regions while lighter zones present the less boron doped regions,[38] in agreement with the Raman mapping *vide supra*.

SECCM CVs were recorded on area I, at each pixel, at a scan rate of 10 V s^{-1}, starting from a position left bottom, and progressing in a raster pattern to top right. All the SECCM scans were performed in air with a 2 μm pixel-pitch, equivalent to 255 individual CVs and a total imaging time of 53 mins (0.82 s per CV with the meniscus in contact with the surface). Although surface termination modification is highly unlikely under the conditions of our experiment (very short residence times at potentials ≥ ± 1 V and the avoidance of acidic solutions), to further ensure negligible O-termination disruption, which may possibly result from electrochemical cathodic treatments (due to partial conversion to H-termination),[51-53] CVs were started at -0.1 V, with the potential scanned anodically to 1.9 V, then reversed back to -2.2 V, before finally scanning again to -0.1 V. Regions with very similar doping levels, as identified from the FE-SEM image, and recorded in the earlier and latter part of the scan, gave very similar CV responses. This indicated that the BDD sample was not adversely affected by being in the ambient atmosphere, prior to contact with the electrolyte droplet.

Twelve typical CVs (six in each facet), in the least doped (indicated by the red circles in Figure 4.2b) and most doped facet (blue circles in Figure 4.2b) are shown in Figures 4.2c and 4.2d. It can immediately be seen that the doping level has a strong effect on the cathodic window, in particular, with the most doped grains being most electrocatalytic, as we highlight further below. Note that current densities were calculated based on a measured circular wetting area diameter, d = 1.94 ± 0.06 μm, using the mean value. d

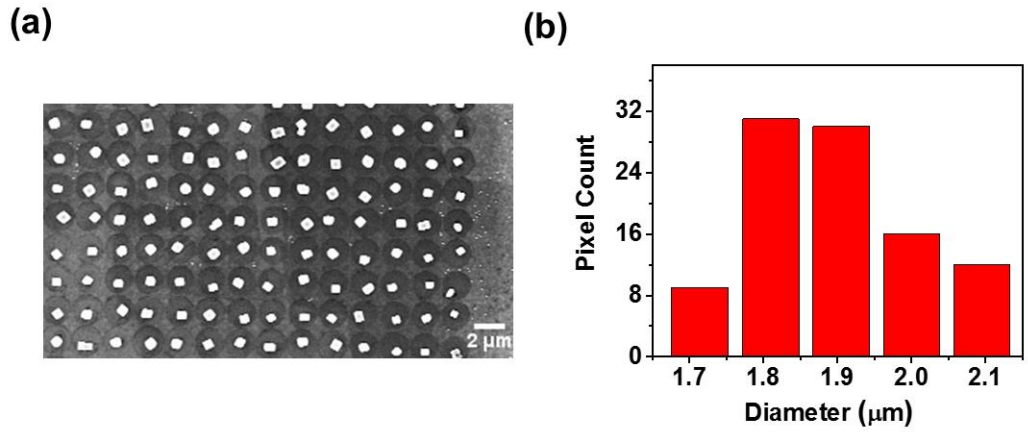

Figure 4.6: (a) FE-SEM image of a part of area I of O-BDD after voltammetric SECCM. (b) Histogram of meniscus size distribution measured from Figure 4.6 (a).

was estimated from the meniscus residues of 86 representative pixels analyzed by FE-SEM, as detailed in Figure 4.6. Within error, the meniscus wetting was independent of boron doping level.

In these twelve microscale CVs, only a double layer region between the solvent window defining anodic and cathodic processes was observed. There was no evidence of an electrochemical sp^2 carbon signal or an oxygen reduction current[17] and no apparent link can be drawn between the solvent window magnitude and the sp^2 levels from Raman microscopy for the higher doped grains (compare the doping level data (image) in Figure 4.2b, electrochemical image in Figure 4.2e to the Raman image in Figure 4.3a). These observations further supported the conclusion that any sp^2 contributions to the electrochemistry are insignificant.

The current densities, *j*, reported in literature to define the solvent window of BDD, range from 0.25 mA cm^{-2} to 2 mA cm^{-2} (at 0.1 V s^{-1} where the capacitive current is negligible).[17,20,54,55] Here, we use 3.5 mA cm^{-2}, because the high scan rates (10 V s^{-1}) employed during our CV analysis, gave an appreciable capacitive current (~2.5 mA cm^{-2}). The value of 3.5 mA cm^{-2} is sufficiently above this background contribution by ca. 1 mA cm^{-2}, which is in the middle of the range defined above for identifying the solvent window. SECCM onset potential maps both for the cathodic and anodic processes are plotted by extracting potential values of every pixel at -3.5 mA cm^{-2} and +3.5 mA cm^{-2}. In Figure 4.2e, the SECCM onset potential map for the cathodic process has a strong correlation with boron doping level that can be gleaned from the contrast in the FE-SEM

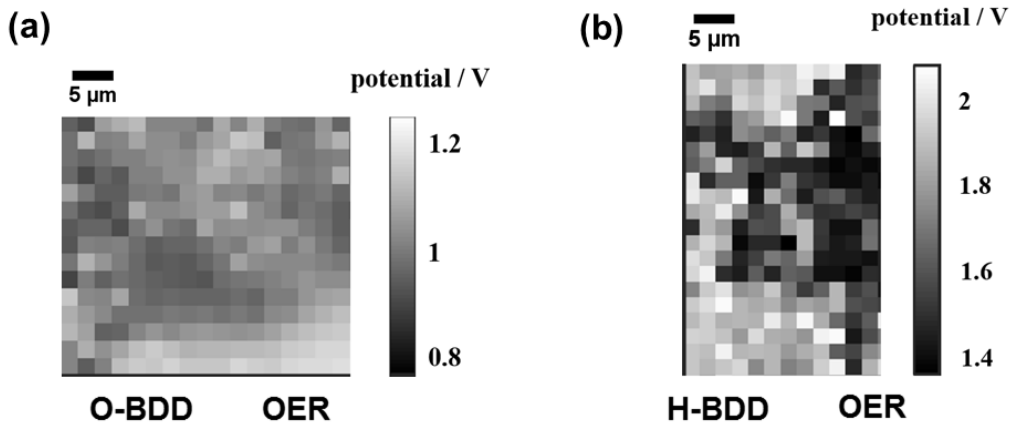

Figure 4.7: (a) SECCM onset potential image of area I recorded at 3.5 mA cm^{-2}. (b) SECCM onset potential image of area I′ recorded at 3.5 mA cm^{-2}.

image in Figure 4.2b, with lower doped facets appearing brighter.[38] It is evident that the more doped facets have a less negative onset potential than the lower doped facets. In contrast, for the anodic process, the onset potential for the higher and lower doped facets is, within error, more or less the same as shown in Figure 4.7a.

Values for the solvent window and the cathodic/anodic onset potentials, are summarized in Table 4.1. Note that these values are averages of all pixels recorded in each of the least doped facets (47 pixels for O-BDD and 32 pixels for H-BDD) and most doped facets (47 pixels for O-BDD and 62 pixels for H-BDD) as marked with red and blue lines (Figure 4.2b for O-BDD and Figure 4.8a for H-BDD). As shown in Table 4.1, for O-BDD, the solvent window of the less doped facet is 45 mV wider than that of the more doped facet, due to differences in the onset potential for the cathodic process.

Table 4.1 Table of solvent window of O-BDD (area I) and H-BDD (area I′).

Surface	Doped facet	Onset potential		Solvent window
		E_{anodic} (V)	$E_{cathodic}$ (V)	ΔE (V)
O-BDD	Less	1.05 (±0.089)	-1.74 (±0.13)	2.79 (±0.22)
	More	1.00 (±0.052)	-1.39 (±0.083)	2.34 (±0.12)
H-BDD	Less	1.88 (±0.090)	-2.16 (±0.072)	4.04 (±0.15)
	More	1.54 (±0.11)	-1.97 (±0.082)	3.52 (±0.20)

Values were obtained from all pixels in the representative most and least doped facets as marked in Figure 4.2b and Figure 4.8a.

To further illustrate the difference in cathodic activity across the scanned area, the surface current, i_{surf}, at a potential of -2.2 V (the maximum cathodic potential investigated), was extracted and plotted as an image, as shown in Figure 4.2f. Clearly, there is a correlation between the SECCM image (Figure 4.2f) and the FE-SEM image (Figure 4.2b), with the lower doped regions showing lower current densities in the cathodic region. The darkest regions in the FE-SEM image, which correspond to the most highly doped regions,[38] show the largest current densities.

The full movie comprising current images with a step of 10 mV between each generated current map (820 different potentials/maps across the forward and reverse scan), is shown in Supporting Information, Movie S3. The movie represents the electrochemical activity of the electrode surface as a function of the applied working electrode potential, and highlights that spatial heterogeneities in anodic and cathodic activity appear at the most extreme potentials, near the solvent windows, in line with the CVs described above.

Macroscopic studies of the solvent window in several supporting electrolytes including chloride solutions, for differently doped nanocrystalline O-BDD electrodes (anodically treated in acid) have been reported.[18] It was also found that the solvent window decreased as the *average* boron doping level increased, and the cathodic onset potential was affected more by doping than the anodic one. However, changes in the anodic onset potential were still observed.[18] In this study, measurements were averaged across a geometric area of 5.72 mm,^{2} and were thus unable to take account of heterogeneity in doping of the surface. In contrast, we have been able to make 255 individual measurements, all at different locations, with the electrochemical response correlated to the properties of individual grains/facets.

4.3.4 Voltammetric SECCM at H-BDD electrode

To explore the impact of surface termination on the solvent window of BDD, the O-BDD electrode was H-terminated using a hydrogen plasma treatment,[25] resulting in a water contact angle of 86° (Figure 4.5b). Voltammetric SECCM scanning at the H-BDD electrode was carried out in a region containing the same facets as area I (Figure 4.2b), 24 × 40 μm, marked as I′ in the FE-SEM image in Figure 4.8a. Again, to minimize oxidation of the H-BDD surface during potential cycling, CVs started at a potential of -0.1 V, with the potential scanned cathodically to -2.2 V, then reversed to 2.2 V and finally back to -0.1 V.

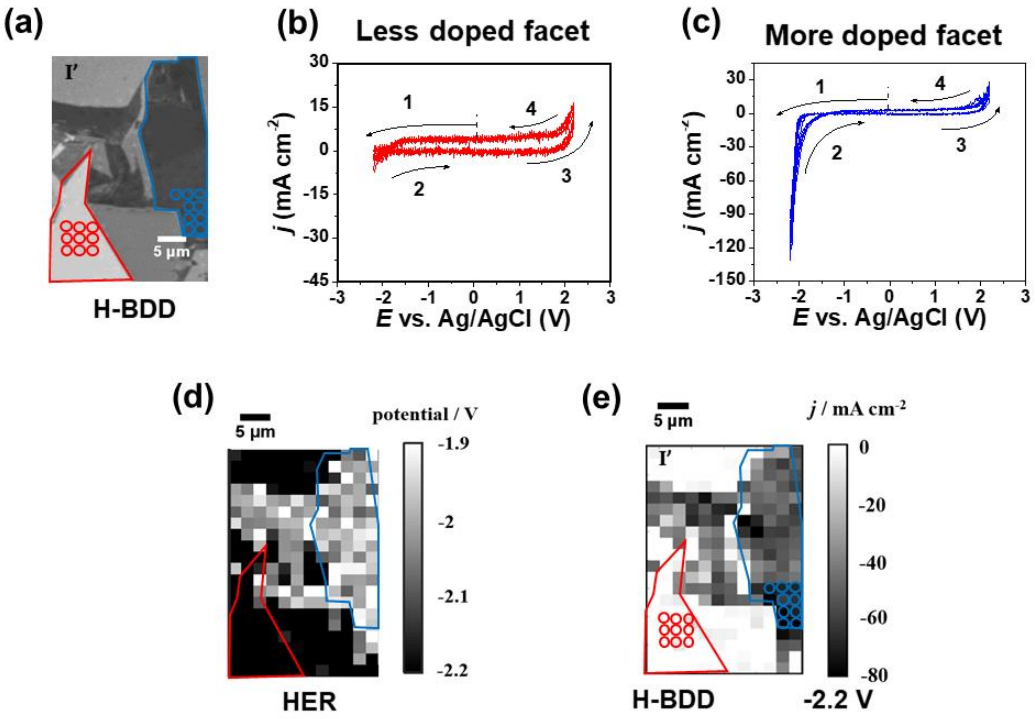

Figure 4.8: (a) FE-SEM image of area I′. (b-c) Corresponding individual CVs for less doped facet (nine individual CVs corresponding to the red circles in a) and more doped facet (nine individual CVs corresponding to the blue circles in a). Note the different current scales in these plots. (d) SECCM onset cathodic potential image of area I′ for a current density of -3.5 mA cm^{-2}. (e) SECCM current density image of area I′ at -2.20 V.

An FE-SEM image of the meniscus residues after scanning is shown in Figure 4.9. The diameter of the meniscus was found to be 696 ± 52 nm (obtained from 118 pixels), much smaller than that on O-BDD (*vide supra*), due to the hydrophobic nature of H-BDD. The meniscus wetting was also found to be independent of doping level.

Eighteen typical CVs (nine in each facet) on a less doped (indicated by the red circles in Figure 4.8a) and more doped facet (blue circles in Figure 4.8a) are shown in Figures 4.8b and 4.8c. The SECCM onset potential image for the cathodic process (assuming a current density of -3.5 mA cm^{-2} which was about 1 mA cm^{-2} in magnitude greater than the background cathodic level of ~ -2.5 mA cm^{-2}) is displayed in Figure 4.8d. The onset potential of the less doped facet is -190 mV more negative than that for the more doped facet (broadly similar to what was found for the O-BDD surface; *vide supra*). However, in contrast to the behavior for the O-BDD surface, on H-BDD the anodic process occurs at a potential value that is 340 mV more positive for the less doped (Figure 4.8b) than the more doped facet. Furthermore, compared to O-BDD, on H-BDD the solvent

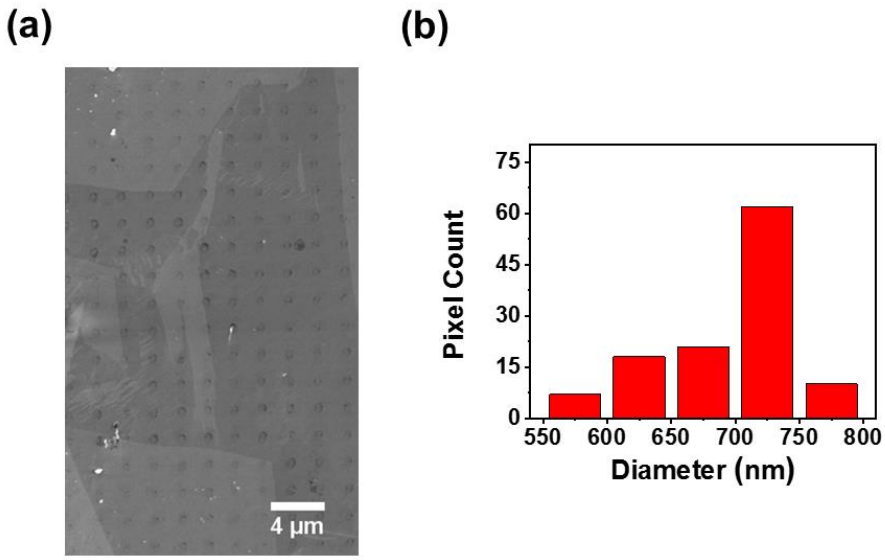

Figure 4.9: (a) FE-SEM image of a part of area I′ of H-BDD after voltammetric SECCM. (b) Histogram of meniscus size distribution measured from Figure 4.9a.

window is significantly larger by 1250 mV on the less doped facet and by 1170 mV on the higher doped grain. The solvent window and onset potential analysis for both the anodic and cathodic processes are summarized in Table 4.1.

To illustrate the facet dependence of the cathodic process activity, an SECCM map at an applied potential of -2.2 V (again representing the maximum applied cathodic potential), selected from potential resolved images, is shown in Figure 4.8e. Clearly, there is a strong correlation between the electrochemical activity image (Figure 4.8e) and the corresponding facets in the FE-SEM (Figure 4.8a), with the more doped facets yielding a higher current density than the less doped facets. A movie of the electrochemical current for the H-BDD surface as a function of potential is given in SI, Movie S4. As for the O-BDD surface, spatial heterogeneities in the activity are evident at the most extreme potentials.

4.3.5 Processes defining the solvent window

Examining the results of Figures 4.2 and 4.8, summarized in Table 4.1, the solvent window is found to be wider for H-BDD than O-BDD. For O-BDD, decreasing the doping level increases the onset potential for the cathodic process, whilst the anodic onset potential stays more or less the same. For H-BDD, both the anodic and cathodic onset potentials increase as the boron doping level decreases.

Considering the cathodic process, the HER controls the current on both surface-terminations of BDD. On diamond electrodes, the reaction is considered to proceed via proton discharge in the presence of a surface adsorbed H radical to produced H_2 (Volmer-Heyrovsky mechanism) i.e.

$$C\text{-}H + H^+_{(aq)} + e^- \rightarrow C^{\cdot} + H_2 \quad (4.1)$$

In contrast for the anodic process, in chloride containing solution, there is competition between OER (equation 4.2, 4.3) and chloride oxidation (equation 4.4).

For OER, the conventional processes, i.e.

$$2H_2O \rightarrow O_2 + 4H^+ + 4e^- \qquad E^o = 1.23\ V \quad (4.2)$$

is not catalytically favoured on BDD[56] and at the extreme electrode potential defining the anodic window, the following can also take place

$$H_2O \rightarrow OH^{\cdot} + H^+ + e^- \qquad E^o = 2.73\ V \quad (4.3)$$

Additionally, chloride oxidation to chlorine is a consideration:

$$2Cl^- \rightarrow Cl_2 + 2e^- \qquad E^o = 1.36\ V \quad (4.4)$$

Our finding of a wider solvent window for H-BDD compared with O-BDD contrasts with previous literature on macroscopic electrodes where the opposite has been seen.[26] The O-BDD electrodes in the literature studies[25,26] were O-terminated using an oxygen plasma treatment (whereas we use a strong acid clean) and measurements were made in either acidic sulfate solutions[26] or PBS buffer solutions.[25] Sulfate can be oxidized to $S_2O_8^{2-}$, but only at very high anodic potentials on BDD electrodes.[57,58] For the phosphate buffered saline (PBS) solutions, the electrolyte ions used are inert, and the anodic process is driven by OER and the cathodic process by HER. Additionally, macroscopic voltammetric measurements on very similar O-BDD material as used by us, but in nitrate media, report a solvent window of 3.6 V for O-BDD,[17] wider than reported here; note only OER is present anodically (via eqs 4.2 and 4.3).

The diminished anodic window that we observe on O-BDD, in chloride solution, indicates that chloride oxidation must play a significant role in defining the onset anodic potential. This is confirmed by comparing the solvent window response of a O-BDD macroelectrode (1 mm diameter and very similar material quality to that used herein) in several different electrolytes (0.1 M KCl, KNO_3 and K_2SO_4) as shown in Figure 4.10. The anodic solvent window is very similar for sulfate versus nitrate; although for sulfate there is a pre-wave prior to the main oxidative current. The origin of this feature has been discussed in some detail in reference 57. However, the onset anodic potential in chloride media is greatly diminished due to chloride oxidation. Evidently, our

microscopic data indicate that for the range of boron-doping levels in the pBDD electrodes used by us, the onset potential for the chloride oxidation process is not appreciably affected by the boron dopant density in these BDD electrodes.

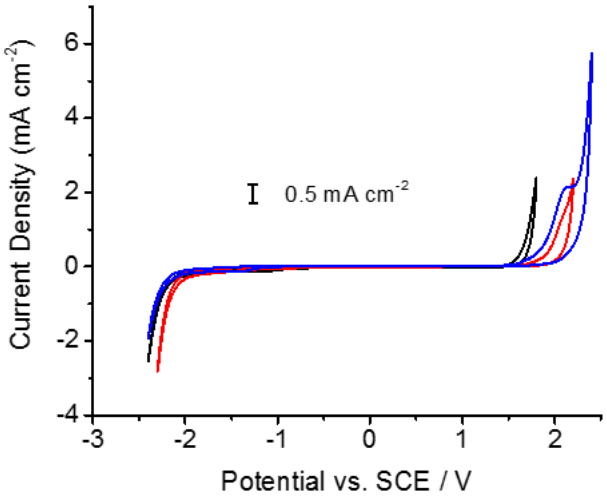

Figure 4.10: CVs in aerated 0.1 M KCl, pH=6.1 (black), 0.1 M KNO_3, pH=6.2 (red), and 0.1 M K_2SO_4, pH=6.9 (blue) recorded at a scan rate of 0.1 V s^{-1}.

In comparison to O-BDD, the much larger anodic onset potential on H-BDD indicates that chloride oxidation must be significantly kinetically hindered on this hydrophobic surface. Moreover, the very large shift in the anodic onset potential for H-BDD means that on the H-BDD surface OER, via equation 4.3, would (at least partly) contribute to the current. Indeed, a switch in the oxidation pathway from chloride oxidation to OER is also suggested by the fact that for the H-terminated surface, the anodic onset potential is dependent on the boron dopant density, whereas there is little such dependence for the O-BDD surface. This is a very interesting observation for which further experimental and theoretical studies could usefully aid understanding.

The level of local boron doping in pBDD has a number of consequences, including affecting the local density of electronic states and the number of boron atoms in the (sub) surface region. Evidently, increasing boron levels in BDD decreases the onset potential for HER on both O-BDD and H-BDD electrodes, as well as the anodic process on the H-BDD surface. For HER, weakly adsorbed H radicals on the surface of the BDD (formed by the transfer of an electron to H^+) are thought to be important in the overall hydrogen discharge process. Calculations[59] have shown that the presence of sub surface C-B bonds has an impact on weakening the bond between an electrochemically formed H radical and the carbon surface, promoting further reaction of this radical with H^+ to

form H_2, which explains the diminished overpotential in the higher doped grains (compared to lower doped grains) of both H-BDD and O-BDD. Our data further suggests this process is favored by O-termination of the surface. For the H-terminated surface, where we propose the OER via eq 4.3 plays a role, such factors could also be important, especially if the adsorption of water on the surface is a limiting step in the process. Further theoretical work is needed to understand these processes in greater detail, and microscopic measurements, such as those herein, will aid the development of a deeper understanding.

4.4 Conclusions

Voltammetric SECCM, which combines SECCM imaging with a CV measurement at each pixel, has proven powerful in highlighting key surface processes that affect the local solvent window of pBDD with both hydrogen and oxygen terminations in chloride solutions. A key feature of this approach is that CVs are recorded at hundreds of spots for correlation between electrochemistry and structure effects, to unambiguously identify correlation between various local material properties of the electrode and the electrochemical activity.

In this work, we have used correlative electrochemical microscopy to investigate the impact of boron dopant concentration and electrode surface termination on the solvent window of BDD. Voltammetric SECCM has revealed that the solvent window is directly linked to the local boron dopant concentration, irrespective of the surface termination, with the solvent window for less-doped facets being wider than for more-doped facets. However, it is noteworthy that the onset potential for the anodic process is relatively insensitive to boron doping level for O-BDD (for the doping levels herein), but doping dependent on H-BDD. This is proposed to be due at least in part to a change in the mechanism to OER, rather than chloride oxidation on the H-BDD. However, further work to probe the processes involved in the anodic processes at the different electrodes is needed. Scanning electrochemical microscopy (tip collection measurements) could be very useful in this regard to attempt to detect the products and intermediates of the electrode process. On both surfaces, the cathodic onset potential is governed by the HER and this is more facilitated at O-terminated surfaces and surfaces of higher boron-doping density.

The results provided by this study are valuable for designing and optimising electrodes where a particular solvent window is desired or, with further direct

confirmation, where a particular reaction in the anodic window is required, for example for water treatment or electrosynthesis. Both the boron dopant concentration and surface termination are key factors that can be tuned to achieve particular properties for practical electrodes, and this study has highlighted how multiple measurements at the single entity (BDD facet) level are particularly powerful in elucidating the overall properties of a complex macroscopic electrode.

4.5 Reference

1 Martin, H. B., Argoitia, A., Landau, U., Anderson, A. B. and Angus, J. C. Hydrogen and oxygen evolution on boron-doped diamond electrodes. *Journal of The Electrochemical Society* **143**, L133-L136 (1996).

2 Macpherson, J. V. A practical guide to using boron doped diamond in electrochemical research. *Physical Chemistry Chemical Physics* **17**, 2935-2949 (2015).

3 Macpherson, J. V. The Use of Conducting Diamond in Electrochemistry. *Electrochemistry of Carbon Electrodes* **16** (2015).

4 Sarada, B., Rao, T. N., Tryk, D. and Fujishima, A. Electrochemical oxidation of histamine and serotonin at highly boron-doped diamond electrodes. *Analytical chemistry* **72**, 1632-1638 (2000).

5 Svítková, J., Ignat, T., Švorc, Ľ., Labuda, J. and Barek, J. Chemical modification of boron-doped diamond electrodes for applications to biosensors and biosensing. *Critical reviews in analytical chemistry* **46**, 248-256 (2016).

6 Härtl, A., Schmich, E., Garrido, J. A., Hernando, J., Catharino, C. S., Walter, S., Feulner, A. Steinmüll and D., Stutzmann, M. Protein-modified nanocrystalline diamond thin films for biosensor applications. *Nature materials* **3**, 736 (2004).

7 Medina-Sánchez, M., Mayorga-Martivez, C. C., Watanabe, T., Ivandini, T. A., Honda, Y., Pino, F., Nakata, K., Fujishima, A, Einaga, Y. and Merkoci, A. Microfluidic platform for environmental contaminants sensing and degradation based on boron-doped diamond electrodes. *Biosensors and Bioelectronics* **75**, 365-374 (2016).

8 Marselli, B., Garcia-Gomez, J., Michaud, P.-A., Rodrigo, M. and Comninellis, C. Electrogeneration of hydroxyl radicals on boron-doped diamond electrodes. *Journal of the Electrochemical Society* **150**, D79-D83 (2003).

9 Michaud, P., Panizza, M., Ouattara, L., Diaco, T., Foti, G. and Comninellis, C. Electrochemical oxidation of water on synthetic boron-doped diamond thin film anodes. *Journal of applied electrochemistry* **33**, 151-154 (2003).

10 Zhi, J.-F., Wang, H.-B., Nakashima, T., Rao, T. N. and Fujishima, A. Electrochemical incineration of organic pollutants on boron-doped diamond electrode. Evidence for direct electrochemical oxidation pathway. *The Journal of Physical Chemistry B* **107**, 13389-13395 (2003).

11 Carter, K. E. and Farrell, J. Oxidative destruction of perfluorooctane sulfonate using boron-doped diamond film electrodes. *Environmental science & technology* **42**, 6111-6115 (2008).

12 Chaplin, B. P., Schrader, G. and Farrell, J. Electrochemical oxidation of N-nitrosodimethylamine with boron-doped diamond film electrodes. *Environmental science & technology* **43**, 8302-8307 (2009).

13 Ferro, S., De Battisti, A., Duo, I., Comninellis, C., Haenni, W. and Perret, A. Chlorine evolution at highly boron-doped diamond electrodes. *Journal of the Electrochemical Society* **147**, 2614-2619 (2000).

14 Vanhove, E., De Sanoit, J., Arnault, J., Saada, S., Mer, C., Mailley, P., Bergonzo and M. Nesladek. Stability of H-terminated BDD electrodes: an insight into the influence of the surface preparation. *physica status solidi (a)* **204**, 2931-2939 (2007).

15 Janssen, G., Van Enckevort, W., Vollenberg, W. and Giling, L. Characterization of single-crystal diamond grown by chemical vapour deposition processes. *Diamond Relat. Mater* **1**, 789-800 (1992).

16 Samlenski, R., Huag, C., Brenn, R., Wild, C., Locher, R. and Kiodl, P. Characterisation and lattice location of nitrogen and boron in homoepitaxial CVD diamond. *Diamond and related materials* **5**, 947-951 (1996).

17 Hutton, L. A., Iacobini, J. G., Bitziou, E., Channon, R. B., Newton, M. E. and Macpherson, J. V. Examination of the factors affecting the electrochemical performance of oxygen-terminated polycrystalline boron-doped diamond electrodes. *Analytical chemistry* **85**, 7230-7240 (2013).

18 Schwarzová-Pecková, K., Vosáhloová, J., Barek, J., Šloufová, I., Pavlova, E., Petrák, V. and Zavázalová, J. Influence of boron content on the morphological, spectral, and electroanalytical characteristics of anodically oxidized boron-doped diamond electrodes. *Electrochimica Acta* **243**, 170-182 (2017).

19 Živcová, Z. V., Frank, O., Petrák, V., Tarábková, H., Vacík, J., Nesládek, M., Kavan, L. Electrochemistry and in situ Raman spectroelectrochemistry of low and high quality boron doped diamond layers in aqueous electrolyte solution. *Electrochimica Acta* **87**, 518-525 (2013).

20 Bennett, J. A., Wang, J., Show, Y. and Swain, G. M. Effect of sp^2-bonded nondiamond carbon impurity on the response of boron-doped polycrystalline diamond thin-film electrodes. *Journal of The Electrochemical Society* **151**, E306-E313 (2004).

21 Ayres, Z. J., Newland, J. C., Newton, M. E., Mandal, S., Williams, O. A. and Macpherson J. V. Impact of chemical vapour deposition plasma inhomogeneity on the spatial variation of sp^2 carbon in boron doped diamond electrodes. *Carbon* (2017).

22 Pleskov, Y. V., Evstefeeva, Y. E., Krotova, M., Varnin, V. and Teremetskaya, I. Synthetic semiconductor diamond electrodes: Electrochemical behaviour of homoepitaxial boron-doped films orientated as (111), (110), and (100) faces. *Journal of Electroanalytical Chemistry* **595**, 168-174 (2006).

23 Bogdanowicz, R., Fabiańska, Golunski, L., Sobaszek, M., Gnyba, M., Ryl, J., Darowicki, K., Ossowski, T., Janssens, S. and Haenen, K. Influence of the boron doping level on the electrochemical oxidation of the azo dyes at Si/BDD thin film electrodes. *Diamond and Related Materials* **39**, 82-88 (2013).

24 Becker, D. and Jüttner, K. Influence of surface inhomogeneities of boron doped CVD-diamond electrodes on reversible charge transfer reactions. *Journal of applied electrochemistry* **33**, 959-967 (2003).

25 Živcová, Z. V., Petrák, V., Frank, O. and Kavan, L. Electrochemical impedance spectroscopy of polycrystalline boron doped diamond layers with hydrogen and oxygen terminated surface. *Diamond and Related Materials* **55**, 70-76 (2015).

26 Yagi, I., Notsu, H., Kondo, T., Tryk, D. A. and Fujishima, A. Electrochemical selectivity for redox systems at oxygen-terminated diamond electrodes. *Journal of Electroanalytical Chemistry* **473**, 173-178 (1999).

27 Liu, F., Wang, J., Liu, B., Li, X. and Chen, D. Effect of electronic structures on electrochemical behaviors of surface-terminated boron-doped diamond film electrodes. *Diamond and related materials* **16**, 454-460 (2007).

28 Patten, H. V., Meadow, K. E., Hutton, L. A., Iacobini, J. G., Battistel, D., Mckelvey, K., Colburn, A. W, Newton, M. E., Macpherson, J. V., Unwin and P. R. Electrochemical Mapping Reveals Direct Correlation between Heterogeneous Electron-Transfer Kinetics and Local Density of States in Diamond Electrodes. *Angewandte Chemie International Edition* **51**, 7002-7006 (2012).

29 Patten, H. V., Lai, S. C., Macpherson, J. V. and Unwin, P. R. Active sites for outer-sphere, inner-sphere, and complex multistage electrochemical reactions at polycrystalline boron-doped diamond electrodes (pBDD) revealed with scanning

electrochemical cell microscopy (SECCM). *Analytical chemistry* **84**, 5427-5432 (2012).

30 Tomlinson, L. I., Patten, H. V., Green, B. L., Iacobini, J., Meadow, K. E., Mckelvey, K., Unwin, P. R., Newton, M. E. and Macpherosn, J. V. Intermittent-contact Scanning Electrochemical Microscopy (IC-SECM) as a Quantitative Probe of Defects in Single Crystal Boron Doped Diamond Electrodes. *Electroanalysis* **28**, 2297-2302 (2016).

31 Patten, H. V., Hutton, L. A., Webb, J. R., Newton, M. E., Newton, M. E. and Unwin, P. R. Electrochemical "read–write" microscale patterning of boron doped diamond electrodes. *Chemical Communications* **51**, 164-167 (2015).

32 Ebejer, N., Schnippering, M., Colburn, A. W., Edwards, M. A. and Unwin, P. R. Localized high resolution electrochemistry and multifunctional imaging: Scanning electrochemical cell microscopy. *Analytical chemistry* **82**, 9141-9145 (2010).

33 Ebejer, N., Güell, A. G., Lai, S. C., Mckelvey, K., Snowden, M. E. and Unwin, P. R. Scanning electrochemical cell microscopy: a versatile technique for nanoscale electrochemistry and functional imaging. *Annual Review of Analytical Chemistry* **6**, 329-351 (2013).

34 Chen, C.-H., Jacobse, L, Mckelvey, K., Lai, S. C., Koper, M. T. and Unwin, P. R. Voltammetric scanning electrochemical cell microscopy: dynamic imaging of hydrazine electro-oxidation on platinum electrodes. *Analytical chemistry* **87**, 5782-5789 (2015).

35 Nie, M., Neodo, S., Wharton, J., Cranny, A., Harris, N., Wood, R., Stokes and K. Electrochemical detection of cupric ions with boron-doped diamond electrode for marine corrosion monitoring. *Electrochimica Acta* **202**, 345-356 (2016).

36 Goodwin, A., lawrence, A. L., Banks, C. E., Wantz, F., Omanović, D., Komorsky-Lovrić, Š., Compton, R. G. On-site monitoring of trace levels of free manganese in sea water via sonoelectroanalysis using a boron-doped diamond electrode. *Analytica chimica acta* **533**, 141-145 (2005).

37 Bentley, C. L., Perry, D. and Unwin, P. R. Stability and Placement of Ag/AgCl Quasi-Reference Counter Electrodes in Confined Electrochemical Cells. *Analytical chemistry* **90**, 7700-7707 (2018).

38 Wilson, N. R., Clewes, S. L., Newton, M. E., Unwin, P. R. and Macpherson, J. V. Impact of grain-dependent boron uptake on the electrochemical and electrical properties of polycrystalline boron doped diamond electrodes. *The Journal of Physical Chemistry B* **110**, 5639-5646 (2006).

39 Sharel, P., Kim, Y.-R., Perry, D., Bentley, C. L. and Unwin, P. R. Nanoscale Electrocatalysis of Hydrazine Electro-Oxidation at Blistered Graphite Electrodes. *ACS applied materials & interfaces* **8**, 30458-30466 (2016).

40 Lai, S., Patel, A. N., McKelvey, K. and Unwin, P. R. Definitive Evidence for Fast Electron Transfer at Pristine Basal Plane Graphite from High-Resolution Electrochemical Imaging. *Angewandte Chemie* **124**, 5501-5504 (2012).

41 Aaronson, B. D., Chen, C.-H., Li, H., Koper, M. T., Lai, S. C. and Unwin, P. R. Pseudo-single-crystal electrochemistry on polycrystalline electrodes: Visualizing activity at grains and grain boundaries on platinum for the Fe^{2+}/Fe^{3+} redox reaction. *Journal of the American Chemical Society* **135**, 3873-3880 (2013).

42 Snowden, M. E., Güell, A. G., Lai, S. C., Mckelvey, K., Ebejer, N., O'Connell, M. A., Colburn, A. W. and Unwin, P. R. Scanning electrochemical cell microscopy: Theory and experiment for quantitative high resolution spatially-

resolved voltammetry and simultaneous ion-conductance measurements. *Analytical chemistry* **84**, 2483-2491 (2012).

43 Ostrovskaya, L., Perevertailo, V., Ralchenko, V., Dementjev, A. and Loginova, O. Wettability and surface energy of oxidized and hydrogen plasma-treated diamond films. *Diamond and Related Materials* **11**, 845-850 (2002).

44 Wild, C., Herres, N. and Koidl, P. Texture formation in polycrystalline diamond films. *Journal of Applied Physics* **68**, 973-978 (1990).

45 Mermoux, M., Marcus, B., Swain, G. M. and Butler, J. E. A confocal Raman imaging study of an optically transparent boron-doped diamond electrode. *The Journal of Physical Chemistry B* **106**, 10816-10827 (2002).

46 Bogdanowicz, R., Fabiańska, A., Golunski, L., Sobaszek, M., Gnyba, M., Ryl, J., Darowicki, K., Ossowski, T., Jannssens, D., Haenen, K., Siedlecka, E. M. Influence of the boron doping level on the electrochemical oxidation of the azo dyes at Si/BDD thin film electrodes. *Diamond and Related Materials* **39**, 82-88 (2013).

47 Halliwell, S., May, P., Fox, N. and Othman, M. Investigations of the co-doping of boron and lithium into CVD diamond thin films. *Diamond and Related Materials* **76**, 115-122 (2017).

48 Zaitsev, A. M. *Optical properties of diamond: a data handbook*. (Springer Science & Business Media, 2013).

49 Ferreira, N., Abramof, E., Corat, E. and Trava-Airoldi, V. Residual stresses and crystalline quality of heavily boron-doped diamond films analysed by micro-Raman spectroscopy and X-ray diffraction. *Carbon* **41**, 1301-1308 (2003).

50 Ayres, Z. J., Cobb, S. J., Newton, M. E. and Macpherson, J. V. Quinone electrochemistry for the comparative assessment of sp^2 surface content of boron doped diamond electrodes. *Electrochemistry Communications* **72**, 59-63 (2016).

51 Salazar-Banda, G. R., Andrade, L. S., Nascente, P. P., Pizani, P. S., Rocha-Filho, R. C. and Avaca, L. A. On the changing electrochemical behaviour of boron-doped diamond surfaces with time after cathodic pre-treatments. *Electrochimica Acta* **51**, 4612-4619 (2006).

52 Girard, H., Simon, N., Ballutaud, D., Herlem, M. and Etcheberry, A. Effect of anodic and cathodic treatments on the charge transfer of boron doped diamond electrodes. *Diamond and related materials* **16**, 316-325 (2007).

53 Salazar-Banda, G. R., de Carvalho, A. E., Andrade, L. S., Rocha-Filho, R. C. and Avaca, L. A. On the activation and physical degradation of boron-doped diamond surfaces brought on by cathodic pretreatments. *Journal of applied electrochemistry* **40**, 1817-1827 (2010).

54 Granger, M. C., Witek, M., Xu, J., Wang, J., Hupert, M., Hanks, A., Koppang, M. D., Butler, J. E., Lucazeau, G. and Mermoux, M. Standard electrochemical behavior of high-quality, boron-doped polycrystalline diamond thin-film electrodes. *Analytical Chemistry* **72**, 3793-3804 (2000).

55 Yoshimura, M., Honda, K., Kondo, T., Uchikada, R., Einaga, Y., Rao, T. N., Tryk, D., Fujishima, A. Factors controlling the electrochemical potential window for diamond electrodes in non-aqueous electrolytes. *Diamond and related materials* **11**, 67-74 (2002).

56 García-Osorio, D., Jaimes, R., Vazquez-Arenas, J., Lara, R. and Alvarez-Ramirez, J. The Kinetic Parameters of the Oxygen Evolution Reaction (OER) Calculated on Inactive Anodes via EIS Transfer Functions: OH· Formation. *Journal of The Electrochemical Society* **164**, E3321-E3328 (2017).

57 Watanabe, T., Fiorani, A., Valenti, G., Paolucci, F. and Einaga, Y. Co-reactant-on-Demand ECL: Electrogenerated Chemiluminescence by the in Situ

Production of $S_2O_8^{2-}$ at Boron-Doped Diamond Electrodes. *Journal of the American Chemical Society* **138**, 15636-15641 (2016).

58 Serrano, K., Michaud, P., Comninellis, C. and Savall, A. Electrochemical preparation of peroxodisulfuric acid using boron doped diamond thin film electrodes. *Electrochimica Acta* **48**, 431-436 (2002).

59 Cai, Y., Anderson, A. B., Angus, J. C. and Kostadinov, L. N. Hydrogen Evolution on Diamond Electrodes by the Volmer-Heyrovsky Mechanism Prediction of Reversible Potentials and Activation Energies. *Journal of the Electrochemical Society* **154**, F36-F43 (2007).

Chapter 5. Electrodeposition of Nickel Hydroxide Nanoparticles on Carbon Nanotube Electrodes: Correlation of Particle Crystallography with Electrocatalytic properties

Two different electrodeposition approaches are used to form nickel hydroxide, $Ni(OH)_2$, nanoparticles (NPs) of different crystallographic orientations on single-walled carbon nanotubes. The two approaches are demonstrated via: (i) the electrochemical generation of OH^- (~ mM), in the presence of Ni^{2+}, resulting in the formation of disordered α-phase $Ni(OH)_2$ NPs by precipitation (direct approach); (ii) the electrodeposition of Ni NPs that are converted to $Ni(OH)_2$ through potential cycling in alkaline media to form the more thermodynamically favourable, ordered β-phase $Ni(OH)_2$ NPs (indirect approach). NPs produced by the direct approach exhibit remarkable electrocatalytic activity towards both methanol and ethanol oxidation, exhibiting excellent specific activities (SA) of ~2.8 kA g^{-1} for 0.5 M methanol and ~3.7 kA g^{-1} for 0.5 M ethanol. In contrast, NPs produced by the indirect approach shows SA values about an order of magnitude lower. This study demonstrates the capability of electrochemistry for the tailored synthesis of $Ni(OH)_2$ nanostructures for electrocatalytic applications, and a powerful, but simple, combinatorial approach for quick activity screening.

5.1 Introduction

The electrocatalytic oxidation of small organic molecules, especially electrochemical oxidation of alcohol, has attracted considerable interest for applications in different areas of electrochemical science, such as fuel cells[1] and electrochemical-based sensors.[2] Methanol (MeOH) and ethanol (EtOH) oxidation is crucial to the development of direct alcohol-based fuel cells.[3] The most widely used catalysts for the alcohol oxidation reaction (AOR) are rather expensive and scarce metals such as platinum and ruthenium.[4] There is thus a need to find alternative, cheaper materials, which perform as well, if not better, in terms of electrocatalytic activity.

Nickel hydroxide ($Ni(OH)_2$) is one such material that exhibits high electrochemical activity and cost effectiveness, and so this electrode has been the focus of considerable attention.[5-10] A variety of different synthetic routes are available for the production of a

wide range of different $Ni(OH)_2$ morphologies.[11] The electrocatalytic activity of $Ni(OH)_2$ results from the oxidized form, Ni(OOH), owing to unpaired d electrons or empty d-orbitals[12-14] which are available to bond with adsorbed species and intermediates.

It is well known that the electrocatalytic activity of materials can be increased significantly when nanostructures, such as nanoparticles (NPs), are employed.[15,16] Among electrocatalytic supports, carbon nanotubes (CNTs) have been shown to be extremely attractive for metal NPs[17,18] and metal oxides[19] due to their exceptional intrinsic properties, such as chemical stability[20] and nanoscale dimensions.[21] Moreover, compared to the more traditional support materials, such as carbon black, CNTs have been shown to offer an increased porosity and enhancement of the kinetic rate constant for the electrocatalytic process of interest (for similar metal NP loadings and carbon surface areas).[22-24] Several approaches have been adopted for depositing metal NPs onto nanotube electrodes, such as sol gel,[25] sonochemistry,[26] and hydrothermal methods.[27] However, these methods can be time-consuming and challenging to use. In contrast, electrochemistry is both rapid and facile, and a good deal of control over the nucleation and growth of metal NPs can be achieved by varying the deposition potential and time.[28,29]

The typical methods for CNT growth contain arc discharge,[30] laser ablation[31] and catalyzed chemical vapor deposition (cCVD).[32] Material produced by the first two methods has mainly been used in electrochemistry, but this contains large amounts of metal NPs and amorphous carbon, making the use of a clean-up procedure after growth mandatory.[33] However, CNTs contain significant amount of metallic impurities, even after extensive purification processes,[34] and these clean-up procedures introduce considerable defects in the single-walled carbon nanotubes (SWNTs).[35] The electrochemical behavior of redox systems can be strongly affected by such impurities and defects, which are particularly problematic for fundamental studies of eletrocatalysis.[36] In contrast, CNTs grown using cCVD method have been shown to exhibit low defect density,[37] high crystallinity and are relatively free of metallic NPs.[38]

The fabrication of $Ni(OH)_2$/CNT composite materials has often involved dispersing CNTs in solution followed by chemical precipitation of $Ni(OH)_2$.[39,40] Herein, we use electrodeposition method to modify $Ni(OH)_2$ NPs on cCVD grown CNTs. $Ni(OH)_2$ NP deposition can be prepared electrochemically using two approaches: (i) the *indirect approach*, whereby Ni NPs are first electrodeposited by direct reduction of Ni^{2+} and

subsequently electrochemically converted to $Ni(OH)_2$ by potential cycling in a basic electrolyte;[41-43] and: (ii) the *direct approach*[44-47] where $Ni(OH)_2$ is precipitated from highly supersaturated solutions by electrochemically generating high concentrations of OH^- at the electrode/electrolyte interface, in the presence of Ni^{2+}. In this chapter, we focus on the indirect approach and its characterizations. Then we compare its electrocatalytic performance towards the EtOH oxidation reaction (EOR) and MeOH oxidation reaction (MOR) with that of $Ni(OH)_2$ NP/SWNT composite prepared by direct approach.

The $Ni(OH)_2$/SWNTs are electrochemically interrogated using the microcapillary electrochemical method (MCEM),[28] which allows multiple electrochemical measurements to be made in different locations on the same electrode, thereby allowing a range of key parameters to be changed and investigated, without the need to make new electrodes and with minimal processing of the SWNTs. Although, SWNTs are attracting considerable attention as a support for electrocatalytic materials,[43,48] in the vast majority of cases, SWNT/NP composites are assessed by immobilizing, or producing, these structures on an electrode (typically glassy carbon),[43,49] which has its own intrinsic electroactivity. In contrast, our approach examines the behavior of the SWNT/NP materials as an electrode alone and study the correlation between $Ni(OH)_2$ NPs structure and their electrocatalytical activities towards AOR by indirect and direct approaches.

5.2 Materials and methodology

5.2.1 Electrodeposition of $Ni(OH)_2$ on SWNT network electrodes

All aqueous solutions were prepared using high purity Milli-Q reagent water (Millipore Corp.) with a resistivity of 18.2 MΩ cm at 25 °C. 10 mM nickel sulphate ($NiSO_4$, Aldrich, 99%) and 10 mM nickel nitrate ($Ni(NO_3)_2$, Aldrich, 99.999%) solutions were used for the electrodeposition of $Ni(OH)_2$ NPs for the indirect and direct approach, respectively, using a droplet method (Figure 5.1a).[50] Electrochemical measurements were carried out in a 3-electrode setup, with the SWNT network acting as the working electrode. Electrical contact to the Au band side contact was made via a pin. A drop of electrolyte solution (~15 µL, 4 mm diameter) was placed on the electrode surface, fairly close to the gold band but without making contact (Figure 5.1a). A platinum wire was used as a counter electrode (CE). AgCl-coated Ag wire acted as a quasi-reference electrode (QRCE), against which all potentials are quoted. This QRCE

was found to be sufficiently stable under the experimental conditions and timescale.[51,52] Both the Pt CE and AgCl-coated Ag wire QRCE were positioned within the droplet of solution to complete the circuit.

For the indirect approach, Ni metal NPs were first electrodeposited by applying a sufficiently negative reduction potential of -1.5 V *vs*. Ag/AgCl, for 5 s, in $NiSO_4$ solution, followed by oxidative potential cycling (+0.1 V to +0.5 V at 5 mV s^{-1} for 10 cycles) in 0.1 M KOH (Aldrich) as illustrated in Figure 5.1b.

For the direct approach, precipitation of $Ni(OH)_2$ on the SWNT network electrode occurred by driving the electroreduction of nitrate (from dissolved $Ni(NO_3)_2$) at the SWNT electrode to form OH^- locally (equation 5.1).

$$NO_3^- + 7H_2O + 8e^- \rightleftharpoons NH_4^+ + 10OH^- \qquad (5.1)$$

This concept is illustrated schematically in Figure 5.1b.[53] To produce NPs it was necessary to produce a high concentration of OH^-, leading to a highly supersaturated solution. This was achieved by driving the reduction process (1) at a negative driving potential of -1.5 V *vs*. Ag/AgCl, for 5 s.[12]

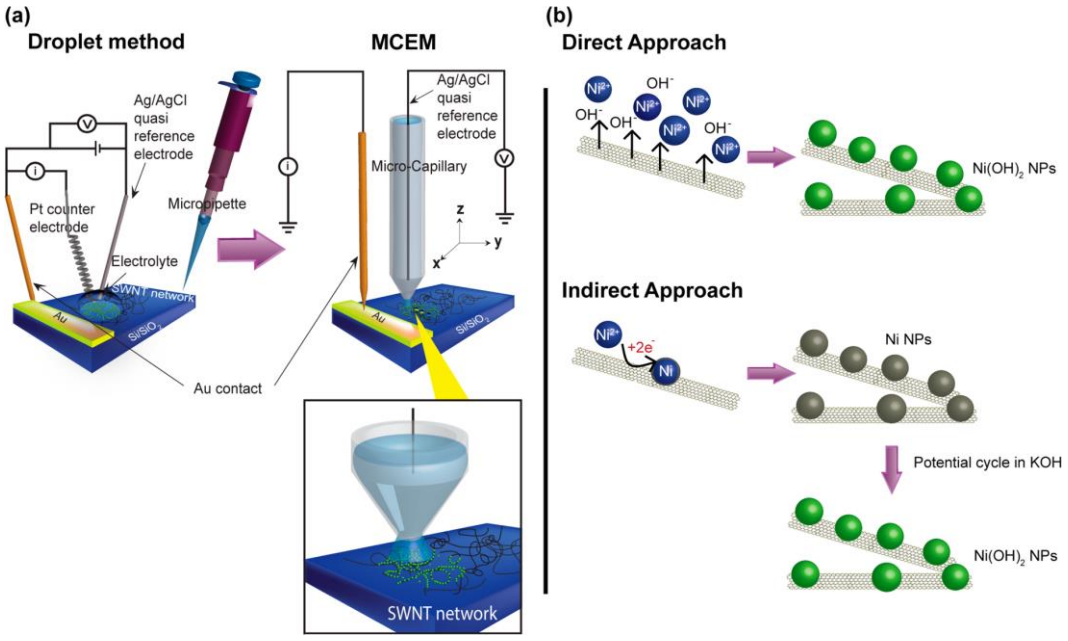

Figure 5.1: Experimental set-up for (a) the electrodeposition of NPs using the droplet method and microscopic electrocatalytic measurements using the MCEM. (b) Illustration showing $Ni(OH)_2$ NPs formation on a SWNT network electrode by both the direct (top) and indirect (bottom) approach.

5.2.2 Material characterization

Bare and functionalized SWNT networks were characterized using both field-emission scanning electron microscopy (FE-SEM: Zeiss Supra 55-VP, 5 kV acceleration voltage) and atomic force microscopy (AFM: tapping mode, Bruker-Nano Enviroscope). Micro-Raman spectra were recorded using a Renishaw inVia Raman microscope (514.5 nm Ar laser, 10 mW). For these techniques, three measurements (n = 3) were recorded per substrate. For high resolution transmission electron microscopy (HR-TEM) sample preparation, $Ni(OH)_2$ NPs were mechanically scratched from the growth substrate using a blade and dispersed in absolute EtOH (Fisher Scientific) solution. The suspension underwent sonication for 4 minutes and centrifugation for 15 minutes (Eppendorf, 10 000 rpm) to cause particle sedimentation. A drop of solution (3 µL), containing the sedimented particles, was then placed onto a lacey carbon TEM grid (Agar Scientific) and left until the EtOH had evaporated. HR-TEM was conducted (n = 3) using a JEM 2100 TEM (JEOL, LaB_6 filament, operated at 200 kV) equipped with energy-dispersive X-ray spectroscopy (EDS) and selected area electron diffraction (SAED) technique.

5.2.3 Electrocatalytic measurements

0.5 M MeOH (VWR, 99%) and 0.5 M EtOH (Fisher, 99.5%) were used for MOR and EOR, respectively, in 0.1 M KOH. All chemicals were used as received. Electrochemical measurements were performed using the MCEM, a localized electrochemical technique which has been described in detail previously.[28,54] The electrochemical cell consisted of a borosilicate glass capillary (1.2 mm outer diameter, 0.69 mm internal diameter, Harvard Apparatus Ltd.), pulled to a sharp tip using a laser pipette puller (P-2000, Sutter Instrument Co.). The end was polished to reveal an aperture in the range 60 - 62 µm (measured using optical microscopy for each capillary) and rendered hydrophobic on the outer walls through immersion in dichlorodimethylsilane (Fisher, ≥99%) for 90 s, with high purity Ar gas flowing through the capillary to prevent any internal silanization. The capillary was filled with the solution of interest and a Ag/AgCl wire as QRCE was inserted. The SWNT-$Ni(OH)_2$ substrate was connected as the working electrode and the capillary was manually lowered towards the electrode using an *x-y-z* micropositioner (Newport 433 series), with the aid of a camera (PixeLINK PL-B776U). A quick tap was applied to the micropositioner, once the capillary was close to the sample surface, so that an electrolyte meniscus formed on the SWNT network, without the capillary itself making contact with the electrode surface. Electrochemical measurements were made in

a 2-electrode arrangement (due to the small currents, < 120 nA), for which the use of a QRCE gives adequate stability,[55,56] using a potentiostat (CH Instruments, Austin, TX; model 730A).

5.3 Results and discussion

5.3.1 $Ni(OH)_2$ formation on SWNT network electrodes

Typical FE-SEM and AFM images shown in Figures 5.2a and 5.2b, respectively, are of a representative pristine (bare) HD SWNT network with a measured SWNT density >>10 μm length of SWNT per μm^2. This density is more than sufficient to ensure that the SWNT network is above the metallic percolation threshold (1.4 - 2.4 μm_{SWNT} μm^{-2}; based on typical SWNTs lengths of 7 - 12 μm).[57] Figure 5.2c shows a representative micro-Raman spectrum of a pristine HD SWNT network. The peaks marked with an (*) at 303 cm^{-1}, 521 cm^{-1} and 950 cm^{-1} originate from the Si/SiO_2 substrate and are used as a reference against which other peak intensities can be compared. The presence of radial breathing modes (RBM) between 100 and 350 cm^{-1} are clearly observed, confirming the presence of SWNTs. Moreover, the *G*-peak (1585 cm^{-1}, sp^2 graphitic carbon) was *ca*. 30 times the intensity of the *D*-peak (1350 cm^{-1}),

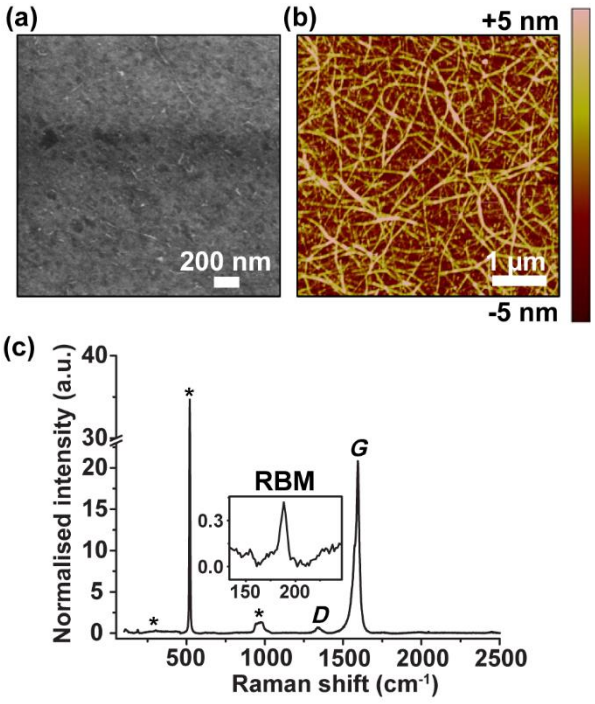

Figure 5.2: Typical (a) FE-SEM and (b) AFM images of HD SWNT network. (c) Corresponding micro-Raman spectrum.

indicating that the networks are of a high quality. The small *D*-peak could arise from defect sites or a small amount of amorphous carbon.

For indirect approach, Ni electrodeposition was achieved by potentiostatic method (formed by electrodeposition at -1.5 V for 5 s in 10 mM $NiSO_4$ solution) and then $Ni(OH)_2$ NPs were synthesized by potential cycling in KOH with cyclic voltammetry (CV). FE-SEM and higher resolution AFM images of the SWNT electrode surface recorded after Ni electrodeposition are shown in Figures 5.3(ai) and 5.3(bi) respectively. The Ni NPs were widely distributed over the HD SWNTs. Due to the reduced lattice spacing and denser nature of the native metal, Ni NPs provide better contrast against the SWNTs in FE-SEM than the $Ni(OH)_2$ NPs (Figure 5.3(ai)).[58]

As determined by AFM, Ni NPs of heights in the range 3 - 25 nm were formed during the initial electrodeposition process. The Ni NPs were then converted to $Ni(OH)_2$ by potential cycling, in 0.1 M KOH, sweeping from +0.1 V to +0.5 V at a potential scan rate of 5 mV s^{-1}, as shown in Figure 5.4. The current decreased significantly over the

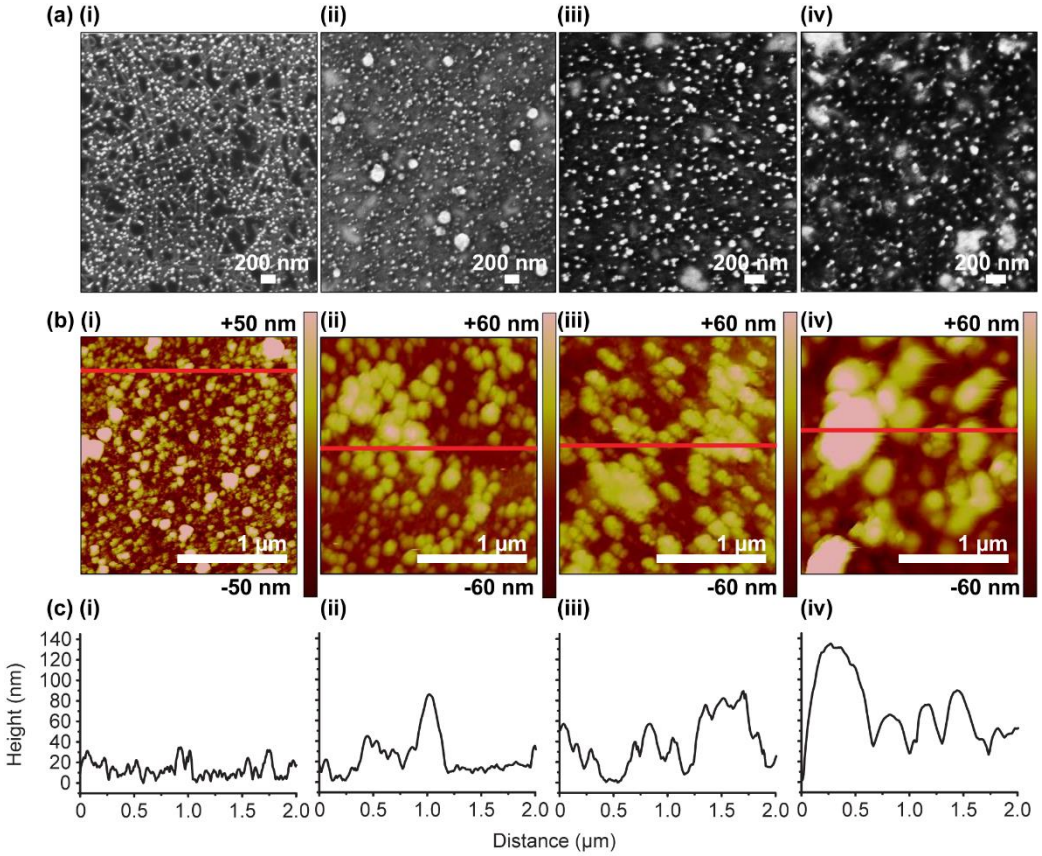

Figure 5.3: Typical (a) FE-SEM and (b) AFM images of HD SWNT networks decorated with Ni NPs (i) before and after (ii) 1 cycle, (iii) 10 cycles and (iv) 50 cycles in 0.1 M KOH. (c) Corresponding height cross sections of the NPs.

first seven cycles as a result of the transformation of metal Ni to $Ni(OH)_2$, and remained relatively stable with further cycles.[59] Figures 5.3(a,b) show typical FE-SEM and AFM images of the surface after (ii) 1 and (iii) 10 cycles. NPs of 6 - 75 nm and 25 - 80 nm in height were found after 1 and 10 cycles, respectively, clearly showing the size of the NPs increases with increasing cycle number (Figure 5.3c). However, it is difficult to determine the actual size of the NPs as there is evidence of NP agglomeration on the SWNTs. Hence, a more detailed analysis of the NPs formed was carried out by HR-TEM (*vide infra*).

As shown in Figure 5.3(a, b and c iv), the Ni NPs were subjected to 50 voltammetric cycles in 0.1 M KOH. The NPs became larger with the further voltammetric cycling. Particle heights of 40 - 130 nm were determined using AFM cross sectional analysis. The result indicates that an electrochemically-induced Ostwald-ripening or agglomeration process likely operates during potential cycling that has to be controlled to avoid particles becoming too large. For electrocatalytic studies, samples with smaller NPs were of interest, i.e. those formed after 10 cycles (*vide infra*).

For direct approach, $Ni(OH)_2$ NPs were prepared by chronoamperometry at -1.5 V for 5 s. A stable current is achieved after a short time which corresponds to a constant flux of electrogenerated OH^-. In the presence of Ni^{2+}, supersaturation of the solution occurs resulting in $Ni(OH)_2$ formation. It is possible to calculate the relative saturation ratio, S:[12]

$$S = (a_{Ni^{2+}} a_{OH^-})/K_{sp} \tag{5.2}$$

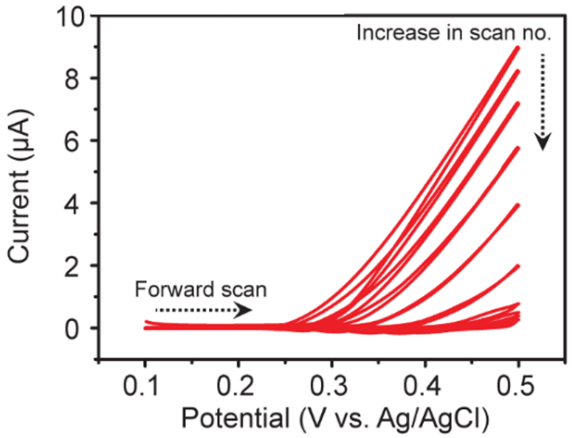

Figure 5.4: Repetitive CVs recorded in 0.1 M KOH on Ni NP deposited SWNT network electrode. The scan rate was 5 mV s^{-1}.

where $a_{Ni^{2+}}$ and a_{OH^-} are the activities of Ni^{2+} and OH^-, and K_{sp} of $Ni(OH)_2$ is 5.48 × 10^{-16} at 25°C.[60] The current flow is due to OH^- production. It can be seen in Figure 5.5a that a relatively stable current is achieved after a short time for $Ni(OH)_2$ NPs deposition, which corresponds to a constant flux of $[OH^-]$ at the electrode surface. The electrogenerated OH^- concentration profile can be calculated using equations (5.3) and (5.4):[61]

$$jo = \frac{i}{nF} \tag{5.3}$$

$$C - Co = \frac{jo\ l}{D}\{\frac{Dt}{l^2} + \frac{3x^2 - l^2}{6l^2} - \frac{2}{\pi^2}\sum_{m}^{\infty}\frac{(-1)^m}{m^2}\exp(-\frac{Dm^2\pi^2 t}{l^2})\cos\frac{m\pi x}{l}\}\ c \tag{5.4}$$

where *C* is the concentration and *C*o is initial concentration; *j*o is the flux and *i* is the current density during electrodeposition; *D* is the diffusion coefficient of OH^- ions (5.6 ×10^{-5} cm^2 s^{-1}),[62] *l* is the separation of electrode surface and a parallel boundary (set as 0.22 cm; unrestricted diffusion from or to the electrode surface), *t* is time, *x* is distance from electrode, and *m* is the number of points used (100) in the analytical expression. Using a time, *t* = 5 s, the resulting OH^- concentration profile is shown in Figure 5.5b (equations 5.3 and 5.4) along with the calculated S values (□), using equation 5.2, by approximating activity as concentration. The high OH^- concentrations generated close to the electrode surface (~2.5 mM), together with the bulk concentration of $[Ni^{2+}]$ (10 mM), result in very high S values of 10^8-10^9, promoting high nucleation rates and the formation of $Ni(OH)_2$ NPs.[12] $Ni(OH)_2$ NPs can be seen to precipitate uniformly on the multiply interconnected HD SWNT networks, as shown in the FE-SEM (Figure 5.6a)

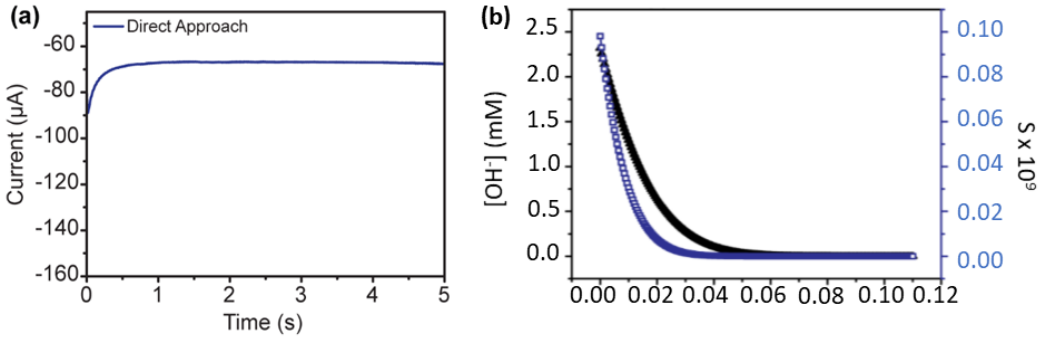

Figure 5.5: (a) A typical current-time curve recorded at a substrate potential of -1.5 V for 5 s in 10 mM $Ni(NO_3)_2$. (b) Concentration profile of OH^- (▲) vs. distance from electrode surface for a time of 5 s and corresponding S values (□), calculated using equation 2.

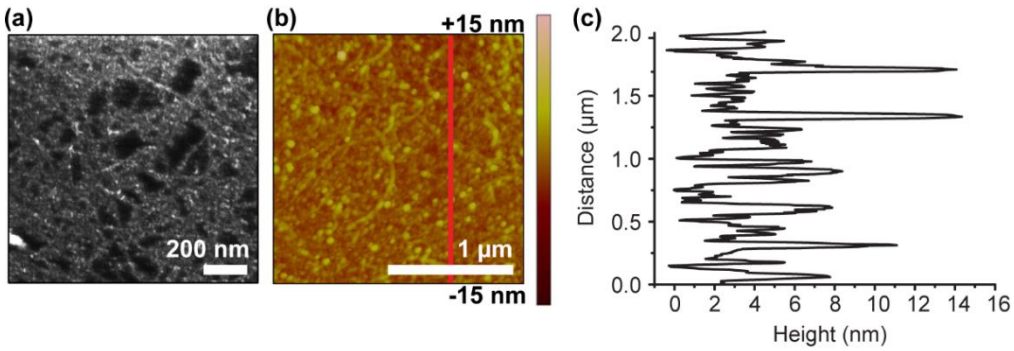

Figure 5.6: Typical (a) FE-SEM and (b) AFM images of a HD SWNT network electrode modified with $Ni(OH)_2$ (deposition parameters 5 s at -1.5 V vs. Ag/AgCl in 10 mM ($Ni(NO_3)_2$ solution). (c) AFM cross sectional height analysis (red line in b) of the NPs.

and AFM (Figure 5.6b) images. Cross-sectional AFM height analysis (Figure 5.6c) reveals NP heights in the range of 3 - 12 nm.

HR-TEM analysis of the $Ni(OH)_2$ NPs is shown in Figures 5.7a-c (direct approach) and Figures 5.7d-f (indirect approach, 10 cycles). The preparation procedure for HR-TEM analysis resulted in significant NP agglomeration (as shown in Figures 5.7a,d) but had the advantage that it was possible to focus on individual particles within the

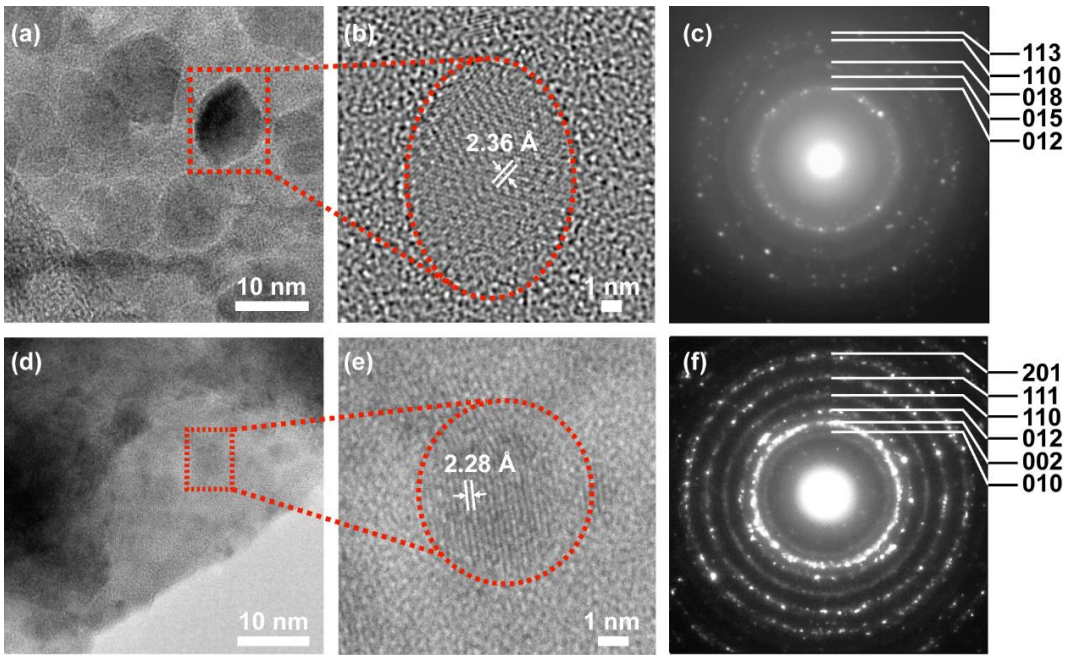

Figure 5.7 Typical (a, d) HR-TEM images and (c, f) SAED patterns of modified HD SWNT network electrode with $Ni(OH)_2$ NPs by the (a-c) direct and (d-f) indirect approaches.

agglomerate to provide more information on individual NP size. For the direct approach, HR-TEM shows the smallest crystallites of $Ni(OH)_2$ were around 5 nm in diameter, whilst the typical size of $Ni(OH)_2$ NPs was 10 nm, as shown in Figures 5.7a-b, in agreement with the AFM data (Figure 5.6b,c). For the indirect approach, HR-TEM shows the smallest crystallites were *ca.* 3 nm in diameter, with a typical size of 5 nm observed, as shown in Figures 5.7d-e, indicating that the larger sized NPs observed by AFM analysis (Figures 5.3b, c (ii-iv)) are due to the agglomeration of smaller NPs.

SAED was performed on NP agglomerates that were in the holes of the supporting lacey carbon, in order to avoid carbon background interference in the TEM analysis. SAED of $Ni(OH)_2$ produced by the direct method indicated the formation of α-phase $Ni(OH)_2$ (Figure 5.7c; Joint Committee on Powder Diffraction Standards (JCPDS) 380715), whilst β-phase $Ni(OH)_2$ (Figure 5.7f; JCPDS 140117) was observed for the indirect method. Figure 5.8a and b show a schematic diagram representing the α and β phases of $Ni(OH)_2$, respectively.[63] Figure 5.8b clearly shows that the β phase (inter-sheet (001) distance, c_o = 4.60 Å) adopts a more close packed (de-hydrated) structure compared to the more disordered (c_o = 7.60 Å) hydrated α phase (Figure 5.8a).[63-65] For the direct approach, it is likely that the rapid precipitation process in the presence of Ni^{2+} and supersaturated concentrations of OH^- (generated electrochemically) is responsible for α-phase formation, favoring the formation of disordered α-$Ni(OH)_2$ (kinetically-

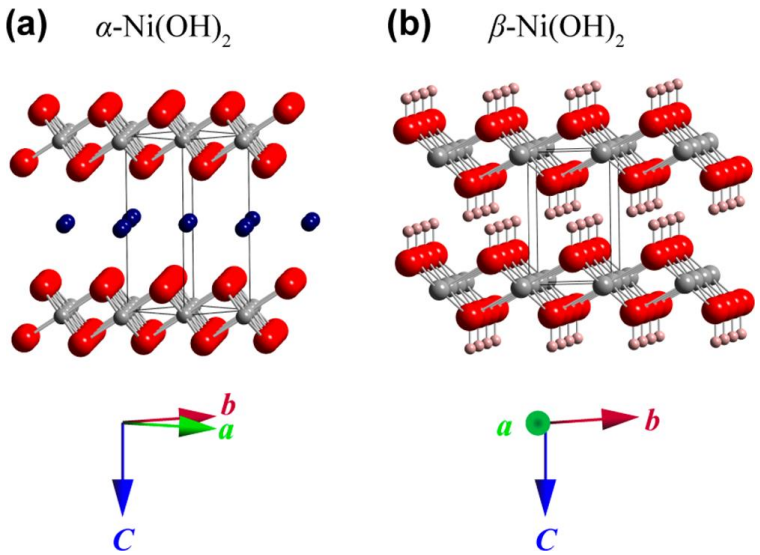

Figure 5.8: Schematic representation of (a) α-$Ni(OH)_2$ phase (small grey spheres, Ni^{2+}; large red spheres, OH^-; medium size blue spheres, H_2O positions) and (b) β-$Ni(OH)_2$ phase (medium grey spheres, Ni^{2+}; large red spheres, O^{2-}; small pink spheres, H^+). In the first structure, H^+ is omitted for clarity.[63]

driven process). For the indirect approach, as the initial electrodeposited metallic Ni has a face-centered cubic (close packed) structure,[66] electrochemical conversion of Ni NPs to β-$Ni(OH)_2$ appears to be favored as β-phase $Ni(OH)_2$ has a similar close-packed structure. Furthermore, the slow process using potential cycling is also likely to favor the formation of the thermodynamically stable β-phase $Ni(OH)_2$.[63]

Figures 5.7b and e show the HR-TEM of a selected NP (n = 3) and the corresponding SAED images (Figures 5.7c and f); for an α-$Ni(OH)_2$ NP (b,c) and β-phase $Ni(OH)_2$ NP (e,f). Note the SAED sample size is ~ 675 nm, and therefore the area around the NP is also sampled. From the HR-TEM images, lattice fringes indicate d spacings of 2.36 Å for the α-$Ni(OH)_2$ NP and 2.28 Å for the β-$Ni(OH)_2$ NP. These d spacings correspond to the (015) and (002) planes, identified using SAED, of the α and β phase $Ni(OH)_2$ NP, respectively, as provided by Figure 5.7c,f and the JCPDS.

5.3.2 MOR and EOR on $Ni(OH)_2$ NP modified SWNT network electrodes

CVs were first recorded in the potential range +0.1 V to +0.55 V, on both the α and β phase $Ni(OH)_2$ modified SWNT electrodes (prepared by the direct and indirect approach, respectively) by cycling in 0.1 M KOH at 5 mV s^{-1} to estimate the amount of electroactive $Ni(OH)_2$, as shown in Figure 5.9. For both cases, the charge associated with Q_{ox} (oxidation of $Ni(OH)_2$; shaded area under the anodic peaks in Figure 5.9) is greater than the charge associated with Q_{red} (reduction of NiOOH), with Q_{ox}/Q_{red} values of 1.4 and 2.5 determined for the α-phase and β-phase $Ni(OH)_2$ NPs respectively. This is likely to be due to the fact that highly electrocatalytic NiOOH can also oxidize adsorbed OH^-, leading to the evolution of O_2 and reduction of NiOOH back to $Ni(OH)_2$. This means there are less NiOOH sites available for electrochemical reduction on the return scan.[67] The effect, however, is small, and we showed in our previous work[12] that the anodic charge was well correlated with the particle size and number, assuming volumetric conversion of $Ni(OH)_2$.

The amount of electroactive $Ni(OH)_2$ (Γ /mol cm^{-2}) is thus reasonably given by:

$$\Gamma = \frac{Q_{ox}}{nFA} \tag{5.5}$$

where n is the number of electrons (n = 1), F is the Faraday constant and A is the area of the capillary opening. Given Q_{ox} values of 24.5 nC and 7.4 nC for the α-phase and β-phase $Ni(OH)_2$ respectively, Γ values of 9 ± 1 nmol cm^{-2} and 3 ± 1 nmol cm^{-2} were obtained. Given the slight enhancement of the charge on the forward sweep compared

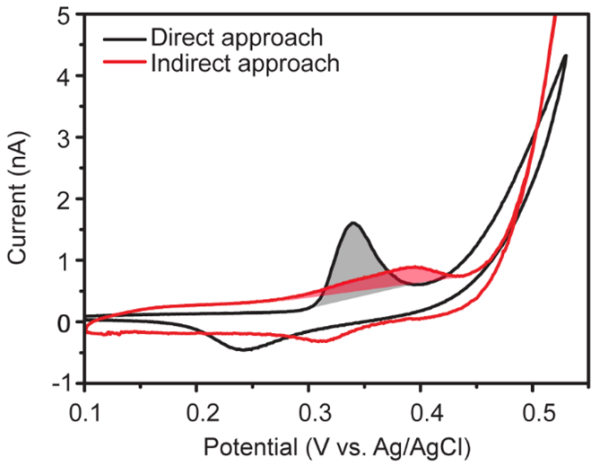

Figure 5.9: Typical CVs recorded using the MCEM with a capillary of 60 µm diameter in 0.1 M KOH, using a $Ni(OH)_2$ modified SWNT network electrode by the direct and indirect approaches. The potential scan rate is 5 mV s^{-1}.

to the reverse sweep, these are maximum values for the amount of electrodeposited $Ni(OH)_2$, and hence the specific activity values that follow are minimum values.

For α-$Ni(OH)_2$ oxidation, the oxidation peak lies 60 mV less positive than that for β-$Ni(OH)_2$ oxidation. Upon oxidation the α-$Ni(OH)_2$ transforms to γ-NiOOH,[68] the latter has a higher oxidation state (+3.5)[69] and nearly identical c_o parameter to α- $Ni(OH)_2$.[70] In contrast, β-$Ni(OH)_2$ transforms to β-NiOOH (+3 oxidation state), which only slowly transforms to γ-NiOOH (with a resulting volume change) upon prolonged (repeated) cycling.[11] In order to maintain charge neutrality during redox cycling, it is important that ions/solvent molecules can penetrate the layered $Ni(OH)_2$ structure (Figure 5.8); thus, as ion/solvent transfer can occur more freely in the disordered α-$Ni(OH)_2$/γ-NiOOH phase structures than in the corresponding β-phase structures.[71] This could be a likely cause of the observed differences in the CV responses in Figure 5.9. The corresponding equations for α-$Ni(OH)_2$ and β-$Ni(OH)_2$ oxidation, are as follows:

α-$Ni(OH)_2$/γ-NiOOH:

$$Ni_{1-x}H_x(OH)_2 0.64H_2O + xK^+ + (x+y)OH^- \leftrightarrow Ni_{1-x}K_xOOH_{2-y}0.64H_2O + (x+y)H_2O + ye^- \quad (5.6)$$

β-$Ni(OH)_2$/ β-NiOOH:

$$Ni(OH)_2 + OH^- \leftrightarrow NiOOH + H_2O + e^- \quad (5.7)$$

The two different $Ni(OH)_2$ structures were investigated for their electrocatalytic response towards the MOR and the EOR. The parallel pathways for the electrocatalytic oxidation of MOR and EOR were shown in Figure 5.10.

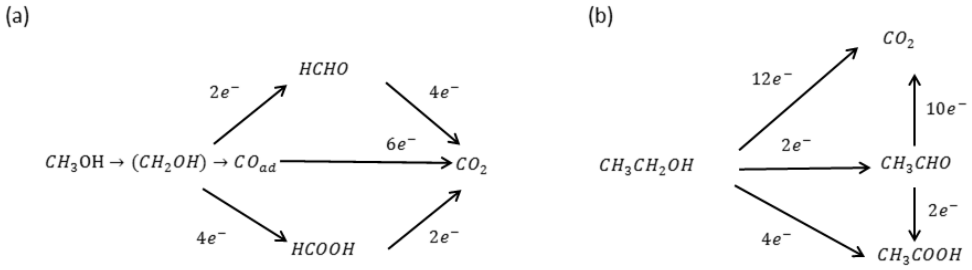

Figure 5.10: Schematics of the parallel pathways for the electrocatalytic oxidation of MOR (a) and EOR (b).

CV measurements, at a potential scan rate of 5 mV s^{-1}, over the potential range +0.1 V to +0.55 V, were carried out in 0.5 M MeOH and 0.5 M EtOH, respectively in 0.1 M KOH. For comparison to literature values, currents were normalized by the mass of electroactive $Ni(OH)_2$ electrodeposited on the SWNT network electrode, to provide a value for specific activity (current / mass = A $g_{Ni(OH)_2}^{-1}$):

$$\text{Specific activity} = \frac{inF}{Q_{ox}M_{Ni(OH)_2}} \tag{5.8}$$

where i is the current and $M_{Ni(OH)_2}$ is the molar mass of $Ni(OH)_2$. The calculated masses of electroactive material were 23.6 pg and 7.0 pg for α-$Ni(OH)_2$ and β-$Ni(OH)_2$, respectively. Note that the MOR and EOR responses for pristine SWNT network electrodes were negligible, even when doubling the alcohol concentration to 1 M, as shown in Figures 5.11a (inset). These data indicate that a bare SWNT network electrode is ineffective towards the electrochemical oxidation of alcohols, within this potential range.

For α-Ni(OH)$_2$, the forward scans in Figures 5.11a-b show a small anodic peak current (1) at +0.28 V and +0.31 V, followed by the appearance of larger (2) current peaks at +0.41 V and +0.48 V in the presence of EtOH and MeOH, respectively. For the reverse scan a cathodic peak current is observed at +0.20 V in both alcohols. Peak 1 is the characteristic signal for the oxidation of Ni(OH)$_2$ to NiOOH. The second larger current peak is due to the oxidation of the alcohol, catalyzed by NiOOH, occurring at +0.3 V and +0.33 V for EtOH and MeOH, respectively. Compared to cycling in 0.1 M KOH alone, Figure 5.11a shows *ca*. 40 times increase in the peak current density for the EOR, which equates to a specific activity of ~3.7 kA g^{-1} and *ca*. 30 times increase in the peak current density for the MOR, which is a specific activity of ~2.8 kA g^{-1} (Figure 5.11b). These values are higher than recent reports using nanostructured catalysts on carbon supports, as shown in Table 1. The small peak observed on the back scan for both the EOR and MOR, is attributed to the reduction of adsorbed intermediates (carbonaceous species not fully oxidized in the forward scan).[72]

For β-Ni(OH)$_2$, Figures 5.11c-d show the CVs recorded from +0.1 V to +0.60 V in the absence (0.1 M KOH only) and presence of 0.5 M EtOH (Figure 5.11c) and MeOH (Figure 5.11d). In contrast to the data in Figure 5.11a, it is not possible to differentiate

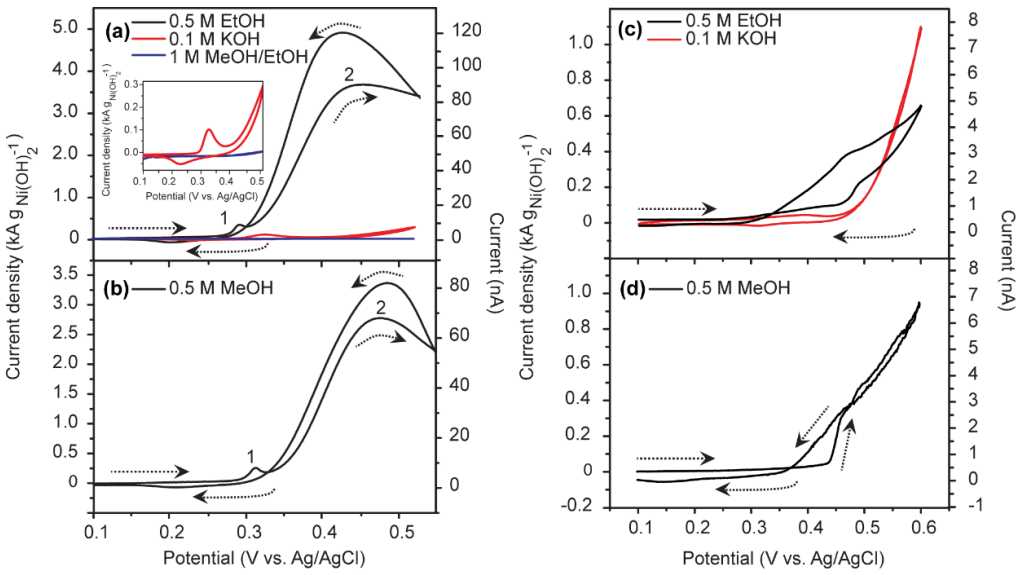

Figure 5.11: CVs at Ni(OH)$_2$ NP-modified SWNT network electrodes using the (a, b) direct and (c, d) indirect approach in a solution of 0.1 M KOH (red) with (a, c) 0.5 M EtOH and (b, d) 0.5 M MeOH (black). Inset: Magnification of the CVs of bare SWNT network electrode (blue) in 0.1 M KOH solution containing 1 M EtOH + 1 M MeOH and Ni(OH)$_2$/SWNT in 0.1 M KOH (red). The potential scan rate was 5 mV s^{-1}.

between oxidation of the $Ni(OH)_2$ and oxidation of the alcohol, instead one single oxidation wave is seen, which itself is not clearly defined. Therefore, it is difficult to define precisely an onset potential for AOR, although the current can be seen to begin increasing from a ~ zero baseline *ca.* +0.34 V and +0.37 V in the presence of EtOH and MeOH, respectively. The CV characteristic is most likely due to the sluggish kinetics of the β-$Ni(OH)_2$ to β-NiOOH conversion and the oxidation of the alcohol. By taking the current at +0.47 V for the EOR and +0.45 V for the MOR, SA values of ~0.4 kA g^{-1} and ~0.3 kA g^{-1} are estimated for the EOR and MOR, respectively. These values are *ca.* 9 times smaller than for the NPs obtained by the direct approach. Cycling β-$Ni(OH)_2$ NPs reduces the catalytic efficiency even further, as shown by the CVs in Figure 5.12, for a β-$Ni(OH)_2$/SWNT in 0.5 M EtOH, with the electrode prepared by 50, rather than 10 potential cycles of electrodeposited Ni NPs in 0.1 M KOH (Figure 5.3vi).

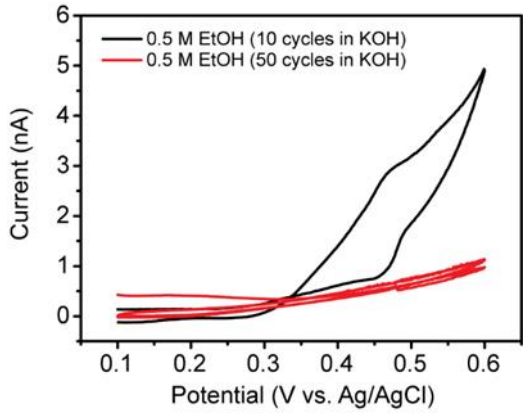

Figure 5.12: Typical CVs of 0.5 M EtOH in 0.1 M KOH at β-$Ni(OH)_2$/SWNT prepared by 10 (black) and 50 (red) potential cycles in 0.1 M KOH.

Overall, it is apparent that α-$Ni(OH)_2$ produced by the direct approach exhibits faster kinetics and superior electrocatalytic (oxidizing) properties, compared to β-$Ni(OH)_2$ produced by the indirect approach. The improved performance of the α-phase over the β-phase could be due to several factors including: (i) the more disordered structure of α-$Ni(OH)_2$/γ-NiOOH which enables ion-solvent intercalation, maintaining charge neutrality during electrocatalysis;[73] (ii) γ-NiOOH has a higher oxidation state than β-NiOOH and, in principle, could act as a more effective electro-oxidation catalyst.[68-70]

Table 5.1 : Nanostructured catalysts for MOR and EOR.

Electrode modification	Electrolyte, Scan rate	Maximum catalytic current ($A\ g_{Ni(OH)2}^{-1}$)		Ref.
		MeOH	EtOH	
Pt-Ru-Ni-P/Carbon supported	0.5 M H_2SO_4 and 0.5 M CH_3OH, 50 mV s^{-1}	459	-	74
Pt-TiO_2/Graphene composites	0.5 M H_2SO_4 and 1 M CH_3OH, 100 mV s^{-1}	1354	-	75
Pt-Ag/Glassy carbon electrode	0.5 M H_2SO_4 and 1 M CH_3OH, 50 mV s^{-1}	400	-	76
Pt-Ru/Carbon supported	0.1 M $HClO_4$ and 0.5 M CH_3OH	300	-	77
Pd-Ag/Graphene oxide	1 M KOH and 1 M CH_3OH, 1 M CH_2CH_3OH, 50 mV s^{-1}	600	1500	78
Cu-Pt-Pd/Carbon supported	0.5 M H_2SO_4 and 1 M CH_3OH, 1 M CH_2CH_3OH, 50 mV s^{-1}	700	1200	79
Pd-Cu-Sn/CNTs	1 M KOH and 0.5 M CH_3OH, 0.5 M CH_2CH_3OH, 50 mV s^{-1}	396	873	80
$Ni(OH)_2$/Boron-doped diamond	0.1 M KOH and 0.5 M CH_3OH, 0.5 M CH_2CH_3OH, 5 mV s^{-1}	990	1010	12
$Ni(OH)_2$/HD SWNT	0.1 M KOH and 0.5 M CH_3OH, 0.5 M CH_2CH_3OH, 5 mV s^{-1}	2800	3700	This work

5.4 Conclusions

The studies herein have revealed detailed information on the structure and electrocatalytic activity of $Ni(OH)_2$ NPs produced by two different electrochemical approaches on HD SWNT networks. For the direct approach, $Ni(OH)_2$ NPs were formed by electro-generating relatively high concentrations of OH^- at the electrode surface in the presence of Ni^{2+}. For the indirect approach, Ni NPs were first electrodeposited on the SWNTs and then electrochemically transformed to $Ni(OH)_2$ by potential cycling in alkaline media.

NP distribution was investigated using FE-SEM, whilst AFM was employed to provide quantitative information on NP size. AFM revealed individual NPs for the direct approach, of size in the range 3 - 12 nm. For the indirect approach, AFM indicated that NP aggregation was a potential problem, revealing a wide size distribution of 25 - 80 nm in the height of nanostructures. HR-TEM was used to provide higher resolution information on the NP deposits. This revealed typical NP crystallites of sizes 10 nm and 5 nm for the direct and indirect approaches, respectively. The latter data supported the idea that the larger nanostructured material, as observed by AFM, was produced by the aggregation of smaller NPs.

A key part of our study was to determine the crystallography of individual NPs using SAED in the HR-TEM. It was possible to assign NPs formed by direct deposition to the disordered (hydrated) α-phase and those formed via indirect deposition to the ordered (de-hydrated) β-phase. The different phases formed by these methods can be rationalized because in the direct approach extremely high supersaturations are generated resulted in the immediate precipitation of the kinetically favored α-phase of $Ni(OH)_2$. In contrast, the potential cycling approach involves a slow conversion of Ni to $Ni(OH)_2$, leading to the more thermodynamically favored β-phase of $Ni(OH)_2$.

α-$Ni(OH)_2$ NPs formed via the direct approach, performed remarkably well in terms of the high specific activities for the MOR (~2.8 kA g^{-1}) and EOR (~3.7 kA g^{-1}), for 0.5 M of alcohol, compared to β-$Ni(OH)_2$ NPs for the MOR (~0.3 kA g^{-1}) and EOR (~0.4 kA g^{-1}) respectively. This difference was mainly attributed to the more disordered nature of α-$Ni(OH)_2$/γ-NiOOH, compared to β-$Ni(OH)_2$/β-NiOOH, leading to more ready ion-solvent intercalation during electrocatalysis in the former case. Furthermore, γ-NiOOH has a higher oxidation state than β-NiOOH which could make it more effective as a catalyst for electro-oxidation.

Finally, it is important to highlight the MCEM as approach to quickly screen electrocatalysts and that our studies have allowed the study of SWNT-$Ni(OH)_2$ nanostructured electrodes without any need for an additional support electrode so that the intrinsic activity of this novel composite is investigated without complications from a substrate electrode.

5.5 Reference

1 Ghenciu, A. F. Review of fuel processing catalysts for hydrogen production in PEM fuel cell systems. *Current opinion in solid state and materials science* **6**, 389-399 (2002).

2 Wang, J. and Musameh, M. Carbon nanotube/teflon composite electrochemical sensors and biosensors. *Analytical chemistry* **75**, 2075-2079 (2003).

3 Miller, T. S., Sansuk, S., E., S. P., Lai, S. C., Machperson, J. V., Unwin, P. R. Pt nanoparticle modified single walled carbon nanotube network electrodes for electrocatalysis: control of the specific surface area over three orders of magnitude. *Catalysis today* **244**, 136-145 (2015).

4 Li, Y., Gao, W., Ci, L., Wang, C. and Ajayan, P. M. Catalytic performance of Pt nanoparticles on reduced graphene oxide for methanol electro-oxidation. *Carbon* **48**, 1124-1130 (2010).

5 Gao, M., Sheng, W. C., Zhuang, Z. B., Fang, Q. R., Gu, S., Jiang, J., Yan, Y. S. Efficient water oxidation using nanostructured α-nickel-hydroxide as an electrocatalyst. *Journal of the American Chemical Society* **136**, 7077-7084 (2014).

6 Gong, M., Zhou, W., Tsai, Mon-Che, Zhou, J., Guan, M., Lin, M.-C., Zhang, B., Hu, Y., Wang, D.-Y., Yang, J., Pennycook, S. J., Hwang, B.-J., and Dai, H. Nanoscale nickel oxide/nickel heterostructures for active hydrogen evolution electrocatalysis. *Nature communications* **5**, 4695 (2014).

7 Li, H., Yu, M., Wang, F. X., Liu, P., Liang, Y., Xiao, J., Wang, C. X., Tong, Y. X., Yang and G. W. Amorphous nickel hydroxide nanospheres with ultrahigh capacitance and energy density as electrochemical pseudocapacitor materials. *Nature communications* **4**, 1894 (2013).

8 Mu, Y., Jia, D., He, Y., Miao, Y. and Wu, H.-L. Nano nickel oxide modified non-enzymatic glucose sensors with enhanced sensitivity through an electrochemical process strategy at high potential. *Biosensors and Bioelectronics* **26**, 2948-2952 (2011).

9 Casas-Cabanas, M., Canales-Vázquez, J., Rodríguez-Carvajal, J. and Palacín, M. R. Deciphering the structural transformations during nickel oxyhydroxide electrode operation. *Journal of the American Chemical Society* **129**, 5840-5842 (2007).

10 Liu, J., Chen, M., Zhang, L., Jiang, J., Yan, J., Huang, Y., Lin, J., Fan, H. J., Sen, Z. X. A flexible alkaline rechargeable Ni/Fe battery based on graphene foam/carbon nanotubes hybrid film. *Nano letters* **14**, 7180-7187 (2014).

11 Oliva, P., Leonardi, J., Laurent, J. F., Delmas, C., Branconnier, J. J., figlarz, M., Fievet, F., Dguibert, A. Review of the structure and the electrochemistry of nickel hydroxides and oxy-hydroxides. *Journal of Power sources* **8**, 229-255 (1982).

12 Hutton, L. A., Vidotti, M., Pate, A. N., Newton, M. E., Unwin, P. R. and Macpherson, J. V. Electrodeposition of nickel hydroxide nanoparticles on boron-doped diamond electrodes for oxidative electrocatalysis. *The Journal of Physical Chemistry C* **115**, 1649-1658 (2010).

13 Reim, R. E. and Van Effen, R. M. Determination of carbohydrates by liquid chromatography with oxidation at a nickel (III) oxide electrode. *Analytical Chemistry* **58**, 3203-3207 (1986).

14 Dai, W., Li, H., Li, M., Li, C., Wu, X., Yang, B. Electrochemical imprinted polycrystalline nickel–nickel oxide half-nanotube-modified boron-doped

diamond electrode for the detection of L-serine. *ACS applied materials & interfaces* **7**, 22858-22867 (2015).

15 Kraeutler, B. and Bard, A. J. Heterogeneous photocatalytic preparation of supported catalysts. Photodeposition of platinum on titanium dioxide powder and other substrates. *Journal of the American Chemical Society* **100**, 4317-4318 (1978).

16 Kleijn, S. E., Lai, S., Koper, M. and Unwin, P. R. Electrochemistry of nanoparticles. *Angewandte Chemie International Edition* **53**, 3558-3586 (2014).

17 Li, W., Liang, C., Zhou, W., Qiu, J., Zhou, Z., Sun, G., Xin, Q. Preparation and characterization of multiwalled carbon nanotube-supported platinum for cathode catalysts of direct methanol fuel cells. *The Journal of Physical Chemistry B* **107**, 6292-6299 (2003).

18 Mu, Y., Liang, H., Hu, J., Jiang, L. and Wan, L. Controllable Pt nanoparticle deposition on carbon nanotubes as an anode catalyst for direct methanol fuel cells. *The Journal of Physical Chemistry B* **109**, 22212-22216 (2005).

19 Corso, B. L., Perez, I., Sheps, T., Sims, P. C., Gül, O. T. and Collins, P. G. Electrochemical charge-transfer resistance in carbon nanotube composites. *Nano letters* **14**, 1329-1336 (2014).

20 Güell, A. G., Ebejer, N., Snowden, M. E., Mckelvey, K., Macpherson, J. V. and Unwin, P. R. Quantitative nanoscale visualization of heterogeneous electron transfer rates in 2D carbon nanotube networks. *Proceedings of the National Academy of Sciences* **109**, 11487-11492 (2012).

21 Heller, I., Kong, J., Heering, H. A., Williams, K. A., Lemay, S. G., Dekker, C. Individual single-walled carbon nanotubes as nanoelectrodes for electrochemistry. *Nano Letters* **5**, 137-142 (2005).

22 Kongkanand, A., Kuwabata, S., Girishkumar, G. and Kamat, P. Single-wall carbon nanotubes supported platinum nanoparticles with improved electrocatalytic activity for oxygen reduction reaction. *Langmuir* **22**, 2392-2396 (2006).

23 Joo, S. H., Choi, S. J., Oh, I., Kwak, J., Liu, Z., Terasaki, O., Ryoo, R. Ordered nanoporous arrays of carbon supporting high dispersions of platinum nanoparticles. *Nature* **412**, 169 (2001).

24 Zhou, X., Xia, Z., Zhang, Z., Ma, Y. and Qu, Y. One-step synthesis of multi-walled carbon nanotubes/ultra-thin Ni $(OH)_2$ nanoplate composite as efficient catalysts for water oxidation. *Journal of Materials Chemistry A* **2**, 11799-11806 (2014).

25 Yang, M., Yang, Y., Liu, Y., Shen, G. and Yu, R. Platinum nanoparticles-doped sol–gel/carbon nanotubes composite electrochemical sensors and biosensors. *Biosensors and Bioelectronics* **21**, 1125-1131 (2006).

26 Zhang, X., Zhang, B., Li, X.-D., Ma, L.-X. and Zhang, J.-W. Sonochemical synthesis of hollow Pt alloy nanostructures on carbon nanotubes with enhanced electrocatalytic activity for methanol oxidation reaction. *International Journal of Hydrogen Energy* **40**, 14416-14420 (2015).

27 Lu, Q., Gao, F. and Zhao, D. One-step synthesis and assembly of copper sulfide nanoparticles to nanowires, nanotubes, and nanovesicles by a simple organic amine-assisted hydrothermal process. *Nano Letters* **2**, 725-728 (2002).

28 Day, T. M., Unwin, P. R. and Macpherson, J. V. Factors controlling the electrodeposition of metal nanoparticles on pristine single walled carbon nanotubes. *Nano Letters* **7**, 51-57 (2007).

29 Miller, T. S., Macpherson, J. V. and Unwin, P. R. Dual-electrode measurements in a meniscus microcapillary electrochemical cell using a high aspect ratio

carbon fibre ultramicroelectrode. *Journal of Electroanalytical Chemistry* **729**, 80-86 (2014).

30 Shi, Z., Lian, Y., Zhou, X., Gu, Z., Zhang, Y., Iijima, S., Zhou, L., Yue, K. T., Zhang, S. Mass-production of single-wall carbon nanotubes by arc discharge method. *Carbon* **37**, 1449-1453 (1999).

31 Munoz, E., Maser, W. K., Benito, A. W., Marinez, M. T., De la Fuente, G. F., Maniette, Y., Righi, A., Anglaret, E. and Sauvajol, J. L. Gas and pressure effects on the production of single-walled carbon nanotubes by laser ablation. *Carbon* **38**, 1445-1451 (2000).

32 Huang, S., Woodson, M., Smalley, R. and Liu, J. Growth mechanism of oriented long single walled carbon nanotubes using "fast-heating" chemical vapor deposition process. *Nano Letters* **4**, 1025-1028 (2004).

33 Hiura, H., Ebbesen, T. W. and Tanigaki, K. Opening and purification of carbon nanotubes in high yields. *Advanced Materials* **7**, 275-276 (1995).

34 Pumera, M. Carbon nanotubes contain residual metal catalyst nanoparticles even after washing with nitric acid at elevated temperature because these metal nanoparticles are sheathed by several graphene sheets. *Langmuir* **23**, 6453-6458 (2007).

35 Rosca, I. D., Watari, F., Uo, M. and Akaska, T. Oxidation of multiwalled carbon nanotubes by nitric acid. *Carbon* **43**, 3124-3131 (2005).

36 Pumera, M. and Iwai, H. Multicomponent Metallic Impurities and Their Influence upon the Electrochemistry of Carbon Nanotubes. *Journal of Physical Chemistry C* **113**, 4401-4405 (2009).

37 Fan, Y. W., Goldsmith, B. R. and Collins, P. G. Identifying and counting point defects in carbon nanotubes. *Nature Materials* **4**, 906-911 (2005).

38 Dumitrescu, I., Wilson, N. R. and Macpherson, J. V. Functionalizing single-walled carbon nanotube networks: Effect on electrical and electrochemical properties. *Journal of Physical Chemistry C* **111**, 12944-12953 (2007).

39 Asgari, M., Maragheh, M. G., Davarkhah, R. and Lohrasbi, E. Methanol electrooxidation on the nickel oxide nanoparticles/multi-walled carbon nanotubes modified glassy carbon electrode prepared using pulsed electrodeposition. *Journal of The Electrochemical Society* **158**, K225-K229 (2011).

40 Xu, C., Sun, J. and Gao, L. Large scale synthesis of nickel oxide/multiwalled carbon nanotube composites by direct thermal decomposition and their lithium storage properties. *Journal of Power Sources* **196**, 5138-5142 (2011).

41 Hopper, M. and Ord, J. An optical study of the growth and oxidation of nickel hydroxide films. *Journal of the Electrochemical Society* **120**, 183-187 (1973).

42 Wolf, J., Yeh, L. R. and Damjanovic, A. Anodic oxide films at nickel electrodes in alkaline solutions—I. Kinetics of growth of the β-Ni $(OH)_2$ phase. *Electrochimica Acta* **26**, 409-416 (1981).

43 Deo, R. P., Lawrence, N. S. and Wang, J. Electrochemical detection of amino acids at carbon nanotube and nickel–carbon nanotube modified electrodes. *Analyst* **129**, 1076-1081 (2004).

44 Pickett, D. F. and Maloy, J. T. Microelectrode studies of electrochemically coprecipitated cobalt hydroxide in nickel hydroxide electrodes. *Journal of the Electrochemical Society* **125**, 1026-1032 (1978).

45 Corrigan, D. A. The catalysis of the oxygen evolution reaction by iron impurities in thin film nickel oxide electrodes. *Journal of the Electrochemical Society* **134**, 377-384 (1987).

46 Jayashree, R. and Kamath, P. V. Nickel hydroxide electrodeposition from nickel nitrate solutions: mechanistic studies. *Journal of Power Sources* **93**, 273-278 (2001).

47 Streinz, C. C., Hartman, A. P., Motupally, S. and Weidner, J. W. The effect of current and nickel nitrate concentration on the deposition of nickel hydroxide films. *Journal of The Electrochemical Society* **142**, 1084-1089 (1995).

48 Liao, S., Holmes, K.-A., Tsaprailis, H. and Birss, V. I. High performance PtRuIr catalysts supported on carbon nanotubes for the anodic oxidation of methanol. *Journal of the American Chemical Society* **128**, 3504-3505 (2006).

49 Luo, H., Shi, Z., Li, N., Gu, Z. and Zhuang, Q. Investigation of the electrochemical and electrocatalytic behavior of single-wall carbon nanotube film on a glassy carbon electrode. *Analytical Chemistry* **73**, 915-920 (2001).

50 Bertoncello, P., Edgeworth, J. P., Macpherson, J. V. and Unwin, P. R. Trace level cyclic voltammetry facilitated by single-walled carbon nanotube network electrodes. *Journal of the American Chemical Society* **129**, 10982-10983 (2007).

51 Zhang, G., Cuharuc, A. S., Güell, A. G. and Unwin, P. R. Electrochemistry at highly oriented pyrolytic graphite (HOPG): lower limit for the kinetics of outer-sphere redox processes and general implications for electron transfer models. *Physical Chemistry Chemical Physics* **17**, 11827-11838 (2015).

52 Cuharuc, A. S., Zhang, G. and Unwin, P. R. Electrochemistry of ferrocene derivatives on highly oriented pyrolytic graphite (HOPG): quantification and impacts of surface adsorption. *Physical Chemistry Chemical Physics* **18**, 4966-4977 (2016).

53 Portemer, F., Delahaye-Vidal, A. and Figlarz, M. Characterization of active material deposited at the nickel hydroxide electrode by electrochemical impregnation. *Journal of the Electrochemical Society* **139**, 671-678 (1992).

54 Dudin, P. V., Unwin, P. R. and Macpherson, J. V. Electrochemical nucleation and growth of gold nanoparticles on single-walled carbon nanotubes: New mechanistic insights. *The Journal of Physical Chemistry C* **114**, 13241-13248 (2010).

55 Zhang, G., Kirkman, P. M., Patel, A. N., Cuharuc, A. S., Mckelvey, K. and Unwin, P. R. Molecular functionalization of graphite surfaces: basal plane versus step edge electrochemical activity. *Journal of the American Chemical Society* **136**, 11444-11451 (2014).

56 Güell, A. G., Meadow, K. E., Dudin, P. V., Ebejer, N., Macpherson, J. V. and Unwin, P. R. Mapping nanoscale electrochemistry of individual single-walled carbon nanotubes. *Nano letters* **14**, 220-224 (2013).

57 Miller, T. S., Macpherson, J. V. and Unwin, P. R. Controlled functionalisation of single-walled carbon nanotube network electrodes for the enhanced voltammetric detection of dopamine. *Physical Chemistry Chemical Physics* **17**, 26394-26402 (2015).

58 Goldstein, J. I., Newbury, D. E., Echlin, P., Joy, D. C., Fiori, C., Lifshin and E. *Scanning electron microscopy and X-ray microanalysis*. (Springer, 2017).

59 Fantini, M. and Gorenstein, A. Electrochromic nickel hydroxide films on transparent/conducting substrates. *Solar Energy Materials* **16**, 487-500 (1987).

60 Lide, D. Handbook of chemistry and physics. CRC Press, Boca Raton, FL. *Handbook of chemistry and physics. 88th ed. CRC Press, Boca Raton, FL.*, - (2007).

61 Crank, J. *The Mathematics of Diffusion: 2d Ed*. (Clarendon Press, 1975).

62 Breiter, M. and Hoffmann, K. Bestimmung der Diffusionskoeffizienten D_{H2}, D_{H+} und D_{OH-} mit der Platinscheibenelektrode. *Berichte der Bunsengesellschaft für physikalische Chemie* **64**, 462-467 (1960).

63 Hall, D. S., Lockwood, D. J., Bock, C. and MacDougall, B. R. Nickel hydroxide and related materials: a review of their strucutres, synthesis and properties. *Proceedings of the Royal Society A* **471**, 20140792 (2015).

64 Song, Q., Tang, Z., Guo, H. and Chan, S. Structural characteristics of nickel hydroxide synthesized by a chemical precipitation route under different pH values. *Journal of Power Sources* **112**, 428-434 (2002).

65 McEwen, R. Crystallographic studies on nickel hydroxide and the higher nickel oxides. *The Journal of Physical Chemistry* **75**, 1782-1789 (1971).

66 Parks, E., Zhu, L., Ho, J. and Riley, S. The structure of small nickel clusters. II. Ni16–Ni28. *The Journal of chemical physics* **102**, 7377-7389 (1995).

67 Ayeb, A. and Notten, P. The oxygen evolution kinetics in sealed rechargeable NiMH batteries. *Electrochimica Acta* **53**, 5836-5847 (2008).

68 Cornilsen, B. C., Shan, X. and Loyselle, P. L. Structural comparison of nickel electrodes and precursor phases. *Journal of power sources* **29**, 453-466 (1990).

69 Kamath, P. V., Dixit, M., Indira, L., Shukla, A. K., Kumar, V. G. and Munichadraiah, N. Stabilized α-$Ni(OH)_2$ as Electrode Material for Alkaline Secondary Cells. *Journal of the Electrochemical Society* **141**, 2956-2959 (1994).

70 Kumar, V. G., Munichandraiah, N., Kamath, P. V. and Shukla, A. On the performance of stabilized α-nickel hydroxide as a nickel-positive electrode in alkaline storage batteries. *Journal of power sources* **56**, 111-114 (1995).

71 French, H. M., Henderson, M. J., Hillman, A. R. and Vieil, E. Ion and solvent transfer discrimination at a nickel hydroxide film exposed to LiOH by combined electrochemical quartz crystal microbalance (EQCM) and probe beam deflection (PBD) techniques. *Journal of Electroanalytical Chemistry* **500**, 192-207 (2001).

72 Maiyalagan, T. and Scott, K. Performance of carbon nanofiber supported Pd–Ni catalysts for electro-oxidation of ethanol in alkaline medium. *Journal of Power Sources* **195**, 5246-5251 (2010).

73 McBreen, J. Nickel hydroxides. in *Handbook of Battery Materials* (Wiley-VCH Verlag GmbH & Co. KGaA, 2011).

74 Ma, Y., Li, H., Wang, H., Mao, X., Linkov, V., Ji, S., Gcilitshana, O. U., Wang, R. Evolution of the electrocatalytic activity of carbon-supported amorphous platinum–ruthenium–nickel–phosphorous nanoparticles for methanol oxidation. *Journal of Power Sources* **268**, 498-507 (2014).

75 Ye, L., Li, Z., Zhang, L., Lei, F. and Lin, S. A green one-pot synthesis of Pt/TiO2/Graphene composites and its electro-photo-synergistic catalytic properties for methanol oxidation. *Journal of Colloid Interface Science* **433**, 156-162 (2014).

76 Fu, G.-T., Ma, R.-G., Gao, X.-Q., Chen, Y., Tang, Y.-W., Lu, T.-H., Lee, J.-M. Hydrothermal synthesis of Pt-Ag alloy nano-octahedra and their enhanced electrocatalytic activity for the methanol oxidation reaction. *Nanoscale* **6**, 12310-12314 (2014).

77 Chen, D. J., Sun, S. G. and Tong, Y. Y. J. On the chemistry of activation of a commercial carbon-supported PtRu electrocatalyst for the methanol oxidation reaction. *Chemical Communications* **50**, 12963-12965 (2014).

78 Li, L., Chen, M., Huang, G., Yang, N., Zhang, L., Wang, H., Liu, Y., Wang, W., Gao, J. A green method to prepare Pd-Ag nanoparticles supported on reduced graphene oxide and their electrochemical catalysis of methanol and ethanol oxidation. *J. Power Sources* **263**, 13-21 (2014).

79 Sieben, J. M., Alvarez, A. E., Comignani, V. and Duarte, M. M. E. Methanol and ethanol oxidation on carbon supported nanostructured Cu core Pt-Pd shell electrocatalysts synthesized via redox displacement. *International. Journel of Hydrogen Energy* **39**, 11547-11556 (2014).

80 Zhu, F., Ma, G., Bai, Z., Hang, R., Tang, B., Zhang, Z., Wang, X. High activity of carbon nanotubes supported binary and ternary Pd-based catalysts for methanol, ethanol and formic acid electro-oxidation. *J. Power Sources* **242**, 610-620 (2013).

Chapter 6. Metal Support Effects in Electrocatalysis at Hexagonal Boron Nitride

Efficient evolution of hydrogen through electrochemical water splitting holds tremendous promise for green energy project in the future, which will ultimately serve as the replacement of traditional fossil fuels. Hydrogen evolution can be easily achieved by employing expensive noble metals (Pt), while it is still challenging to develop highly active catalysts based on materials that are more abundant at lower prices. Very recently, as low cost and highly stable two-dimensional material, hexagonal boron nitride (h-BN) has attracted much attention in electrocatalysis. A scanning electrochemical droplet cell technique has been employed to screen the intrinsic electrocatalytic hydrogen evolution reaction (HER) activity of hexagonal boron nitride (h-BN) nanosheets supported on different metal substrates (Cu and Au). Local (spatially-resolved) voltammetry and Tafel analysis reveals that electronic interaction with the underlying metal substrate plays a significant role in modulating the electrocatalytic activity of h-BN, with Au-supported h-BN exhibiting significantly enhanced HER charge-transfer kinetics (exchange current is *ca.* two orders of magnitude larger) compared to Cu-supported h-BN.

6.1 Introduction

Electrochemical water splitting is widely recognized as the most sustainable method for generating hydrogen (H_2), a fuel that is in growing demand[1] for use in green energy technologies (*e.g.*, fuel cells) as the world moves towards a decarbonized future.[2] Noble metal based materials (*e.g.*, Pt) are the most efficient HER electrocatalysts in aqueous acid media, with fast reaction kinetics resulting in low overpotentials.[3] However, due to the high cost and relative scarcity of these materials, there is an ongoing search for cheap, earth-abundant HER electrocatalysts, for example, two-dimensional (2D) materials such as transition metal dichalcogenides,[4] carbon nitride,[5] and sandwich structures based on 2D crystals,[6] which in recent years have shown great promise, with certain classes exhibiting considerable catalytic activity and high (electro)chemical stability.[7] Although it is intrinsically insulating (*i.e.*, band gap of 3.6 to 7.1 eV),[8] hexagonal boron nitride (h-BN) has attracted considerable attention in oxygen reduction reaction (ORR)[9,10] and hydrogen evolution reaction (HER) catalysis.[11] This is because the band gap of

monolayer h-BN can be considerably reduced by introducing defects such as B/N vacancies and impurities,[12] and tuned to an extent through decoration with hydrogen atoms.[13] Moreover, as electron tunnelling through ultrathin h-BN layers is possible,[14] electronic interaction with the underlying metal support substrate (*i.e.*, through mixing of the d_z^2 metal orbitals with the N-p_z and B-p_z orbitals of h-BN) can tune electrochemical (electrocatalytic) activity.[15]

In this study, we explore the tunable electronic properties of h-BN in the context of (electro)catalysis by considering the HER activity of as-grown h-BN nanosheets supported on Cu (denoted as h-BN/Cu) and Au (denoted as h-BN/Au) substrates. The intrinsic electrocatalytic properties of h-BN has been probed using scanning electrochemical microscopy (SECCM, see Figure 1a),[16,17] a scanning droplet cell technique that allows characteristic surface sites to be targeted and electrochemically characterized at the 'single-entity' level.[16-18] SECCM has been deployed in the voltammetric hopping mode,[18-20] where the droplet (meniscus) cell formed at the end of an electrolyte-filled (0.1 M $HClO_4$, herein) nanopipette (tip diameter, d_t = 150 to 300 nm, herein) is approached to (contacted with) the sample (working electrode) surface sequentially at a series of predefined locations, and upon each landing a spatially-resolved linear-sweep voltammogram (LSV) is recorded. In other words, in a single SECCM experiment, thousands of spatially-independent nano-electrochemical cells are formed, with the probed area defined by the footprint of the meniscus (droplet) cell, allowing the HER activity of individual h-BN nanosheets to be compared and visualized directly, providing new insights into the catalytic properties of these promising non-precious metal electrocatalysts.

6.2 Materials and methodology

6.2.1 Chemicals and materials

Copper (Cu) foil was purchased from Alfa Aesar (purity 99.8 %, 0.025 mm thick). Perchloric acid ($HClO_4$, 70%) and ammonia borane (NH_3-BH_3, 97%) were purchased from Sima-Aldrich and used as received. All aqueous solutions were prepared from ultrapure water (18.2 MΩ cm resistivity at 25 °C) produced by a Purite Integra HP system (U.K.). The silver/silver chloride (Ag/AgCl) quasi reference counter electrode (QRCE) was prepared by anodic polarization of an Ag wire (0.125 mm diameter, Goodfellow, 99.99 %) in saturated KCl solution. The QRCE potential was calibrated

against a commercial saturated calomel electrode (SCE) in 0.1 M $HClO_4$ solution after each experiment, and was found to possess a stable potential1 of ca. 0.21 V vs. SCE.

6.2.2 h-BN electrodes preparation

Hexagonal boron nitride (h-BN) was grown on polycrystalline Cu foils by the atmospheric pressure CVD method.[21] In order to achieve this, the Cu foil was first chemically polished using a solution of 0.4 M $FeCl_3$ in 0.8 M HCl. After drying with compressed N_2 gas, the polished foil was loaded into the centre of a 25 mm diameter tube furnace, before being pumped to a pressure of 15 mTorr. After pre-annealing at 1015 °C for 30 min with a mixture gas of 16 standard cubic centimeters (sccm) of H_2 (99.99 %) and 260 sccm of Ar (99.99%), 1 mg ammonia borane was placed in a specially designed boat and loaded in the upstream of the CVD growth tube as the precursor of h-BN. The precursor temperature was controlled by a heating belt around the tube, separated from the heating zone of the furnace. The growth of h-BN was achieved in 60 min at 1065 °C. After growth, the system was quickly cooled down to <200 °C under the same gas flow. The rear surface of the sample was fixed to an evaporated Au (300 nm) film on Si/SiO_2 wafer by using silver paint (Agar Scientific, Ltd, U.K.). The whole sample was then connected to a copper wire for subsequent electrochemical measurements.

For preparing the transferred h-BN/Au substrate using polymethyl-methacrylate (PMMA) method,[22] the as-grown h-BN on Cu foil was spin-coated with PMMA (AR-P. 679.04, ALLRESIST, GmbH) at 4000 rpm for 50 s. The Cu foil was then etched away by floating on the surface of an aqueous solution of 0.4 M $FeCl_3$ for 5 h. After that, the PMMA film was washed with deionized water and placed on the target substrate, which consisted of an evaporated Au film (*ca.* 300 nm thick) on SiO_2/Si. The PMMA film on the target substrate was then heated to 150 °C to remove any adventitious water, as well as promote good adhesion of the PMMA to the target substrate (Au on SiO_2/Si). Following this, the PMMA film was removed by dissolving in acetone and the substrate was subsequently annealed under nitrogen gas at 350 °C for 5 min. Similar to above, the sample was connected to a copper wire for electrochemical characterization. After scanning (see below), the h-BN/Cu and h-BN/Au substrates were imaged using a ZEISS GEMINI 500 FE-SEM, at 2 keV with the InLens mode.

6.2.3 Fabrication and characterization of nanopipettes

Single-barrel nanopipettes were pulled from glass capillaries (GC120F-10, Friedrich & Dimmock, Inc, U.S.A., with filament) using a P-2000 laser puller (Sutter Instruments, USA) with a two-step protocol. For the first step, the parameters were heat 330, filament 3, velocity 30 and delay 220. For the second step, the parameters were heat 350, filament 3, velocity 40, delay 180 and pull 120. The dimensions of the nanopipette orifice were measured using field emission scanning electron microscopy (FE-SEM) on a Zeiss Supra 55VP system, which was operated at an accelerating voltage of 2 kV. After fabrication, the nanopipette probes were back filled with 0.1 M $HClO_4$ solution and a layer of silicone oil (DC 200, Fluka) sequentially using a MicroFil syringe (World Precision Instrument Inc., U.S.A.), before inserting the Ag/AgCl QRCE (detailed above) for electrochemical measurement.

6.2.4 SECCM setup and electrochemical measurements

The instrumental setup of single-barrel SECCM has previously been reported[18] and is shown in Figure 6.1. During operation, the prepared nanopipette probe (detailed above) was mounted on a *z*-piezoelectric positioner (P-753.3CD, Physik Instrumente), and the substrate (*i.e.*, h-BN/Cu or h-BN/Au) was mounted on an *xy*-piezoelectric positioner (P-622.2CD, Physik Instrumente). SECCM was operated in the voltammetric hopping mode, as previously reported.[20] In this mode, the nanopipette probe is approached to the surface of interest at a series of pre-defined locations in a grid. During *z*-approach, contact between the meniscus (droplet) cell located at the end of the nanopipette probe and substrate surface (note that the nanopipette itself did not make contact) was detected through surface current (i_{surf}) feedback, using a threshold current of 1 pA herein. Upon each landing, a linear-sweep voltammogram (LSV) measurement was carried out at a voltammetric scan rate (v) of 1 V/s. After each measurement, the nanopipette probe was retracted and moved laterally (*i.e.*, in *xy* space) to the next point that was located at a pre-defined distance away ('hopping distance', equal to 500 nm herein), where the same procedure was implemented. The potential applied ($-E_{app}$) to the QRCE (with respect to the ground) was controlled, and h-BN sample (working electrode, ground) current, namely i_{surf}, was detected. The current was measured every 4 μs, which was averaged 513 times to give a data acquisition rate of 2052 μs per point. The current signal was filtered using an 8th order low-pass filter at a time constant of 2 ms.

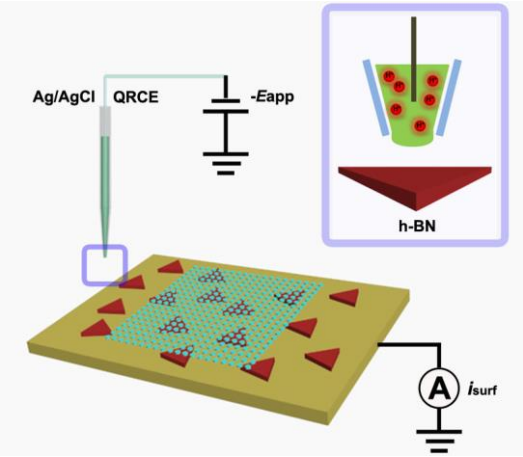

Figure 6.1: Schematic showing the electrochemical measurements performed on h-BN using SECCM. On the right is an enlarged diagram of the probed h-BN interface during a single 'hop' of a scanning experiment.

To perform LSV measurements using SECCM in the absence of air, the nanopipette tip and h-BN/Cu sample were placed in an environmental chamber that was constantly purged with humidified argon gas, as previously reported.[23,24]

Data acquisition and fine control of all the instruments were obtained by using an FPGA card (PCIe-7852R) controlled by a LabVIEW 2016 (National Instrument, U.S.A.) interface running the Warwick Electrochemical Scanning Probe Microscopy (WEC-SPM, www.warwick.ac.uk/electrochemistry) software. After collection, the raw data were processed with Matlab R2015b and OriginPro 2016 software packages.

6.3 Results and discussion

6.3.1 h-BN samples characterization

As detailed in the experimental section, the h-BN nanosheets were grown on polycrystalline Cu foils (h-BN/Cu) by an atmospheric pressure chemical vapour deposition (CVD) method.[21] The as-grown h-BN was subsequently transferred onto the Au substrate (h-BN/Au) by the polymethyl-methacrylate (PMMA) method.[22] The morphologies of as-grown h-BN/Cu and transferred h-BN/Au were observed directly by field emission scanning electron microscopy (FE-SEM), as depicted in Figure 6.2a and 6.2b. Considering Figure 6.2a, the h-BN nanosheets are triangular in shape and show a much darker contrast compared than the underlying Cu support, with sizes ranging from *ca.* 5 to 12 μm, in agreement with previous reports.[25] It should be noted that the white particles on the h-BN/Cu surface are comprised of borazine, arising from the

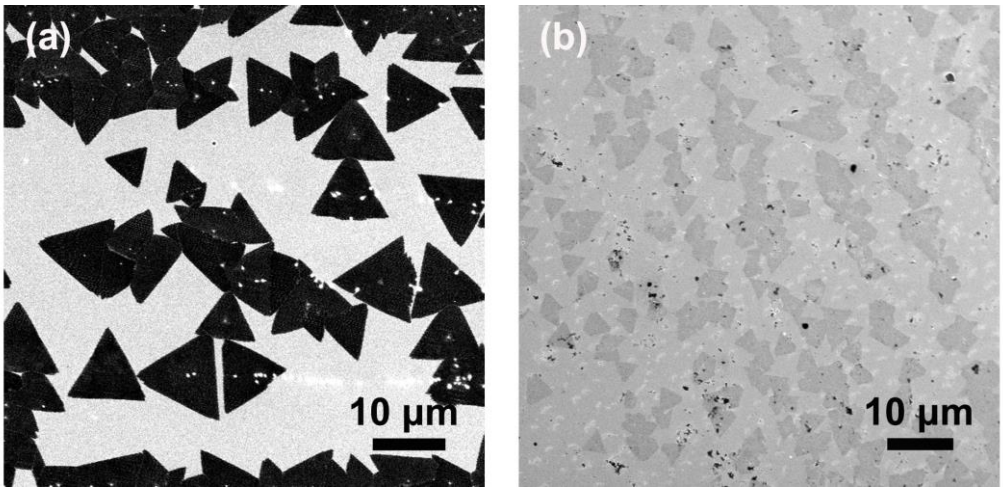

Figure 6.2: FE-SEM image of as-grown h-BN/Cu (a) and transferred h-BN/Au (b).

decomposition of the ammonium borane precursors.[26] Considering Figure 6.2b, the morphology of transferred h-BN/Au is quite similar with that of h-BN/Cu, with h-BN nanosheets (dark regions in Figure 6.2b) of approximately *ca.* 5 μm in size dispersed on the underlying Au support (light regions in Figure 6.2b).

6.3.2 HER at as-grown h-BN/Cu

In acidic solution, HER is postulated to be a two-electron process and three possible elemental reaction steps have been proposed. The first step is a primary discharge step (Volmer reaction):

$$H_3O^+ + e^- \rightarrow H_{ads} + H_2O \quad (6.1)$$

where the H_{ads} denotes a hydrogen atom adsorbed on the surface. Following the formation of H_{ads} on the active sites, H_2 is formed either by the electrochemical desorption step (Heyrovsky reaction):

$$H_{ads} + H_3O^+ + e^- \rightarrow H_2 + H_2O \quad (6.2)$$

or recombination step (Tafel reaction):

$$H_{ads} + H_{ads} \rightarrow H_2 \quad (6.3)$$

Energetics of the intermediate state (H_{ads}) play an important role in determining the HER rate. The famous "volcano" relations between rate, or exchange current density of HER and various forms of interaction between electrode and hydrogen were demonstrated.[27-29] The Gibbs free-energy of the intermediate state, $\Delta G_{H(a)}$, has been considered as a major descriptor of the HER activity for a wide variety of catalysts. It is known that an ideal HER catalysts should possess a thermoneutral free energy of adsorbed atomic hydrogen, that is, $\Delta G_{H(a)} \approx 0$.

The electrocatalytic activity of h-BN/Cu towards the HER was screened using voltammetric SECCM, where hundreds of local (spatial resolution or 'hopping distance' of 500 nm) LSV measurements were performed with a nanopipette probe of $d_t \approx 300$ nm (see Figure 6.3a). Note that the ORR was found to make a negligible contribution to the electrocatalytic current measured on the basal surface of h-BN/Cu during cathodic polarization, revealed by performing point measurements in an environmental chamber under an inert (argon) atmosphere (*i.e.*, in the presence and absence of air),[23,24] as explored in Figure 6.4. For this reason, all SECCM experiments were carried out without environmental control (*i.e.*, in the presence of air), and the electrocatalytic current can be attributed to the HER alone. An FE-SEM image of the area scanned with SECCM is shown in Figure 6.5a; the individual droplet 'footprints' are visible on the h-BN surface (light regions), as are exposed regions of the underlying Cu support (dark regions with sharp outlines). Representative LSVs, taken from 45 points across the h-BN surface and normalized by the area of individual footprints (Figure 6.5a), as well as the average LSV recorded from all points on the surface of the h-BN nanosheets (684 individual measurements) are shown in Figure 6.5b. The LSVs measured at h-BN/Cu are highly reproducible, reflected in the histogram constructed from the current density (j)

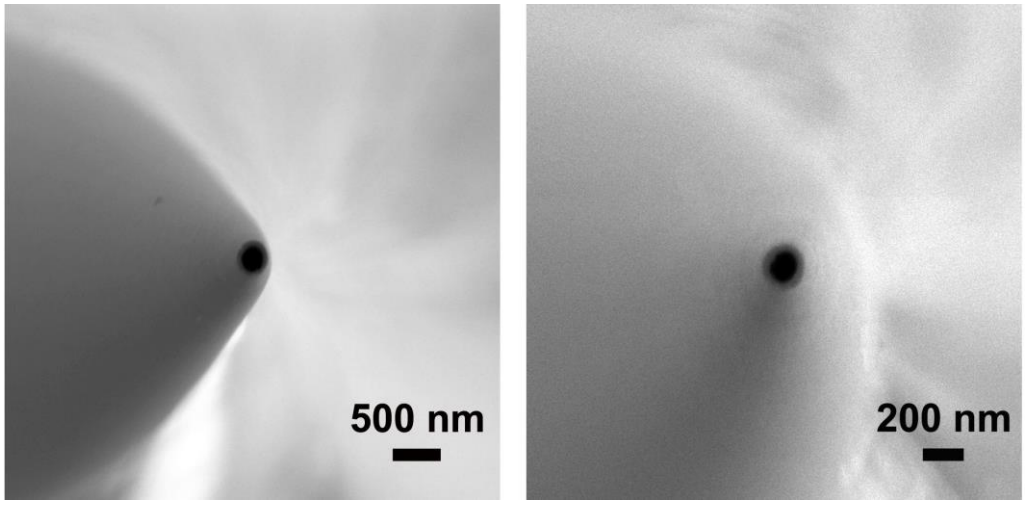

Figure 6.3: Representative FE-SEM images of the end (tip) of single-barrel nanopipettes used in experiments on the (a) h-BN/Cu and (b) h-BN/Au substrates.

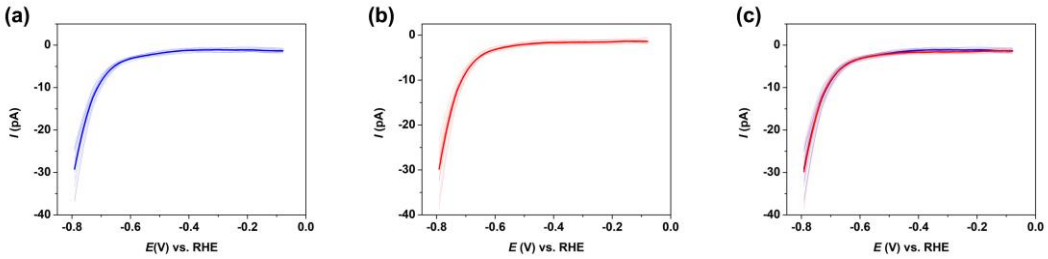

Figure 6.4: Typical LSVs at the surface of h-BN/Cu obtained from the (a) 12 points (transparent blue) in the presence of air and representative average LSV (blue), and (b) 12 points (transparent red) in the environmental chamber (i.e., absence of air) and representative average LSV (red). (c) HER activity comparison between the average LSVs obtained in the presence (blue) and absence (red) of air. Note that all measurements were performed with the same probe. These LSVs were obtained from a 0.1 M $HClO_4$ solution at a voltammetric scan rate (v) of 1 V s^{-1}.

measured at -0.688 V *vs.* the reversible hydrogen electrode (RHE), shown in Figure 6.5c, which is Gaussian in shape ($N = 684$), with a peak (mean) value of 10 (± 2) mA cm^{-2}.

The overpotential (η) required to achieve a j of 20 mA cm^{-2} (termed η_{20}) at h-BN/Cu is *ca.* 0.77 V, indicating that the HER is kinetically sluggish on this material (The HER activity of Cu substrate is much more active, see Figure 6.6a). Although this value is much larger than literature values for HER nanocatalysts such as metallic WS_2 nanosheets on graphite[30] and nanocrystalline MoS_2 on Au,[4] such measurements were performed exclusively by bulk (macroscopic) measurements on ensembles of material, where the number (*i.e.*, surface area) and type (*i.e.*, basal plane vs. edge plane) of exposed surface site is not known, making normalization to the true electrochemical surface area (ECSA) impossible. This is an important advantage of SECCM over macroscopic (bulk) voltammetry, as particular surface sites can be targeted (*i.e.*, the basal surface of h-BN), with the exposed surface area accurately known from the droplet 'footprint' (Figure 6.5a), allowing the true intrinsic catalytic activity to be extracted by semi-quantitative Tafel analysis (*vide infra*).[19] In any case, it is worth noting that the η_{20} value measured at h-BN/Cu (0.77 V) is much lower than the reported value of a boron nitride modified graphite electrode (1.15 V),[31] indicating the underlying Cu substrate can promote the HER performance of h-BN, which is usually considered to be an insulator.

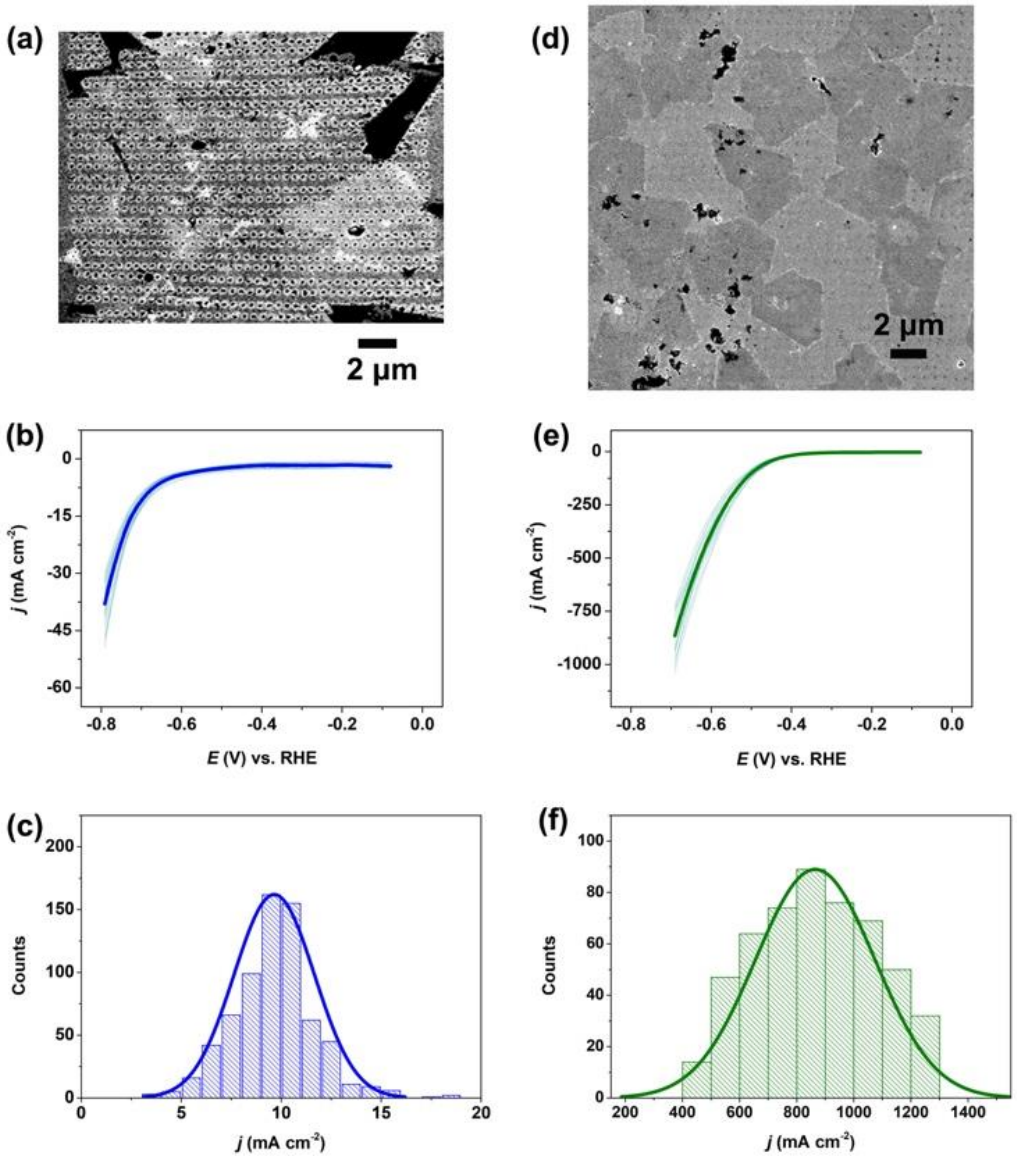

Figure 6.5: (a) FE-SEM image of an area of the h-BN/Cu scanned using SECCM (individual droplet footprints are visible). (b) Representative LSVs (transparent) obtained from 45 points across the surface of h-BN/Cu and average LSV (blue) obtained from all points on h-BN/Cu (684 individual measurements). (c) Histogram (N = 684) showing the distribution in j values measured at the surface of h-BN/Cu at an applied potential of -0.688 V *vs.* RHE. (d) FE-SEM image of an area of the h-BN/Au scanned using SECCM (individual droplet footprints are visible). (e) Representative LSVs (transparent) obtained from 35 points across the surface of h-BN/Au and average LSV (green) obtained from all points on h-BN/Au (515 individual measurements). (f) Histogram (N = 515) showing the distribution in j values measured at the surface of h-BN/Au at an applied potential of -0.688 V *vs.* RHE. All LSVs were obtained from a 0.1 M $HClO_4$ solution at a voltammetric scan rate (v) of 1 V s^{-1}.

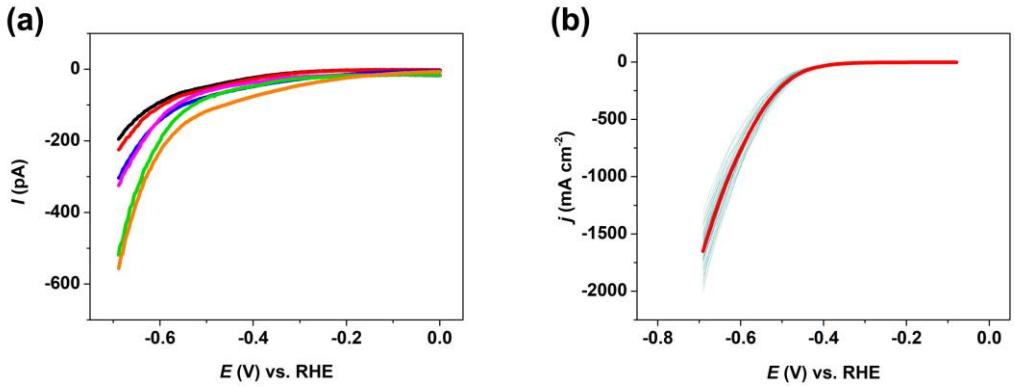

Figure 6.6: Representative linear sweep voltammograms (LSVs) obtained the (a) Cu and (b) Au support substrates during SECCM. Also shown in (b) is an average LSV (red trace) obtained from all points on exposed Au. These LSVs were obtained from a 0.1 M $HClO_4$ solution at a voltammetric scan rate (ν) of 1 V s^{-1}.

6.3.3 HER at transferred h-BN/Au

The electrocatalytic activity of h-BN/Au towards the HER was also screened using voltammetric SECCM ($d_t \approx 150$ nm, see Figure 6.3b); an FE-SEM image of the scan area is shown in Figure 6.5d. The dark regions represent the surface of the individual h-BN nanosheets, while the light regions correspond to exposed Au substrate (droplet 'footprints' also seen in the image). Representative LSVs, taken from 45 points across the surface of the h-BN nanosheets, as well as the average LSV recorded from all points on the surface of h-BN/Au (515 individual measurements) are shown in Figure 6.5e. Evidently, the electrocatalytic activity of h-BN/Au for the HER is much higher than that of h-BN/Cu (albeit, still lower than the underlying Au support, see Figure 6.6b), with an η_{20} value of 0.47 V for the former, compared to 0.77 V for the latter (*vide supra*). This is also reflected in the histogram constructed from the *j* values measured on h-BN/Au at -0.688 V *vs.* RHE, shown in Figure 6.5f, which is Gaussian in shape ($N = 515$), with a peak (mean) value of 900 (± 200) mA cm^{-2}, approximately two orders of magnitude larger than that measured at h-BN/Cu. These results unequivocally demonstrate that interaction with the underlying metal support can have a significant effect on the electronic properties of h-BN, evident from the vastly different HER catalytic activities measured when supported on Au and Cu.

6.3.4 Tafel slope and exchange current comparison

A direct comparison of the average area normalized LSVs measured on h-BN/Cu, h-BN/Au and the Au substrate is shown in Figure 6.7a. Evidently, while the measured *j* at

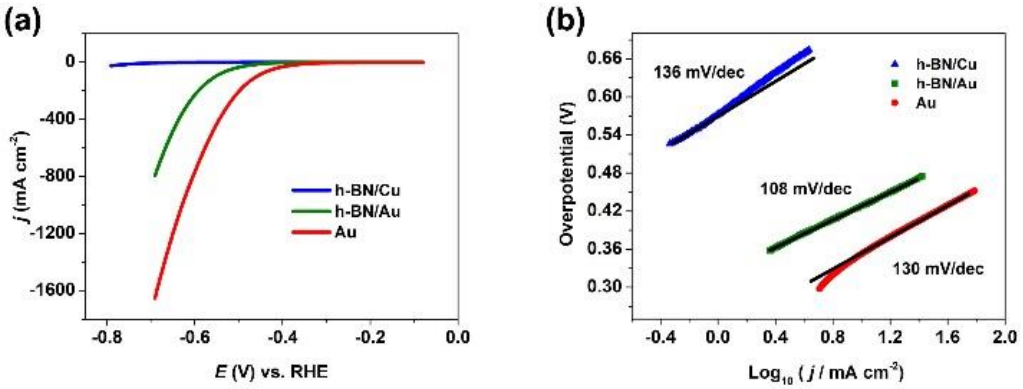

Figure 6.7: LSVs (area normalized) and (b) corresponding Tafel plots obtained from the HER on h-BN/Cu (blue curve), h-BN/Au (green curve) and Au substrate (red curve). These data were obtained from a 0.1 M $HClO_4$ solution at ν = 1 V s^{-1}. Linear least-squares fit (black traces, slope indicated on plot) are also shown in (b).

a given potential is *ca.* 2 orders of magnitude larger on h-BN/Au compared to h-BN/Cu (*e.g.*, j = 10 and 900 mA cm^{-2} at -0.688 V vs. RHE on h-BN/Cu and h-BN/Au, respectively), the former material is still less active than underlying Au substrate (*i.e.*, j ≈ 1600 mA cm^{-2} at 0.688 V *vs.* RHE on Au). This was confirmed by semi-quantitative Tafel analysis, which η was plotted against $log_{10}(j)$. As shown in Figure 6.7b. the value of all materials possess similar Tafel slopes of *ca.* 120 mV per decade (136, 108 and 130 mV per decade at h-BN/Cu, h-BN/Au and Au, respectively), which is consistent with rate determining step being the initial discharge of H^+ at the electrode surface (termed the Volmer step in the classical Volmer-Tafel-Heyrovsky mechanism of hydrogen evolution), although this conclusion should be treated *cum grano salis*, as the specific mechanism of the HER cannot be unambiguously determined from the Tafel slope alone.[19]

The exchange current density (j_0), was estimated directly by extrapolation of the linear Tafel region and the data for the point of intersection on the *x*-axis was extracted (η=0). The j_0 value reflects the relative catalytic activity of the materials, with values of *ca.* 4 × 10^{-8} A cm^{-2}, 1 × 10^{-6} A cm^{-2}, and 4 × 10^{-6} A cm^{-2} measured at h-BN/Cu, h-BN/Au and Au, respectively. As noted above, making a meaningful comparison between these data and literature data on h-BN is difficult, as the quantity and type of exposed surface site is often not known in macroscopic ensemble-type studies. Nevertheless, the Tafel slope and j_0 values measured in this study are far less favourable (in the catalytic sense) compared to those previously measured at macroscopic h-BN/Au ensembles, where optimal values of *ca.* 30 mV per decade and 4.6 × 10^{-5} A cm^{-2}, respectively were

reported.[11] This suggests that the edges of h-BN, which would be exposed in the bulk measurements (as in Ref 11) but not the local ones (as carried out here), are likely to be predominantly responsible for the observed macroscopic activity in h-BN/Au ensembles. In any case, the j_0 of h-BN/Au is orders of magnitude lower than polycrystalline Pt (j_0 = 3×10^{-3} A cm^{-2}),[32] but is comparable to that measured on the basal plane of bulk (natural crystal) MoS_2 ($j_0 = 2.5 \times 10^{-6}$ A cm^{-2})[19] and a monolayer MoS_2 film supported on glassy carbon ($j_0 = 1.1 \times 10^{-6}$ A cm^{-2}).[33]

6.3.5 Effect of underlying metal substrate

As a wide band gap semiconductor, h-BN in its native form is assumed to be electrochemically (and electrocatalytically) inert.[34] In this study, h-BN supported on either Cu or Au substrates exhibits moderate catalytic activity towards the HER, with the enhancement effect of Au being much more pronounced than that of Cu. From this, we conclude that the substrate-dependent HER activity of h-BN is attributable to the interaction with the underlying metal support. As alluded to above, it has been reported that the strength of chemical bonding at the interface of h-BN and transition metal substrates is determined mainly by the strength of the d and π orbital hybridization.[35,36] On Cu(111), h-BN has previously been shown to be only weakly chemisorbed,[37] evidenced by scanning tunneling microscopy and spectroscopy experiments.[38] On the other hand, theoretical calculations have predicted a perturbation of the electronic states of h-BN when interacting with an Au substrate.[9] This is consistent with the fact that various forms of BN (nanotubes, nanosheets and sputter deposited BN) have been shown to the significantly lower the overpotential associated with ORR at Au substrates, but have either no or a hindering effect at glassy carbon and Pt electrodes, respectively.[39] It is generally accepted that the ideal HER electrocatalyst should possess a near thermoneutral free energy of adsorbed atomic hydrogen, that is, $\Delta G_{H^*} \approx 0$ eV.[40] We postulate that the significantly different HER activities of h-BN/Cu and h-BN/Au likely arises from different ΔG_{H^*} values at these two substrates. In other words, electronic coupling of h-BN and Au might result in more optimal adsorption-desorption processes (*i.e.*, $\Delta G_{H^*} \rightarrow 0$), greatly facilitating the HER. On this basis, we propose that further theoretical studies of metal-support effects on ΔG_{H^*} at h-BN at could be very interesting and usefully aid understanding in HER electrocatalysis.

6.4 Conclusions

In summary, SECCM has been employed to screen the electrochemical activity (*i.e.*, HER electrocatalysis) of h-BN supported on Cu and Au substrates. Local voltammetric measurements revealed that the HER charge-transfer kinetics are *ca.* two orders of magnitude larger at the basal surface of h-BN when it is supported at Au (*i.e.*, h-BN/Au) compared to Cu (*i.e.*, h-BN/Cu). This significant enhancement was attributed to differences in the substrate effect between h-BN and Au/Cu, opening up the possibility of tuning reactivity (*e.g.*, catalytic activity) through the underlying metal support. Overall, these findings pave the way towards rational design of h-BN based electromaterials, with the ultimate goal being the replacement of noble metals with inexpensive and (electro)chemically stable metal-free counterparts in HER electrocatalysis.

6.5 References

1 Jiao, Y., Zheng, Y., Jaroniec, M. and Qiao, S. Z. Design of electrocatalysts for oxygen-and hydrogen-involving energy conversion reactions. *Chemical Society Reviews* **44**, 2060-2086 (2015).

2 Gasteiger, H. A. and Marković, N. M. Just a dream—or future reality? *science* **324**, 48-49 (2009).

3 Li, Q., Wu. L., Wu, G., Su, D., Lv, H., Zhang, S., Zhu, W., Casimir, A., Zhu, H., Mendoza-Garcia, A. and Sun, S. New approach to fully ordered fct-FePt nanoparticles for much enhanced electrocatalysis in acid. *Nano letters* **15**, 2468-2473 (2015).

4 Jaramillo, T. F., Jørgensen, K. P., Bonde, J., Nielsen, J. H., Horch, S., Chorkendorff, I. Identification of active edge sites for electrochemical H_2 evolution from MoS_2 nanocatalysts. *science* **317**, 100-102 (2007).

5 Zheng, Y., Jiao, Y., Zhu, Y., Li, L., Han, Y., Chen, Y., Du, A., Jaroniec, M., Qiao. Hydrogen evolution by a metal-free electrocatalyst. *Nature communications* **5**, 3783 (2014).

6 Yang, J., Voiry, D., Ahn, S., Kang, D., Kim, A., Chhowalla, M. and Shin, H. Two-dimensional hybrid nanosheets of tungsten disulfide and reduced graphene oxide as catalysts for enhanced hydrogen evolution. *Angewandte Chemie* **125**, 13996-13999 (2013).

7 Deng, D., Novoselov, K. S., Fu, Q., Zheng, N., Tian, Z. and Bao, X. Catalysis with two-dimensional materials and their heterostructures. *Nature nanotechnology* **11**, 218 (2016).

8 Solozhenko, V., Lazarenko, A., Petitet, J.-P. and Kanaev, A. Bandgap energy of graphite-like hexagonal boron nitride. *Journal of Physics and Chemistry of Solids* **62**, 1331-1334 (2001).

9 Uosaki, K., Elumalai, G., Noguchi, H., Masuda, T., Lyalin, A., Nakayama, A. and Taketsugu, T. Boron nitride nanosheet on gold as an electrocatalyst for oxygen reduction reaction: Theoretical suggestion and experimental proof. *Journal of the American Chemical Society* **136**, 6542-6545 (2014).

10 Koitz, R., Nørskov, J. K. and Studt, F. A systematic study of metal-supported boron nitride materials for the oxygen reduction reaction. *Physical Chemistry Chemical Physics* **17**, 12722-12727 (2015).

11 Uosaki, K., Elumalai, G., Dinh, H., Lyalin, A., Taketsugu, T. and Noguch, H. Highly efficient electrochemical hydrogen evolution reaction at insulating boron nitride nanosheet on inert gold substrate. *Scientific reports* **6**, 32217 (2016).

12 Azevedo, S., Kaschny, J., De Castilho, C. and de Brito Mota, F. Electronic structure of defects in a boron nitride monolayer. *The European Physical Journal B* **67**, 507-512 (2009).

13 Zhou, J., Wang, Q., Sun, Q. and Jena, P. Electronic and magnetic properties of a BN sheet decorated with hydrogen and fluorine. *Physical Review B* **81**, 085442 (2010).

14 Britnell, L., Gorbachev, R. V., Jalil, R., Belle, B. D., Schedin, F., Katsnelson, M. I., Morozov, S. V., Mayorov, A. S., Peres, N. R., Neto, A. C., Leist, J., Geim, A. K., Ponomarenko, L. A. and Novoselov, K. S. Electron tunneling through ultrathin boron nitride crystalline barriers. *Nano letters* **12**, 1707-1710 (2012).

15 Gao, M., Lyalin, A. and Taketsugu, T. Oxygen activation and dissociation on h-BN supported Au atoms. *International Journal of Quantum Chemistry* **113**, 443-452 (2013).

16 Ebejer, N., Güell, A. G., Lai, S. S., Mckelvey, K., Snowden, M. E. and Unwin, P. R. *Annual Review of Analytical Chemistry* **6**, 329-351 (2013).
17 Bentley, C. L., Kang, M. and Unwin, P. R. Scanning electrochemical cell microscopy: New perspectives on electrode processes in action. *Current Opinion in Electrochemistry* **6**, 23-30 (2017).
18 Bentley, C. L., Kang, M. and Unwin, P. R. Nanoscale Structure Dynamics within Electrocatalytic Materials. *Journal of the American Chemical Society* **139**, 16813-16821 (2017).
19 Bentley, C. L., Kang, M., Maddar, F. M., Li, F., Walker, M., Zhang, J. and Unwin, P. R. Electrochemical maps and movies of the hydrogen evolution reaction on natural crystals of molybdenite (MoS_2): basal vs. edge plane activity. *Chemical science* **8**, 6583-6593 (2017).
20 Chen, C.-H., Jacobse, L., Mckelvey, K., Lai, S. S., Koper, M. T. and Unwin, P. R. Voltammetric scanning electrochemical cell microscopy: dynamic imaging of hydrazine electro-oxidation on platinum electrodes. *Analytical chemistry* **87**, 5782-5789 (2015).
21 Stehle, Y., Meyer III, H. M., Unocic, R. R., Kidder, M., Polizos, G., Datskos, P. G., Jackson, R., Smirnov, S. N. and Vlassiouk, I. V. Synthesis of hexagonal boron nitride monolayer: control of nucleation and crystal morphology. *Chemistry of Materials* **27**, 8041-8047 (2015).
22 Li, X., Zhu, Y., Cai, W., Borysiak, M., Han, B., Chen, D., Piner, R. D., Colombo, L. and Ruoff, R. S. Transfer of large-area graphene films for high-performance transparent conductive electrodes. *Nano letters* **9**, 4359-4363 (2009).
23 Chen, C.-H., Meadows, K. E., Cuharuc, A., Lai, S. C. and Unwin, P. R. High resolution mapping of oxygen reduction reaction kinetics at polycrystalline platinum electrodes. *Physical Chemistry Chemical Physics* **16**, 18545-18552 (2014).
24 Aaronson, B. D., Lai, S. C. and Unwin, P. R. Spatially resolved electrochemistry in ionic liquids: surface structure effects on triiodide reduction at platinum electrodes. *Langmuir* **30**, 1915-1919 (2014).
25 Guo, N., Wei, J., Fan, L., Jia, Y., Liang, D., Zhu, H., Wang, K. and Wu, D. Controllable growth of triangular hexagonal boron nitride domains on copper foils by an improved low-pressure chemical vapor deposition method. *Nanotechnology* **23**, 415605 (2012).
26 Chang, R.-J., Wang, X., Wang, S., Sheng, Y., Porter, B., Bhaskaran, H. and Warner, J. H. Growth of Large Single-Crystalline Monolayer Hexagonal Boron Nitride by Oxide-Assisted Chemical Vapor Deposition. *Chemistry of Materials* **29**, 6252-6260 (2017).
27 Conway, B. and Bockris, J. O. M. Electrolytic hydrogen evolution kinetics and its relation to the electronic and adsorptive properties of the metal. *The Journal of Chemical Physics* **26**, 532-541 (1957).
28 Nørskov, J. K., Bligaard, T., Logadottir, A., Kitchin, J. R., Chen, J. G., Pandelov, S. and Stimming, U. Trends in the exchange current for hydrogen evolution. *Journal of the Electrochemical Society* **152**, J23-J26 (2005).
29 Parsons, R. The rate of electrolytic hydrogen evolution and the heat of adsorption of hydrogen. *Transactions of the Faraday Society* **54**, 1053-1063 (1958).
30 Lukowski, M. A., Daniel, A. S., English, C. R., Meng, F., Forticaux, A., Hamers, R. J. and Jin, S. Highly active hydrogen evolution catalysis from metallic WS_2 nanosheets. *Energy & Environmental Science* **7**, 2608-2613 (2014).

31 Wirth, S., Harnisch, F., Weinmann, M. and Schröder, U. Comparative study of IVB–VIB transition metal compound electrocatalysts for the hydrogen evolution reaction. *Applied Catalysis B: Environmental* **126**, 225-230 (2012).

32 Greeley, J., Jaramillo, T. F., Bonde, J., Chorkendorff, I. and Nørskov, J. K. Computational high-throughput screening of electrocatalytic materials for hydrogen evolution. *Nature Materials* **5**, 909-913 (2006).

33 Yu, Y., Huang, S.-Y., Li, Y., Steinmann, S. N., Yang, W. and Cao, L. Layer-dependent electrocatalysis of MoS_2 for hydrogen evolution. *Nano letters* **14**, 553-558 (2014).

34 Yang, G.-H., Shi, J.-J., Wang, S., Xiong, W.-W., Jiang, L.-P., Burdab, C. and Zhu, J.-J. Fabrication of a boron nitride–gold nanocluster composite and its versatile application for immunoassays. *Chemical Communications* **49**, 10757-10759 (2013).

35 Rokuta, E., Hasegawa, Y., Suzuki, K., Gamou, Y., Oshima, C. and Nagashima, A. Phonon dispersion of an epitaxial monolayer film of hexagonal boron nitride on Ni (111). *Physical review letters* **79**, 4609 (1997).

36 Preobrajenski, A., Vinogradov, A. and Mårtensson, N. Ni 3d–BN π hybridization at the h−BN/Ni (111) interface observed with core-level spectroscopies. *Physical Review B* **70**, 165404 (2004).

37 Preobrajenski, A., Vinogradov, A. and Mårtensson, N. Monolayer of h-BN chemisorbed on Cu (111) and Ni (111): The role of the transition metal 3d states. *Surface science* **582**, 21-30 (2005).

38 Joshi, S., Ecija, D., Koitz, R., Iannuzzi, M., Seitonen, A. P., Hutter, J., Sachdev, H., Vijayaraghavan, S., Bischoff, F., Seufert, K., Barth, J. V. and Auwarter, W. Boron nitride on Cu (111): an electronically corrugated monolayer. *Nano letters* **12**, 5821-5828 (2012).

39 Elumalai, G., Noguchi, H. and Uosaki, K. Electrocatalytic activity of various types of h-BN for the oxygen reduction reaction. *Physical Chemistry Chemical Physics* **16**, 13755-13761 (2014).

40 Benck, J. D., Hellstern, T. R., Kibsgaard, J., Chakthranont, P. and Jaramillo, T. F. Catalyzing the Hydrogen Evolution Reaction (HER) with Molybdenum Sulfide Nanomaterials. *ACS Catalysis* **4**, 3957-3971 (2014).

Chapter 7. Summary

In this thesis, the electrochemistry of carbon materials, including sp^3 (BDD) and sp^2 (graphene and carbon nanotubes) materials, and the graphene-like material h-BN has been investigated using a range of experimental techniques on length scales ranging from the macroscale to the nanoscale. Macroscale measurements that use a droplet method, allow for the electrodeposition of $Ni(OH)_2$ NPs on SWNTs either through an indirect approach or direct approach and their electrocatalytic activities towards the AOR has been studied by using MCEM. By employing high resolution SECCM, combined with other correlative and co-located microscopy techniques, such as SEM and Raman mapping, spatially resolved studies of the fundamental electrochemical properties at local features (facets, number of layers and edges) are possible. The correlation between electrochemical activity and structure in complex systems can be directly observed and a deeper understanding of the electrochemical processes at the nanoscale can be attained. This strategy has been used to study the ET kinetics of graphene on a Cu foil where the graphene structure is made up of varying numbers of layers, the facet-resolved solvent window properties of O-BDD and H-BDD in aqueous chloride solutions and to probe the HER activities of metal supported h-BN.

In chapter 3 we investigated how the number of graphene layers affects the ET kinetics of as-grown graphene on a Cu foil. Without any transfer the ET kinetics of graphene can be obtained and compared to data in the literature for more conventional Si/SiO_2 supports. Using the $Ru(NH_3)_6^{3+/2+}$ redox couple, voltammetric SECCM has demonstrated that monolayer graphene on Cu exhibits faster ET behaviour than that observed for bi- and multilayer graphene, which is the opposite trend compared to graphene on Si/SiO_2. The $E_{1/2}$ value of monolayer graphene was shown to be more positive than that for over the bilayer and multilayer regions. Furthermore, the $|E_{3/4} - E_{1/4}|$ value strongly varied with different numbers of graphene layers and suggested that the reduction of $Ru(NH_3)_6^{3+}$ is more reversible on the monolayer graphene. Additionally, it was found that the SECCM methodology employed was able to resolve pinholes in the graphene through to the Cu foil with positive currents that result from the corrosion of the electrolyte containing Cl^- ions seen over exposed Cu. Such pinholes would contribute to the electrochemistry on the macroscale, but are easily eliminated through high resolution electrochemical mapping. The crystal orientation effects of the

underlying Cu foil on the ET kinetics of graphene was also investigated by SECCM. The results reveal that no ET kinetics variation was detectable across different crystal orientation grains.

Chapter 4 presented a systematic examination of the microscopic factors affecting the aqueous solvent (electrolyte) window of BDD electrodes in chloride-containing salt solutions by using SECCM in conjunction with EBSD and Raman microscopy. It was found that the solvent window was affected by the local boron dopant concentration, with the solvent window of less-doped facets being wider than that of those which were more-doped, irrespective of the surface termination. It was noted that the onset potential for the anodic process was relatively insensitive to the boron dopant concentration for O-BDD, but was doping dependent on H-BDD. However, the cathodic onset potential was boron doping dependent and more facilitated at O-BDD. As a result, both the boron dopant concentration and surface termination are key factors affecting the solvent window properties of BDD.

Chapter 5 explored the structure-electrocatalytic activity relationships of $Ni(OH)_2$ NPs produced by two different electrochemical approaches on HD SWNT networks. For the indirect approach, the Ni NPs were electrodeposited on the SWNTs and then transformed to $Ni(OH)_2$ by electrochemical potential cycling in alkaline solution. For the direct approach, $Ni(OH)_2$ NPs were formed by electrochemical generation of relative high concentration of OH^-, in the presence of Ni^{2+}. A correlation between structure and electrocatalytic activity for $Ni(OH)_2$ NPs was revealed by HR-TEM. α-$Ni(OH)_2$ NPs formed via the direct approach, exhibited remarkable specific activities (SA) of ~2.8 kA g^{-1} for 0.5 M methanol and ~3.7 kA g^{-1} for 0.5 M ethanol. However, β-$Ni(OH)_2$ NPs formed via the indirect approach showed SA values about an order of magnitude lower.

In chapter 6, a systematic study of HER activity for h-BN on metal substrates was carried out using high resolution electrochemical imaging. The electrocatalytic activity of h-BN/Cu was investigated by single-barrel SECCM coupled with FE-SEM. The Tafel slope associated with the h-BN/Cu was found to be 136 mV per decade and its exchange current density (j_0) was estimated to be 4×10^{-8} A cm^{-2}. After transferring the h-BN onto Au substrate, the h-BN/Au shows much better electrocatalytic performance towards HER, with a Tafel slope of 108 mV per decade and a j_0 value of 1×10^{-6} A cm^{-2}. This significant enhancement was attributed to differences in the substrate effect between h-BN and Au/Cu, opening up the possibility of tuning reactivity (*e.g.*, catalytic activity) through the underlying metal support.

To conclude, correlative high resolution SECCM, a powerful tool for exploring structure-electrochemical activity correlation, can be used to study fundamental electrochemical properties of new carbon materials including graphene, carbon nanotubes and BDD, which was evident in our experimental results. In future work, it would be interesting to investigate electrocatalytic activities of 2D heterostructures for HER, ORR or OER.